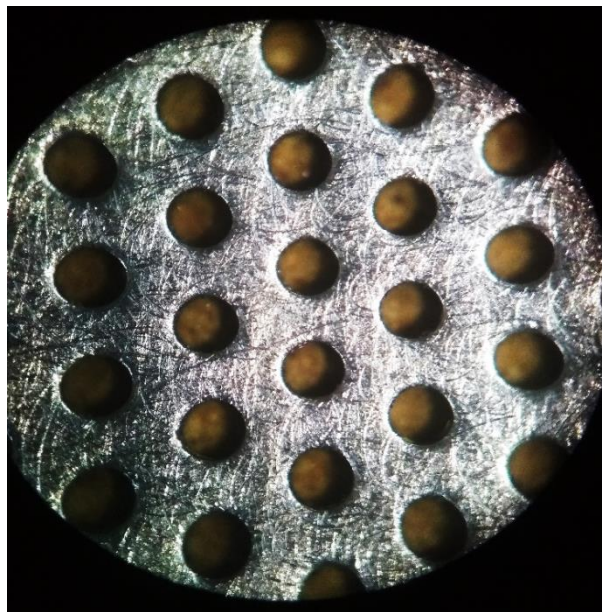




POTENTIAL USE OF FIBRE- STEEL LAMINATES IN HYBRID DECK SYSTEMS

Alex Dreaves



JULY 13, 2018

TU DELFT

Potential Use of Fibre-Steel Laminates in Hybrid Deck Systems

By

A. Dreaves

in partial fulfilment of the requirements for the degree of

Master of Science

in Civil Engineering

at the Delft University of Technology,

to be defended publicly on **Friday July 13, 2018 at 13:30 PM.**

Daily Supervisor: Dr. M. Pavlovic TU Delft

Thesis committee: Prof. dr. M. Veljkovic,(chair) TU Delft

Ir. R. Grefhorst, Infracore Company

Dr. Ir. F.P. Van der Meer, TU Delft

Ir. L. Houben, TU Delft

An electronic version of this thesis is available at <http://repository.tudelft.nl/>.



ABSTRACT

Over the last two decades Fibre-Reinforced Polymer (FRP) constructions have infiltrated the infrastructure market, particularly in the Netherlands. This is due to the increased number of short-span pedestrian and cycle bridges which are used to traverse canals and waterways. FRP bridges are desirable as they are lightweight, require low maintenance, are easily pre-fabricated and can be installed in a matter of hours.

However, the main drawback of FRP constructions is that they lack stiffness meaning they are often vastly over-designed with regards to strength. The stiffness of glass fibre-reinforced polymers (GFRP), one of the most common types of FRP and the focus of this thesis, is approximately 5 times less than steel (1). For this reason, it is desirable to increase the stiffness of GFRP members; one way of doing such is to add a stiffer material to the laminate to create a hybrid-composite material. Hybrid-composites look to combine the advantageous properties of two materials, to produce a material superior to both of its individual component materials.

This project focuses on the development and feasibility review of a fibre-steel hybrid-composite material, combining GFRP and steel into one laminate. A review of the state of the art of hybrid-composites guides the reader to potential problems that may arise with this combination. Through the testing and analytical estimation of the properties of the material and its component materials, the behaviour of the fibre-steel laminate (FSL) is discussed and evaluated. Using the established properties, a design case study of a hybrid deck system reviews the economic feasibility of the use of FSL ahead of the GFRP equivalent.

The results of this two-fold approach form recommendations for the next steps of the investigation into the use of this material. It is recommended that the main focus of subsequent studies revolve around the improvement of the steel-GFRP interface as this was found to be a weak point in the material given the difference in in-plane properties of the two materials.

ACKNOWLEDGEMENTS

I would like to take this opportunity to thank my daily supervisor, Dr. Marko Pavlovic, who has guided me through the twists and turns of the project, encouraging me and developing my knowledge in a patient and supportive manner. I also would like to extend my gratitude to the rest of the graduation committee for their professional advice and feedback.

Finally, I would like to thank my friends and family in Delft and in the UK for their continued support and encouragement through a journey that wouldn't have been at all possible without them.

Alex Dreaves

Delft, July 2018

TABLE OF CONTENTS

Abstract.....	IV
Acknowledgements.....	V
Table of Figures	X
1 Introduction	1
1.1 Background of Composites and Hybrid Composites	1
1.2 Project Motivation.....	2
1.3 Objectives, Scope & Limitations	3
1.4 Research Questions	4
1.5 Thesis Overview.....	4
1.5.1 Literature Study & Background Information.....	4
1.5.2 Experimental Material Development	5
1.5.3 Composite Deck Case-Study.....	5
2 Literature Review & Background Info	6
2.1 Fibre-Reinforced Polymers.....	6
2.2 Fibre-Metal Laminates	8
2.2.1 Material Behaviours.....	9
2.3 Current Research of Fibre-Steel Laminates	18
2.3.1 Production.....	18
2.3.2 Component Material Behaviours	19
2.3.3 Steel-FRP Interface	20
2.3.4 Cutting of FSL.....	27
2.3.5 Summary	30
2.4 Composite Deck Systems	31
3 Fibre-Steel Laminate Material Investigation	33
3.1 Introduction.....	33

3.2	Fibre-Steel Laminate	33
3.3	Experimental & Supplementary Investigations.....	34
3.3.1	Uniaxial Tensile Tests.....	34
3.3.2	Inter-Laminar Shear Tests	42
3.3.3	Flexural Behaviour: Fibre-Steel Laminate (FEA/CLT).....	51
3.3.4	Thermal Behaviour (FEA/CLT)	52
3.4	Summary.....	54
4	Advanced Composite Deck Systems.....	56
4.1	Introduction	56
4.1.1	Aims	56
4.1.2	Methodology & Scope.....	57
4.1.3	Geometry	58
4.1.4	Loading.....	59
4.1.5	Material Properties	61
4.2	Optimised System Design	63
4.2.1	General	63
4.2.2	FSL Cellular Deck Design.....	67
4.2.3	FSL Solid Slab Deck Design.....	80
4.2.4	GFRP Cellular Deck.....	85
4.2.5	Design Summary	87
4.3	Results & Comparison.....	88
4.3.1	System Verifications	88
4.3.2	Shear Interaction	92
4.3.3	Longitudinal Direction	92
4.3.4	Transverse Direction.....	100
4.3.5	Global Buckling Analysis	103
4.3.6	Inter-Laminar Shear Strength	105

4.3.7	Cost Comparison.....	107
4.4	Summary & Discussion.....	109
4.4.1	FSL Cellular Deck.....	110
4.4.2	Solid Slab FSL Deck.....	111
4.4.3	Most Effective System.....	112
5	Summary & Conclusions.....	113
5.1	Fibre-Steel Laminate Material Investigation.....	114
5.2	Composite Deck Case-Study.....	114
5.3	Outlook & Future Studies.....	115
	References.....	117
	Appendix A: Production & Cutting of FSL.....	122
	Component Materials.....	123
	Cutting.....	125
	Appendix B: Hybrid Deck Hand Calculations.....	126
	General Details.....	126
	FSL Cellular.....	127
	Appendix C: Hybrid System Finite Element Model.....	136
	Model Geometry.....	136
	Boundary Conditions & Constraints.....	137
	Evaluation of FE Model.....	138
	Outcomes.....	147
	Appendix D: Base Material Costs.....	148
	Appendix E: Self-Supporting Deck Analysis.....	149
	FSL Deck.....	149
	GFRP Deck.....	149
	Cost Analysis.....	149

TABLE OF FIGURES

Figure 2.1: Laminate composition, where: 1-Longitudinal (0°), 2-Transverse (90°) (3).....	6
Figure 2.2: Inter-laminar shear strength of FRP and FML counterparts (14)	9
Figure 2.3: Delamination within a 6/5 Carbon-fibre steel laminate (42).....	10
Figure 2.4: Difference between isotropic metal (a) and composite (b) fatigue crack formation and propagation (18).....	10
Figure 2.5: Alternate load path/crack bridging mechanism of FML (15) (11).....	11
Figure 2.6: Crack propagation time between FMLs and 2024-T3 aluminium (6).....	12
Figure 2.7: Infracore Inside Technology (56).....	12
Figure 2.8: Impact damage in Carbon/epoxy laminate (21) (10)	13
Figure 2.9: A comparison of GLARE 3 and other aerospace materials (6).....	13
Figure 2.10: Static strength loss due to impact damage (21)	14
Figure 2.11: Predicted and experimental creep data based on Ascione’s model, shown in right figure (23)....	15
Figure 2.12: Comparison of acid-bath corrosion in ARALL-3 (left) and 2024-T3 (right) (26)	16
Figure 2.13: Comparison of delamination growth rate in two samples of ARALL on the basis of cyclic stress in the non-delaminated aluminium sheets (13).....	17
Figure 2.14: Influence of metal thickness ratio on laminate performance (27)	17
Figure 2.15: (A) Force/displacement curves & failure photographs for different manufacturing techniques of FSL (28)	18
Figure 2.16: (A) Sandwich panel damaged by initial impact, (B) Propagation of delaminating crack, causing catastrophic failure (56).....	19
Figure 2.17: Cross-section schematic of debonding process during rebound phase of impact test (29).....	19
Figure 2.18: Interlocking projection definition (34) (35)	21
Figure 2.19: Tensile Single lap-shear testing of structured and un-structured metal-FRP interfaces (33)	22
Figure 2.20: Analysis of projection pattern and stress distribution (35).....	22
Figure 2.21: (A) CFRP-steel interface, showing structures cutting into carbon fibres (B) Sacrificial natural fibres inter-ply, (C) Sand-blasted structures with carbon fibres moulded around blunted shape (36)	23

Figure 2.22: Comparison of structured and unstructured hybrid composites, from double lap shear tests (38)	24
Figure 2.23: (A) Comeld™ joint created with Surfi-Scuplt™ technology, (B) Comparison of Comeld double lap joint and adhesive control joint (39) (40)	25
Figure 2.24: Interlaminar Shear Strength of CFRP-Steel interface based on (A) different surface treatments and (B) different compositions (42)	26
Figure 2.25: Mode I & Mode II Cracking Definitions (57)	27
Figure 2.26: Edge quality comparison: Conventional milling (left) and laser machining (right) (43)	28
Figure 2.27: Comparison of laser and waterjet cutting (45)	28
Figure 2.28: (A) Waterjet cutter without abrasives, (B) AWJ - Abrasive waterjet cutter (46)	29
Figure 2.29: Comparison of ILSS based on cutting technique (44)	29
Figure 2.30: (A) Water-wedging effect (46), (B) Back-face delamination caused by stunted water propagation (58)	29
Figure 2.31: Composite action in steel beam-concrete slab composite deck structure (59) (60)	32
Figure 3.1: Ply stack layup of FSL for experimental analysis	33
Figure 3.2: Specimen Cutting for Anisotropic Material	34
Figure 3.3: Axial Stress v Strain Graph for 0° Fibre Orientation	36
Figure 3.4: Failed 0° Sample	36
Figure 3.5: Stress v Strain graph for 90° fibre orientation	37
Figure 3.6: Failed 90° Sample	37
Figure 3.7: Stress v Strain Curves: Perforated Steel	38
Figure 3.8: Merging of Perforations in Steel Samples	39
Figure 3.9: Failed Perforated Steel Sample	39
Figure 3.10: Stress - Strain Relations of Individual Components and Hybrid-Composite	41
Figure 3.11: Short-beam Shear Test Schematic with (left) Shear Stress and (centre) Flexural Stress Distributions Overlaid	42
Figure 3.12: Flexural Stress-Strain Relationship for Longitudinal FSL Samples	43
Figure 3.13: Initial Delamination	44

Figure 3.14: Elastic and Plastic Deformation of GFRP and Steel Plies Respectively	44
Figure 3.15: Fracture Energy Comparison FSL v GFRP	44
Figure 3.16: Flexural Stress-Strain Relationship for Transverse FSL Samples.....	45
Figure 3.17: Flexural Stress-Strain Relationship for GFRP Samples	46
Figure 3.18: Failed GFRP ILSS Samples.....	47
Figure 3.19: (left) Comparison of Inter-Laminar Shear Stress Using Continuum Shell Elements with and without Cohesive Interface Properties Defined for FSL, (right) Inter-Laminar Shear Stress Distribution in GFRP	48
Figure 3.20: FE Images Showing Initiation and Propagation of Shear Damage in FSL.....	49
Figure 3.21: Comparison of FSL Inter-Laminar Shear Stress Distribution with Layup Change	50
Figure 3.22: Inter-Laminar Shear Stress Distribution due to Differential Thermal Expansion at 50°C.....	53
Figure 4.1: Longitudinal & Transverse Definition (47).....	56
Figure 4.2: A) Deck geometry, B) Beam geometry, C) Axle-load geometry	58
Figure 4.3: Floor Plan of Typical Car Park Level.....	59
Figure 4.4: Beam Spacing Schematic.....	65
Figure 4.5: Floor Plan of Typical Car Park Level.....	65
Figure 4.6: (A) Sandwich panel damaged by initial impact, (B) Propagation of delaminating crack, causing catastrophic failure (56).....	67
Figure 4.7: Infracore Inside Technology (56)	67
Figure 4.8: Vertical stress & strain distribution at mid-span with and without foam cores	69
Figure 4.9: Average Longitudinal Stress in Skin, Left - With Foam Cores; Right - Without Foam Cores. Top – Top Skin; Bottom – Bottom Skin.....	69
Figure 4.10: Average Longitudinal Stress at Mid-Span	70
Figure 4.11: Force - displacement curve for FRP decks with and without foam cores and beam only as benchmark	70
Figure 4.12: (A) (B) Longitudinal stress and strain plotted along length of deck at interface with beam, (C)(D) Longitudinal stress/strain plotted at mid-span cross-section	72
Figure 4.13: Average Longitudinal Stress in Skin, Left - With FSL Webs; Right – With GFRP Webs. Top – Top Skin; Bottom – Bottom Skin.....	73

Figure 4.14: Force - displacement curve for FSL deck with (A) GFRP webs and (B) FSL webs	74
Figure 4.15: Longitudinal stress/strain in top and bottom skin of 100mm and 200mm FSL decks, plotted along length of deck	75
Figure 4.16: Longitudinal stress/strain for 100mm and 200mm FSL decks, plotted at vertically at mid-span cross-section	76
Figure 4.17: FSL Cellular Deck Isotropic View, Skin Laminate Layup & Cross-Section	78
Figure 4.18: GFRP Deck Dimensions.....	85
Figure 4.19: Average Longitudinal Stress Distribution Across Width of Various Decks	93
Figure 4.20: Longitudinal Stress Distribution Across Width of Bottom Skin of Deck	95
Figure 4.21: FE output showing the longitudinal stress distributed over bottom skin of each deck, from left to right: FSL Cellular, FSL Solid Slab, GFRP Cellular	95
Figure 4.22: Longitudinal Stress Distribution Across Width of Top Skin of Deck	97
Figure 4.23: FE output showing the longitudinal stress distributed over top skin of each deck, from left to right: FSL Cellular, FSL Solid Slab, GFRP	97
Figure 4.24: Vertical Distribution of Longitudinal Stress/Strain at Mid-Span Cross-Section.....	98
Figure 4.25: Force v Displacement Curves for ULS/SLS	99
Figure 4.26: : Transverse Stress Plotted over Bottom Skin of Each Deck, clockwise from top left: FSL-1, FSL-2, Solid Slab, GFRP	100
Figure 4.27: Transverse Stress Distribution Over Bottom Skin, from left to right: FSL Cellular, FSL Solid Slab, GFRP Cellular.....	101
Figure 4.28: Transverse Stress Plotted Across Width of Bottom Skin of Deck Plotted at Mid-Span	101
Figure 4.29: Transverse Stress Plotted Across Width of Top Skin of Deck Plotted at Mid-Span.....	102
Figure 4.30: Transverse Stress Distribution Over Top Skin, from left to right: FSL Cellular, FSL Solid Slab, GFRP Cellular.....	102
Figure 4.31: Buckling Modes Incorporating Deck Buckling, clockwise from left: FSL Cellular, FSL Solid Slab FSL, GFRP Cellular.....	103
Figure 4.32: Inter-Laminar Shear Stress at Support Location.....	106
Figure 4.33: System Cost Comparison	107
Figure 4.34: Cost per Longitudinal Composite Stiffness Unit Comparison.....	108

Figure A.0.1: Resin Micro-Structures Forming Through the Perforations in the Steel	123
Figure A.0.2: Magnified Image of Treated Steel	123
Figure A.0.3: (top) Dry E-Glass Fibres, (bottom) De-gassing of Resin.....	124
Figure A.0.4: Delamination Caused by Abrasive Water-jet Cutter	125
Figure A.0.5: Non-localised Corrosion of Steel due to Water Ingress from Cutting Attempt	125
Figure A.0.6: Material Damaged by Inappropriate Saw	125
Figure 0.7: A) Deck span symmetry, B) Beam span symmetry	136
Figure 0.8: Longitudinal Bending Moment at Mid-Span in FE Model Expressed in N.mm	138
Figure 0.9: Reduction in Longitudinal Stress in Deck due to Interaction with Beam.....	139
Figure 0.10: Theoretic Bending Moment Curve for Central Section of Continuous Beam.....	140
Figure 0.11: Transverse Bending Moment at Support Location from FE Model (N.mm/m).....	140
Figure 0.12: Transverse Bending Moment at mid-span Location from FE Model (N.mm/m).....	140
Figure 0.13: Transverse Stress Distribution Across Deck with Mid-Span and Support Location Transverse Moments Superimposed.....	141
Figure 0.14: Stress and strain distribution at mid-span of beam plotted across vertical cross-section	142
Figure 0.15: Longitudinal strain and stress distributions along length of deck (to mid-span).....	143
Figure 0.16: Force - displacement comparison between deck with and without shear interaction	144
Figure 0.17: Single cross-section Definition (53).....	144

1 INTRODUCTION

1.1 BACKGROUND OF COMPOSITES AND HYBRID COMPOSITES

The philosophy behind composite materials is to combine the attributes of two materials, to form one single material that has functional benefits over its individual components. In structural engineering, many fibrous materials are combined with polymer resins, to combine the strength of the fibres with a binding agent that also provides stability to the fibres, known as **Fibre-Reinforced Polymers (FRP)**. Examples of such materials include glass fibre-reinforced polymers and carbon fibre-reinforced polymers, GFRP and CFRP respectively. Reinforced-concrete is another example of a composite material that uses steel to negate concrete's poor tensile properties, while maintain the concrete's high compressive strength.

Hybrid composite materials add one further component into the composition, which can provide a new range of properties that improve the performance of the original composite material. Many modern hybrid composites combine advancements into FRPs with lightweight, metal alloys. These materials are combined to utilise the high strength to weight properties of FRP with the inherent stiffness and plasticity of the metal alloys. For this reason, when compared to each of the individual materials, the fibre-metal laminate (FML) can offer an improved performance. Table 1 shows how the combination of FRP and a typical metal alloy can use the strengths of one material to address the weaknesses of the other and vice versa.

Table 1.1: Individual Component Strengths/Weaknesses

Material	Strengths	Weaknesses
FRP	<ul style="list-style-type: none">• Fatigue• Strength to Weight Ratio• Corrosion Resistance	<ul style="list-style-type: none">• Damage Tolerance (brittle)• Stiffness
Metal Alloys	<ul style="list-style-type: none">• Damage Tolerance (ductile)• Stiffness	<ul style="list-style-type: none">• Fatigue• Corrosion Resistance

However, the merging of the two materials into laminated structures is where the difficulty arises. The achievable bond strength between metal plies and FRP plies in the laminated structure is often found to be inadequate and is therefore the main hurdle for the development of these materials.

The nomenclature for continuous fibre-reinforced polymers combined with metal alloys in a laminated structure is fibre-metal laminates (FMLs). Some of the most commercially available FMLs include

combinations of aluminium alloy with glass, carbon or aramid fibre-reinforced resin layers (known as GLARE, CARALL and ARALL respectively).

The aerospace and automotive industries have long used fibre-metal laminates (FMLs) to achieve the greater performance and increased weight-savings, that constant technological and societal advances demand. In these fields, lower weight body panels for the respective vehicles allows higher fuel economy, and with fossil fuels becoming more scarce and environmental concerns becoming more prevalent, the advancements have outgrown single material use. However, with weight saving being the primary goal in these industries, steel is seldom used as the metal ply in FMLs due to its higher self-weight when compared to other metals like aluminium or even titanium in some applications.

The barrier of the poor adhesion between the plies has been overcome in these industries by using a high pressure, high temperature autoclave machine which stamps the two materials together, this process also enables easier mass production and automation (2). This, however, requires costlier thermoplastic resins that are generally unsuitable for infrastructure applications, due to their cost and often poor time-dependent behaviour under constant static loading (3).

1.2 PROJECT MOTIVATION

This research looks to develop a hybrid composite material that will optimise GFRP structural components that are utilised in civil and infrastructure applications - without compromising their current economical state with advanced manufacture and materials. This means that thermoplastic resins, autoclave production and light-weight metal alloys like aluminium or titanium are not feasible.

The design of GFRP structural components are driven by serviceability criteria and are often over designed with regards to their ultimate strength. This is because of the low stiffness of the material (around 5 times less than steel (1)). Given its increased stiffness and low cost, steel is the logical choice of metal to include as an inter-ply. Other secondary benefits of this combination could be the improved fatigue behaviour and durability of GFRP compared to steel and the improved plastic behaviour of steel compared to GFRP. Conversely, an increase in the self-weight of the material will have to be accepted due to the high density of steel (in comparison to GFRP). This material will be hereby referred to as a fibre-steel laminate (FSL).

In order to maintain the low costs of the material, traditional FRP production techniques are desirable, one of the most economical of these is vacuum assisted resin transfer moulding (VARTM). However, the level of adhesion achievable through this technique is lesser than that of the autoclave technology due to the lower pressure used. It is therefore important to consider the improvement of this interface through mechanical or chemical means. This project will establish the properties of the hybrid-composite material with basic interface improvement, with the idea of obtaining the lower bound of interface strength (inter-laminar shear strength (ILSS)).

1.3 OBJECTIVES, SCOPE & LIMITATIONS

Given the infancy of the development of fibre-steel laminates, there are a myriad of topics that require further research before this material becomes a commercially available product. However, the scope of this thesis must be refined to comprehensively cover just a few of these research points. The most pressing and fundamental of these points are the material's behaviours and its effective implementation. Beyond this laminate level investigation, a micro-scale study should be undertaken to further understand the materials behaviours on ply and fibre levels

The primary idea behind the addition of steel inter-ply is to increase the stiffness of the laminate; therefore, the key material property to test for is the Young's modulus, which is established through tensile testing. The underpinning factor of whether the material can perform as envisaged, is the strength between the laminae - the inter-laminar shear strength (ILSS). The ILSS was already highlighted in a previous study as a potentially major weakness, thus, it will be the second material property that will be tested. This is experimentally determined by a short-beam shear test, which encourages the specimen to fail at the ends in mode I cracking (representative of a delamination within the laminate (see [section 2.3](#))).

A final objective of the study is to investigate the feasibility of the use of this material in a composite system. This is because recent research has shown how GFRP can be used in place of a concrete deck in a composite system to achieve easier erection and lower maintenance structures. To do this, a case-study investigating the use of fibre-steel laminates for car parking structures will be developed. The systems will be optimised to minimise material and construction depth. Comparisons will be given between different FSL and GFRP designs to evaluate them based on performance and cost.

As previously mentioned, the development of this material is at a very early stage, so naturally there are research points that are outside the scope of this thesis but are instrumental to the future development of fibre-steel laminates. The following are just a few of the most crucial aspects to explore:

- Long-term behaviour
 - Differing creep behaviour of the two materials
 - Fatigue response
- Environmental behaviour
 - Differing corrosive behaviours
- Connection to other members (shear connection to steel beams specifically)
 - Mechanical connection
 - Adhesive connection
- Resin flow optimisation through hybrid-composite
- Alternate production techniques
- Chemical and mechanical improvement of steel-GFRP interface

1.4 RESEARCH QUESTIONS

The project can be split into two main parts, a case study and an experimental investigation, which aim to answer the following research questions:

1. Based on the VARTM manufacturing technique what are the properties of a fibre-steel laminate?
 - Using basic interface improvements, what is the achievable inter-laminar shear strength of a fibre-steel laminate?
 - Will this strength inhibit the use of the material in commercial application?
2. Can fibre-steel laminates be effectively used in a composite system?
 - What is the most effective configuration of an FSL composite system, with regards to material and cost reduction?
 - Is it superior to the GFRP equivalent?

1.5 THESIS OVERVIEW

1.5.1 Literature Study & Background Information

A review of current literature will be undertaken to provide a background, motivation and update of the state-of-the-art of this material and its predecessors and individual components. The literature study will be undertaken in **section 2** and aims to cover:

- Fibre-reinforced polymers (FRP)
- Fibre-metal laminates (FML)
- The current state of the art of fibre-steel laminates (FSL)
- Fibre-metal interface
 - Difficulties
 - Improvement
 - Testing
- Cutting of FSL/FMLs
- Interaction between FRP and steel girders
 - Shear connection
 - Composite behaviour

1.5.2 Experimental Material Development

The experimental phase aims to cover the basic material properties required to design with FSL, such as tensile strength and inter-laminar shear strength; this will be used to validate models and strength predictions of the material.

First the individual components (GFRP and perforated steel) will be tested in uniaxial tension, this will give the stiffness and ultimate tensile strength of the various plies. Using this data, the properties of the fibre-steel laminate can be estimated.

Next, a plate of fibre-steel laminate will be produced at the Infracore facility (with basic steel surface treatment). Upon completion of production of the plate, the most suitable cutting technique will be investigated and various cutting methods will be trialled to see which yields the best samples.

Once the plate of material has been cut into suitable samples it will be tested to evaluate the inter-laminar shear strength of the laminate. This is the resistance to mode I cracking also known as delamination - a likely weak point of the material.

To summarise, the experimental testing period will include:

- Component material uniaxial tensile tests:
 - GFRP (both directions of unidirectional laminate)
 - Perforated steel
- Cutting of FSL
- Short-beam shear tests:
 - GFRP
 - FSL

Full details are available in [section 3](#).

1.5.3 Composite Deck Case-Study

As a method to exhibit the most efficient use of fibre-steel laminates, a case-study, investigating the application of FSL decks in parking structures will be developed. The case-study will be limited to the use of composite beam-deck systems that are commonly used in parking facilities. Performance comparisons between different FSL designs will be given with specific regard to the decks ability to transfer forces between the beams and its resistance to the longitudinal compression induced by the bending of the supporting beams. Economic comparisons with current GFRP systems will also be given to evaluate the economic viability of fibre-steel laminate decks.

Full details are available in [section 4](#).

2 LITERATURE REVIEW & BACKGROUND INFO

2.1 FIBRE-REINFORCED POLYMERS

Fibre-reinforced polymers (FRP) are a type of composite material that combine layers of very small ($\varnothing=12\mu\text{m}$ (4)) but high strength fibres with a viscous resin matrix; upon curing of the viscous matrix a unique composite material is born with highly desirable properties. There are a number of materials that can make up an FRP composite, with a range of resin and fibre types that yield different properties upon combination. However, most of them possess high strength to weight and corrosion resistance attributes. There are also a number of production techniques each with their own circumstantial advantages and disadvantages.

Fibres can be made from a range of materials, including glass, carbon and aramid and generally have a very high tensile strength in the longitudinal direction (carbon fibres up to 7GPa (1)). Glass fibres are the most commonly used in civil engineering applications due to their low cost ($\sim\text{€}2/\text{kg}$ (1)). Fibres are very anisotropic, meaning that in order to create a suitable, structural material fibres must be placed in different alignments to provide strength in various directions. Figure 2.1 shows the creation of a laminate where unidirectional fibres are placed in plies at different angles to create a material with load carrying ability in each of the directions.

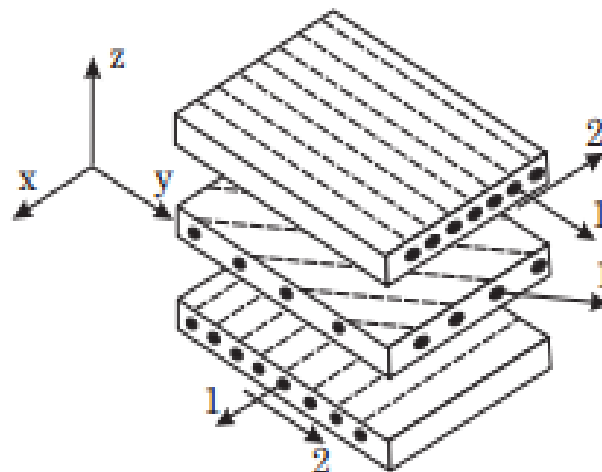


Figure 2.1: Laminate composition, where: 1-Longitudinal (0°), 2-Transverse (90°) (1)

While the fibres give the material most of their strength, the resin also performs a key role in bonding the fibres together. This bond restrains the fibres from buckling under compressive load; due to the very small size of the dry fibres they can buckle very easily under minimal load if they are not restrained. The resin also provides environmental protection to the fibres, which is leading to FRP becoming a serious competitor to steel and reinforced concrete in the infrastructure sector, due to lower levels of maintenance required for bridges (1).

Due to the high strength of the fibres the material has a high strength to weight ratio, which is beneficial in a number of applications. For this reason, many new applications which benefit from high strength, low weight structures have adopted FRP ahead of traditional materials or new-age metal alloys. Other benefits over conventional materials like steel and concrete include: more favourable fatigue behaviour, pre-fabrication possibilities and the ability to design the strengths in each direction.

Initially due to the higher cost of the material when still in its infancy, it was taken up by high performance and financially well supported applications like Formula 1 motor sports. Beneficial in this instance as the lower weight means, less fuel consumption and higher speeds. The modern consumer automotive industry looks to take this up now as cheaper mass production methods have been developed and weight reduction becomes ever more pertinent in a world with diminishing levels of fossil fuels. Continued research and development from early adopters has led to refined manufacturing and production techniques that paved the way for a range of markets, such as: cryogenics, sports equipment and the aerospace and naval industries.

However, FRP is not without its limitations. Due to the relatively low stiffness of the material, when compared with traditional construction materials like steel, serviceability criteria govern many FRP designs. FRP doesn't have the ability to deform plastically and hence exhibits a brittle failure mode, this means that it struggles to continue to provide structural performance after impact damages.

It is worth noting that the term "FRP" accounts for a broad range of materials that have a large variance in properties depending on the type, orientation and distribution of fibres as well as resin and manufacture type.

2.2 FIBRE-METAL LAMINATES

In the aerospace industry aluminium is used a lot due to its low weight, however, the fatigue properties of aluminium are less desirable and so in the 1970's research was undertaken to combine aluminium with FRP layers in order to address the fatigue issues whilst retaining a lightweight structure. This is what is known as a fibre-metal laminate (FML). FML's are now a mainstay of aircraft construction, being used in fuselage panels of the Airbus A380 series (5) (6). Some of the most commercially available FMLs include combinations of aluminium alloy with glass, carbon or aramid fibre-reinforced resin layers (known as GLARE, CARALL and ARALL respectively).

Table 2.1: Material Properties

Material	Longitudinal Young's Modulus (GPa)	Transverse Young's Modulus (GPa)	Longitudinal Tensile Strength (MPa)	Density (kg/m ³)
Aluminium 2024 T3 (7)	74	74	300	2780
Steel S235 (7)	210	210	235	7800
Polyester Resin (8)	3.8	3.8	70	1080
E-Glass Fibres (4)	72.5	72.5	1900	2590
GFRP (UD with Polyester) (7)(1)	37.9	11.3	903	1850
GLARE – 1 2/1 Layout (6)	66	54	525	2520

The mechanical properties of FMLs are a product of their components. Generally, the metal alloy provides a high bearing strength and stiffness and the FRP provides strength in-plane and out-of-plane (depending on fibre orientation).

Experimental studies into GLARE have shown that some of the basic material properties are (approximately) linearly dependent on the Metal Volume Fraction ratio (MVF); for example, ultimate failure strength, yield strength, shear modulus and Young's modulus (9).

FRP has a relatively low stiffness compared to metal alloys and hence, most pure FRP designs are governed by serviceability criteria. Conversely, metals, and steel in particular, has a high stiffness and serviceability criteria are often less of an issue. This makes FMLs particularly useful as the weakness of one material is addressed by the strengths of the other. Within the infrastructure sector, this may become a very useful feature as it will allow the overdesign with regards to serviceability criteria to be reduced and less FRP material can be used. In the current construction market, FRP materials have a higher cost than steel, it could therefore be financially beneficial to reduce the over-design of FRP members through the addition of steel into the laminate.

2.2.1 Material Behaviours

2.2.1.1 Delamination

Delaminations are separations of two materials caused by the failure of the bond between them. Delaminations occur due to inter-laminar shear stresses at the interface, caused by the elongation of fibres due to applied loading, either statically or dynamically (fatigue cracking) (10). Temperature and moisture are also known to cause issues in the interface between fibre and matrix (11).

In FMLs delamination growth can be restricted when the metal plates are plastically deformed by the applied load, leading to a reduction in the amount of inter-laminar shear stress at the boundary of the interface (12) (13). This cannot happen in pure FRP elements as there is negligible plastic deformation within the material.

However, this does not mean that FMLs outperform pure FRP in terms of inter-laminar shear strength; quite the contrary – the ply interfaces where delaminations tend to occur, are mostly where there are large variations of the in-plane properties of the different plies (10). Hence, it is most likely that delaminations will occur at metal-FRP interfaces. This can be observed in figure 2.3 where it can be seen that there are a number of delaminations at either side of the specimen at the metal-fibre interface. Botelho et al (14) show in figure 2.2, that when comparing pure FRP materials with their FML counterpart they outperform them by more than double.

Specimen	τ (MPa)
Carbon fiber/epoxy	84.5 ± 2.1
Glass fiber/epoxy	87.2 ± 1.1
Caral	38.1 ± 1.2
Glare	40.2 ± 1.7

Figure 2.2: Inter-laminar shear strength of FRP and FML counterparts (14)

Some fatigue delaminations often occur at the interface due to the cyclic shear stresses caused by the crack bridging effect, shown in figure 2.5 (15). Dynamic delamination is a result of the redistribution of stresses after fibre failure. This causes shear stresses at the interface causing dynamic delamination (16).

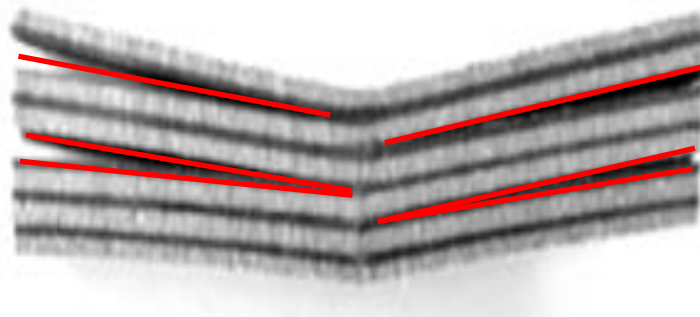


Figure 2.3: Delamination within a 6/5 Carbon-fibre steel laminate (42)

2.2.1.2 Fatigue Behaviour

Research and testing performed at TU Delft in the 1970's has shown that one of the key features of FMLs (compared to their monolithic alloys), is the high fatigue life (12) (17). This is due to the different crack mechanisms that take place in the two materials. Under external cyclic loading the metal alloy will begin to crack, and a sharp defined crack tip will split through the isotropic material; whereas the composite material has millions of crack arresting microstructures, that require the crack to turn up to 90° in order to continue to propagate. This redirection of the crack-tip dissipates energy through broken bonds in the fibre-matrix, as a result transferring the loads to adjacent fibres via matrix shear (18). Hence, the crack propagation time in FRP is much greater than in monolithic alloys. The two different mechanisms of crack propagation are highlighted in figure 2.4.

Through the combination of the two materials, advantages over monolithic metal alloys can be achieved. Within FMLs, once the metal has begun to crack, the fibres of the FRP will still be intact due to their superior strength and hence, some of the load will be distributed to them. This allows a new load path to form through the FRP layer (shown in figure 2.5) – reducing the stress concentration factor at the crack tip and slowing down the rate of the propagating crack (13) (19). Thus, greatly increasing the fatigue life compared to the pure alloy; meaning weight savings of up to 30% can be achieved in fatigue critical aircraft components, such as the lower wing skin and fuselage (19).

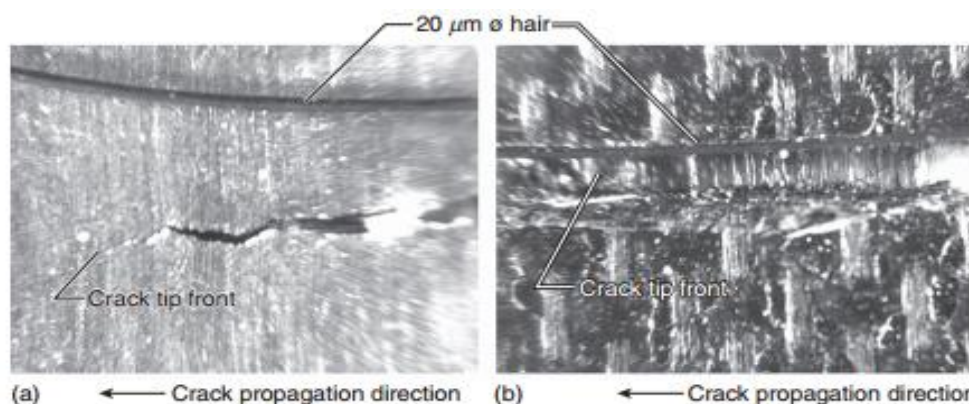


Figure 2.4: Difference between isotropic metal (a) and composite (b) fatigue crack formation and propagation (18)

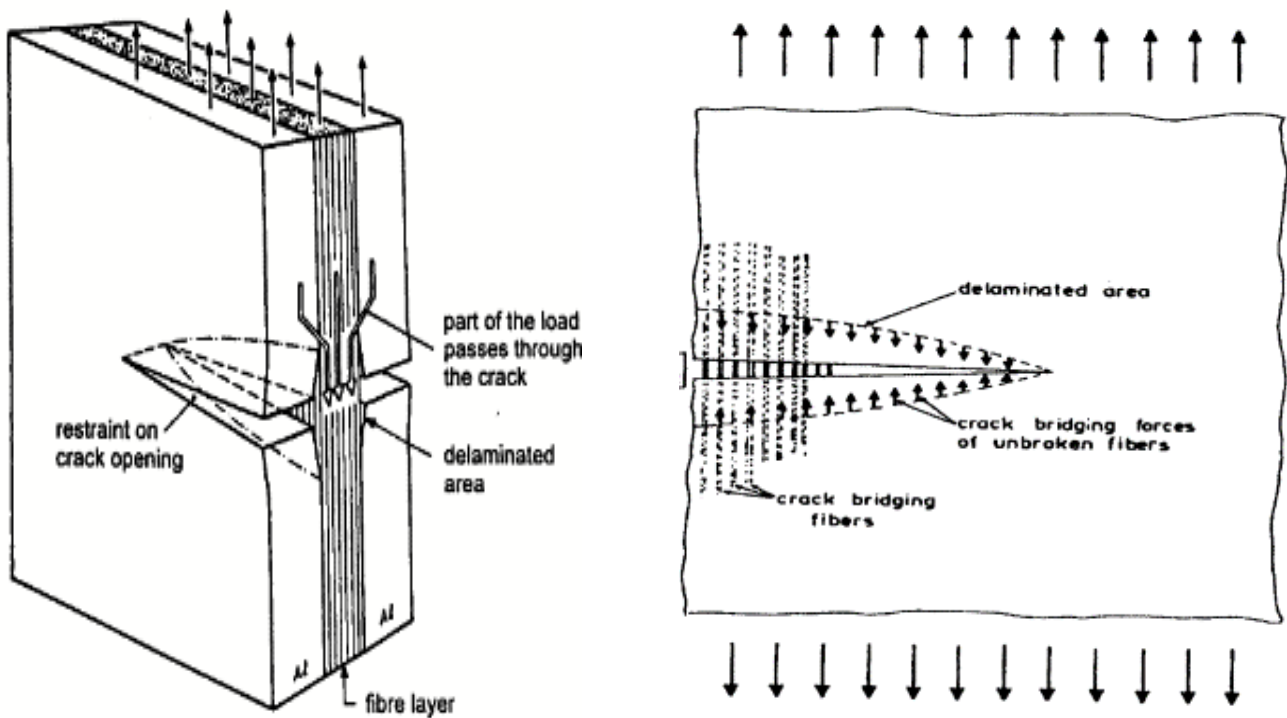


Figure 2.5: Alternate load path/crack bridging mechanism of FML (15) (11)

However, some fatigue delamination may occur at the crack edges due to the cyclic shear stresses at the interface (15). This is actually beneficial as without a small amount of delamination the fibres would rupture under the tensile load. However, the delamination should not exceed a certain length as this would lead to a very fast crack propagation (11).

The findings of Wu and Yang (6) back up the research of Sinmazcelik et al (19) suggesting that the FML offers a significant delay in crack propagation time. The graph in figure 2.6 highlights that for the monolithic aluminium alloy, the characteristic governing fatigue life, is crack initiation, whereas in the FML composite, the crack propagation characteristic governs (6). This is desirable in infrastructure and aerospace as it allows time for inspections to detect any cracks, before they become a severe problem.

Cracks that go unnoticed can become a big problem if they can propagate without any arrest mechanism, this is where Infracore's patented Z-shaped profile technology becomes relevant. Through the interlocking and layering of many Z-shaped profiles to form a structural member, any cracks from fatigue delamination or impact damage cannot propagate due to the discontinuity of the sections – the crack would have to cross a fibre, rather than run along its longitudinal span. Images of this design are shown in figure 2.7.

It is difficult to accurately quantify the fatigue life of an FRP structure due to the interaction of cracking modes, for example interlaminar shear stresses causing delamination which will impact normal fatigue behaviour (20). However, through the studies into FML, discussed above it can be seen that the addition of FRP to metal alloys improves the fatigue behaviour.

In infrastructure, where pure FRP is more widely used, a decrease in the fatigue life is likely upon the merging with steel to create fibre-steel laminates, due to the metals inferior fatigue behaviour. Figure 2.14 shows the effect of increasing metal ratio on FML properties.

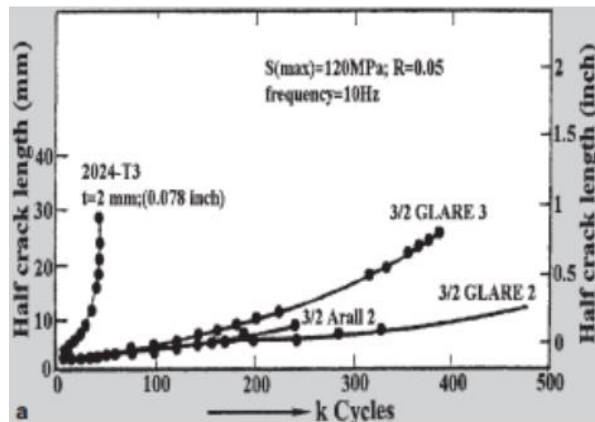


Figure 2.6: Crack propagation time between FMLs and 2024-T3 aluminium (6)

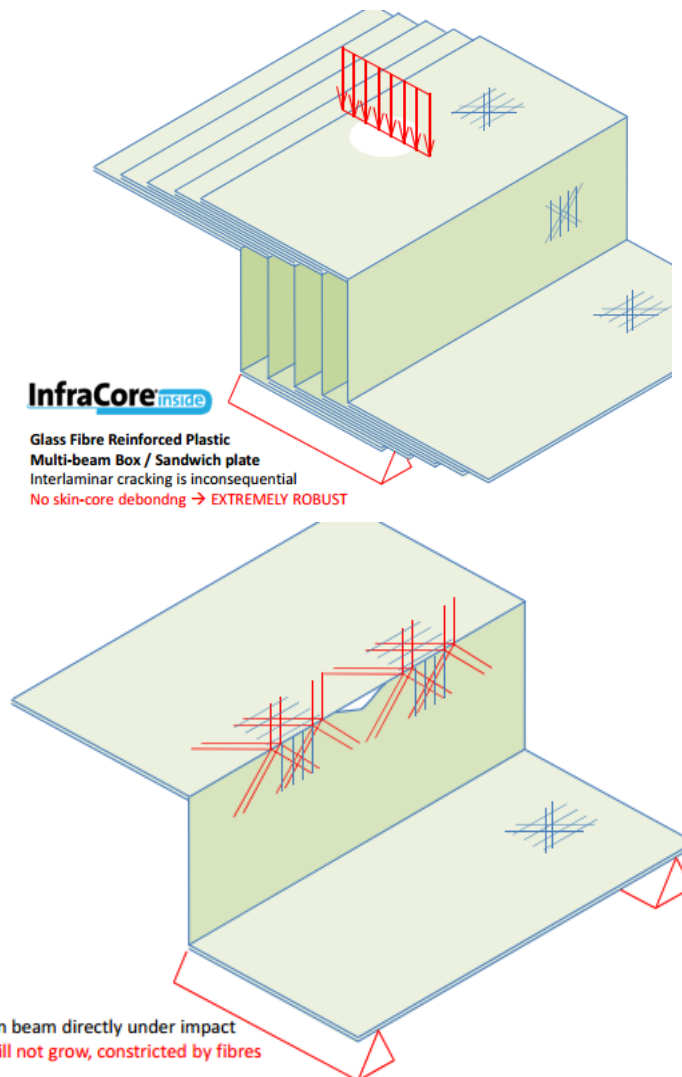


Figure 2.7: Infracore Inside Technology (56)

2.2.1.3 Damage Tolerance

Damage tolerance is a materials ability to continue to perform its structural role after receiving some form of damage, often an incidental impact, like bird strike in aerospace applications or a load falling from a lorry in infrastructure applications.

In fibre-reinforced polymers, impacts are known to cause delaminations within sub-layers, matrix cracking and in some cases, fibre crushing (10) (21), such damages are visible in [figure 2.8](#). When damaged by an impact, the tensile strength of the fibres is rarely affected, however, the cracking of the matrix means that it can no longer restrain fibres against buckling due to compressive forces (10) (21).

Glass fibres are known to have significantly greater impact resistance properties when compared to carbon fibres (6) (21) (22). Wu and Yang (6) attribute this to the high strain-rate strengthening phenomenon that occurs in the glass fibres.

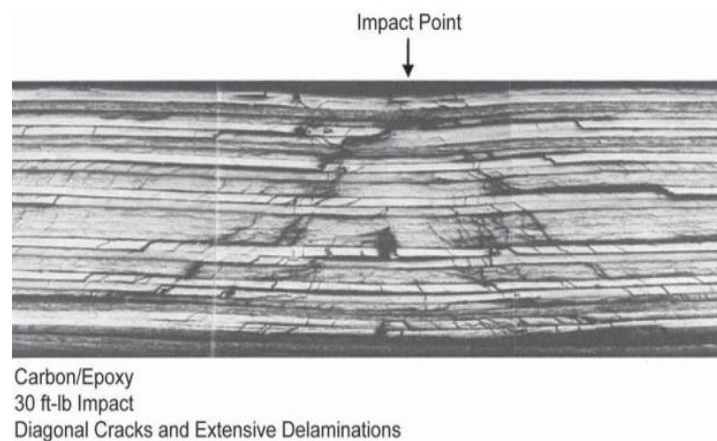


Figure 2.8: Impact damage in Carbon/epoxy laminate (21) (10)

Tsartsaris et al (22) found through experimental data and finite element modelling that FMLs are capable of absorbing energy through the plastic deformation of the plates (as discussed in section 2.7). This is highlighted in [figure 2.9](#), where Wu and Yang (6) show that GLARE outperforms two Carbon/PEEK FRP materials and also a pure aluminium alloy (2024-T3) in various impact damage tests.

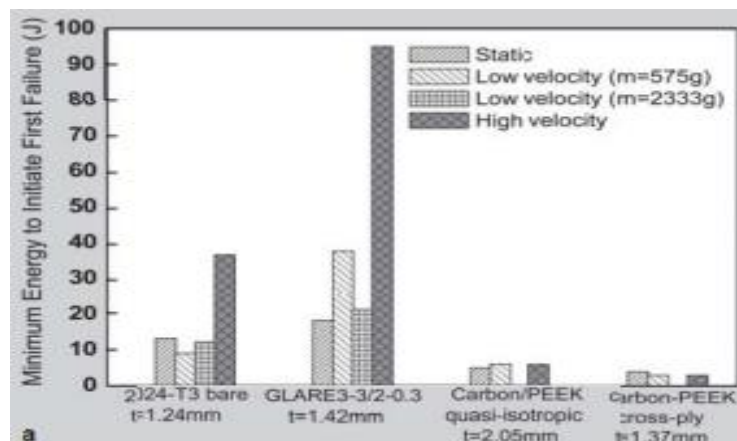


Figure 2.9: A comparison of GLARE 3 and other aerospace materials (6)

This is a key attribute of FMLs and is one of the unique benefits of combining the two materials – addressing the relatively poor damage tolerance behaviour of pure FRP, by combining it with a metal that allows the hybrid composite some plastic deformation, thus improving the damage tolerance behaviour.

The damages caused by impacts are much greater than the damages caused by single ply delaminations, visible from [figure 2.10](#). Low velocity impacts are very dangerous as the damage caused can be difficult to detect upon inspection and most probably will have damages deeper below the surface as seen in [figure 2.8](#) (6) (22).

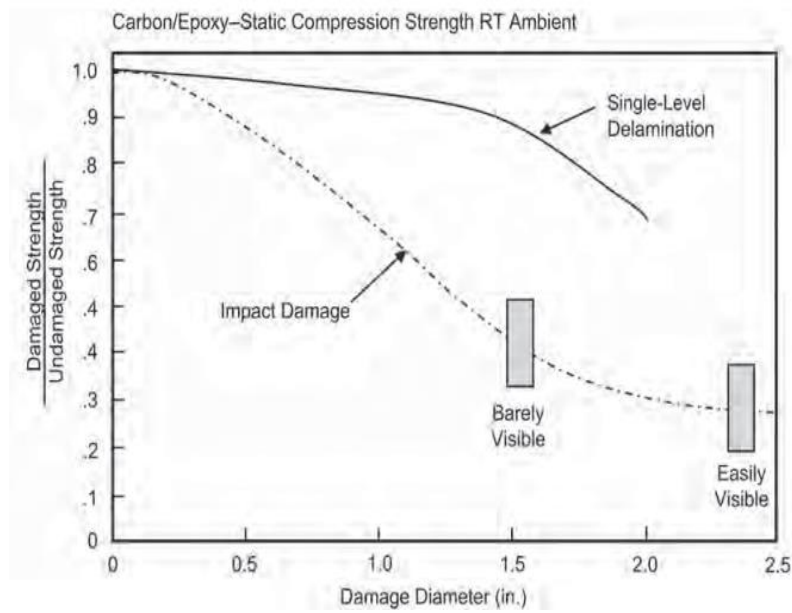


Figure 2.10: Static strength loss due to impact damage (21)

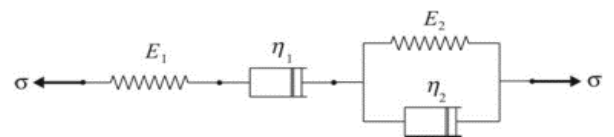
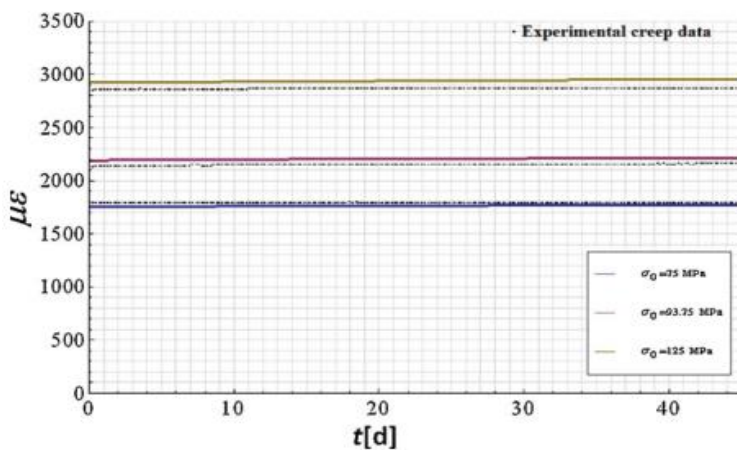
2.2.1.4 Creep Behaviour

Ascione et al (23), formulated and validated a model that predicts the long-term behaviour of FRP laminates based on the behaviour of its matrix and fibre properties, shown in figure 2.11.

Where the values of E_x and η_x , are values obtained from experimental data. This model and subsequent testing was used to show that three samples of GFRP used in civil applications outperformed their expected behaviour according to aeronautical literature and exhibited limited deferred strains (<2%) (23).

The experimental data also highlights that the long-term deformation of the fibres is negligible and the resin dominates. Figure 2.11, shows the correlation between the model and experimental results.

Campbell (21) states that due to the thermostatic behaviour of thermoplastics, such as polyethylene, they cannot be used in civil engineering applications as they creep under continuous load, even at moderate temperatures. Whereas thermosetting resins cure permanently at elevated temperatures, through the irreversible cross-linking of long chain polymers (24). Thus, making thermoset resins a desirable choice for structural applications.



$$\varepsilon(t) = \sigma_0 \cdot [c_1 + c_2 \cdot (t - t_0) + c_3 \cdot (1 - e^{-(t_0-t)(c_4/c_3)})],$$

where:

$$c_1 = \frac{1}{E_1}, \quad c_2 = \frac{1}{\eta_1}, \quad c_3 = \frac{1}{E_2}, \quad c_4 = \frac{1}{\eta_2}.$$

$$J(t, t_0 = 0) = \frac{\varepsilon(t)}{\sigma_0} = \frac{\varepsilon_m(t)}{\sigma_0}.$$

Figure 2.11: Predicted and experimental creep data based on Ascione's model, shown in right figure (23)

The creep behaviour of steel is known to be much slower than the matrix-dominated behaviour of FRP materials. This will need to be investigated during the study of FSL as different rates of creep will cause different levels of strain within the individual layers of each material and this difference can in turn cause further stresses between layers – potentially leading to delamination. This process would be accelerated further under the influence of temperature.

2.2.1.5 Corrosion Resistance

Due to the customisable nature of FRP and its constituent parts, the environmental resistance of FRP is often regarded as an improvement over that of metals, however, the FRP material must be designed with environmental resistance in mind. Resin choice is pivotal to suitable environmental protection and must be tailored based on the environment of the application. Service temperature ranges are crucial as freeze-thawing cycles cause a reduction of ultimate strength (25) and elevated temperatures can cause resin softening and deterioration of structural performance (10) (21).

Glass fibres are largely unaffected by moisture, however, effects on the surface of the FRP can have a substantial effect. The surface may be damaged by certain finishes or binders that can allow water ingress along the fibre-matrix interface, affecting inter-laminar shear strength (25).

Figure 2.12, displays corrosion damage of ARALL 3 and aluminium alloy 2024-T3 when in acid bath conditions. It can be seen that the aluminium alloy on the right has been corroded all the way through the thickness of the material, whereas, the ARALL specimen has only corroded through to the first layer of FRP (26). This suggests the FRP provides a greater resistance to the acid bath corrosion than the monolithic aluminium.

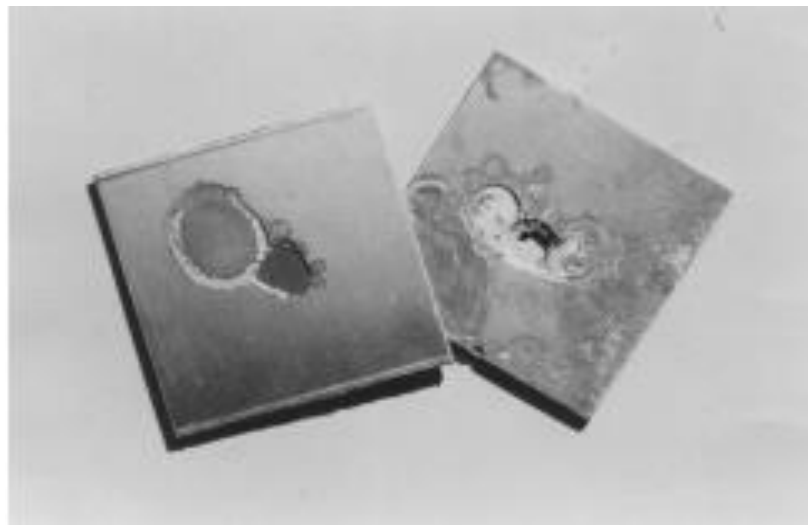


Figure 2.12: Comparison of acid-bath corrosion in ARALL-3 (left) and 2024-T3 (right) (26)

2.2.1.6 Effect of Laminate and Metal Thickness

Marissen (13) investigated delamination in ARALL caused by fatigue loading and concluded that for thinner metal layers (0.25-0.9mm tested), the delamination growth rates decrease, however, the stress in the thinner aluminium layers is much greater, which can be seen in figure 2.13. Similarly, Roebroeks (27) suggests that the ratio of metal thickness to laminate thickness determines the behaviour of the sample, based on aluminium thickness within ARALL laminates, shown in figure 2.14. The results shown, are as expected, for example as the amount of metal within the laminate increases, the fatigue behaviour will decrease due to metals relatively poor fatigue behaviour; similarly, the stiffness will increase given the metals greater stiffness than FRP.

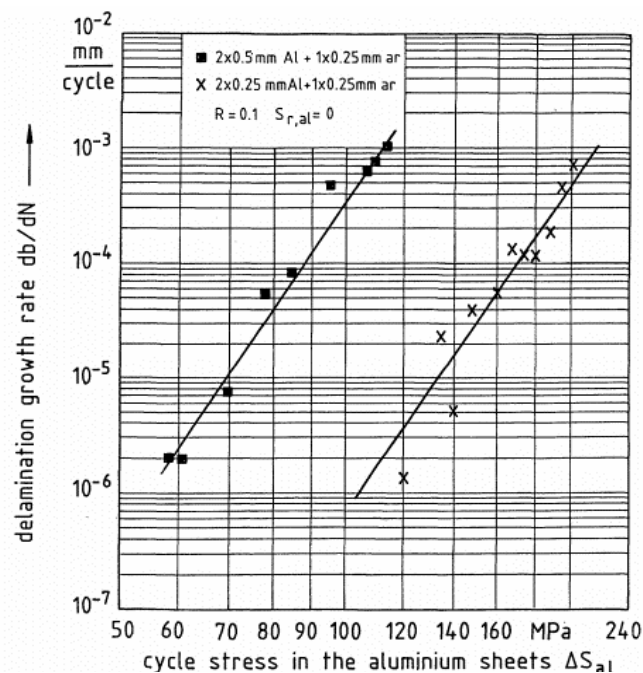


Figure 2.13: Comparison of delamination growth rate in two samples of ARALL on the basis of cyclic stress in the non-delaminated aluminium sheets (13)

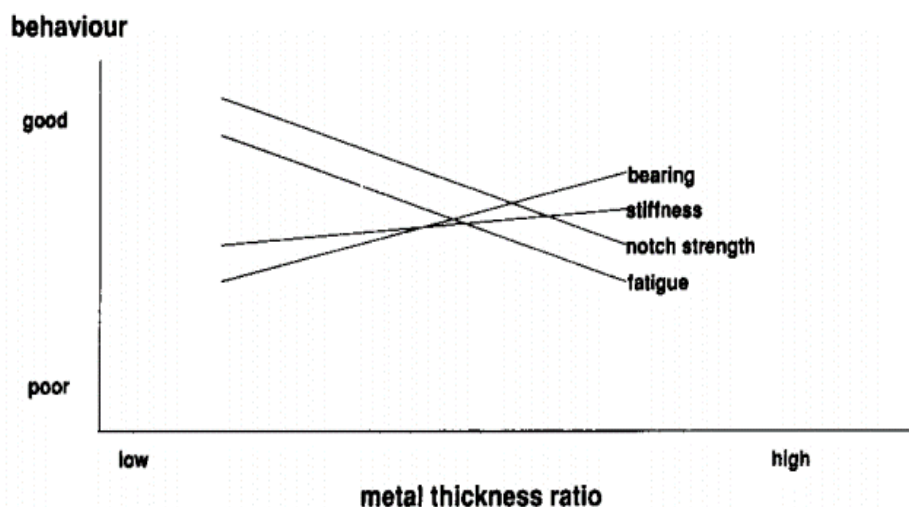


Figure 2.14: Influence of metal thickness ratio on laminate performance (27)

2.3 CURRENT RESEARCH OF FIBRE-STEEL LAMINATES

Although the concept of FMLs is not new, the concept of using steel within hybrid composites is relatively new and thus, minimal research has been undertaken, especially within the field of civil engineering.

However, important lessons can still be learnt from the research of other industries with regards to the design and improvement of the metal-composite interface, but they need to be critically analysed before they can be applied to civil and infrastructure applications given the differing techniques and materials being used.

2.3.1 Production

Langdon and Rowe (28) undertook research into the blast resistance of fibre-steel laminates (FSLs) with up to four steel plates separating 3 layers of GFRP (total thickness 13.5mm). An investigation into how manufacturing techniques effected the interface strength was simultaneously performed, showing that a single stage process, in which all layers are pressed and heated together, was the most effective production method, see figure 2.15. The study found that the back-face displacement of the material was lower than aluminium FMLs, but 20% higher than monolithic steel under impact loading. Through 3-point bending tests (ASTM D5023), it was found that the flexural modulus of the samples decreased as panel thickness increased. The longitudinal Young's modulus of the FRP layup used was 11GPa and when combined with steel rose to 38GPa (28).

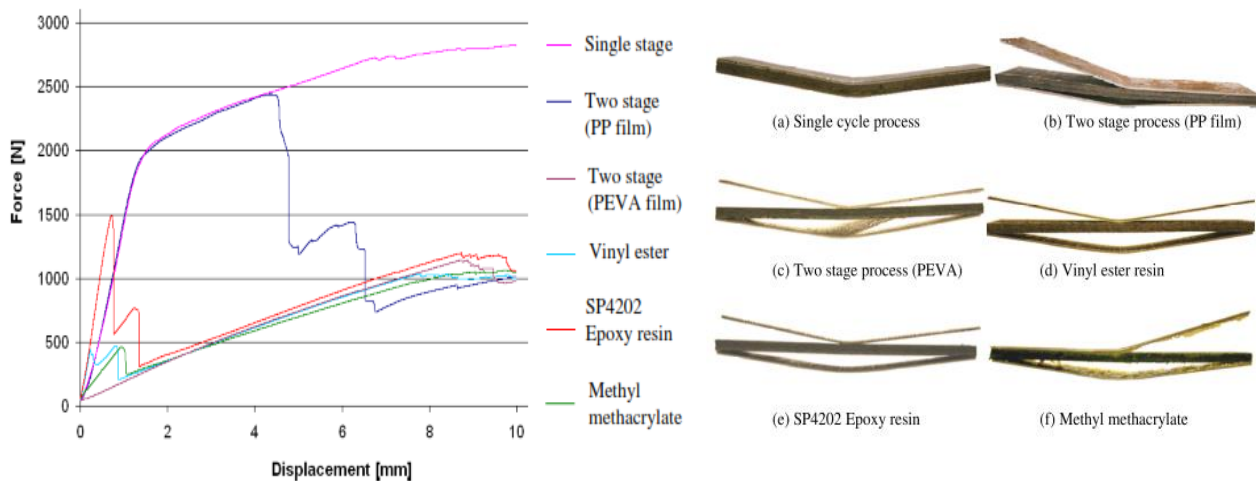


Figure 2.15: (A) Force/displacement curves & failure photographs for different manufacturing techniques of FSL (28)

This production method is similar to that used in automotive and aeronautical applications, in that thermoplastic resins were used in an autoclave-type production set up. However, it is highlighted that a single stage production (like VARTM) is preferred to multi-stage production processes, even if at a lower temperature and pressure.

2.3.2 Component Material Behaviours

A secondary advantage of this hybrid composite is the addition of plastic deformation, provided by the steel plies, to the brittle FRP material. Impact resistance is a particular weakness of FRP in infrastructure applications, as a small impact can provide the necessary initiation of a delaminating crack, which can then propagate under further loading (figure 2.16). By combining the FRP with steel to make an FSL, greater impact resistance is a potential benefit, although this won't form part of the primary investigation. Moreover, the best way to negate the propagation of any type of delamination in FRP and FSL components is to avoid designing members that have continuous resin-dominated pathways, like those shown in figure 2.16.

However, there are also drawbacks to the difference in plastic/elastic behaviour of the FSL. Peel stresses are generated at the steel-GFRP interface when the component is subjected to flexural loading. If the steel plastically deforms, it will retain a curved profile after loading; whereas the linear elastic behaviour of the FRP means it will release elastic strain energy, until it returns to its original shape (straight) – or the fibres fracture (29). The amount of stress generated at this interface depends on the strain at failure level of the fibres. These peel stresses lead to debonding if they cannot be sustained by the interface – see figure 2.17. This provides another key reason to improve said interface.

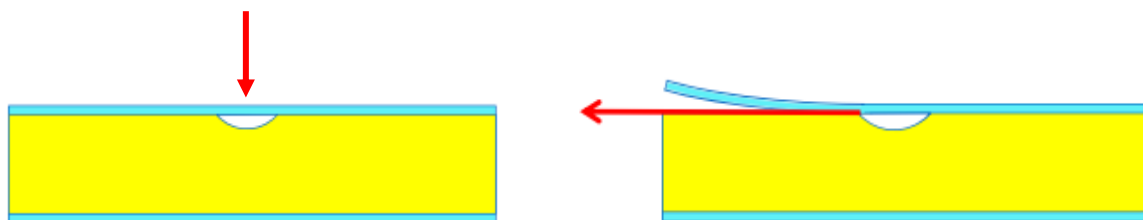


Figure 2.16: (A) Sandwich panel damaged by initial impact, (B) Propagation of delaminating crack, causing catastrophic failure (56)

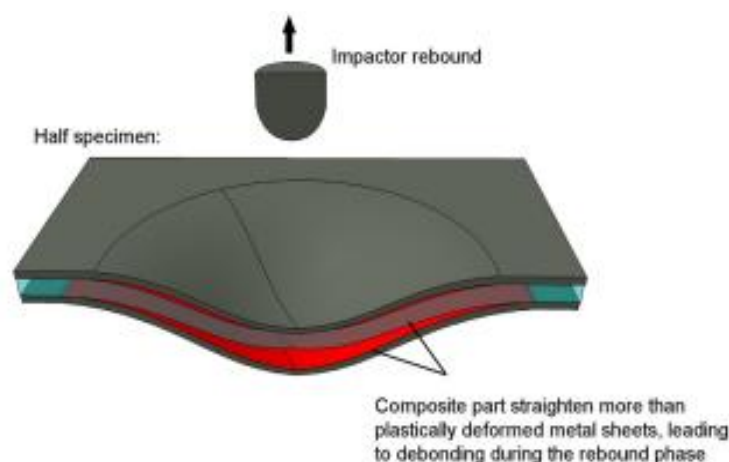


Figure 2.17: Cross-section schematic of debonding process during rebound phase of impact test (29)

2.3.3 Steel-FRP Interface

As some of the literature discussed so far has covered, the interface between the two materials is the main weakness that undermines the other advantages of FSLs. This was also highlighted by this authors pre-cursor study into the production of fibre-steel laminates with the VARTM method. In this study, the steel plies were treated with acetone and abraded to increase bonding surface area; additionally, the steel plates were perforated to allow vertical transmission of resin through the laminate.

Much of the literature that covers FSLs investigates how to optimise the FRP-steel interface, either through chemical or mechanical enhancement. This is because without adequate adhesion between plies within the laminate, the theoretical advantages of the hybrid composite cannot be realised.

2.3.3.1 Chemical Improvement

The primary chemical improvements that can be made, are through the addition of inter-ply and coatings that are designed to enhance the chemical bonding between the two materials by providing a supplementary interface that each material can more easily bond to.

Gall et al (30) found that through the addition of a compatible polymeric inter-ply placed at the interface of the FRP and steel they could increase the mode I fracture toughness by one order of magnitude when compared to untreated interfaces.

The selection of resin is fundamental to the level of adhesion that can be achieved. Often in pure-FRP components epoxy based resins are thought to provide some of the highest levels of ILSS, however, due to their different chemical structures, steel and epoxy combinations yield a low ILSS (19) (31).

2.3.3.2 Mechanical Improvement

Mechanical improvement of the interface involves the modification of one of the components (normally the metal), to achieve a higher level of adhesion. In traditional applications of mechanical improvement of metal surfaces (such as paint or coating applications), it is common to try to increase the surface area available for bonding. This is done through sand-blasting or abrasion; creating striations, micro-channels and pockets within the previously sleek surface of the metal – thus increasing surface area.

Other methods of improvement involve the manipulation of the metal in order to create a physical interlock at the FRP-steel interface. The interlocking of two materials to create a joint or connection is a widely used practice in timber constructions. Many connections between two timber members are formed with steel plates which have sharp teeth that dig into the two pieces of timber, thus providing an interlocking connection.

2.3.3.2.1 Micro – level Enhancements

In advanced applications, micro-level enhancements can be made using lasers and other tools to ablate the surface of the steel, increasing surface area in largely the same way as sand-blasting. Undertaking these enhancements is largely outside of the scope of this research, primarily due to costs, however, important lessons can be adapted from the knowledge conveyed in the following studies.

Pärnänen et al (29) investigated the effect of the steel surface morphology on the extent of metal-composite debonding. They found that in CFRP with steel, the surface morphology of the steel had a negligible effect on the extent of debonding (treatments used: nitric-acid etching and electropolishing), this was likely because the two treatments essentially reduced the steels surface area when compared to its original state.

Hopmann et al (32) investigated the micro-mechanical improvement of the interface through laser structuring. This creates $\sim 60\mu\text{m}$ deep channels in the steel which could then be filled with the composite before curing. They found that in tensile single lap shear tests they could achieve a shear strength 9.42N/mm^2 and that the level of bonding at the interface didn't affect the uniaxial tensile strength achievable, however, it did of course affect the flexural strength.

2.3.3.2.2 Interlocking

In a series of investigations, published in the Euro Hybrid conference proceedings of 2014 and 2016, there has been a desire to study the feasibility and effect of creating structures on the surface of the steel that will be produced with FRP to create an interlocking interface. The basic idea and schematic of the interlocking structures used in each of the studies is displayed in figure 2.18.

Initially, it was found that by creating surface structures a 30% increase in transferable force could be achieved when compared to non-structured metals under single lap shear testing, see figure 2.19 (33). As can be seen in figure 2.19, an increase in plastic behaviour can be noticed, suggesting that the improved interface is adding some structural robustness to the joint.

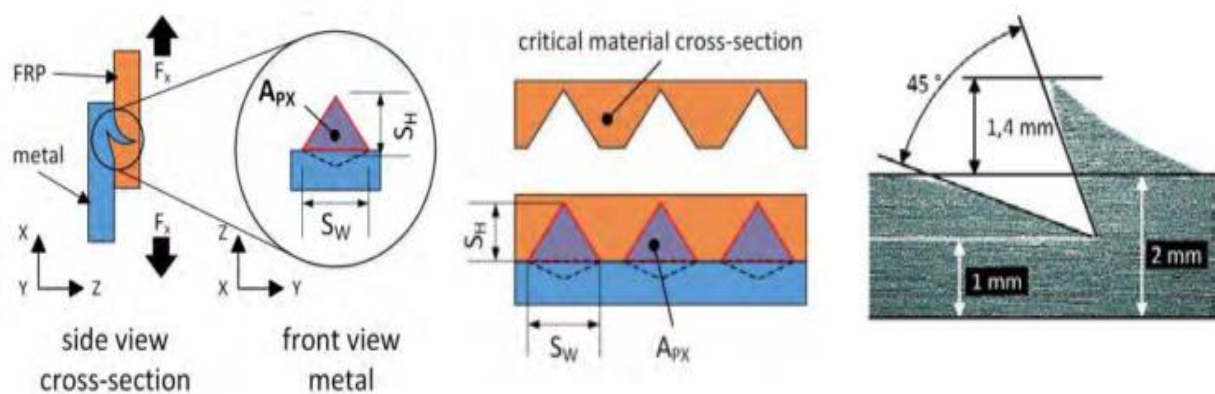


Figure 2.18: Interlocking projection definition (34) (35)

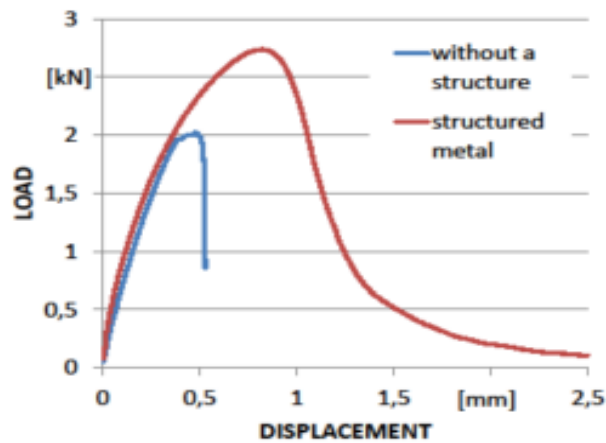


Figure 2.19: Tensile Single lap-shear testing of structured and un-structured metal-FRP interfaces (33)

Brand et al (34) (35) subsequently investigated the impact of the pattern, size and quantity of the surface structures. The investigation found a maximum tensile load transferred per interlocking structure of 600N. The study also went on to classify that the greater the area and number of projections, the higher the transferable force - up to a critical limit of the cross section of FRP remaining (as the number and area of projections reduce the available cross-section of FRP, see figure 2.18). With regard to the pattern of the structures, it was found that between a U-shaped configuration and a circular configuration, the circular pattern can transmit higher loads but has a quicker first structure failure (due to uneven stress distribution), figure 2.20.

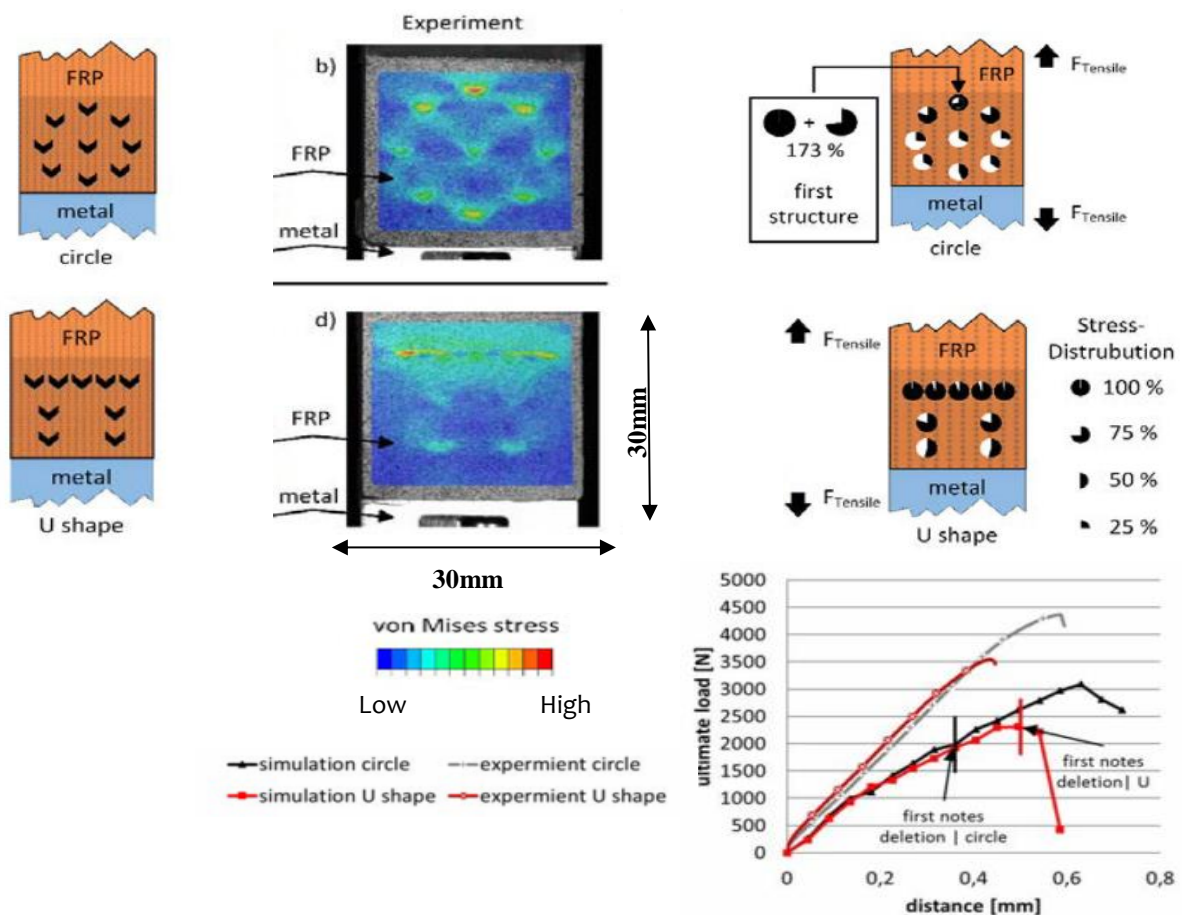


Figure 2.20: Analysis of projection pattern and stress distribution (35)

A further follow up study analysed the microscopic behaviour of the interlocking part and the adjacent fibres. It was found that there could be a problem arising because of the sharp structures tearing the fibres adjacent to the interface. The suggested remedies for this problem were to sand-blast the steel after it has been structured – blunting the structures; or to include an additional, sacrificial ply of natural fibres that will be damaged instead of the reinforcing fibres. Microscopic images of the samples are shown in [figure 2.21](#) (36).

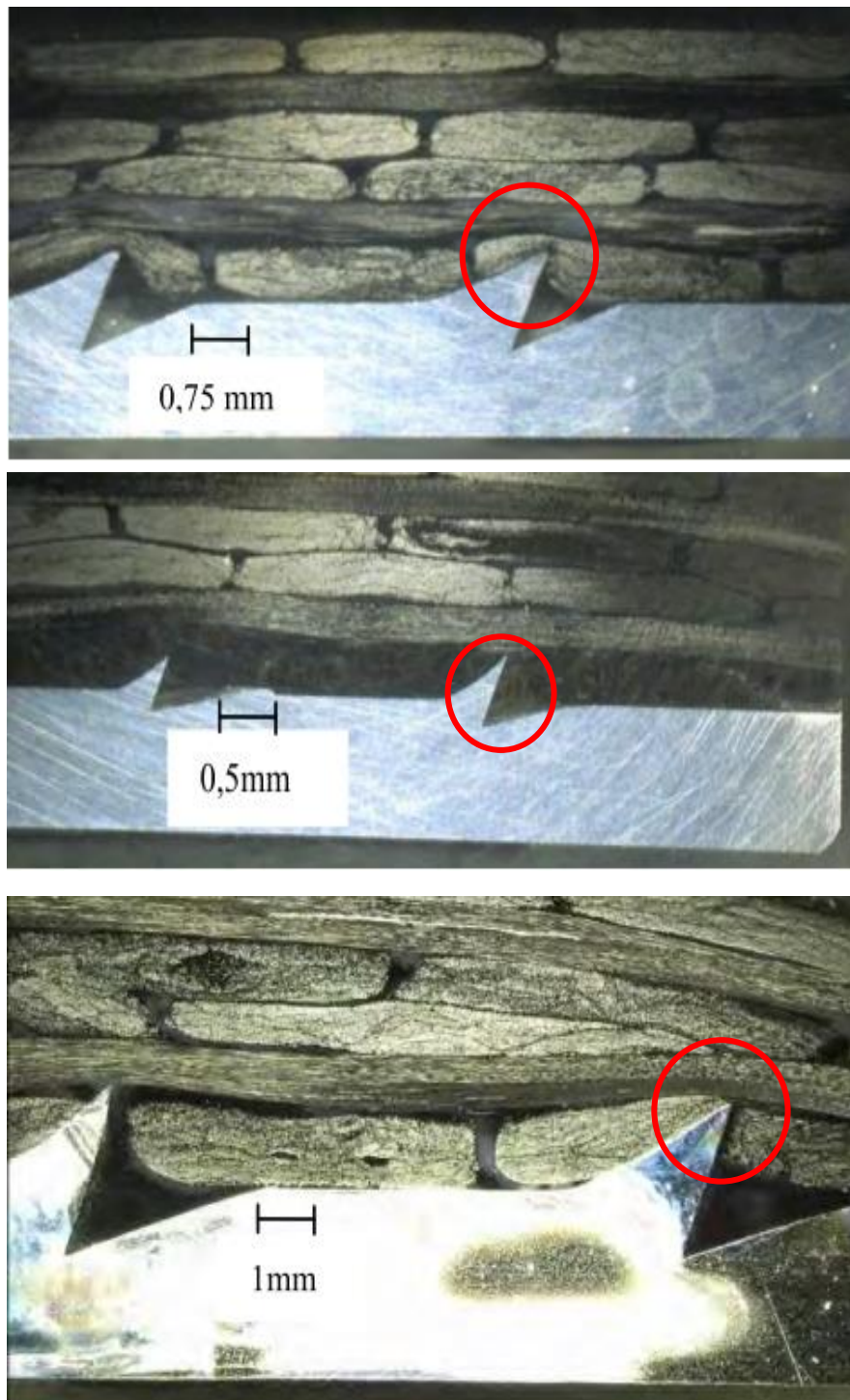


Figure 2.21: (A) CFRP-steel interface, showing structures cutting into carbon fibres (B) Sacrificial natural fibres inter-ply, (C) Sand-blasted structures with carbon fibres moulded around blunted shape (36)

Alternatively, interlocking structures can be created through cold-metal transfer welding (CMT). This process is applied in aeronautical and automotive industries for joining CFRP and metal alloys. CMT uses the introduction of high current to create small structures from a welding wire, which are then fused to the parent metal. Through the process, minimal dislocations to the parent metal occur meaning less damage and smaller heat affected zones than traditional welding methods. This allows the joining of two relatively different materials, such as aluminium and steel, which is not normally possible due to the difference in thermal behaviour (37). The structures, once fused to the metal plate, will allow a hybrid composite that is bonded not only through the normal adhesive bond, but also now through the interlocking effect of the pins (37) (38).

Ucsnik et al (38) found a significant increase in properties when comparing double lap shear joints utilising 3.0mm CMT created interlocking pins with adhesive only connections. One type of pin structure increased the ultimate force by 52%, mean local strains at failure by 1000% and energy absorption capacity by a factor of 30, see figure 2.22. These results highlight the importance of the strength of the interface; if ultimate load capacity is increased then the structure can be lighter - the primary goal in automotive and aeronautical designs. Furthermore, if the energy absorption capacity has increased then clearly some plastic deformation has occurred, whereas in the reference samples it hasn't - despite the presence of the metal. This suggests that the bond between the layers failed much before the metal was able to absorb any energy. This is an important property to have in infrastructure applications as this energy absorption would really aid the material in a road collision scenario - which is a current weakness of pure-FRP constructions.

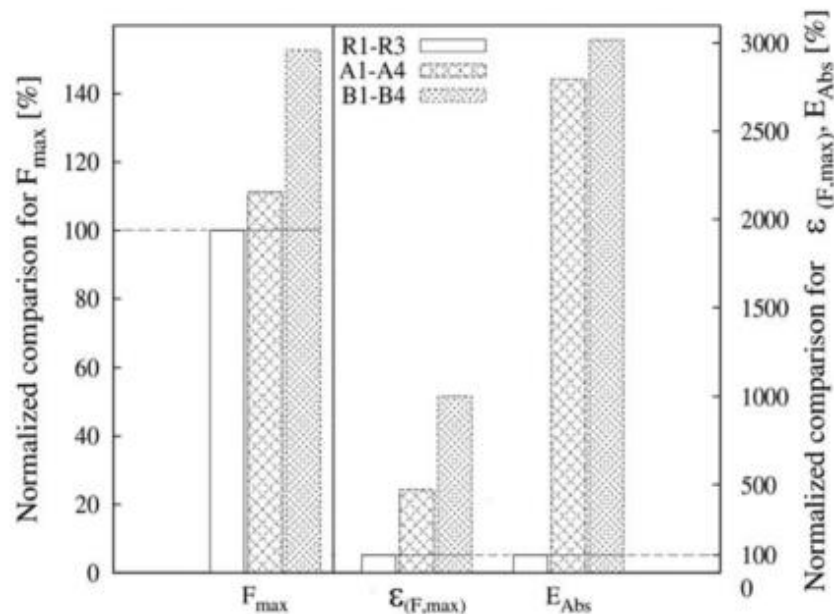


Figure 2.22: Comparison of structured and unstructured hybrid composites, from double lap shear tests (38)

Surfi-sculpt™ is a novel creation by TWI, that uses an electron beam process to sculpt the surface of metals to create structures on the surface, which can then be used with vacuum injection to create an enhanced connection between FRP and metal. The Welding Institute (TWI) have developed a connecting technology known as Comeld™, shown in figure 2.23A, which has been highlighted to increase the amount of energy absorbed and the ultimate load at which the connection will fail, shown in figure 2.23B (39) (40). It should also be noted that in a study undertaken by Smith (40), it was noticed that failure modes of the control and Comeld™ joints were rather different. Failure of the control samples (with no teeth), occurred at the interface of the composite and the metal, however, in the Comeld™ joints the load was able to reach a point where the composite started to experience matrix cracking and the teeth of the Comeld™ joint experienced plastic deformation. The graph shown in figure 2.23B, goes to show how much greater the amount of energy absorbed was – reinforcing the findings that regard the strength of the metal-FRP interface discussed in the previous paragraph of this section.

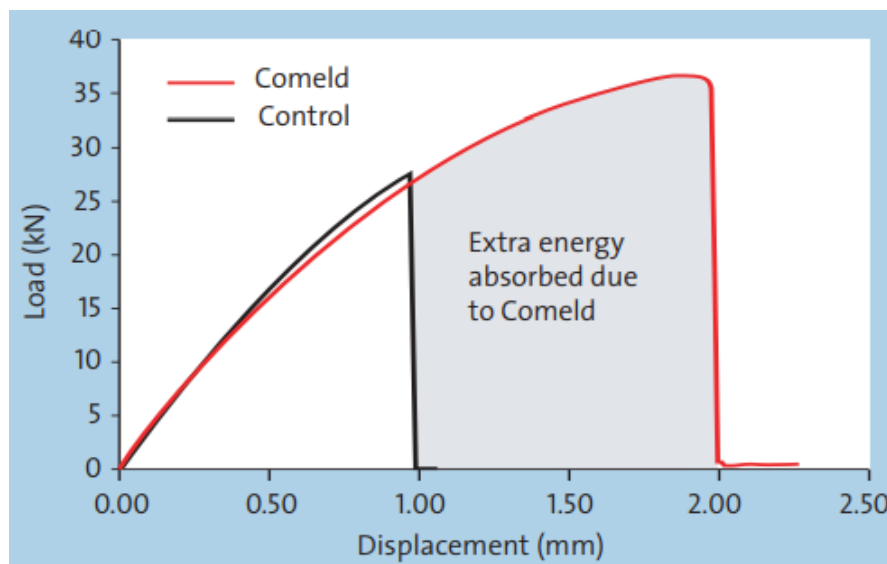


Figure 2.23: (A) Comeld™ joint created with Surfi-Sculpt™ technology, (B) Comparison of Comeld double lap joint and adhesive control joint (39) (40)

2.3.3.2.3 Surface Treatments

Van Rooijen et al (41) and Dymáček (42) tested a number of steel surface treatments and found that the highest shear strength at the steel-FRP interface was achieved through sandblasting and subsequent cleansing with acetone (42) or silane (41), see [figure 2.24A](#). Dymáček also warned that this method of treatment may lead to extensive steel warping (when using a 0.25mm sheet). It was also found that with the use of the mentioned layups, a maximum inter-laminar shear strength of 69.0 MPa was achieved, when testing with longitudinally orientated fibres with EN 2563 standard (short beam 3-Point bending test), see [figure 2.24B](#) (42). This suggests that the highest ILSS can be achieved when the fibres adjacent to the steel are orientated in the longitudinal direction, possibly due to being more similar (to the steel) with regards to strength and stiffness, than in the transverse direction.

Surface treatment	1	2	3	4	5	6	7	8
Shear strength τ_u [MPa]	6.9	6.8	6.7	7.5	9.3	20.7	19.2	14.1

1 - degreasing in acetone + sandpaper 220

2 - degreasing in acetone + pickling in chromosulphuric acid

3 - degreasing in acetone + sandpaper 220 + pickling in HCl+H₂O₂+CH₂

4 - degreasing in acetone + pickling in HCl+H₂O₂+CH₂

5 - degreasing in acetone

6 - degreasing in acetone + sandblasting

7 - degreasing in acetone + sandblasting + coating with primer PFL 120

8 - degreasing in acetone + coating with primer PFL 120

Set of specimens	IA	IB	IC	ID
ILSS τ_u [MPa]	60.4	69.0	40.6	59.3

IA - laminate 3/2, longitudinally oriented fibers

IB - laminate 6/5, longitudinally oriented fibers

IC - laminate 3/2, transversely oriented fibers

ID - laminate 6/5, transversely oriented fibers

Figure 2.24: Interlaminar Shear Strength of CFRP-Steel interface based on (A) different surface treatments and (B) different compositions (42)

2.3.3.3 Testing of Steel-FRP Interface

After establishing the best method to improve the interface, the strength of the bond must be effectively tested. It is ideal to measure resistance to certain fracture modes, mainly mode I (opening) and II (in-plane), shown in figure 2.25, however, there is no standardised test method for establishing this within FMLs or FSLs at the time of writing.

In research undertaken to date, authors have used various testing methods, not limited to but including: single (32) (33) (34) (35) and double (38) (40) lap shear tests for joint-based research and short-beam (31) (42) and double-cantilever (30) tests for laminate based research. Others include drop impact tests (29) and floating roller peel tests (19) (41) used for slightly different applications (aerospace related).

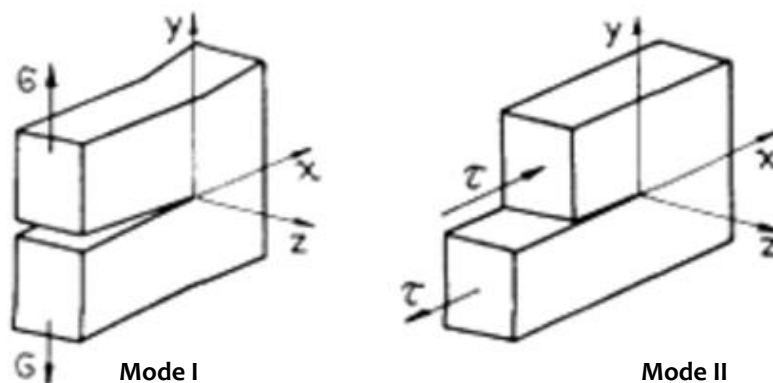


Figure 2.25: Mode I & Mode II Cracking Definitions (57)

Samples for interface testing require a high-quality edge due to the property we are trying to test for: if a sample is cut leaving a very rough edge, then this low-quality edge will act like a notch in the sample. The notch will remove the required crack-initiation energy, as the crack has already been initiated by the notch and will yield a lower inter-laminar shear strength than a sample with a higher quality edge.

2.3.4 Cutting of FSL

Prior to the testing of the individual samples of the hybrid composite, the manufactured panel of material must be cut into smaller test geometries. Due to the difference in the two component materials' properties, there are difficulties when cutting larger panels down to smaller shapes.

Investigations into the use of lasers to cut composites have shown their suitability when cutting through composites like FRP (43), and more recently hybrid-composites like FMLs and FSLs (44) (45). Figure 2.26 shows the difference in edge quality achievable when comparing a fibre laser and conventional milling techniques.

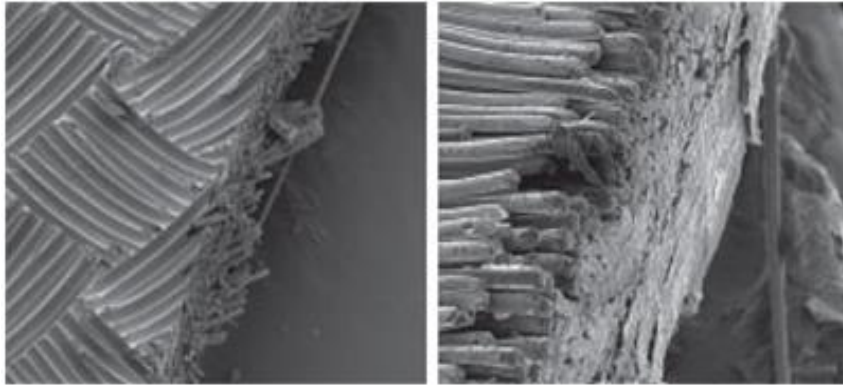


Figure 2.26: Edge quality comparison: Conventional milling (left) and laser machining (right) (43)

Neugebauer et al (45) found that when comparing water-jet cutting and laser cutting, the affected zone of material caused by each cutting method is relatively similar (within $20\mu\text{m}$). The results are shown in figure 2.27 and can be attributed to the difference in reaction of the two materials to the waterjet cutter, whereas they exhibit more similar behaviour when cut with the laser cutter. However, the study concluded that both techniques were applicable to FSLs.

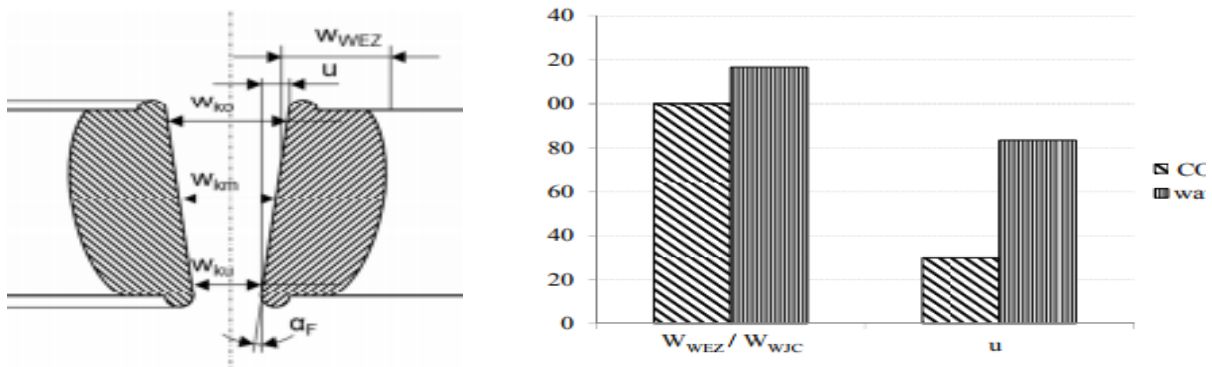


Figure 2.27: Comparison of laser and waterjet cutting (45)

Jaeschke et al (44) compared the inter-laminar shear strength achievable after cutting fibre-metal laminates with a waterjet, a laser and conventional milling techniques. The conventionally milled samples gave the greatest ILSS and the laser cut samples the lowest, as can be seen in figure 2.29.

In an analysis of the differing types of waterjet cutter available, Shanmugam et al (46) found that abrasive water jet cutters (with abrasives in the water), provide a much cleaner cut, than without abrasives, when cutting CFRP (figure 2.28). It was also found that the main cause of delamination damage is from the shock wave caused by the initial impact of the water hitting the surface of the material; further damage is caused by the dispersion of the water into the interfaces, figure 2.30.

The use of milling techniques to cut the samples is a further alternative but depends on the specifications of the saw blade, the cutting speed and dimensions of the cut. Milling of metallic materials also generates a significant amount of heat that could cause the resin in the plies to burn, it is therefore recommended that the blade be cooled during the cutting process of a hybrid composite.

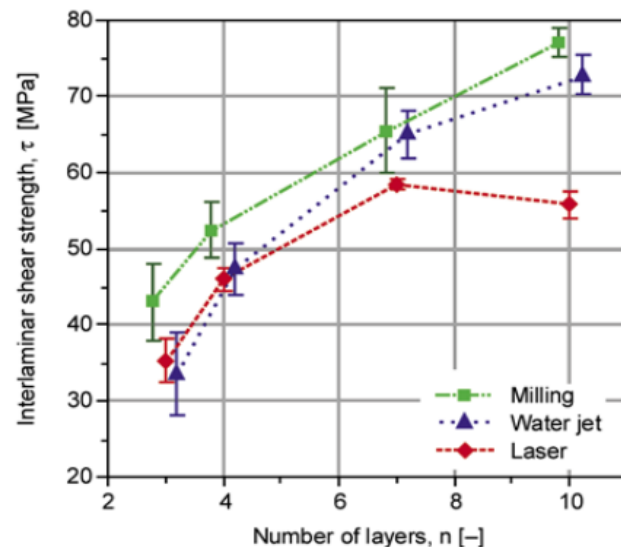


Figure 2.29: Comparison of ILSS based on cutting technique (44)

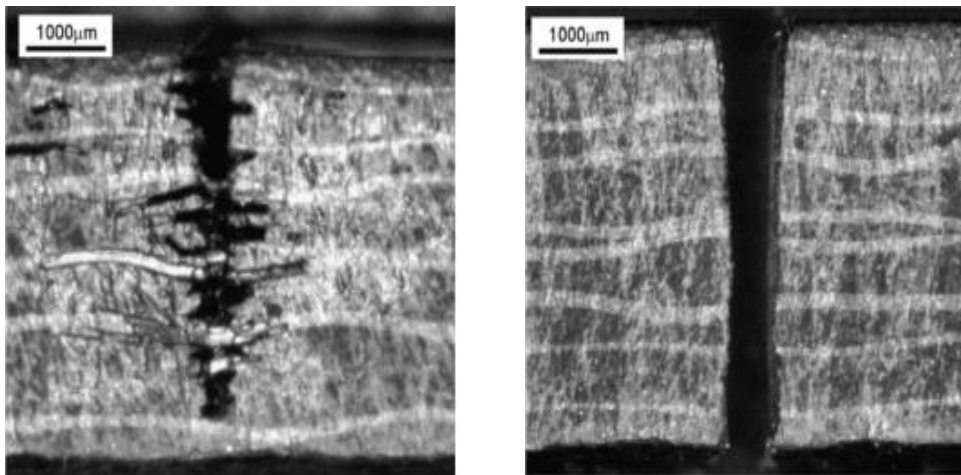


Figure 2.28: (A) Waterjet cutter without abrasives, (B) AWJ - Abrasive waterjet cutter (46)

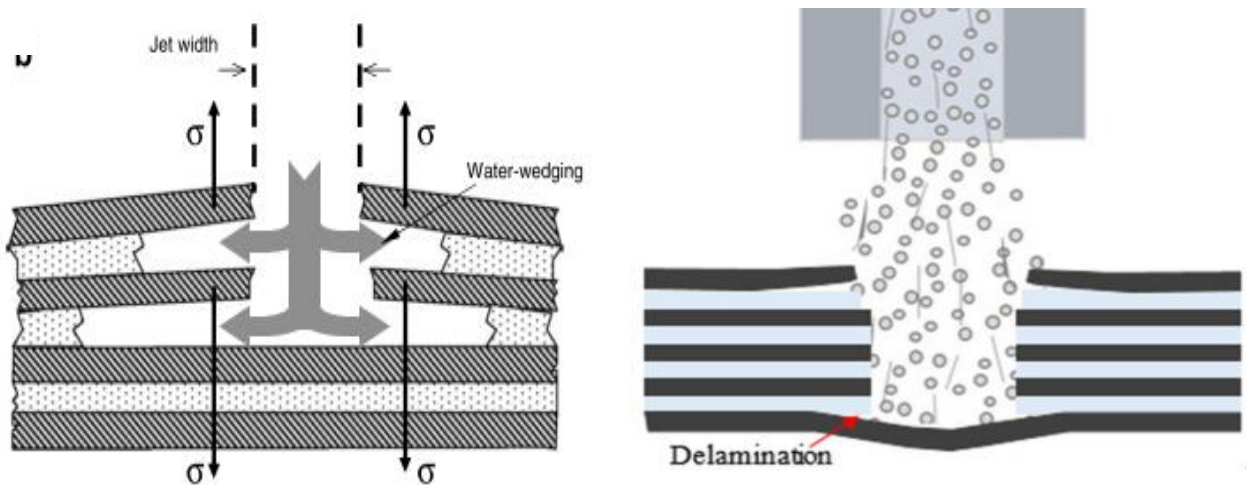


Figure 2.30: (A) Water-wedging effect (46), (B) Back-face delamination caused by stunted water propagation (58)

2.3.5 Summary

The primary reason for the inclusion of steel plies into an FRP laminate is to increase the stiffness of the laminate and reduce the serviceability driven design of these elements which is caused by the inherently low stiffness of FRP laminates. Given the difference in material costs of FRP and steel, with steel being cheaper, the reduction in the amount of FRP is likely to be financially beneficial. However, an increase in the self-weight of the laminate must be taken into account, especially when considering one of the key proponents of FRP structures are their light-weight and resulting easy erection.

The difference in mechanical and environmental behaviours of the individual components of the hybrid-composite lead to a concerning weakness in the joining of the two materials. The interface between steel and FRP plies is likely to be the inhibiting factor behind the successful implementation of this material. Stresses are generated here due to the different stiffnesses, thermal and long-term behaviour of the two materials. The interface can, however, be improved through chemical and mechanical means. The most effective method of improvement is likely a combination of both of these categories. Careful selection of resin that will promote the best adhesion between the two layers is imperative, additionally, the increase of the bonding surface area of the steel through abrasion or grit blasting is highly recommended.

Using the research covered in the previous sections, a pathway for this current research can be more clearly defined. The initial investigations will take the shape of rudimentary experiments that will look to identify the key properties of the material. Before the testing period can begin, the material must be cut into the test geometries. The research to date suggests that among the best techniques is the waterjet cutting technique, as it provides a good-quality edge and is easily programmable.

To establish the best method to cut the material, different cutting approaches will be made including abrasive water-jet technology and various sawing and milling methods. Once trial cuts have been made the methods will be evaluated to see which has produced the best quality of sample, with no delamination and a high-quality edge. Following this evaluation, a full set of samples can be cut and tested.

The samples can then be evaluated for their inter-laminar shear strength and compared to a reference sample which will utilise 'unstructured' steel. In order to evaluate the material, the short beam shear (SBS) tests will be used due to the simplicity of the testing procedure and sample geometry when compared to the other methods.

2.4 COMPOSITE DECK SYSTEMS

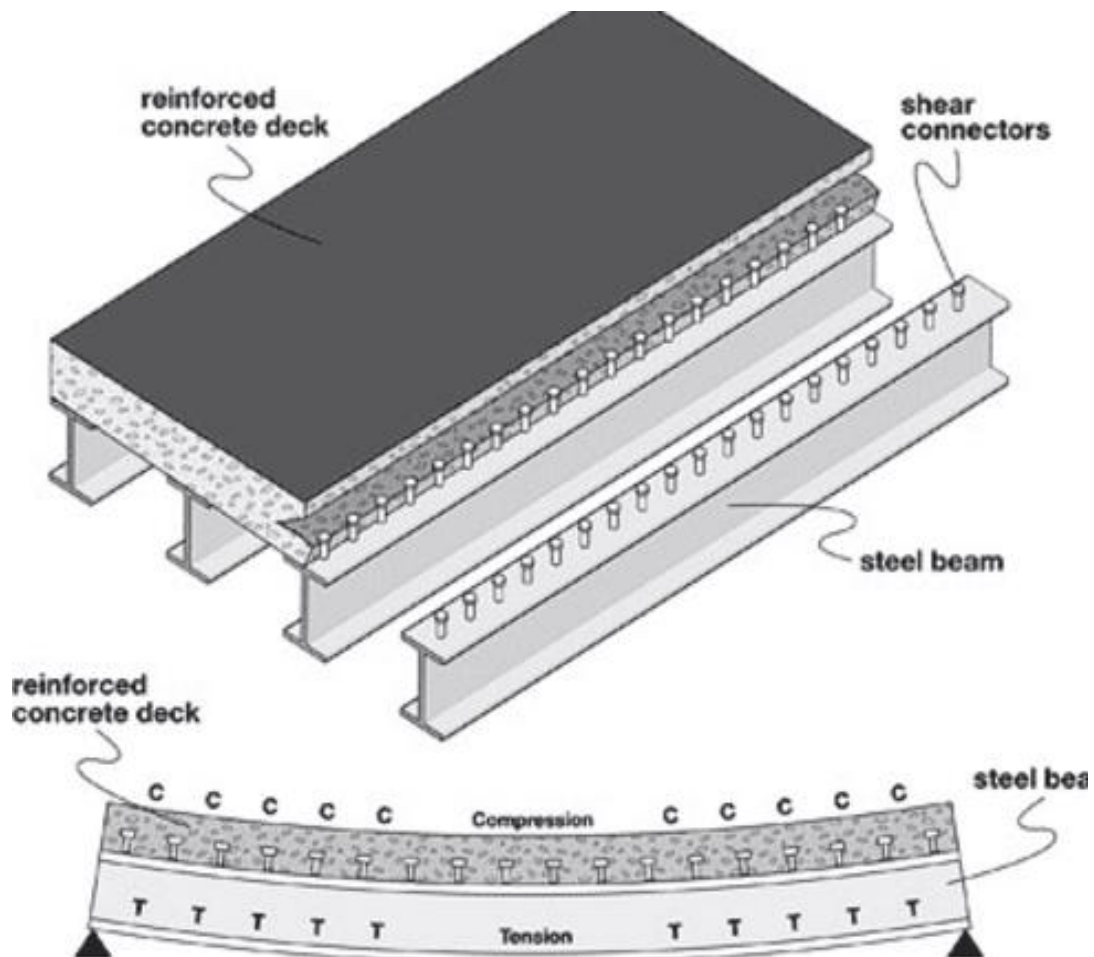
Conventional composite deck systems utilise a concrete deck and steel supporting beams which are connected along the length of the beam with shear connectors. The level of shear connection, determined by the number and spacing of the connectors, dictates the amount of composite action that the beam-deck structure can support. The composite action allows the deck and the beam to act in unison, with the deck behaving like a compression flange to the beam, thus increasing the second moment of area, and therefore the bending stiffness of the whole system.

The primary advantage of this type of construction is that it allows greater spans (or smaller sections), due to the increased performance of the composite section. A system with full interaction will experience negligible slip between the two elements, whereas, a system with partial or no interaction will experience a more significant amount of slip between the deck and the beam. Partial connectivity is achieved through the correct prescription of bolted shear connectors, which can provide higher ductility and rotational capacity than a full shear connection. However, for the purpose of this study, full shear interaction is used, which will simulate an adhesive connection. The different levels of composite action are shown further in [figure 2.31](#).

Concrete elements have a limited service life and require frequent maintenance to ensure their safety during the later years of the structure's lifecycle. For this reason, many concrete decks are being replaced or repaired with FRP products, that offer low maintenance systems with high strength-to-weight properties. This is becoming increasingly popular with composite systems, especially given the latest advancements in demountable decks and connectors that allow the easy replacement of an old deck with a new one, in a 'plug-and-play' fashion (47).

Moreover, one of the most exploited advantages of replacing concrete decks with their FRP counterparts is the reduction in self-weight on the supporting structure, which can bring financial and environmental benefits to almost any project. In road and rail situations this is particularly useful as the deck can be replaced in a short period of time, meaning shorter road/rail closure times (which are very costly). Secondly, due to the increasing amounts of traffic we now have, compared to when most bridges were designed and built (post second world war), the loads on the foundations and abutments of traffic bridges are already higher than initially perceived; if the self-weight of the deck can be reduced, then in some projects the foundations and other supporting elements may not need to be replaced along with the deck.

FRP-steel composite systems work particularly well together due to the high strength-to-weight properties of the FRP and the increased stiffness that the steel beam can offer to the otherwise serviceability-driven design of the FRP deck.



	No interaction	Partial interaction	Complete interaction

Figure 2.31: Composite action in steel beam-concrete slab composite deck structure (59) (60)

3 FIBRE-STEEL LAMINATE MATERIAL INVESTIGATION

3.1 INTRODUCTION

This section will provide an overview and in-depth analysis of the various tests that will help to establish and estimate the properties of the fibre-steel laminate. Due to restrictions in the project, tensile tests of the fibre-steel laminate cannot be completed. For this reason, the properties will be estimated by testing the individual component materials that are used to produce the hybrid-composite: GFRP and perforated steel.

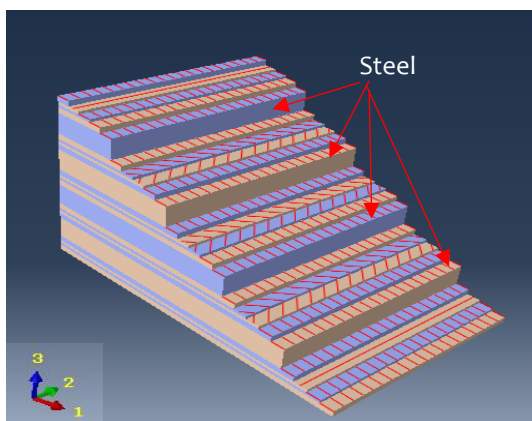
Full details of the production and cutting of the materials can be found in [Appendix A](#).

3.2 FIBRE-STEEL LAMINATE

The laminate produced for testing features 4x1mm perforated steel plates uniformly distributed throughout the laminate, separated by GFRP plies. The laminate is symmetric as shown in the figures below denoted by the subscript S following the laminate layup in [table 3.1](#). The fibres used in this design are 300g/m² which give a ply thickness of 0.26mm. The laminate has an approximate fibre density of 40%.

Table 3.1: FSL Composition

Laminate Layup	[0, 0/90, 0, steel, 0, ±45, 0, steel, 0, ±45] _s
Laminate thickness	7.9mm
Ply thickness	0.26mm
Fibre areal density	300g/m ²
Laminate density	4886kg/m ³



Name	Angle	Thickness	Material
0	0.0	0.26	E-Glass & Polyester Resin
0/90	0.0	0.13	E-Glass & Polyester Resin
0/90	90.0	0.13	E-Glass & Polyester Resin
0	0.0	0.26	E-Glass & Polyester Resin
Steel	0.0	1.0	Perforated Steel & Polyester
0	0.0	0.26	E-Glass & Polyester Resin
+45	45.0	0.13	E-Glass & Polyester Resin
-45	-45.0	0.13	E-Glass & Polyester Resin
0	0.0	0.26	E-Glass & Polyester Resin
Steel	0.0	1.0	Perforated Steel & Polyester
0	0.0	0.26	E-Glass & Polyester Resin
+45	45.0	0.13	E-Glass & Polyester Resin
-45	-45.0	0.13	E-Glass & Polyester Resin

Figure 3.1: Ply stack layup of FSL for experimental analysis

3.3 EXPERIMENTAL & SUPPLEMENTARY INVESTIGATIONS

This section will cover the investigation of the materials properties, evaluated through experimental and supplementary means. Key experiments will be performed on the individual components of the fibre-steel laminate (GFRP and perforated steel) to establish their individual properties which can be used in finite element and classic laminate theory software to predict the properties of the fibre-steel laminate.

It should be stated that the failure of hybrid-composite materials is extremely complex and can be a result of a number of failure modes, including interface failure, delamination and matrix and/or fibre failure. Thus, the experimental values may be inconsistent with the analytically derived values.

3.3.1 Uniaxial Tensile Tests

To begin the experimental phase the individual components of the fibre-steel laminate will be tested separately. This allows an understanding of how the individual materials behave independent of influences from the other. The tests to be conducted are uniaxial tensile tests, performed in both directions for the GFRP elements and in one direction for the perforated steel due to its isotropic nature. The properties to be established from these tests are:

- Young's Modulus
- Strain at failure
- Ultimate tensile strength

3.3.1.1 Unidirectional GFRP

The GFRP samples are made from a series of unidirectional plies, all oriented in the same direction. They are then cut in perpendicular directions as shown in figure 3.2. This allows the establishment of the properties in each direction – essential given the materials' anisotropy.

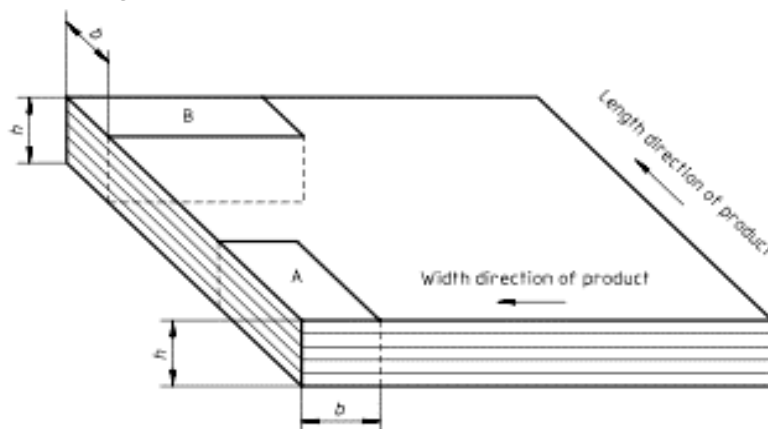


Figure 3.2: Specimen Cutting for Anisotropic Material

Tables 3.2-3.4 show the results from the testing of the GFRP and perforated steel samples respectively. A brief description of each of the results and statistics will be provided prior to analysis and discussion of the results and their meaning.

- **F_{max}** – The maximum force required for the complete failure of the sample, expressed in kilonewtons.
- **S_{max}** – The maximum displacement of the testing apparatus, expressed in millimetres. Can be somewhat inaccurate with regards to the actual displacement of the sample as this value also takes into account any slip, load cell displacement and a number of other contributing, non-load-based displacements. Although they have tried to be minimised where possible.
- **ε_{max}** – The maximum strain within the sample, expressed as a percentage elongation of the original length. The values for strain are obtained through sensors attached to the sample during testing. For GFRP samples resistance-based strain gauges were used, and for the steel samples a contact-based extensometer was used.
- **f_{ult}** – The maximum engineering stress at failure of the sample, expressed in megapascals. Calculated by dividing the force at failure by the cross-sectional area of the sample.
- **E** – Young's modulus of the specimen, expressed in gigapascals. Determined using Hooke's Law, in this case by calculating the gradient of the linear part of the stress v strain graphs.
- **Average** – Mean average, obtained by the summation of all values divided by the total number of values for that variable.
- **SD** – Standard deviation of the results. Used to quantify the dispersion of the data set – small standard deviation means low dispersion of values within the data set.
- **CV** – Coefficient of variation of the results, expressed as a percentage. Allows a more relative view of the dispersion of the data set as it is expressed as a percentage, giving the ratio of standard deviation to the mean. Hence, CV is also known as relative standard deviation.

3.3.1.1.1 0° Direction

Table 3.2: Uniaxial tensile test results for 0° fibre orientation

	Specimen A	Specimen B	Specimen C	Specimen D	Specimen E	Average	SD	CV (%)
F_{max} (kN)	110.530	110.878	108.526	109.668	100.076	107.94	4.49	4.16
S_{max} (mm)	10.318	10.460	10.122	10.815	10.077	10.36	0.30	2.88
ϵ_{max} (%)	2.356	2.377	2.291	2.447	2.276	2.35	0.07	2.94
f_{ult} (MPa)	491.244	492.790	482.339	487.414	476.553	486.07	6.68	1.37
E (GPa)	29.874	28.721	28.538	28.626	30.747	29.30	0.97	3.32

The samples tested in the 0° direction showed good correlation and exhibited the expected behaviour, with a relatively linear curve finishing at an average failure stress of 486MPa. The average Young's modulus of the samples (29.3GPa) is reliable given the low (3%) coefficient of variation, however is lower than the values expected from the JRC 2016 stated values. This is because of the minor cross-stitching of the 'unidirectional' laminate – the laminate is not 100% unidirectional, in fact 23% of the fibres are perpendicular to the primary direction to allow some integrity to the fabric. Figure 3.4 shows the typical failed sample showing ruptured fibres which highlights the explosive nature of this failure mode.

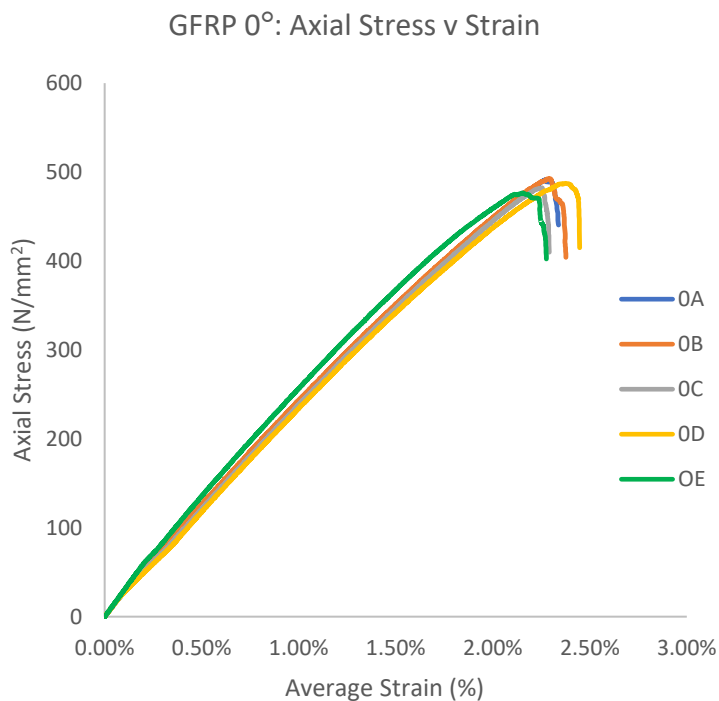


Figure 3.3: Axial Stress v Strain Graph for 0° Fibre Orientation



Figure 3.4: Failed 0° Sample

3.3.1.1.2 90° Direction

Table 3.3: Uniaxial tensile test results for 90° fibre orientation

	Specimen A	Specimen B	Specimen C	Specimen D	Specimen E	Average	SD	CV (%)
F_{max} (kN)	38.293	38.666	38.190	36.977	37.853	37.996	0.639	1.682
S_{max} (mm)	11.162	10.955	11.034	10.497	10.684	10.866	0.271	2.491
ϵ_{max} (%)	2.542	2.479	2.515	2.399	2.468	2.481	0.054	2.187
f_{ult} (MPa)	170.192	171.848	169.731	164.341	168.236	168.870	2.840	1.682
E (GPa)	6.805	6.606	5.687	6.678	6.962	6.548	0.500	7.633

The 90° samples exhibit a clear bi-linear stress – strain curve, the change in gradient is caused by a combination of the yielding of the matrix and the redistribution of stresses to the 23% of fibres oriented in the direction of the loading. As fibres fail, the stress is redistributed to the other fibres until they all ultimately fail. Since the ultimate strain of the resin is higher than that of the fibres the matrix remains largely in-tact (figure 3.6). The Young’s modulus is extracted from the second linear part of the graph as this corresponds to the strain limits for transverse compressive and tensile strength specified in the JRC design guidelines. Allowing a more realistic damaged stiffness value to be used, ahead of the initial stiffness which overestimate the stiffness when in application.

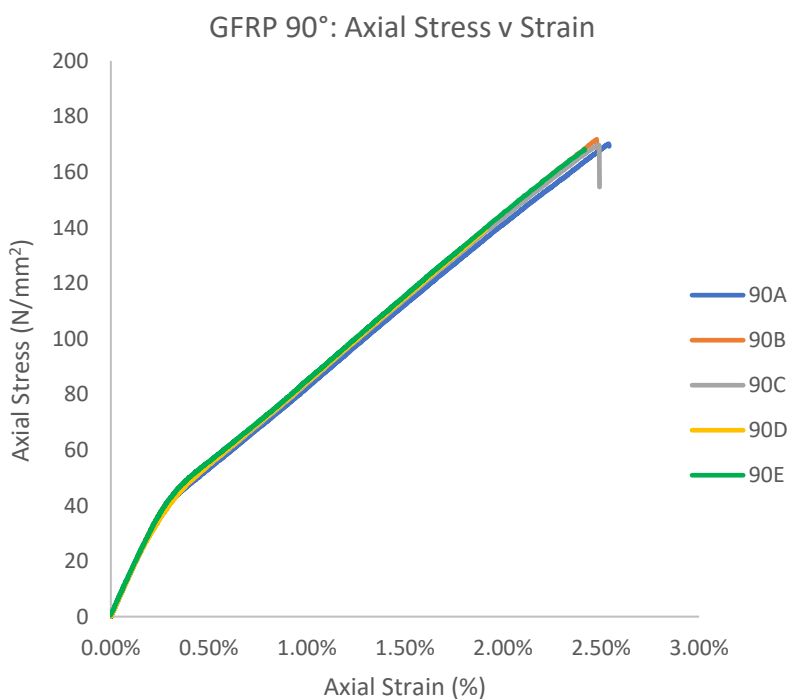


Figure 3.5: Stress v Strain graph for 90° fibre orientation



Figure 3.6: Failed 90° Sample

3.3.1.2 Perforated Steel

Table 3.4: Uniaxial tensile test results for perforated steel samples

	Specimen A	Specimen B	Specimen C	Specimen D	Specimen E	Specimen F	Specimen G	Specimen H	Average	SD	CV (%)
F_{max} (kN)	3.14	3.11	3.14	3.12	3.14	3.11	3.13	3.12	3.13	0.01	0.39
S_{max} (mm)	10.22	9.49	10.41	9.29	10.47	9.35	11.10	10.20	10.07	0.64	6.32
ϵ_{max} (%)	5.62	5.95	6.58	5.81	6.65	5.78	6.84	6.53	6.22	0.48	7.66
f_{ult} (MPa)	203.96	201.85	202.54	202.59	203.62	202.03	203.18	202.66	202.80	0.74	0.36
E (GPa)	135.9	124.24	149.9	137.5	155.3	150.98	161.5	139.0	144.3	12.20	8.45

Perforated Steel: Axial Stress v Strain

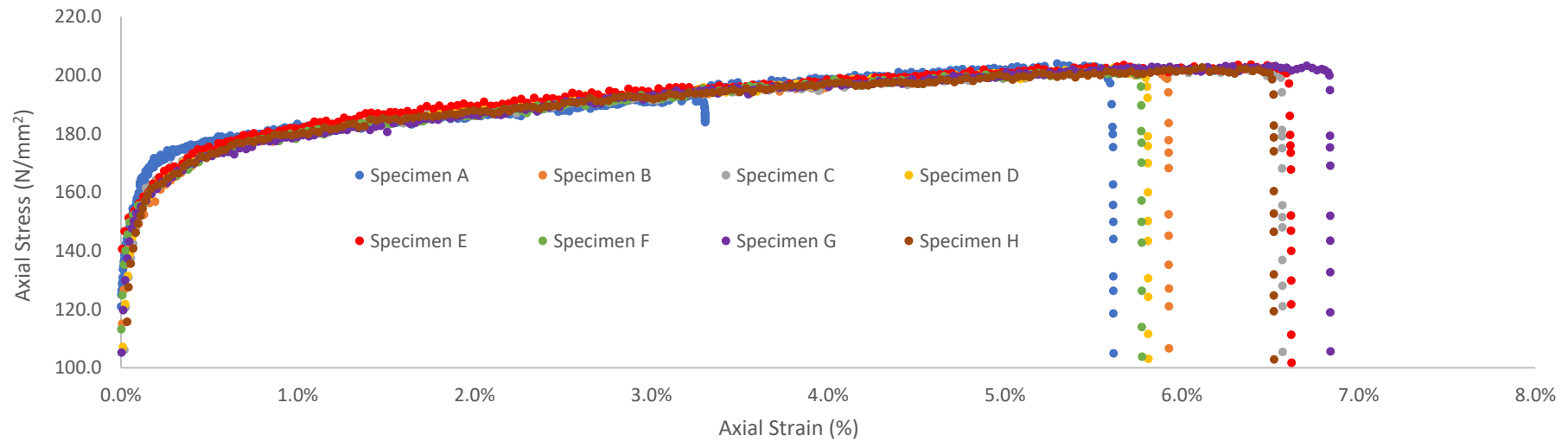


Figure 3.7: Stress v Strain Curves: Perforated Steel

The perforated steel samples of grade S235 did not reach the expected results that are widely known for steel, being a Young's modulus of 210GPa and a yield strength in this case of 235MPa. This is due to the perforations in the steel which reduce the cross-section of material. The steel still, however, exhibits a ductile behaviour in comparison to the GFRP samples. This ductility is also limited by the perforations as the holes elongate, necking in the region between holes, before eventually merging into one slice across the cross-section. This process can be seen in [figure 3.8](#).

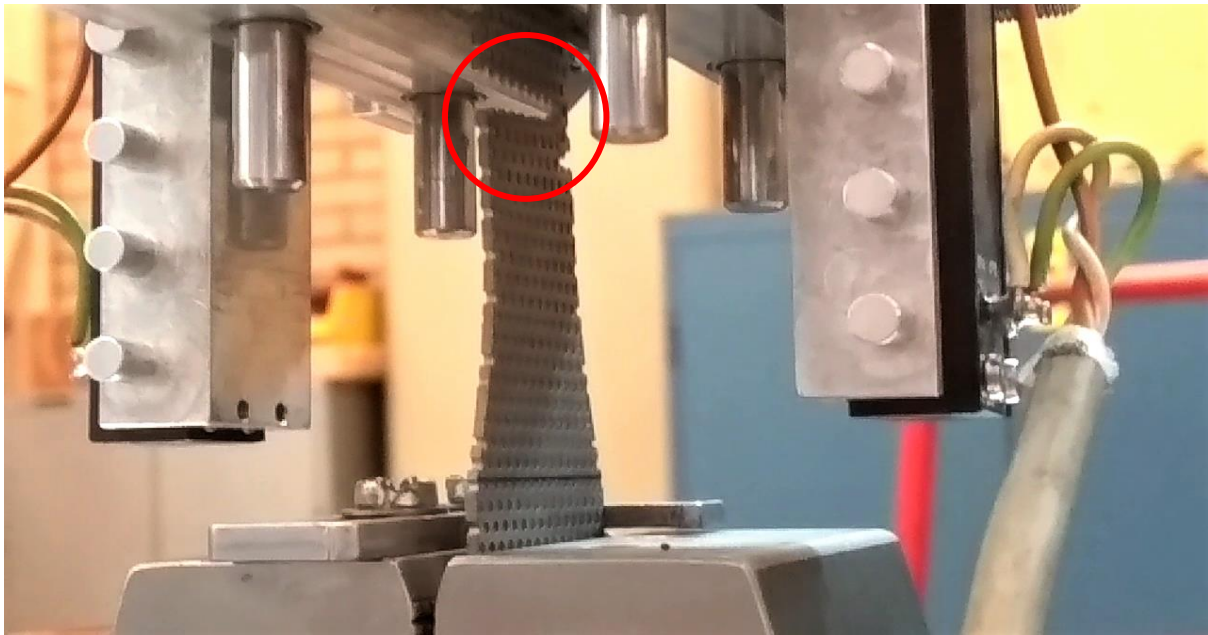


Figure 3.8: Merging of Perforations in Steel Samples



Figure 3.9: Failed Perforated Steel Sample

3.3.1.3 Fibre-Steel Laminate (FEA/CLT)

Using the results from the individual component materials the axial stiffness of the material can be estimated using classic laminate theory (CLT) software. Furthermore, using finite element software to simulate an experimental procedure these values can be verified. The laminate exploration software ‘eLamX²’ will be used for the classic laminate theory estimations and Abaqus 6.14 CAE to confirm CLT results.

In the finite element investigation, the stress-strain relation will be limited to the elastic region given the complexity and magnitude of uncertainty surrounding the composite behaviour of the material and its failure.

Table 3.5: Axial Stiffness Comparison

	Classic Laminate Theory	Finite Element Analysis
E _{xx} (GPa)	92.5	92.6
E _{yy} (GPa)	84.8	85.0

The characteristic yield and ultimate strength of the fibre-steel laminate can be estimated using the following formulae respectively:

$$\sigma_{i,y,FSL,Rk} = \frac{E_{i,FSL}}{E_s} * f_{s,y}$$

$$\sigma_{i,ult,FSL,Rk} = f_{s,ult} * MVF + \left[E_{i,FRP} * \left(\frac{t_{i,FRP}}{t_{skin}} \right) + E_{i\pm 1,FRP} * \left(\frac{t_{i\pm 1,FRP}}{t_{skin}} \right) \right] * \epsilon_{i,FRP,ult}$$

Table 3.6 shows the estimated strength values based on the experimental data established from the tests on the individual components. Figure 3.10 shows a comparison of the stress strain relations of the individual components and the estimated properties of the hybrid-composite.

Table 3.6: Estimated FSL Axial Strength Values

	Longitudinal (Direction 1=0°)	Transverse (Direction 2=90°)
$\sigma_{y,FSL,Rk}$ (MPa)	102	94
$\sigma_{ult,FSL,Rk}$ (MPa)	287.5	167

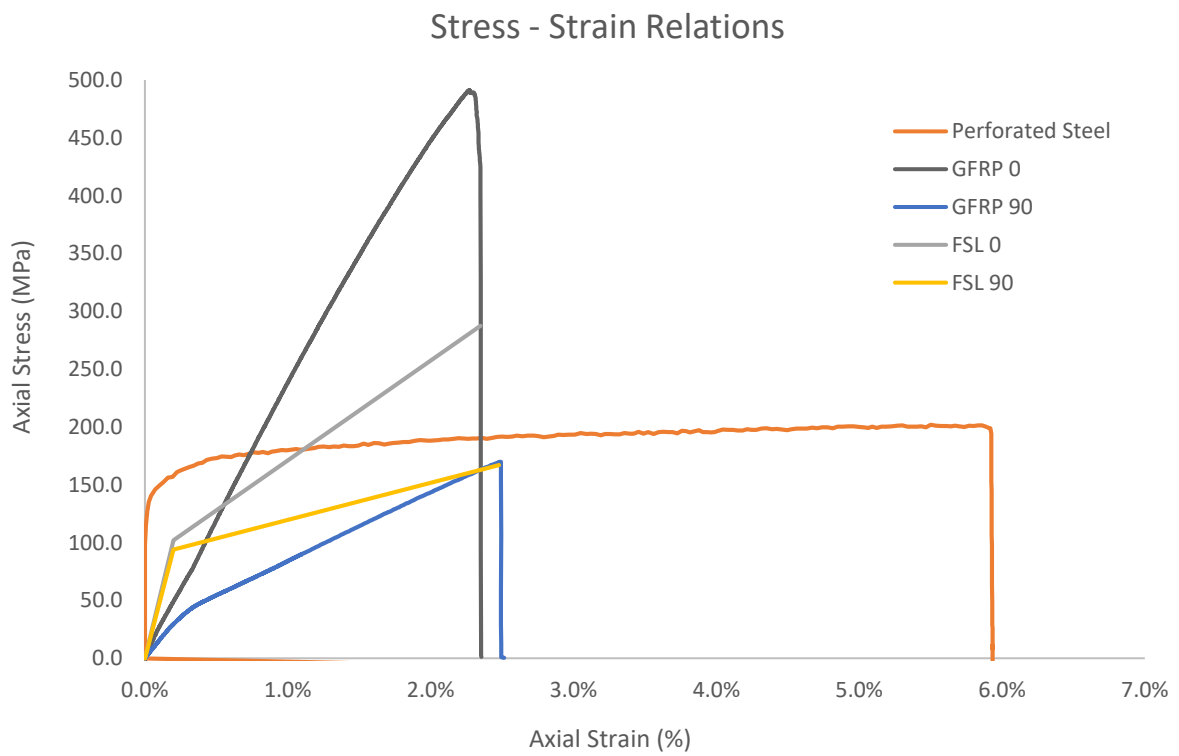


Figure 3.10: Stress - Strain Relations of Individual Components and Hybrid-Composite

3.3.2 Inter-Laminar Shear Tests

The tests will be based around the NEN-ISO 14130:1997 standard for short beam shear test of fibre-reinforced polymer specimens. The short beam shear test is a three-point bending test with the two supports at close proximity, this is to encourage the development of shear stresses at the mid-plane of the sample, where the flexural stresses are zero, shown in [figure 3.11](#).

3.3.2.1 Fibre-Steel Laminate

The experimental investigation into the fibre-steel laminate will be limited to the testing of the inter-laminar shear strength (ILSS). This property is of great importance, as if the ILSS is insufficient then the benefits of combining the two materials is irrelevant as the material will delaminate under relatively low stresses or temperatures. There are various options available to mechanically or chemically improve this interface, as discussed in [section 2.3.3.2](#), however, to give an idea of the lower bound of the ILSS only basic treatments have been applied to this fibre-steel laminate. The improvements are limited to: the abrasion and degreasing of the steel surface and the perforations within the steel that will allow through-thickness transmission of resin. The resin used is a polyester-based resin which is known to be less effective in adhesion than for example epoxy-based resins. It should be noted that some samples are of slightly different width to others due to inaccuracies in the cutting process, this will be taken into account in the calculations.

The dimensions of the samples are as follows:

- Length (l) – 100mm
- Width (b) ~ 50mm
- Thickness (h) – 7.9mm
- Support span (L) – 50mm

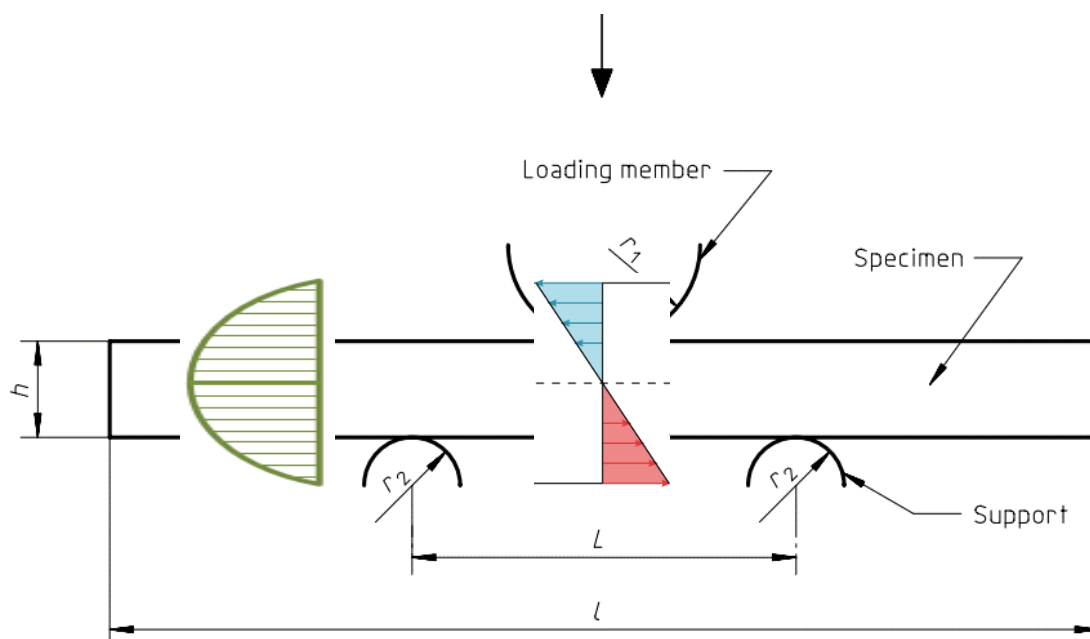


Figure 3.11: Short-beam Shear Test Schematic with (left) Shear Stress and (centre) Flexural Stress Distributions Overlaid

The inter-laminar shear strength can be established from the experimental results using the following formula:

$$\tau = \frac{3 FL}{4 bh}$$

Using the maximum force reached during the testing procedure will yield the inter-laminar shear strength just before delamination, as the force in the sample will decrease post-delamination. Due to the close proximity of the supports a shear failure mode is encouraged rather than a flexural failure mode, meaning that the shear deformation of the sample is not negligible as in a flexural three-point bending test.

3.3.2.1.1 0° Direction

Table 3.7: Inter-laminar Shear Test Results Longitudinal FSL Samples

Sample	OB	OC	OD	OE	OF	Average	Standard Deviation	Coefficient of Variation (%)
Force (kN)	6.41	7.64	7.58	7.93	6.44	7.20	0.72	9.98
Flexural Stress (MPa)	154.16	179.93	171.82	179.75	161.15	169.36	11.45	6.76
ILSS (MPa)	12.18	14.21	13.57	14.20	12.73	13.38	0.90	6.76

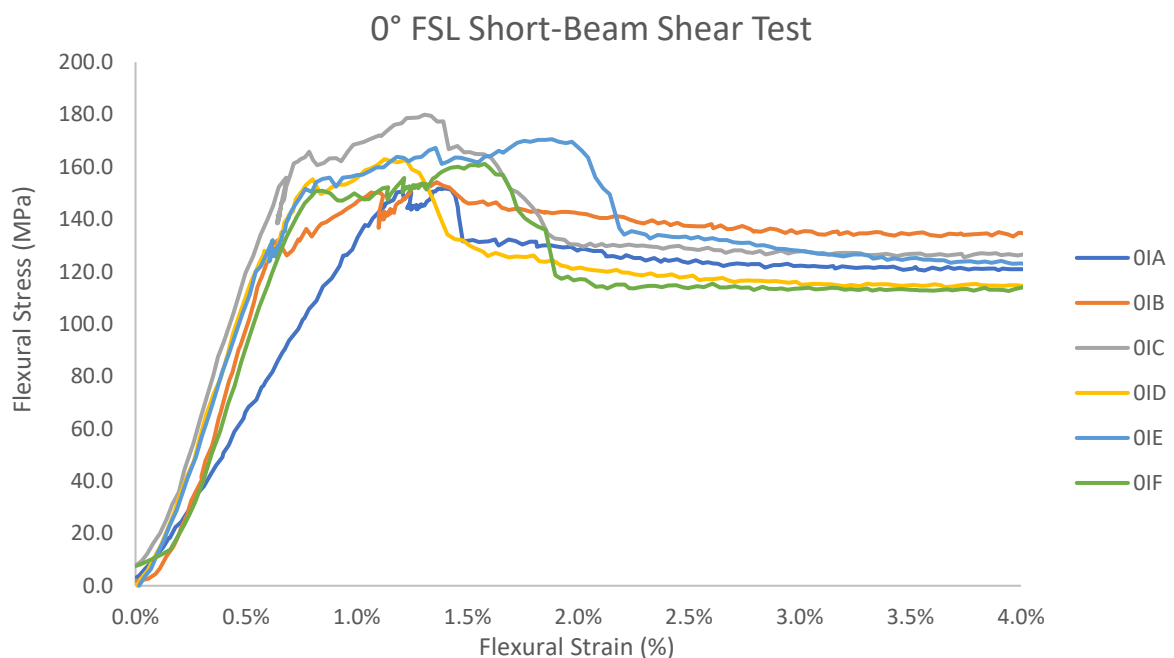


Figure 3.12: Flexural Stress-Strain Relationship for Longitudinal FSL Samples

From table 3.7 it can be observed that the inter-laminar shear strength of the longitudinally oriented samples is consistently around 13MPa (7% coefficient of variation). It should be noted that sample '01A' has been removed as an anomalous result. Figure 3.12 displays the flexural stress and strain relationship of each of the samples. The initial portion of the graph (between 0-3% flexural strain) show the samples behaviour up until delamination, with each of the curves showing a similar response. The first linear portion of the graph corresponds to the elastic deformation of both the fibres and the steel, until deviations appear as a result of fibre failure, before the stress is redistributed to longitudinal fibres and continues to rise. As the steel also begins to plastically deform the gradient of the curve begins to change until a major delamination occurs (figure 3.13) resulting in a reduction in stress. However, the delamination isn't the ultimate failure of the material as it can still sustain a certain portion of the load, this continues in the plateau of the graph (flexural strain >3%) as the steel continues to plastically deform. In the comparison graph shown in figure 3.15, it can be seen that the fracture energy up to the initial delamination is greater in the GFRP sample, however, post the initial delamination the FSL sample can continue absorbing energy through the plastic deformation of the steel.

Due to the elastic nature of the GFRP material, upon unloading of the sample major delaminations occur between almost all plies. This happens because the steel has plastically deformed into the deformed shape of the sample and the GFRP plies have elastically deformed into the same shape, so when the force is released the GFRP snaps back into its original position causing peel stresses at the steel-FRP interface, which lead to the delamination pattern shown in figure 3.14.

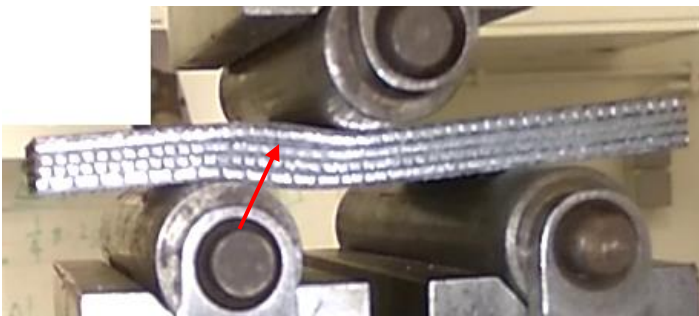


Figure 3.13: Initial Delamination

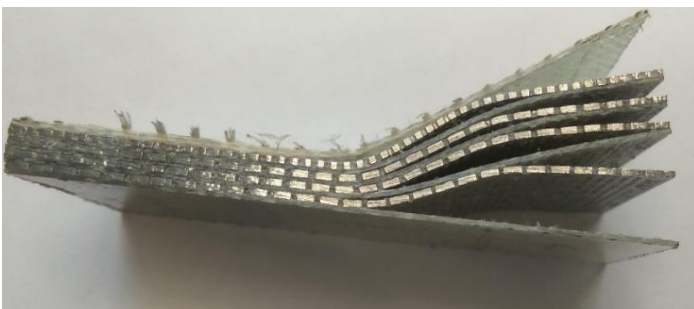


Figure 3.14: Elastic and Plastic Deformation of GFRP and Steel Plies Respectively

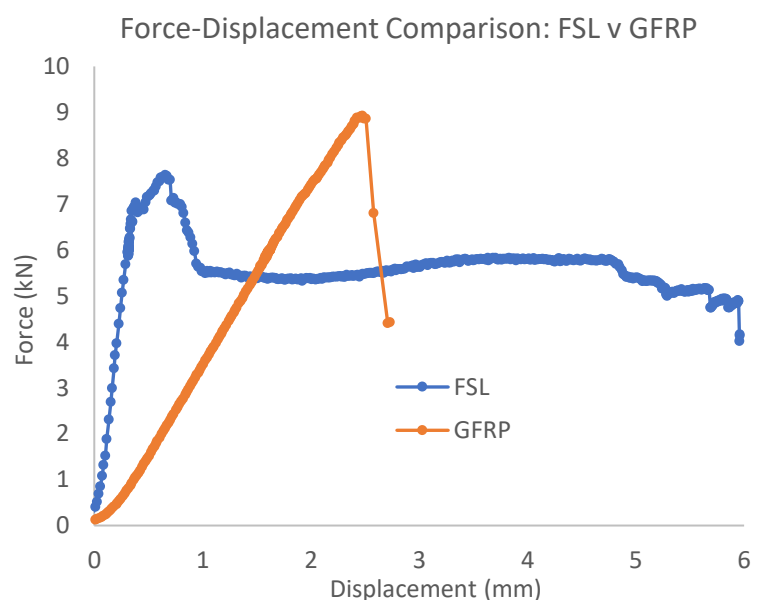


Figure 3.15: Fracture Energy Comparison FSL v GFRP

3.3.2.1.2 90° Direction

Table 3.8: Inter-laminar Shear Test Results Transverse FSL Samples

Sample	90A	90B	90C	90D	90E	Average	Standard Deviation	Coefficient of Variation (%)
Force (kN)	5.88	6.13	6.34	5.83	5.99	6.03	0.206	3.42
Flexural Stress (MPa)	141.36	147.31	152.35	142.91	143.95	145.58	4.372	3.00
ILSS (MPa)	11.17	11.64	12.04	11.29	11.37	11.50	0.345	3.00

90° FSL Short-Beam Shear Test

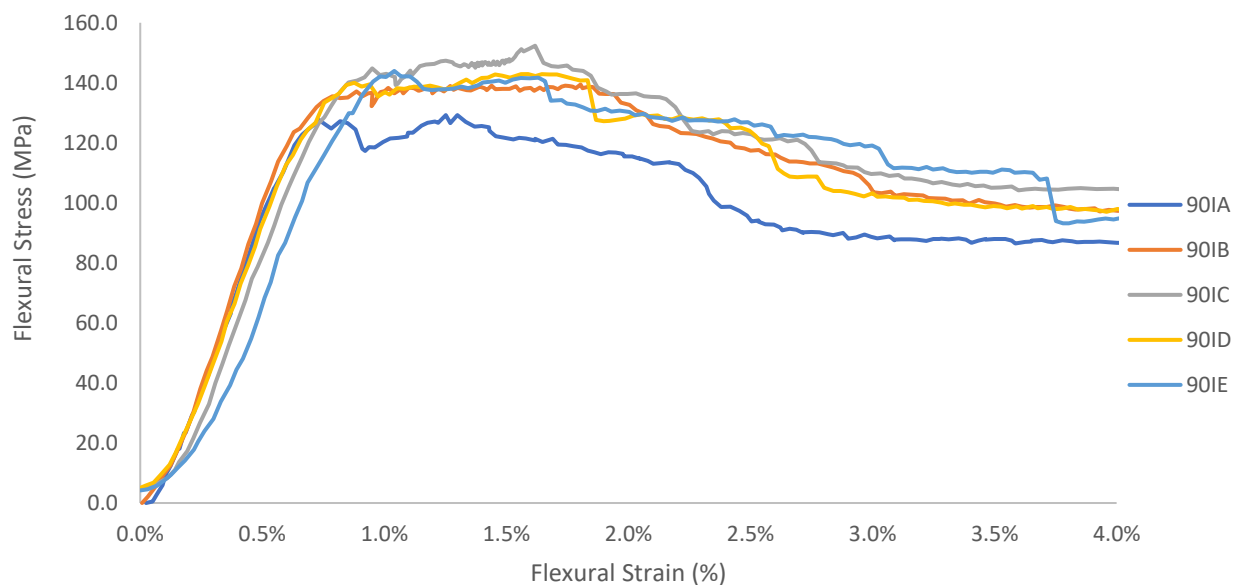


Figure 3.16: Flexural Stress-Strain Relationship for Transverse FSL Samples

The samples in the 90° direction have an average ILSS of 11.5MPa which is consistent across the 5 samples with a coefficient of variation of 3%. This is slightly lower than the samples that are oriented in the 0° direction, this is due to the difference in Young's modulus of the two adjacent plies at the steel-FRP interface. There is a greater difference in the moduli of the fibres in the transverse direction and the steel, than the fibres in the longitudinal direction and the steel, this causes additional stresses at the interface causing it to fail earlier.

Figure 3.16 highlights the different stress redistribution behaviour between the two orientations; in the 0° direction, the stress is redistributed to other longitudinal fibres, allowing an increase in stress, whereas in this case the stress is redistributed to the steel which plastically deforms, leading to the plateau seen at 1.25-2.5% flexural strain.

3.3.2.2 Unidirectional GFRP

Short-beam shear tests will also be performed on the unidirectional GFRP samples in order to compare the effectiveness of the FRP-FRP interface to the effectiveness of the FRP-steel interface. This will help to quantify the expected decrease in interface performance expected from the hybrid-composite.

The test will be performed as described in section 3.4.2, with the following dimensions:

- Length (l) – 100mm
- Thickness (h) – 4.9mm
- Width (b) ~ 50mm
- Support span (L) – 50mm

Table 3.9: Inter-laminar Shear Test Results GFRP Samples

Sample	0A	0B	0C	0D	0E	0F	Average	Standard Deviation	Coefficient of Variation (%)
Force (kN)	8.92	7.21	7.81	7.95	8.12	8.12	7.84	0.51	6.33
Stress (MPa)	580.70	459.43	497.57	506.80	507.30	528.53	499.93	36.52	7.31
ILSS (MPa)	28.45	22.51	24.38	24.83	24.86	25.90	24.50	1.79	7.31

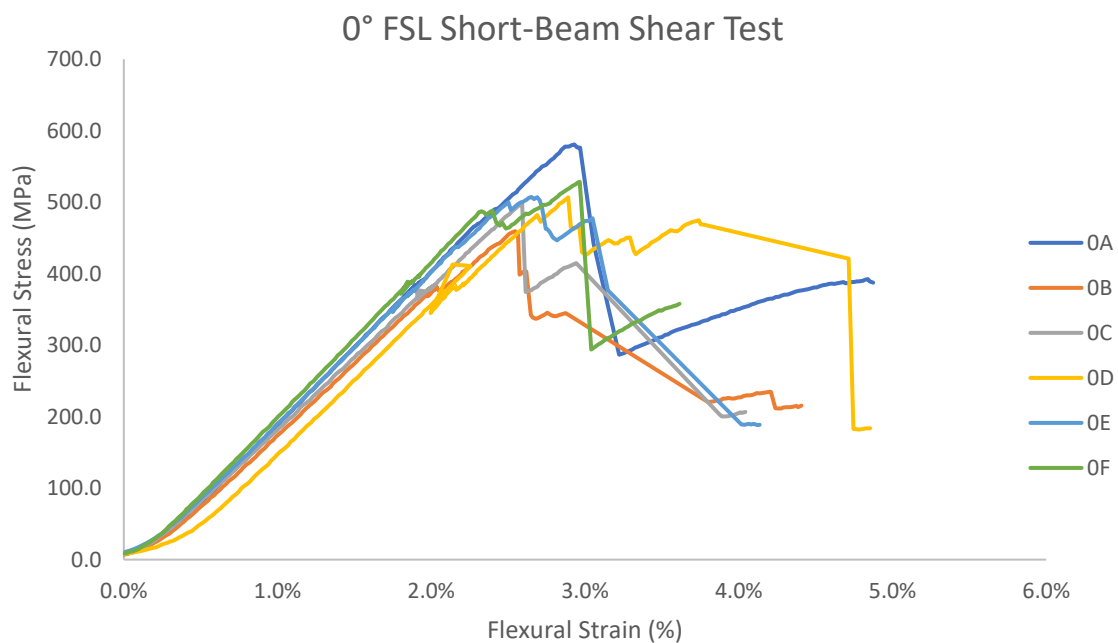


Figure 3.17: Flexural Stress-Strain Relationship for GFRP Samples

The average ILSS of the GFRP samples oriented in the longitudinal direction is approximately double that of the FSL samples. The ratio of ILSS in the pure-FRP compared to the equivalent FML is consistent with that found in literature, see [table 2.2](#) of the literature review. This is due to a number of factors related to the difference of the materials at the interface, a key reason is the difference in stiffness values but other reasons include the unfavourable adhesive surface of the steel in comparison to the dry glass-fibres which can be easily impregnated by the resin.

From [figure 3.17](#) the flexural stress-strain relation can be observed for the longitudinal GFRP samples. It can be seen that at in a range of 300-400MPa each of the samples experience a discontinuity in the linear portion at the start of the experiment. Using the characteristic compressive strain limits prescribed by the JRC design guidelines and imagery from the experiments, it can be estimated that this discontinuity is a compressive failure of fibres at the surface of the laminate that is compressed by the loading pin. Using the prescribed strain limit of 1.44%, the stress at which the initial compressive failure of certain fibres occurs at, is approximately 325MPa. Following this initial failure, the stress is redistributed to other fibres and the stress in the samples continue to rise until a delamination occurs, where a significant drop in the stress can be seen. Due to this compressive failure it can be said that the inter-laminar shear strength derived from this experiment is not truly accurate, as the influence of the fibres that have failed in compression will lead to earlier onset of failure. For this reason, the established ILSS is a minimum or lower-bound value. The failed samples can be seen in [figure 3.18](#).

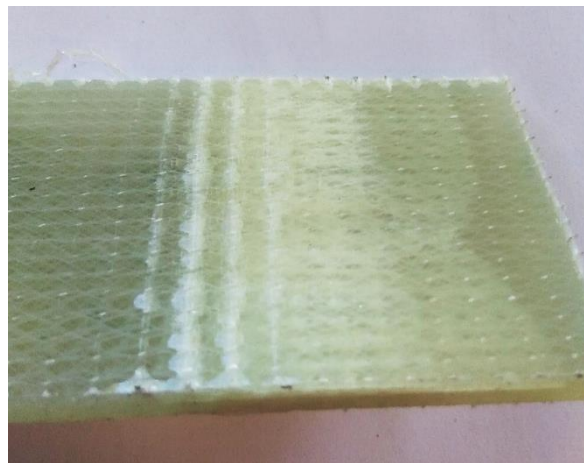


Figure 3.18: Failed GFRP ILSS Samples

3.3.2.3 Finite Element Modelling

To validate the results from the experiment, and to provide further details into the through-thickness behaviour of the material, a finite element model of the short-beam shear test has been developed. The model is comprised of continuum shell elements that allow for stresses to be read vertically through the thickness of the laminate. Two models have been produced, one that models the damage of the sample shown in [figure 3.21](#) using cohesive zone modelling and one that models the inter-laminar shear stress distribution through the thickness of the sample, [figure 3.20](#).

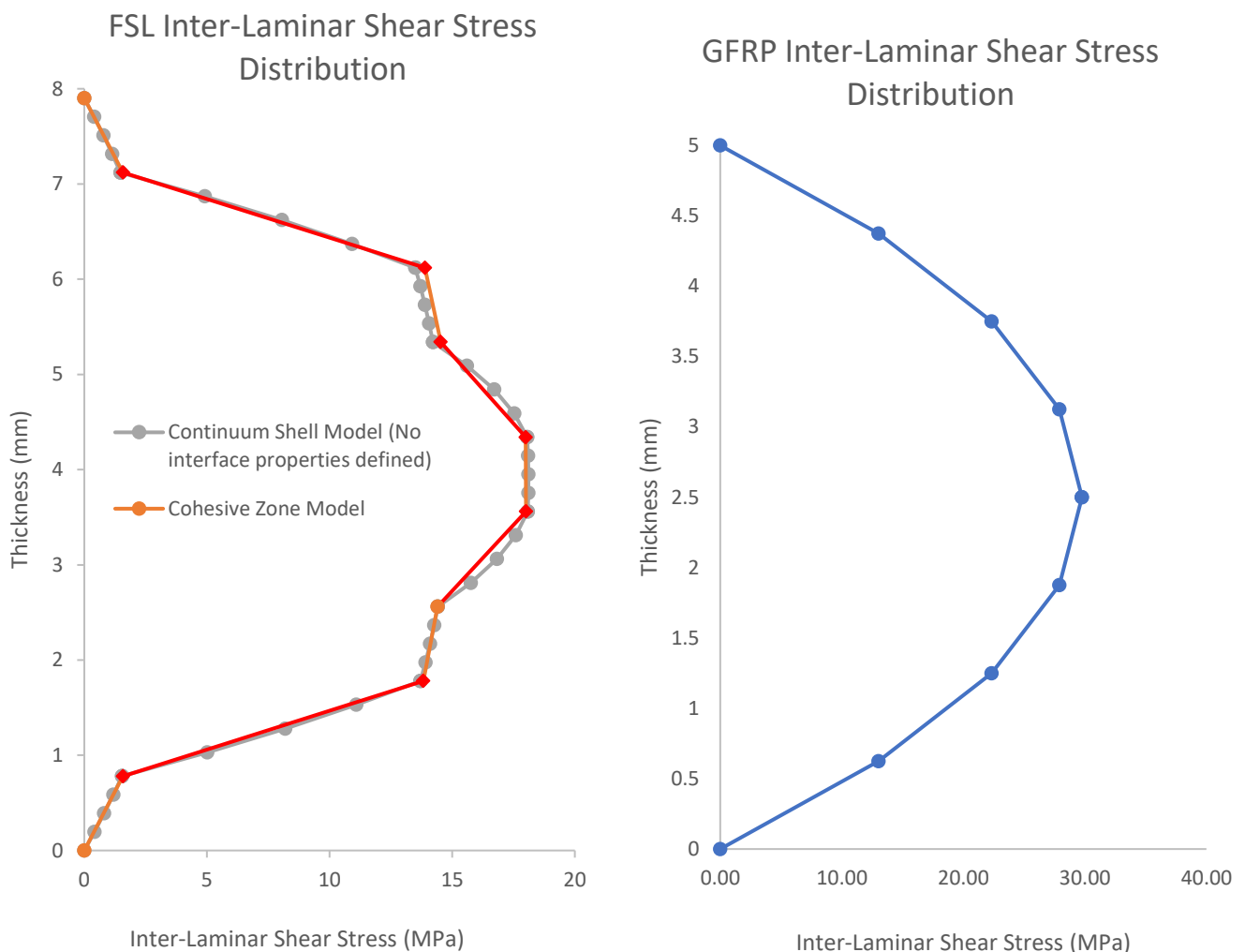


Figure 3.19: (left) Comparison of Inter-Laminar Shear Stress Using Continuum Shell Elements with and without Cohesive Interface Properties Defined for FSL, (right) Inter-Laminar Shear Stress Distribution in GFRP

As can be seen, the results are in good agreement with each other showing that the model without cohesive properties can be used to gain an accurate impression of the through thickness stress distributions. The expected parabolic distribution can be roughly seen although given that the material is inhomogeneous the deviation from this shape is allowable. The change in gradient of the lines signify the change in material, where the stiffer plies (shown in red) can be attributed to the steel and the more vertical lines to the less stiff GFRP plies.

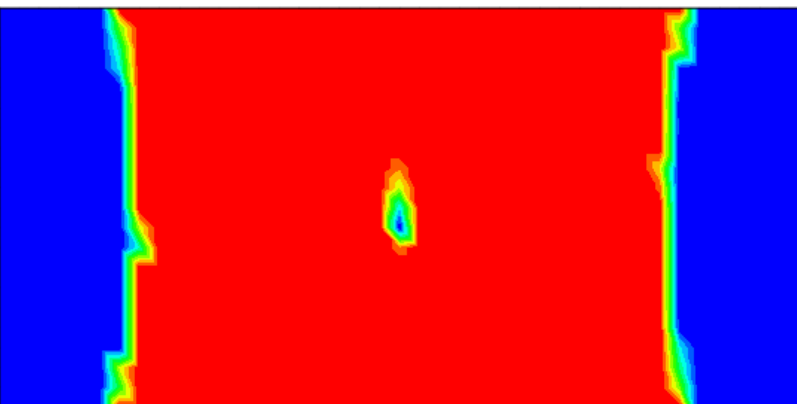
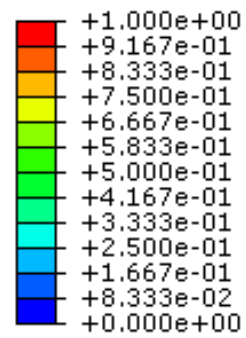
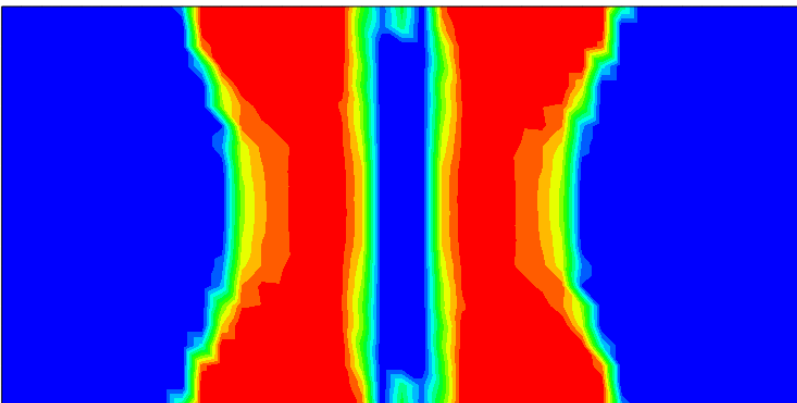
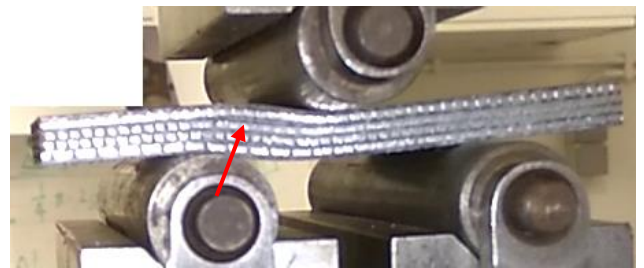
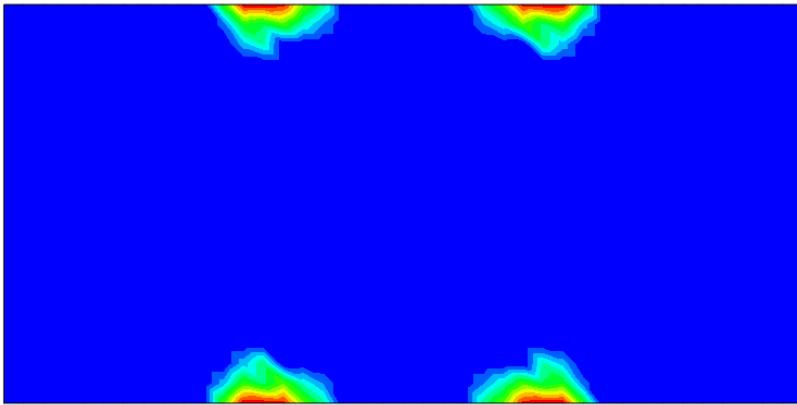
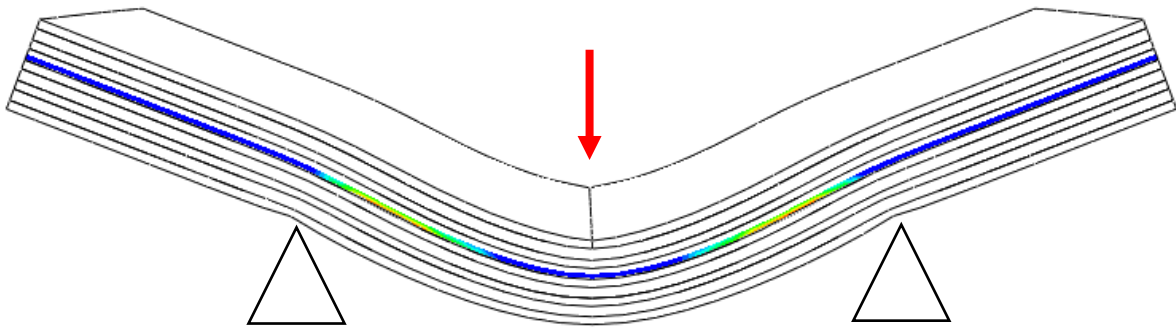


Figure 3.20: FE Images Showing Initiation and Propagation of Shear Damage in FSL

Figure 3.20 shows how the damage initiates at the edges of the sample and propagate inwards towards the centre of the sample. The damage also propagates outwards, towards and over the supports, evidence of which is also shown from the images of the experiment.

Using the distributions shown in figures 3.19 it can be stated that the formula given in the experimental standard can still be applied to the FSL material, although it should depend on the distribution of the steel. When the steel is distributed uniformly through the thickness of the laminate it is expected that the material will act more homogeneously than it would if the steel was focused at the extremes of the laminate. Figure 3.21 shows a comparison between a laminate with steel distributed uniformly throughout the thickness and another laminate with the steel focused at the extremes. It can be seen that actually both laminates exhibit a roughly parabolic shape, in which case the original formula still applies here. By calculating the ratio of the applied stress to the whole stress block, the actual coefficient can be found, in the two cases presented a coefficient of 0.62 and 0.68 can be applied to the laminate with the uniformly distributed steel and the steel focused at the extremes respectively. Thus, the stated coefficient of 0.75 is actually slightly non-conservative in both of these cases.

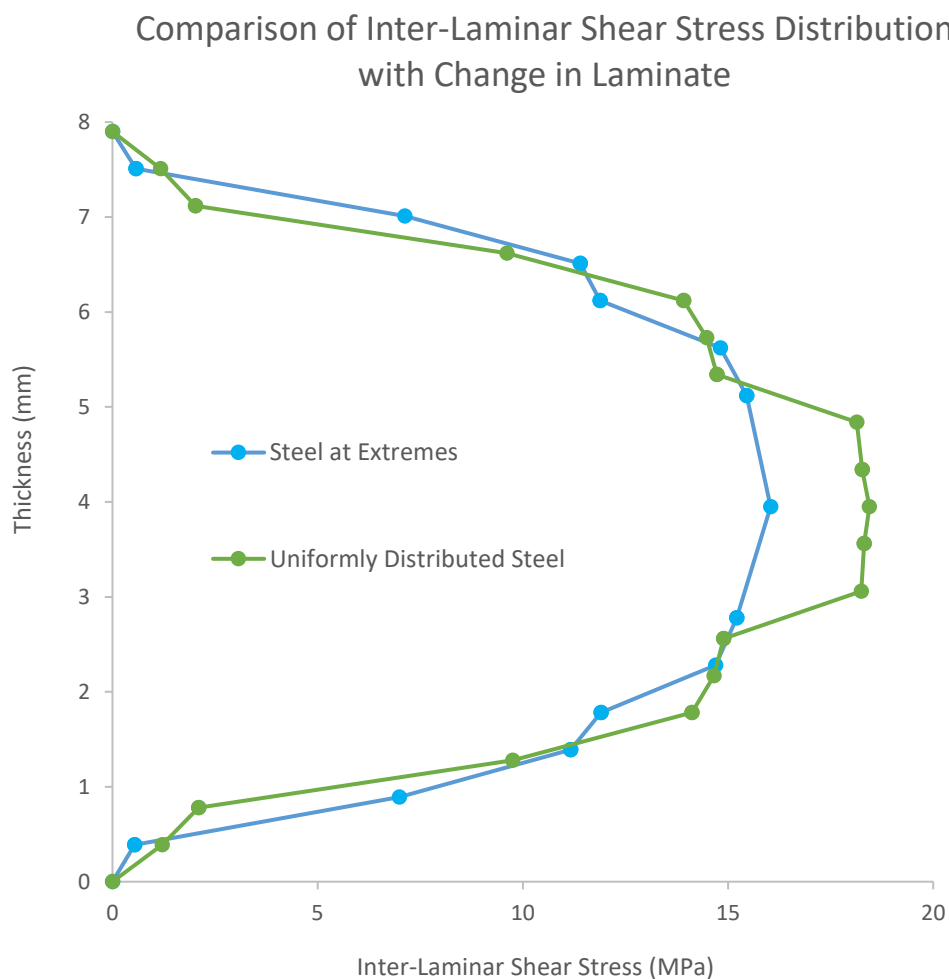


Figure 3.21: Comparison of FSL Inter-Laminar Shear Stress Distribution with Layup Change

3.3.3 Flexural Behaviour: Fibre-Steel Laminate (FEA/CLT)

Using the results from the individual component materials the flexural stiffness of the material can be estimated using classic laminate theory (CLT) software. Furthermore, using finite element software to simulate an experimental procedure these values can be verified. The laminate exploration software ‘eLamX²’ will be used for the classic laminate theory estimations and uniaxial tensile and flexural bending tests will be performed in Abaqus 6.14 CAE to confirm CLT results. Table 3.10, shows a comparison of the results.

Table 3.10: Comparison of Flexural Stiffness Values

	Composite Laminate Theory	Finite Element Analysis
E_{xx} (GPa)	78.0	75.1
E_{yy} (GPa)	68.3	65.7

It can be seen that the values provide reasonable agreement but could be improved, this is due to the approach of the classic laminate theory which neglects the shear deformation of the sample. The finite element results are lower as they do take into account the shear deformation, however, the amount of shear deformation is minimised through the dimensions of the experimental set up being simulated.

3.3.4 Thermal Behaviour (FEA/CLT)

The coefficients of thermal expansion for steel and GFRP plies are different to each other, meaning that the two materials within the laminate will expand or contract at a different rate under the same temperature. The plies are bonded together and so differential expansion is restricted. This induces additional stresses on the plies as well as inter-laminar shear stresses between plies which may contribute to failure. Using a service temperature of 50°C, and the thermal expansion coefficients from the JRC 2016 guidelines (48), shown below, the stresses generated can be calculated using classic laminate theory and finite element analysis. Finally, these stresses can be compared to the strengths of the individual plies.

Table 3.11: Coefficient of Thermal Expansion for UD Ply of E-Glass and Polyester (48)

V_f	UD plies			
	$\alpha_{resin} = 50 \cdot 10^{-6} \text{ K}^{-1}$		$\alpha_{resin} = 120 \cdot 10^{-6} \text{ K}^{-1}$	
	$\alpha_1 [\cdot 10^{-6} \text{ K}^{-1}]$	$\alpha_2 [\cdot 10^{-6} \text{ K}^{-1}]$	$\alpha_1 [\cdot 10^{-6} \text{ K}^{-1}]$	$\alpha_2 [\cdot 10^{-6} \text{ K}^{-1}]$
40 %	8.2	27.7	13.0	62.1
45 %	7.7	25.4	1.6	56.3
50 %	7.2	23.2	10.5	50.8
55 %	6.9	21.1	9.6	45.5
60 %	6.6	19.1	8.8	40.4
65 %	6.3	17.1	8.1	35.5
70 %	6.1	15.2	7.5	30.7

The more conservative of the two sets of values will be used given the uncertainty surrounding the coefficient of thermal expansion of the resin. This gives a coefficient of $10.5 \cdot 10^{-6}/\text{K}$ and $50.8 \cdot 10^{-6}/\text{K}$ for the longitudinal and transverse directions respectively. The coefficient of thermal expansion for steel is $12 \cdot 10^{-6}/\text{K}$ (49). The maximum stresses generated in each ply at 50°C (323K) temperature gradient are given in table 3.12.

Table 3.12: Maximum Stress per Ply Generated at 50°C Temperature Gradient

Method	Ply Material	Maximum Longitudinal Stress in Ply (MPa)	Maximum Transverse Stress in Ply (MPa)	Maximum Inter-Laminar Shear Stress (MPa)
CLT	GFRP	-1.50	-12.62	N.A
	STEEL	3.25	10.22	
FEA	GFRP	-1.27	-12.61	55.5
	STEEL	3.10	10.15	

The in-plane stresses developed through the differential expansion of the two materials are of relatively low concern when considered by themselves, however, when considered in combination with mechanical loads this will contribute to earlier onset of failure given the already low strength of the material. Moreover, the inter-laminar shear stresses that develop at the interface of the two materials exceed the ILSS by a factor of 4. However, these stresses are concentrated at the very edges of the sample where free expansion is possible and decrease with proximity to the centre. Therefore, it becomes important to experimentally test this with a structural member to determine the effect this would have as the centre of the laminate is approached.

It should be noted that greater stresses are found in the transverse direction due to the magnitude of difference in thermal expansion coefficients in that direction when compared to the longitudinal direction.

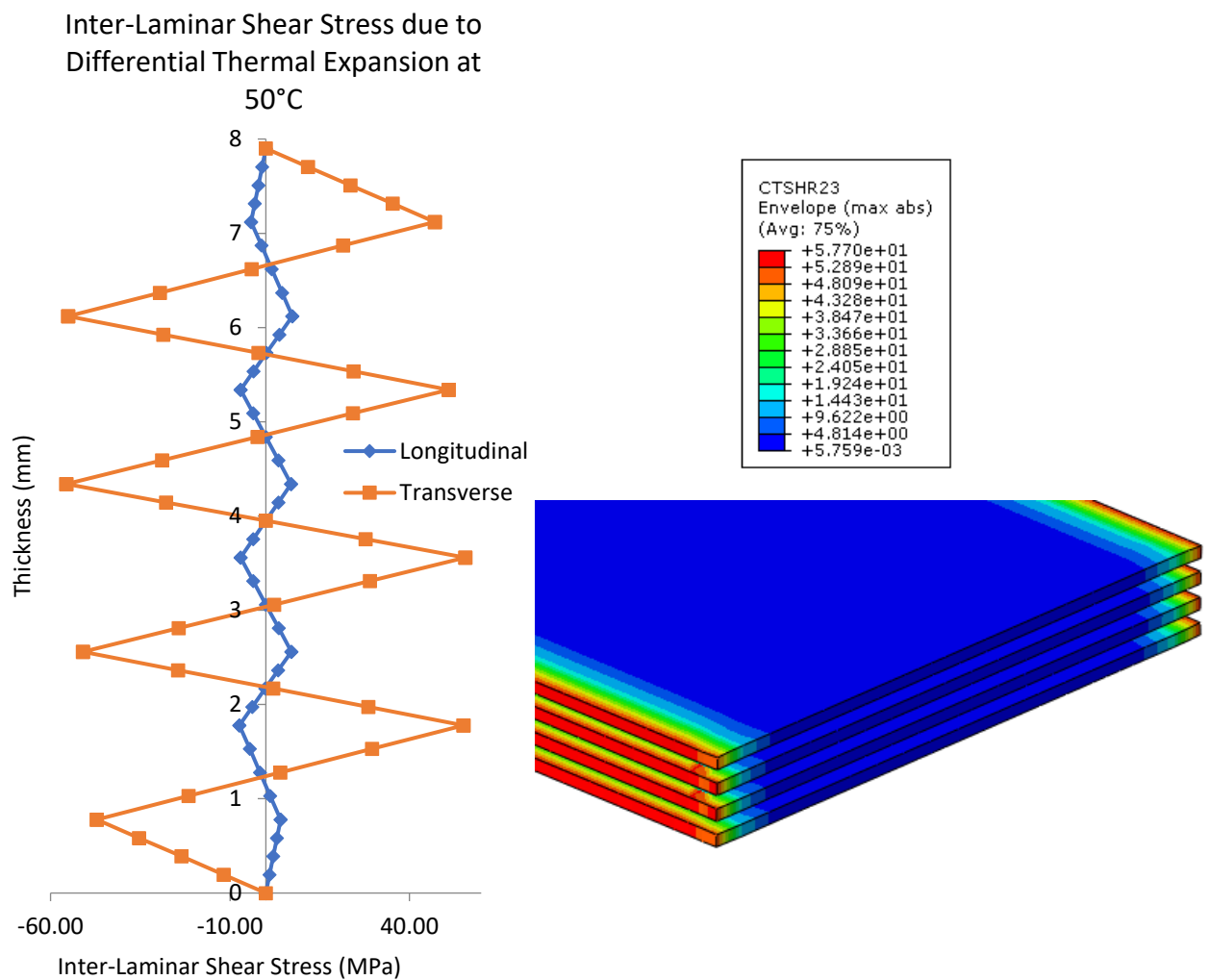


Figure 3.22: Inter-Laminar Shear Stress Distribution due to Differential Thermal Expansion at 50°C

3.4 SUMMARY

An essential part of the production process of fibre-steel laminates is the surface treatment of the steel plies. The steel should be abraded to increase the surface area, this can be done through a number of methods from the rotary hand-sanding machine used in this study to the likely, more effective sand/grit blasting. The surface of the steel should also be degreased with acetone to remove any residues that could influence the level of adhesion to adjacent plies. The perforation of the steel allows resin microstructures to form through the holes, creating an interlocking effect – the impact on interface performance of such microstructures was not investigated further.

When cutting the material, milling or the use of conventional saws like a band saw is recommended, however, trial cuts should be performed in any case due to the uncertainty surrounding production quality. Waterjet cutting was found to be inappropriate as it caused delaminations and water ingress into the sample.

The Young’s modulus of the individual components used to produce the hybrid-composite (GFRP and perforated steel) were established and used to estimate the axial and flexural stiffness values of the fibre-steel laminate. The values were established through classic laminate theory and verified through finite element analysis, the two methods yield values in reasonable agreement. Analytical methods were used with the experimental results of the individual components to calculate the axial yield and ultimate strengths. The established values are reported in [table 3.13](#).

Table 3.13: FSL Material Properties

	Property	Longitudinal (0°)	Transverse (90°)
Axial	Young’s Modulus (GPa)	92.6	85.0
	Ultimate Strength (MPa)	287.5	167
Flexural	Young’s Modulus (GPa)	75.1	65.7
	Inter-laminar Shear Strength (MPa)	13.5	11.5

Short-beam shear tests were performed on both FSL and GFRP samples separately to establish the inter-laminar shear strength of the materials. The ILSS of the GFRP was found to be approximately double that of the FSL material. The specimen showed some post delamination plastic deformability. Major delaminations occurred upon the unloading of the FSL samples due to the GFRP samples elastically snapping back to their original position following the plastic deformation of the steel.

The impact of differential thermal expansion was investigated for the hybrid-composite, finding that the effect of the differential expansion over a temperature difference of 50°C, is allowable for in-plane stresses. However, the inter-laminar shear stresses caused at free edges exceed the ILSS by a factor of 4. These stresses are concentrated at the edges though so the effect throughout the laminate should be quantified by an experimental investigation.

4 ADVANCED COMPOSITE DECK SYSTEMS

4.1 INTRODUCTION

4.1.1 Aims

The primary aim of this investigation is to examine the feasibility and find the most effective way to utilise a fibre-steel laminate when applied in a composite deck system with steel girders. The application used to illustrate this comparison, will be the deck of a parking structure, with full details taken from the relevant Eurocodes (EN 1991-1-1:2002). The study will look in depth at the performance of the deck in two key areas, that were highlighted in the 2017 study performed by Pavlovic & Veljkovic (47):

- Transfer of forces between steel girders – via bending of deck
- Longitudinal compression in deck caused by bending in direction of steel beams

Other common failure modes of FRP deck structures will also be reviewed and the most applicable will be compared across deck designs and material compositions. The failure verifications and safety factors used will come from the JRC 2016 design guidelines (48).

Additionally, an economic comparison will be performed to determine the applicability of this material in comparison to GFRP systems.

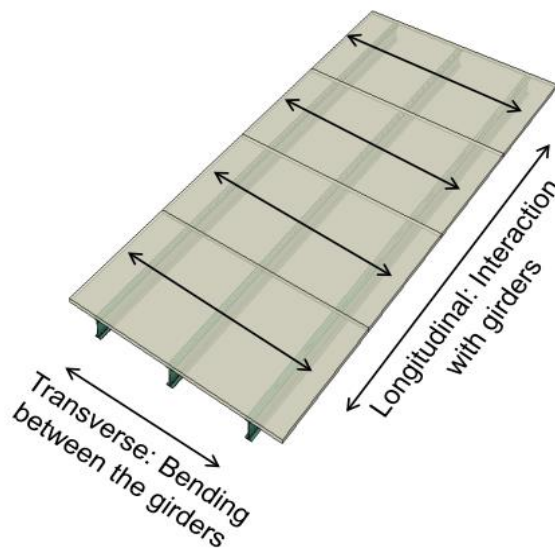


Figure 4.1: Longitudinal & Transverse Definition (47)

4.1.2 Methodology & Scope

To achieve these aims, hand calculations and finite element analysis will be performed simultaneously in an iterative process, to design two different FSL composite deck systems. The JRC 2016 design guidelines will be used to obtain factorised design strengths, which can be compared to stresses obtained from the finite element model to verify the structural performance of the different designs. Global and local, static verifications will be performed for the key ULS and SLS design checks that are relevant to this application. This design will be performed and detailed in [section 4.2](#). Fatigue, dynamic and full buckling analyses will not be provided, but are recommended for further study, as well as a thorough investigation into the most suitable connection type.

The key design requirements for a car parking facility, with regards to the entire structure are:

- Greatest possible beam spacing – (less columns – more car parking spaces and easier to navigate)
- Lowest possible construction depth – allows more levels in a smaller space, particularly relevant in underground or city centre locations.
- Lightest possible deck structure – for multi-storey applications, savings in mass add up and can help to reduce the size and cost of the supporting structure.

[Appendix C](#) will evaluate the accuracy and validity of the finite element model by comparing the FE output to expected values from hand-calculations.

In order to determine the most effective use of the material, a closer look at the stresses and strains in the systems will enable the reader to examine how well the different designs perform with regards to structural utilisation of the material. Additionally, the associated costs and construction depth will be considered to guide the user to the most effective design. These analyses can be found in [section 4.3](#).

[Section 4.4](#) will summarise the analyses and comparisons of the previous section, before giving suggestions on the most effective use of the material, and justifications of the author's views. Recommendations for the continuation of the development of the material will also be given.

4.1.3 Geometry

The geometry of the system to be studied is representative of a commercial deck structure used in car parking facilities. The deck, of varying design, will be supported by steel girders at a spacing to be determined in [section 4.2.1.2](#). The girders will be designed based on the mass of the deck but will consistently be manufactured from grade S355 steel and have a clear span of 16m.

Each car parking berth will have dimensions of 2.5m * 5.25m. The floor plan for a typical level of the car parking facility can be seen in [figure 4.3](#). The access ramp and other access facilities have been neglected to allow a simplified case study, showing the effect of the different systems and material compositions.

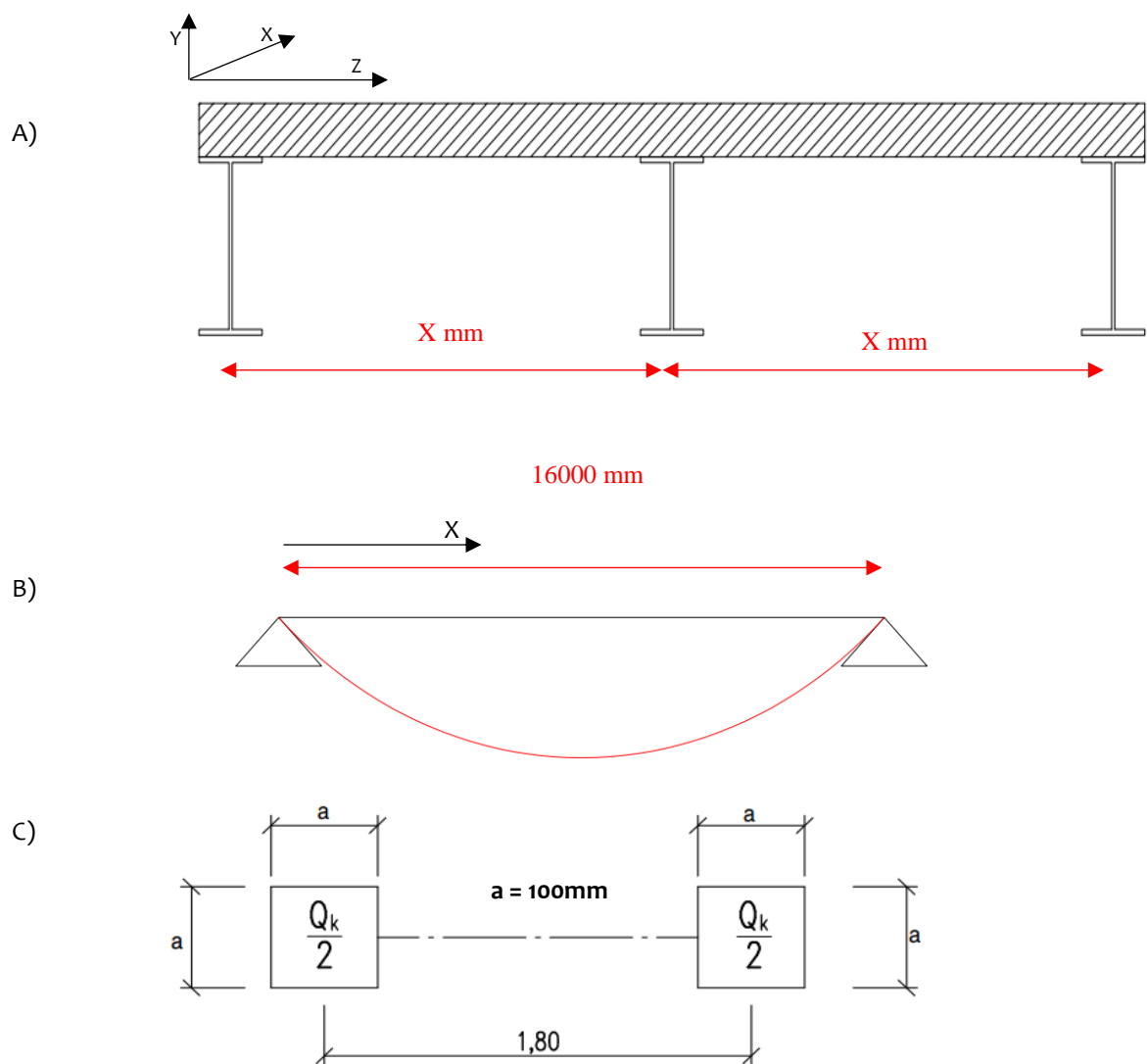


Figure 4.2: A) Deck geometry, B) Beam geometry, C) Axle-load geometry

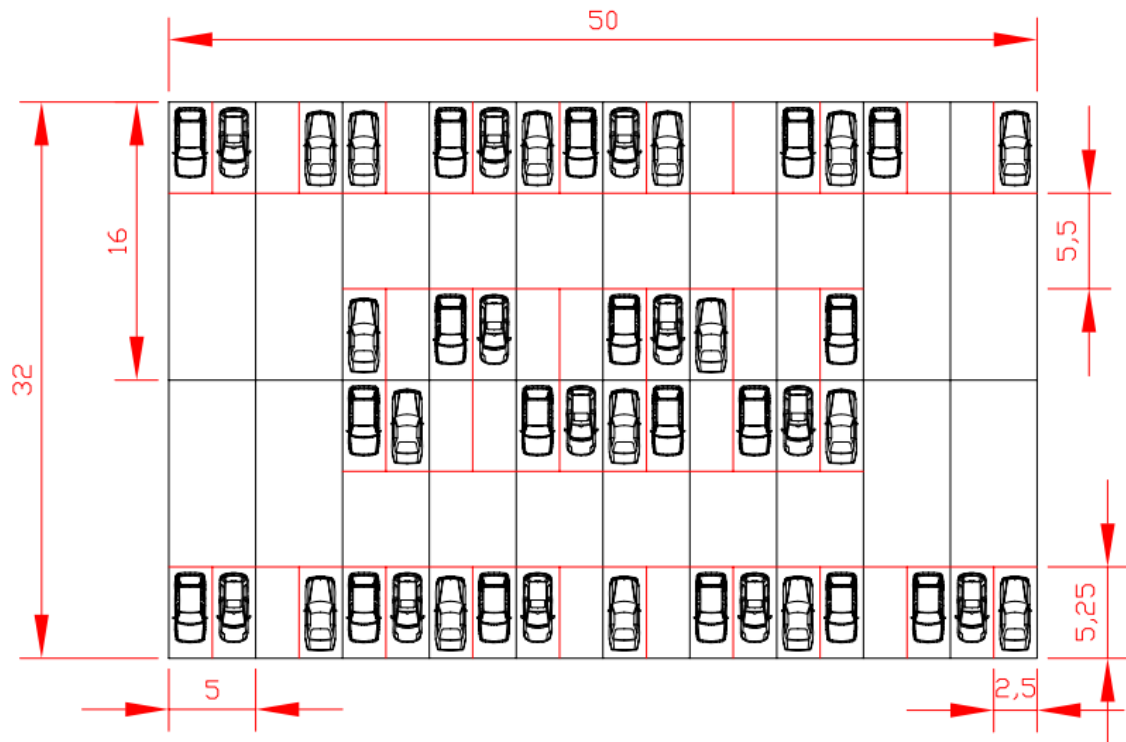


Figure 4.3: Floor Plan of Typical Car Park Level

4.1.4 Loading

4.1.4.1 Global Effects

The load conditions applied in this investigation will be applied according to EN 1991-1-1:2002, which stipulates a 2.5kN/m^2 load across the full face of the deck. This is designed to simulate the loading of a category F traffic area (parking areas and garages for up to 9-person cars) (50). An additional 0.5kN/m^2 will be applied over the whole deck to simulate the load from the asphalt finishing of the car park. The self-weight of the beams and deck will also be taken into account as a global effect. The effects of wind and snow will be discounted from this load case.

4.1.4.2 Local Effects

To determine the effects locally from vehicular loads the code prescribes a 20kN axle load to be positioned at the least favourable location in the system. The details of the geometry of the axle loading from the Eurocode is given in figure 4.2. The least favourable position which will generate the maximum local effects is to have the axle loads at the mid-span of the skin spanning between the webs of the deck.

4.1.4.3 Load Cases

To combine the various loadings into design values, the limit state approach prescribed by EN1990: Basis of Structural Design (51) will be used.

4.1.4.3.1 Ultimate Limit State (ULS)

The ultimate limit state combines the least favourable actions on the structure; namely the self-weight of the structure and surface layer (G_k) and the imposed loading expected for a parking structure (weight of cars and their passengers) (Q_k). The combination when used in this application can be given as:

$$E_{d,ULS} = \sum_{j \geq 1} \gamma_{G,j} \cdot G_{k,j} + \gamma_{Q,1} \cdot Q_{k,1}$$

Where the prescribed safety factors from Table A1.2(B) – Design values of actions (STR/GEO) (Set B) EN1990 (51) are given as:

$$\gamma_G = 1.35$$

$$\gamma_Q = 1.50$$

4.1.4.3.2 Serviceability Limit State (SLS)

The serviceability limit state considers the functioning of the structure under normal use. It is primarily used to verify the structure for the comfort of its users, with regards to deflections and vibrations experienced by said user. For this application the quasi-permanent combination will be used to verify the long-term serviceability state of the structure, it can be expressed as:

$$E_{d,SLS} = \sum_{j \geq 1} G_{k,j} + \sum_{i \geq 1} \psi_{2,i} \cdot Q_{k,i}$$

According to Category F of Table A1.1 - Recommended values of ψ factors for buildings from EN1990 Annex A1 (51), the reduction value can be given as:

$$\Psi_2 = 0.6$$

During the manufacture of the deck the longitudinal and transverse deflection of the deck from the self-weight of the structure and its surface layer loading (G_k) will be negated by pre-cambering the deck, thus, the value of dead load can be neglected from the serviceability limit state combination. Further reduction factors will be applied to the ply stiffness values to take into account the long-term behaviour of the material; reduction values will be taken from the JRC 2016 guidelines (48).

4.1.5 Material Properties

The properties of the base materials that comprise the hybrid composite and comparative materials for design will be discussed in this section.

4.1.5.1 Steel

Table 4.1: Steel Properties

	Steel for Girders	Steel within Laminate
Young's Modulus (GPa)	210	210
Yield Strength (MPa)	355	180
Density (kg/m ³)	7800	7800

4.1.5.2 Glass Fibre-Reinforced Polymer (GFRP)

The stiffness values of each laminate will be determined by classical laminate theory, which will be dependent on the layup of the laminate and stiffness of one unidirectional ply of the materials. The values used for individual plies were obtained from uniaxial tensile tests (in both fibre directions) on unidirectional GFRP laminates and can be seen in [table 4.1](#), the full set of test results can be found in [section 3](#).

Table 4.2: Individual GFRP Ply Values

Longitudinal Young's Modulus (GPa)	29.3
Transverse Young's Modulus (GPa)	6.5
Shear Modulus (GPa)	3.8
Density (kg/m ³)	1850

4.1.5.3 Polyurethane Foam

Polyurethane foam is used in the cellular deck systems to infill the voids between the webs and skins of the deck. The foam is prescribed as light weight foam with minimal strength and stiffness properties.

Table 4.3: Polyurethane Foam Properties

Young's Modulus (MPa)	6
Density (kg/m ³)	35

4.1.5.4 Fibre-Steel Laminate

To estimate the properties of the fibre-steel laminate the properties of the individual components will be used in conjunction with the safety factors and limiting values from the relevant design code. Furthermore, the properties of the individual plies will be used in classic laminate theory to predict the axial and flexural stiffness of the fibre-steel laminates.

The JRC 2016 prospective FRP design guidelines (48) has been used to calculate the safety factors and limiting values used for the strength of the materials. This is done through the limiting value of 1.2% flexural strain and 1.6% shear strain, using the limiting strain values the design failure strength of fibre-steel laminates can be estimated as:

$$\sigma_{i,FSL,Rk} = MVF * f_y + (1 - MVF) * E_{i,GFRP} * \varepsilon_{1.2\%} \quad \sigma_{i,FSL,Rd} = \sigma_{i,FSL,Rk} \cdot \frac{\eta_{c.s.i}}{\gamma_M}$$

Where 'i' denotes the longitudinal or transverse direction of the fibres. The full calculation of the limiting properties and design resistance values can be found in [Appendix B](#). It should be noted that this formula neglects the small contribution of fibres not oriented in the required direction, assuming that the MVF is calculated by also neglecting the thickness of these fibres.

4.2 OPTIMISED SYSTEM DESIGN

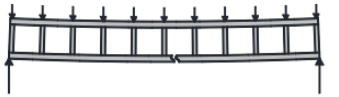
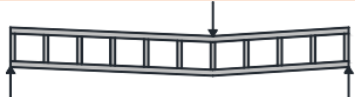
4.2.1 General


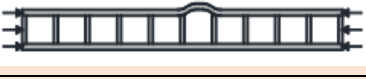

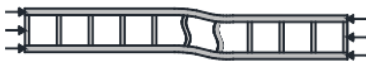
To begin the design of the deck it is important to have an overview of the verifications and checks that the systems will be designed upon. Table 4.4 provides a description, and where applicable an image of the type of failure mode the verification applies to.

A preliminary design will be performed to understand the suitable beam spacings for these types of systems, following this a beam spacing will be decided upon and taken forward into the detailed design of the system. For the purpose of this investigation, the connection type is assumed to be an adhesive connection that provides full interaction with the supporting beams.

4.2.1.1 Verifications to be Performed

Table 4.4: Description of design verifications to be used in the composite system designs, images from JRC 2016 (48)

	Verification	Description	
Ultimate Limit State	Beam Shear Verification	Ultimate shear verification of supporting beam	
	Beam Stress Verification	Check to see that the stress in the beam does not exceed yield stress	
	Beam Plastic Moment Verification	Plastic moment verification of the supporting beam	
	Composite System Plastic Moment Verification	Plastic moment verification of the effective composite system (effective width of deck + beam)	
	Longitudinal Facing Failure (UDL)	Longitudinal failure of the deck skins from uniformly distributed global loading	
	Longitudinal Facing Failure (PL)	Longitudinal failure of the deck skins from local axle loading	
	Transverse Facing Failure (UDL)	Transverse failure of the deck skins from uniformly distributed global loading	
	Transverse Facing Failure (PL)	Transverse failure of the deck skins from local axle loading	
	Transverse Shear Failure (UDL)	Transverse shear failure of deck from uniformly distributed global loading	

	Transverse Shear Failure (PL)	Transverse shear failure of deck from local axle loading	
	Face Wrinkling	Buckling of deck skins when compressive stress reaches a critical value, may buckle inward or outward.	 
	Local Buckling of Webs	Buckling of webs under vertical compressive force	
	Global Buckling	Buckling of system as a whole, due to longitudinal compressive stresses induced from bending in beam direction. Analysed as part of FE model.	
	Shear Crimping 0°	Mode of longitudinal shear failure of deck, can occur as a consequence of global buckling, depending on face thickness and core shear strength	
	Shear Crimping 90°	Mode of transverse shear failure of deck, can occur as a consequence of global buckling, depending on face thickness and core shear strength	
	Strain Failure 0°	Verification of ultimate strain levels reached in longitudinal direction of deck	
	Strain Failure 90°	Verification of ultimate strain levels reached in transverse direction of deck	
Serviceability Limit State	Global Deflection	Maximum longitudinal deflection of composite system under long-term loading (creep coefficients applied). Limited to $L/250$	
	Transverse Deflection (UDL)	Maximum transverse deflection of deck span between beams under uniformly distributed global loading. Limited to $B/250$	
	Transverse Deflection (PL)	Maximum transverse deflection of deck span between beams under local axle loading. Limited to $B/250$	
	Vibrations	Analysis of vibrations of deck, limited to 3Hz	

4.2.1.2 Beam Spacing

In car parking applications it is desirable to have the greatest beam spacing possible – this means fewer columns and therefore more space for parking vehicles. It is also desirable to have a construction depth that is as low as possible. However, by increasing the beam spacing the loads on the system increase and often require a deeper system to support this increase.

Preliminary checks have been performed with a 130mm deep cellular FSL deck with a beam spacing of 3m, which show the system to be underutilised when applying the imposed car park loading. Thus, the beam spacing has been increased to 5m, the results and comparison of the most critical verifications can be seen in [table 4.5](#). Following this a beam spacing of 5m will be taken forward, see [figure 4.4](#). The complete floor plan of the typical car park level to be used in the rest of the case-study can be seen in [figure 4.5](#). The spacing of the parking spots and their dimensions complies with Dutch National Standards NEN 2443:2013 (52).

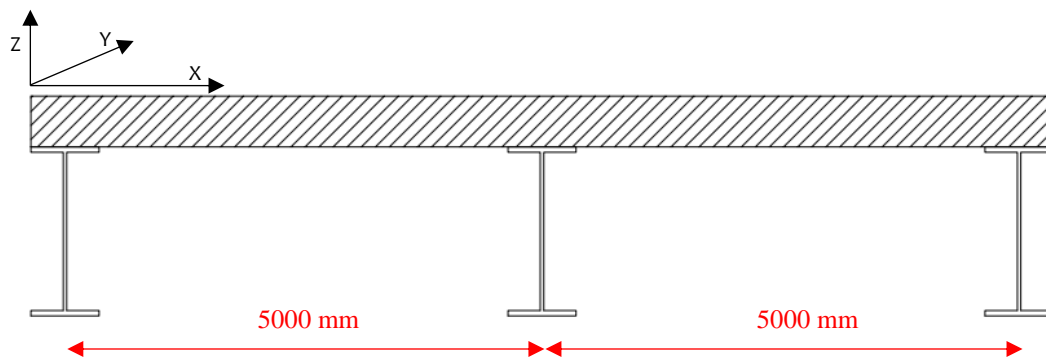


Figure 4.4: Beam Spacing Schematic

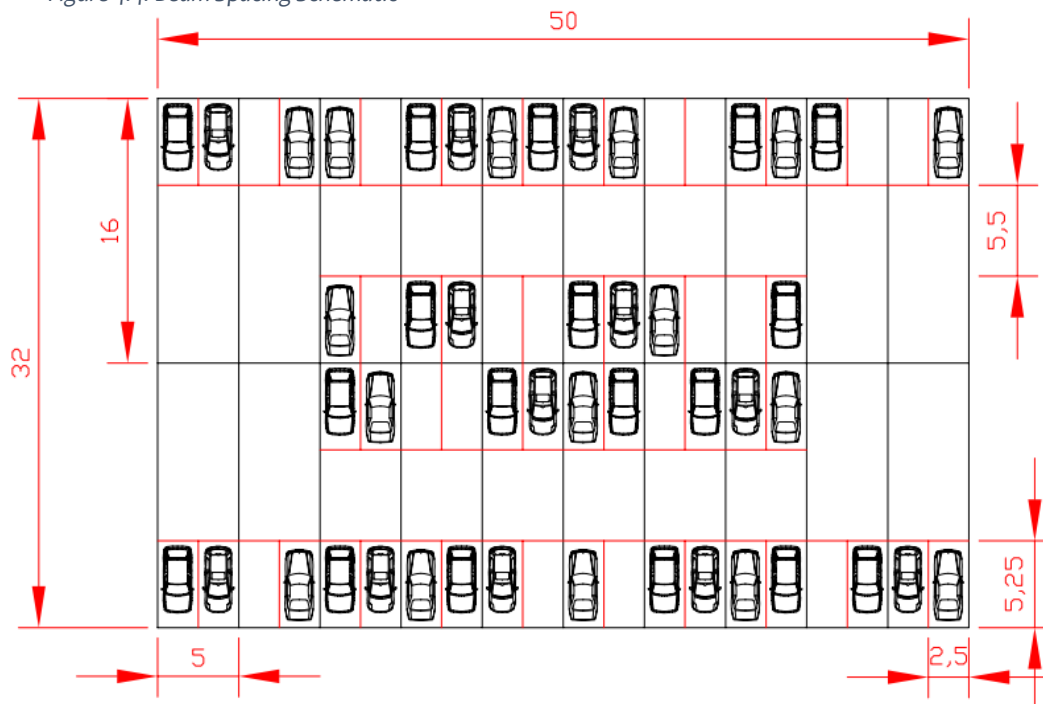


Figure 4.5: Floor Plan of Typical Car Park Level

Table 4.5: Critical verifications for beam spacing with FSL-CELLULAR

		Spacing =3m	Spacing =5m
ULS	Plastic Moment (composite system)	0.52	0.73
	Transverse Facing Failure (UDL)	0.34	0.76
SLS	Global Deflection (Imposed Loading)	0.50	0.77
	Vibrations	0.79	0.95

Pushing the beam spacing beyond 5m makes little sense as the verification is already almost eclipsed for vibrations. It is also convenient that one parking space has a width of 2.5m, meaning that two car parking spaces can fit in between the column spacings.

4.2.2 FSL Cellular Deck Design

4.2.2.1 Introduction

This deck will be comprised of FSL webs and skins forming a series of cells that have polyurethane foam inserts in the middle to assist the webs shear resistance. The foam is specified as light-weight material and has negligible structural properties ($E=6\text{MPa}$). This type of design is in itself not particularly robust, in that it has long resin dominated pathways that would be prone to cracking and unhindered development of said cracks. An example of this is shown in figure 4.6, where a delamination resulting from an impact load is allowed to propagate, unrestricted, along the longitudinal pathway between the foam and the skin.

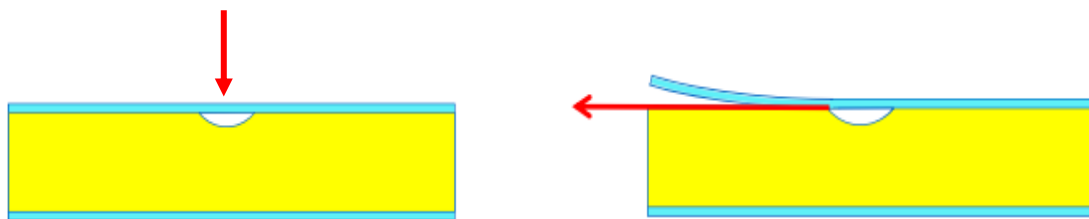


Figure 4.6: (A) Sandwich panel damaged by initial impact, (B) Propagation of delaminating crack, causing catastrophic failure (56)

The patented technology introduced by Infracore looks to counter this vulnerability with a multitude of Z-shaped layers of fibres that form an oblique layered material (OLM). This ensures that there are no solely resin dominated pathways, as there are now reinforcing fibres in these pathways that will restrict further crack propagation. This technology is shown in figure 4.7, where overlapping Z-shaped layers form the transition of the upper skin to the web to the bottom skin. The restricted crack pathways significantly increase the robustness of this design.

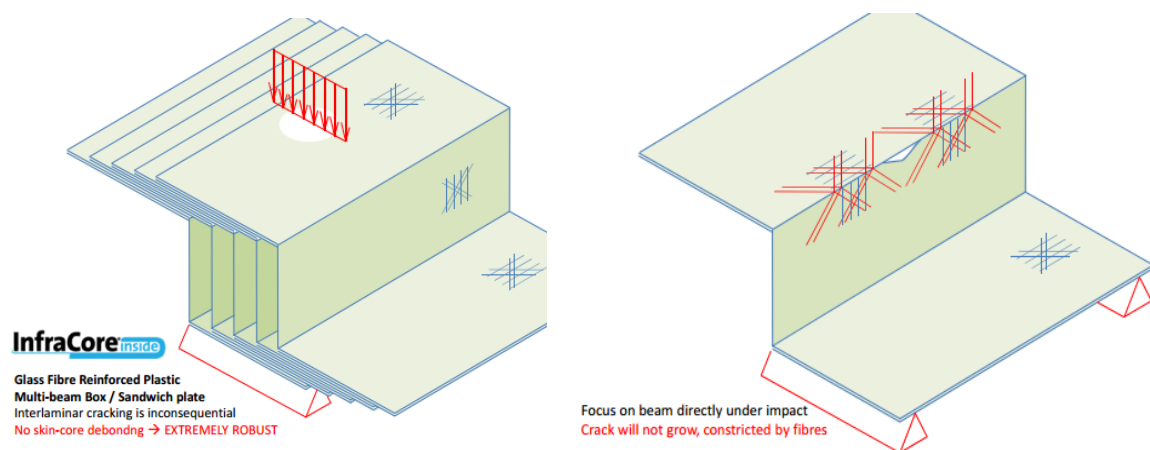


Figure 4.7: Infracore Inside Technology (56)

It is however, outside the scope of this investigation to consider such complex failure behaviour of the material and thus, this crack-bridging effect will not be considered in the finite element model and calculations.

4.2.2.2 Core Stiffness

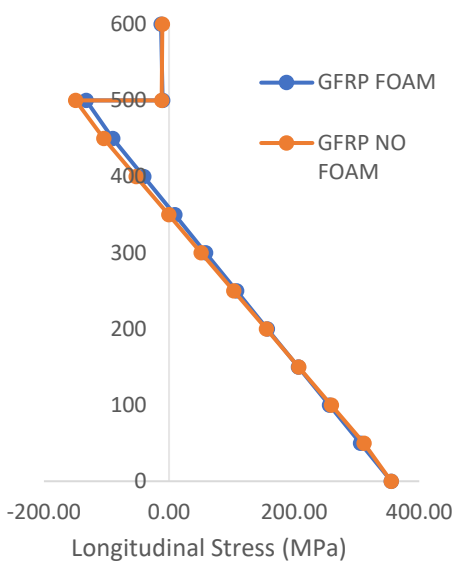
Within cellular decks the majority of the resistance of the deck comes from the two faces or skins. They are connected to each other through the core area, which is comprised of foam cores and webs spanning in the transverse direction of the system (between girders). The core acts as a load path between the bottom and top skin, and so the stiffness of this core area determines the effectiveness of the load path. The following sub-sections will analyse the effect of changing the parameters that influence the core stiffness. The stiffness of the core largely impacts the in-plane shear stiffness of the whole deck.

4.2.2.2.1 Foam Cores

Foam cores are used in sandwich panel FRP decks to create a greater distance between the two skins, which due to the neutral axis theory increases structural performance. Lightweight foams are used so that the benefit of the light FRP deck is not compromised. Given that the foam doesn't provide any real strength or stiffness of its own, due to its lesser properties ($E=6\text{MPa}$), it is usually discounted in design. While the foam provides negligible strength, it does increase the stiffness of the core of the deck (compared to when there are no foam inserts, like in pultruded decks), this helps to facilitate the transfer of forces from the bottom skin to the top skin of the deck. Without adequate transmission of forces, the deck will be unequally utilised and the majority of the stresses will remain in the lower skin, whilst the upper skin is underutilised. A further benefit of having the foam cores is that they can provide some additional stability to the webs and prevent them from buckling. In order to show these effects, a comparison of two identical GFRP decks with and without the foam cores will be presented.

When investigating the force transfer between the two deck skins, it is important to look at the stress and strain distributions of a vertical cross section of the deck, this will signify how much of the force is being transferred to the top skin. In [figure 4.8](#), the longitudinal stress and strain distribution is plotted for a vertical cross-section at the mid-span location. Following the orange line in the figures, it can be seen that when there are no foam cores present, the compression at the top skin is less than at the bottom skin – the opposite is present in the deck that has foam cores. This means that more force is being transferred through the foam cores, from the beam to the deck. Furthermore, the greater force transmission means less shear lag and a greater effective width as more of the deck is engaged, shown in [figure 4.9](#).

Vertical Distribution of Longitudinal Stress at Mid-Span Cross-Section



Vertical Distribution of Longitudinal Strain at Mid-Span Cross-Section

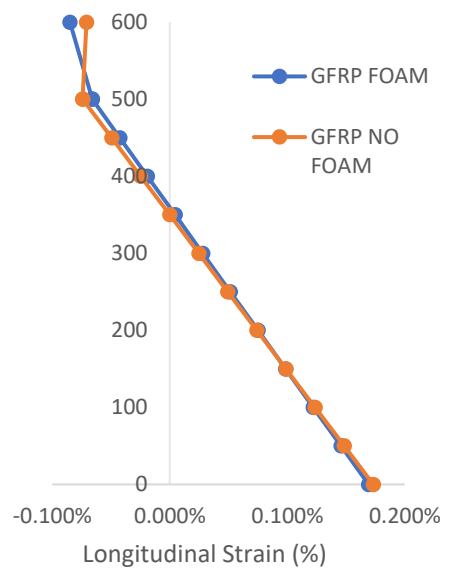


Figure 4.8: Vertical stress & strain distribution at mid-span with and without foam cores

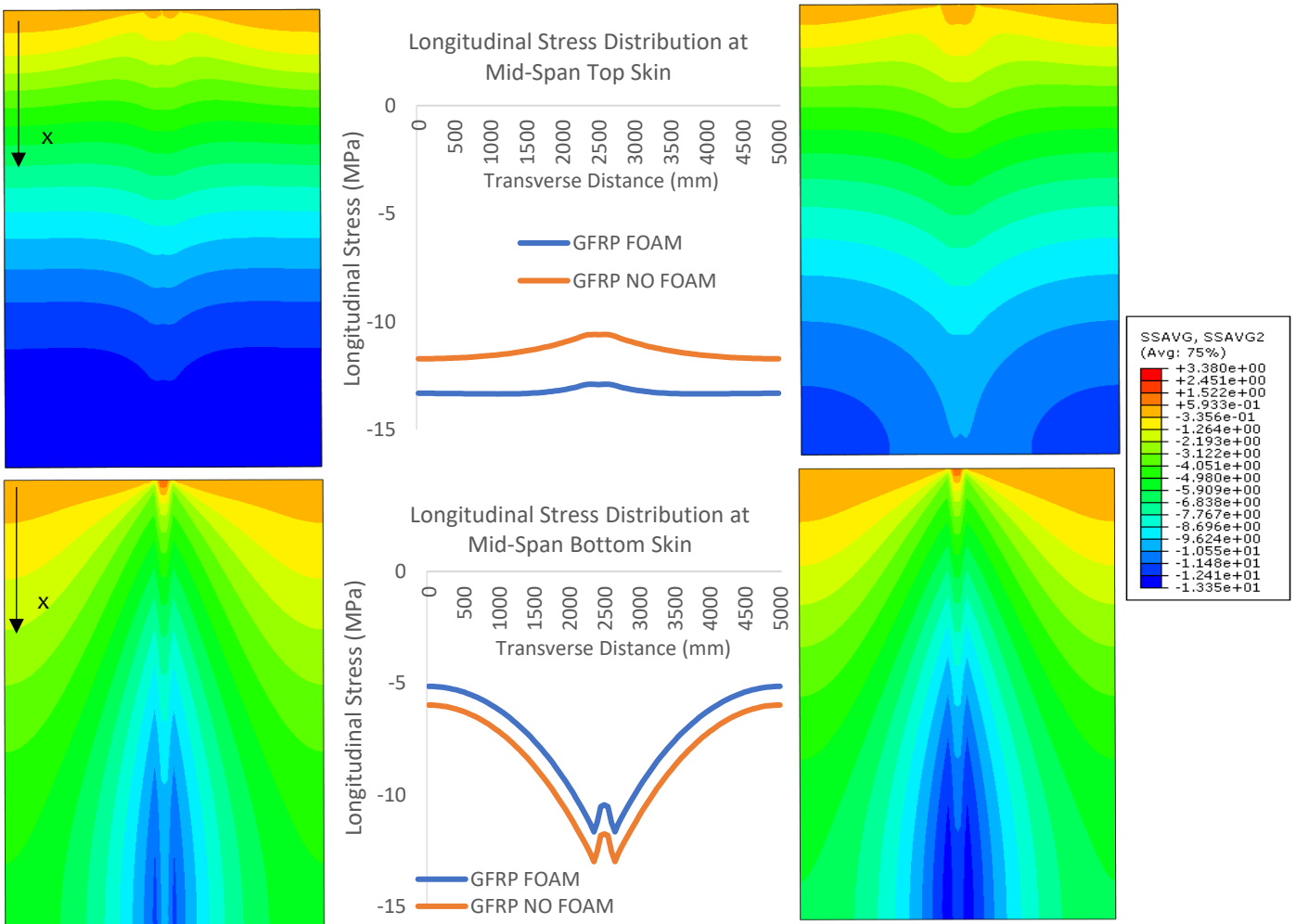


Figure 4.9: Average Longitudinal Stress in Skin, Left - With Foam Cores; Right - Without Foam Cores. Top - Top Skin; Bottom - Bottom Skin

The differences shown in figure 4.9 highlight the lower stress in the top skin of the deck without foam and higher stress in the bottom skin of the deck, confirming the lesser transfer of forces. From figure 4.10 it is clear that the average stress is higher in the deck with foams – leading to a higher effective width and therefore composite stiffness (5% greater than without the foams). The neutral axis of the composite section with and without the foam cores doesn't change significantly (<10mm), confirming the poor stiffness properties of the foam. However, through the additional composite stiffness that the increased force transmission provides, the deck with foam cores has a reduced global deflection of ~7mm when compared to the same deck without the foam.

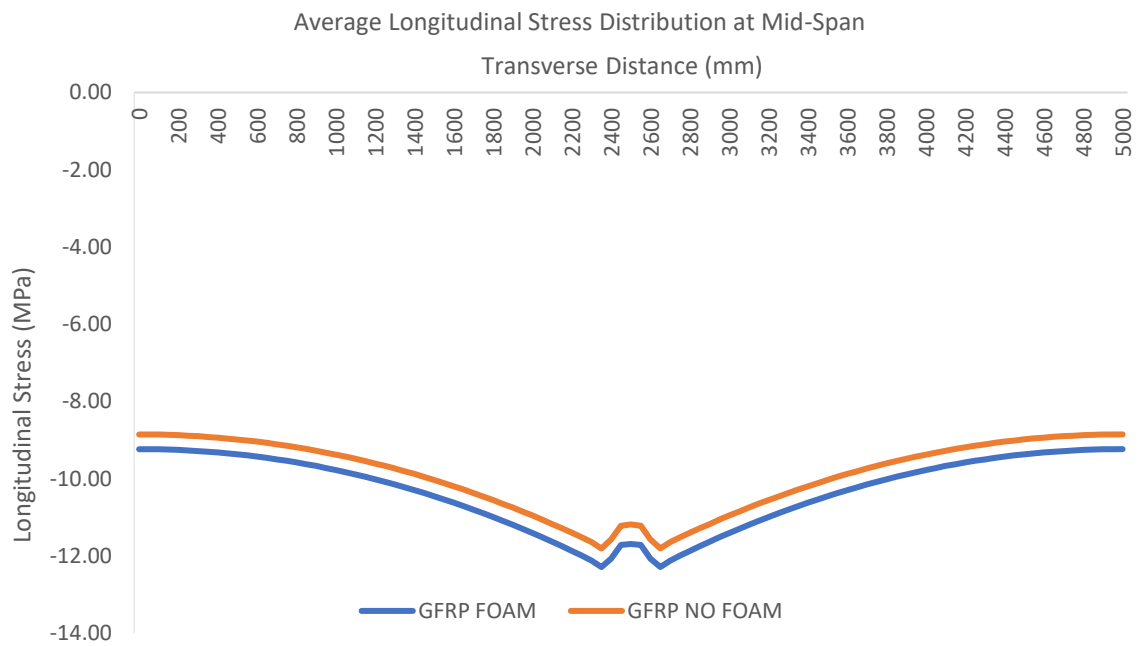


Figure 4.10: Average Longitudinal Stress at Mid-Span

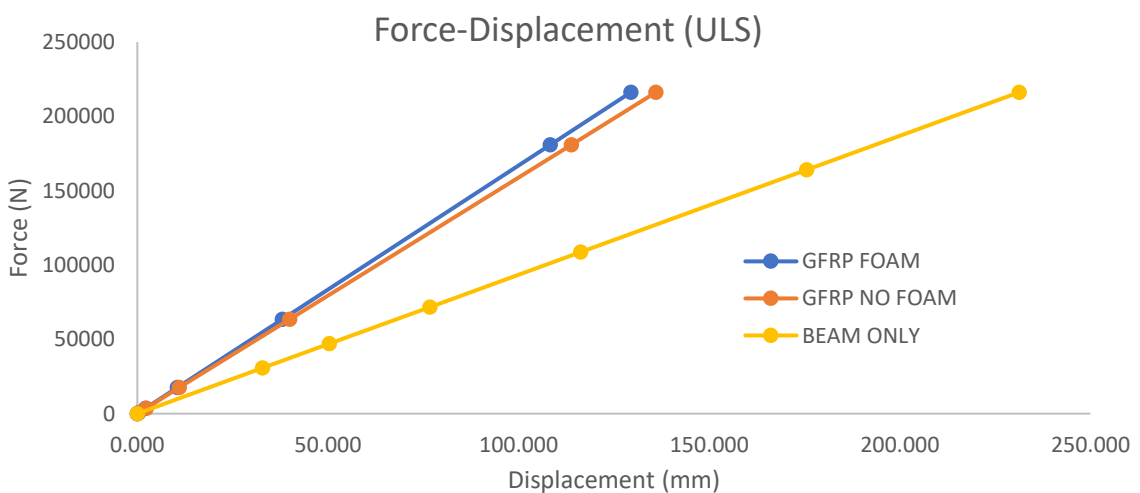


Figure 4.11: Force - displacement curve for FRP decks with and without foam cores and beam only as benchmark

4.2.2.2.2 Steel in Webs

In order to increase the engagement of the deck and transfer more stresses between the bottom and top skins, the pathway between them can be further stiffened. This is done by adding steel to the GFRP webs of the deck to form a Z shaped profile of fibres/steel between the foam cores, shown in figure 4.7. The effect that stiffening the webs has on the transmission of forces can be seen by analysing the stress and strain distributions in the two skins of the deck, between two models – one with FSL webs and one with GFRP webs.

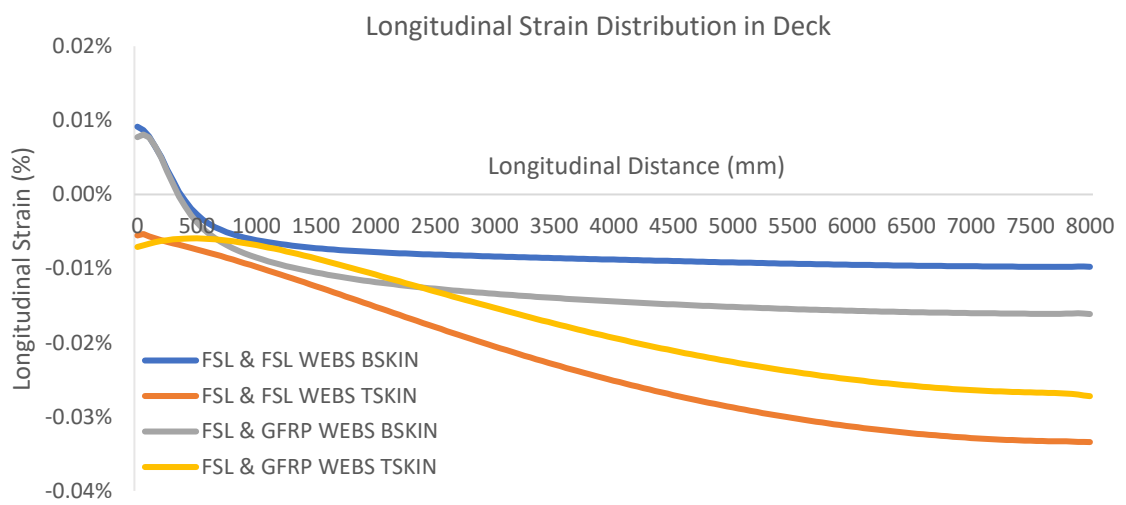
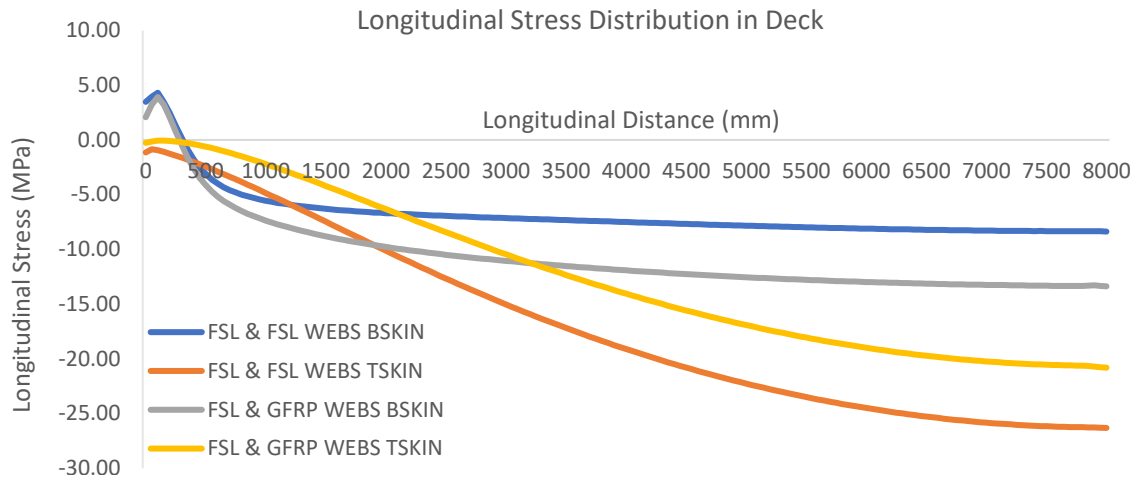
Figure 4.12, shows a higher stress/strain in the top skin of the deck with FSL webs than the deck with GFRP webs, this is due to the increased force transfer between the two skins, facilitated by the stiffer webs, again noted by the higher stress in the bottom skin of the deck with GFRP webs. It can be seen that the strain line in the system with FSL webs is almost completely linear through the beam and the deck. This means that the forces can be transferred more readily through the deck.

Tensile stresses in the bottom skin of each of the decks can be noticed at the support location ($x=0\text{mm}$), in figure 4.12A. These stresses are due to the interaction with the deck; in a system with no interaction there would be slip at the interface of the top flange of the beam and the bottom skin of the deck, as this is prevented by the shear interaction tensile stresses are caused at the support location.

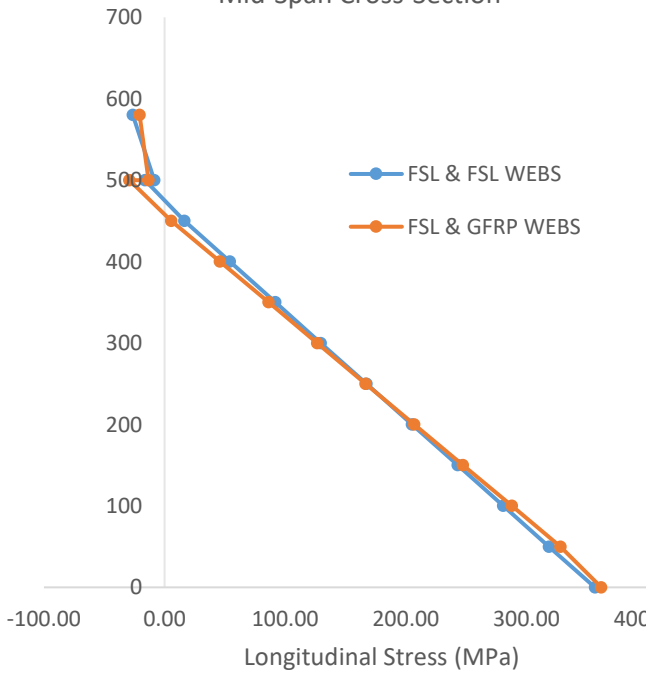
From figure 4.13 it can be seen that the inclusion of steel in the webs provides a more uniform stress distribution across the face of the deck due to the increased shear stiffness of the core of the deck. The improvement of the webs allows the system a 7% higher composite stiffness.

The webs span in the transverse direction, hence, the most substantial improvements can be realised in that direction. A 65% reduction in transverse deflection can be seen when comparing the deck with GFRP webs and the deck with FSL webs.

Due to the higher density of steel than the GFRP an increase in overall self-weight of the deck must be accepted when prescribing FSL webs. For a deck with a depth of 100mm the overall density of the deck increases by approximately 100kg/m^3 . The increased stiffness of the webs also reduces the global deflection and transverse deflection when looking solely at imposed loading, however, given the additional mass of the deck, the deflection due to self-weight will increase. This can be pre-cambered out of the system to allow the deflection to be governed by the imposed loading at serviceability limit state.



Vertical Distribution of Longitudinal Stress at Mid-Span Cross-Section



Vertical Distribution of Longitudinal Strain at Mid-Span Cross-Section

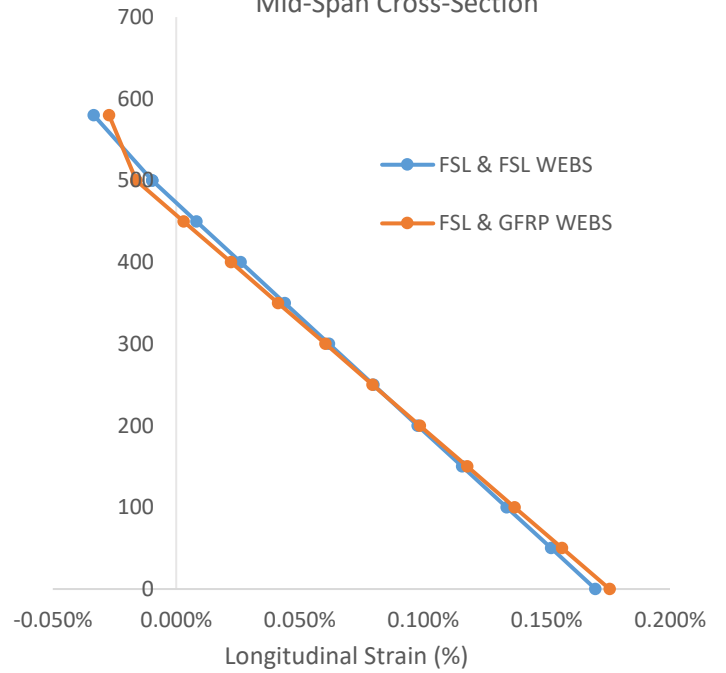


Figure 4.12: (A) (B) Longitudinal stress and strain plotted along length of deck at interface with beam, (C)(D) Longitudinal stress/strain plotted at mid-span cross-section

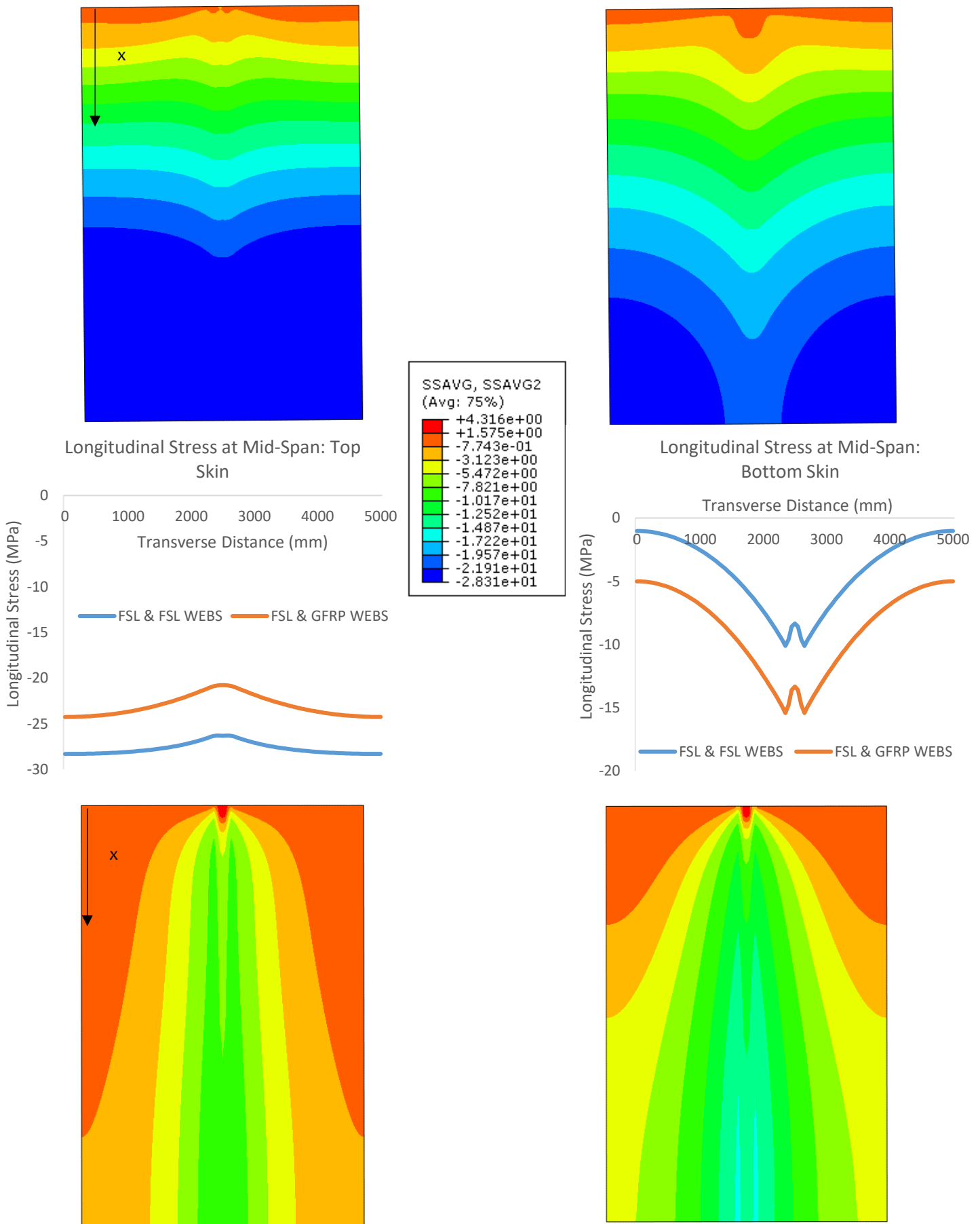


Figure 4.13: Average Longitudinal Stress in Skin, Left - With FSL Webs; Right - With GFRP Webs. Top - Top Skin; Bottom - Bottom Skin

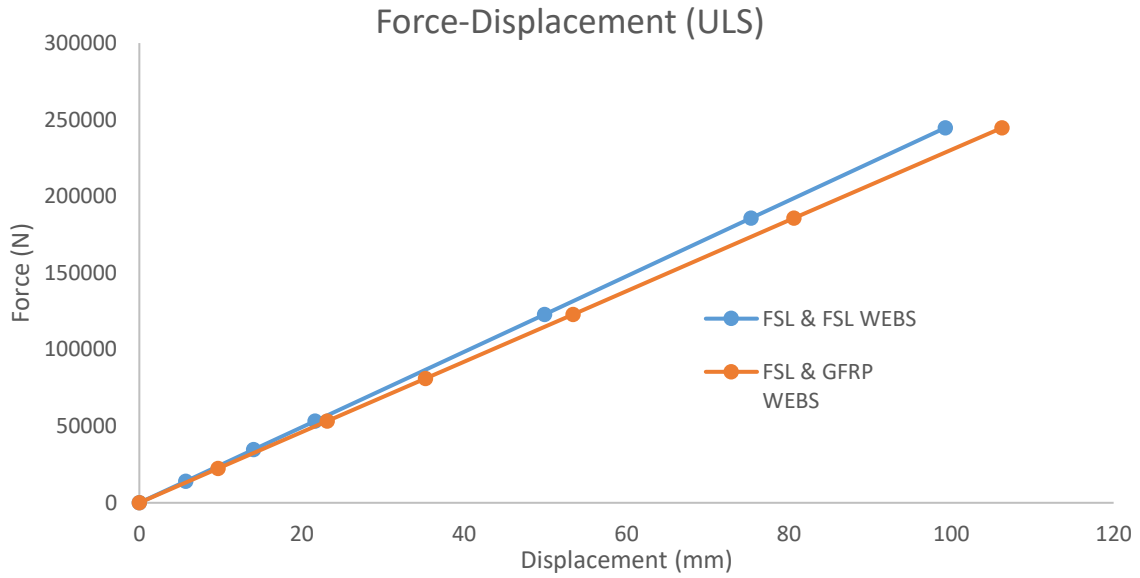


Figure 4.14: Force - displacement curve for FSL deck with (A) GFRP webs and (B) FSL webs

4.2.2.2.2.1 FSL Web Design

The FSL webs have been designed to be effective in flexure and in shear. Firstly, the majority of the fibres are oriented at $\pm 45^\circ$ to maximise shear stiffness. Secondly, the steel plies are located at the extremes of the web laminate, to increase the local flexural stiffness of the webs to bending between the skins. Finally, the direction of the 0° fibres is in the transverse direction of the deck to assist in the transverse bending of the deck between steel girders. The total thickness of the FSL webs is 5mm and has the following stiffness properties:

Table 4.6: FSL Webs Composition

Laminate Layup	[0, steel, $\pm 45_4$] _s
Laminate thickness	5.0mm
Total steel thickness (per web)	2mm
Ply thickness	0.26mm
Fibre areal density	300g/m ²
Laminate density	4246kg/m ³
Primary Orientation (0°)	Transverse (across deck)

This layup composition yields the following flexural and axial stiffness in the laminates of the webs:

- $E_{xx} = 146315 \text{ MPa}$
- $E_{yy} = 138340 \text{ MPa}$
- $G_{xy} = 35260 \text{ MPa}$
- $E_{xx} = 102210 \text{ MPa}$
- $E_{yy} = 97360 \text{ MPa}$
- $G_{xy} = 35260 \text{ MPa}$

4.2.2.3 Deck Height

The depth of the deck is determined by the capacity of the system and so will vary based on the design of the deck and the properties of its materials. However, the smaller the depth of the deck the more optimised, with regards to the amount of material used, the construction depth and ultimately the cost of the whole system (if the amount of material is reduced).

Using the example of the cellular profiled deck, the following figures will show that through decreasing the gap between the top and bottom skins, the core of the sandwich will become less flexible and allow more of the stress to be transferred to the top skin. The models used for comparison will feature two cellular FSL decks, under the same loading, with FSL webs and foam cores but with a depth of (A) 100mm and (B) 200mm.

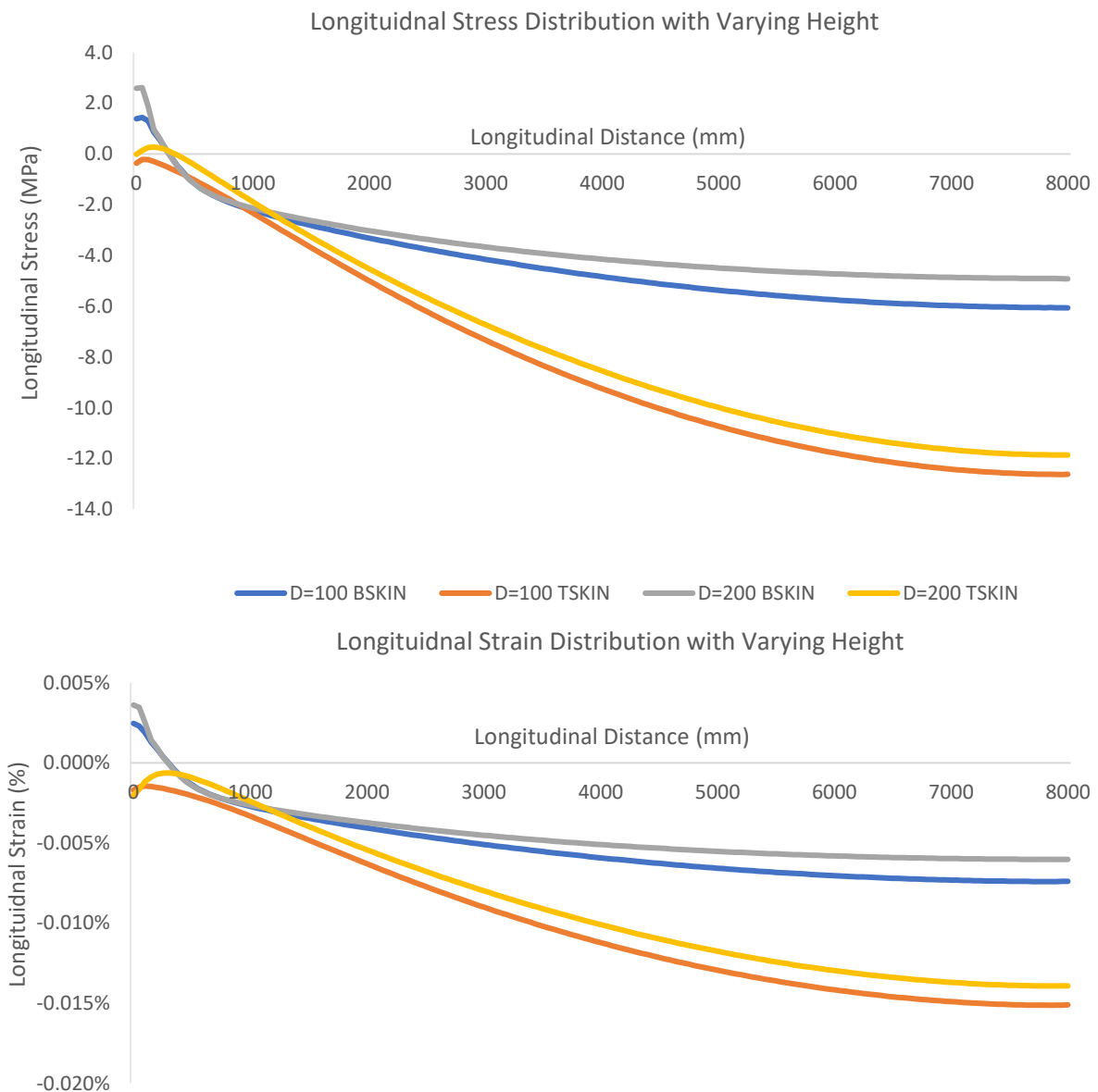


Figure 4.15: Longitudinal stress/strain in top and bottom skin of 100mm and 200mm FSL decks, plotted along length of deck

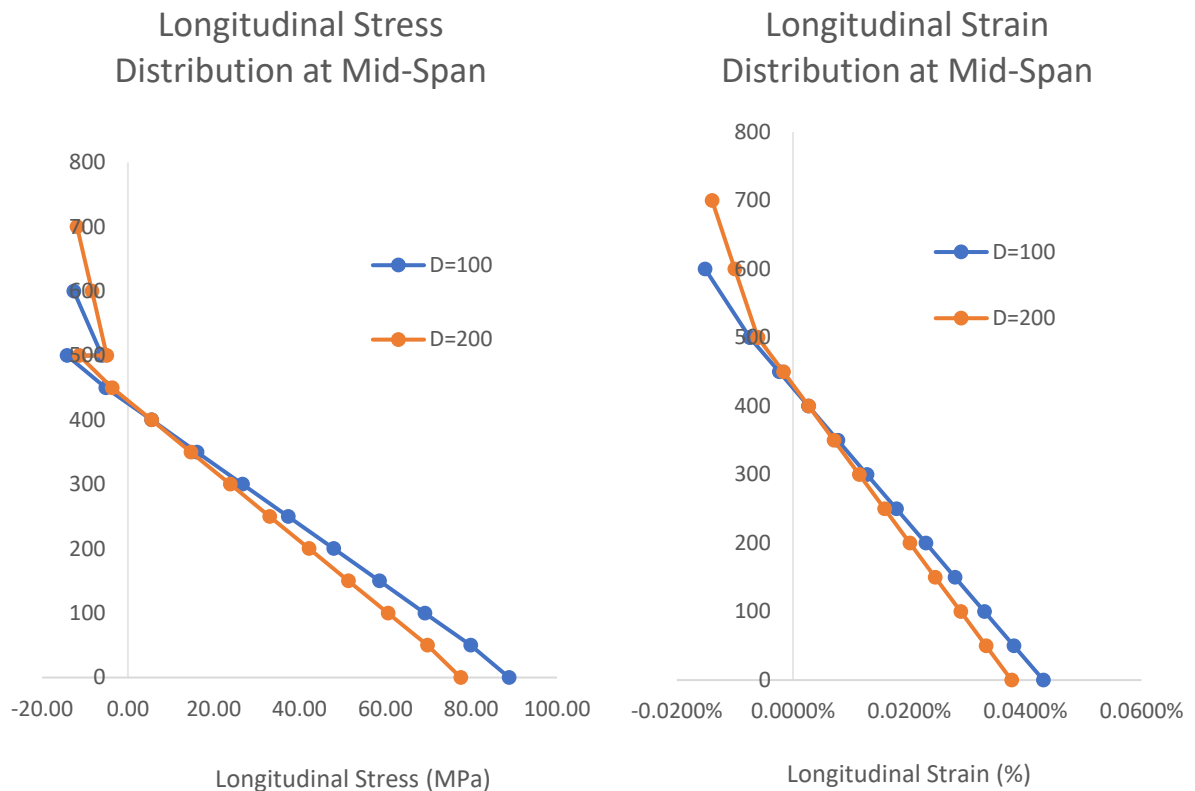


Figure 4.16: Longitudinal stress/strain for 100mm and 200mm FSL decks, plotted at vertically at mid-span cross-section

From the longitudinal strain distribution at the mid-span location, shown in figure 4.16, the change in gradient of the strains from the beam to the deck can be seen as much greater in the 200mm deck than in the 100mm deck. This is because of the greater centre-to-centre distance of the facings of the deck, making the core less stiff and therefore less able to transmit stresses through the deck. This means there is a greater shear lag effect leading to a lower effective width and subsequently lower composite stiffness (based on effective width only, not taking into account the increased depth).

The higher stress in each of the skins of the 100mm deep deck shows that the deck is more utilised than the 200mm deck. This coincides with a reduction in the amount of material used. However, it is important to check that the deck still passes strength verifications given that the inertia of the deck has been reduced by decreasing the depth of the deck. These verifications are the determining factor as to how much the depth of the deck can be reduced by and are dependent on the properties of the design and materials used.

In the transverse direction, a deck with a lower depth is less stiff and therefore experiences a greater amount of bending, resulting in higher transverse stresses in the facings. This is an important consideration when trying to minimise depth, especially with composite materials, as there are large safety factors applied to both stiffness and strength values in the transverse direction.

4.2.2.4 Laminate Design

The fibre-steel laminate layup is designed with the steel plies at the extremes of the laminate, this increases the local flexural stiffness of the skin by around 35% in each direction. Given the web spacing of 100mm this doesn't produce a significant reduction in local deflection and provides a motive to increase the web spacing. However, this isn't possible in the GFRP cellular deck so the web spacing of 100mm will be retained.

4x1mm plies of steel have been used in each skin (two at the top and two at the bottom), this quantity is given so as to increase the stiffness of the laminate to an acceptable level, without compromising strength to the point where the laminate cannot withstand the stresses applied. The assigned thickness of each skin is set to 12mm, this allows a smaller overall construction depth as thinner skins would require a deeper deck to provide the necessary properties. The laminate is symmetric but features a middle 90° ply denoted in table 4.7 by the underlined ply. The majority of the fibres (~50%) are oriented in the 0° direction, which in the scheme of the deck is oriented in the transverse direction – spanning between beams.

Table 4.7: FSL Composition for Cellular Deck

Laminate Layup	[0, steel, 0, steel, 0, <u>0/90</u> , ±45, 0/90, ±45, 0/90, <u>90</u>] _s
Laminate thickness	12mm
Total thickness of steel (per skin laminate)	4mm
Ply thickness	0.26mm
Fibre areal density	300g/m ²
Laminate density	3859kg/m ³
Primary Orientation (0°)	Transverse
Mass of Deck	109kg/m ²

This layup composition yields the following local flexural and axial stiffness values respectively:

- $E_{xx} = 146070 \text{ MPa}$
- $E_{yy} = 140800 \text{ MPa}$
- $G_{xy} = 35400 \text{ MPa}$
- $E_{xx} = 88125 \text{ MPa}$
- $E_{yy} = 85620 \text{ MPa}$
- $G_{xy} = 21300 \text{ MPa}$

4.2.2.5 FSL Cellular Deck Geometry

With the laminate of the skins and the webs both designed, the final design is of the required depth of deck. This is determined by the various design verifications specified in [section 4.2.1.1](#). Further iterations have also been performed regarding the change of skin thickness and layup, however, due to the iterative nature of this process, the report presents the final design as given in [section 4.2.2.4](#). The deck will feature FSL webs that have been detailed in [section 4.2.2.2.1](#) and foam cores discussed in [section 4.2.2.2.1](#).

The final dimensions for the deck designed with the fibre-steel laminate can be seen in [figure 4.17](#), which shows an isotropic view, the skin laminate layup and a transverse cross section of the deck. A summary of the design verifications for this system can be seen in [table 4.8](#), and the full calculations can be found in [Appendix B](#).

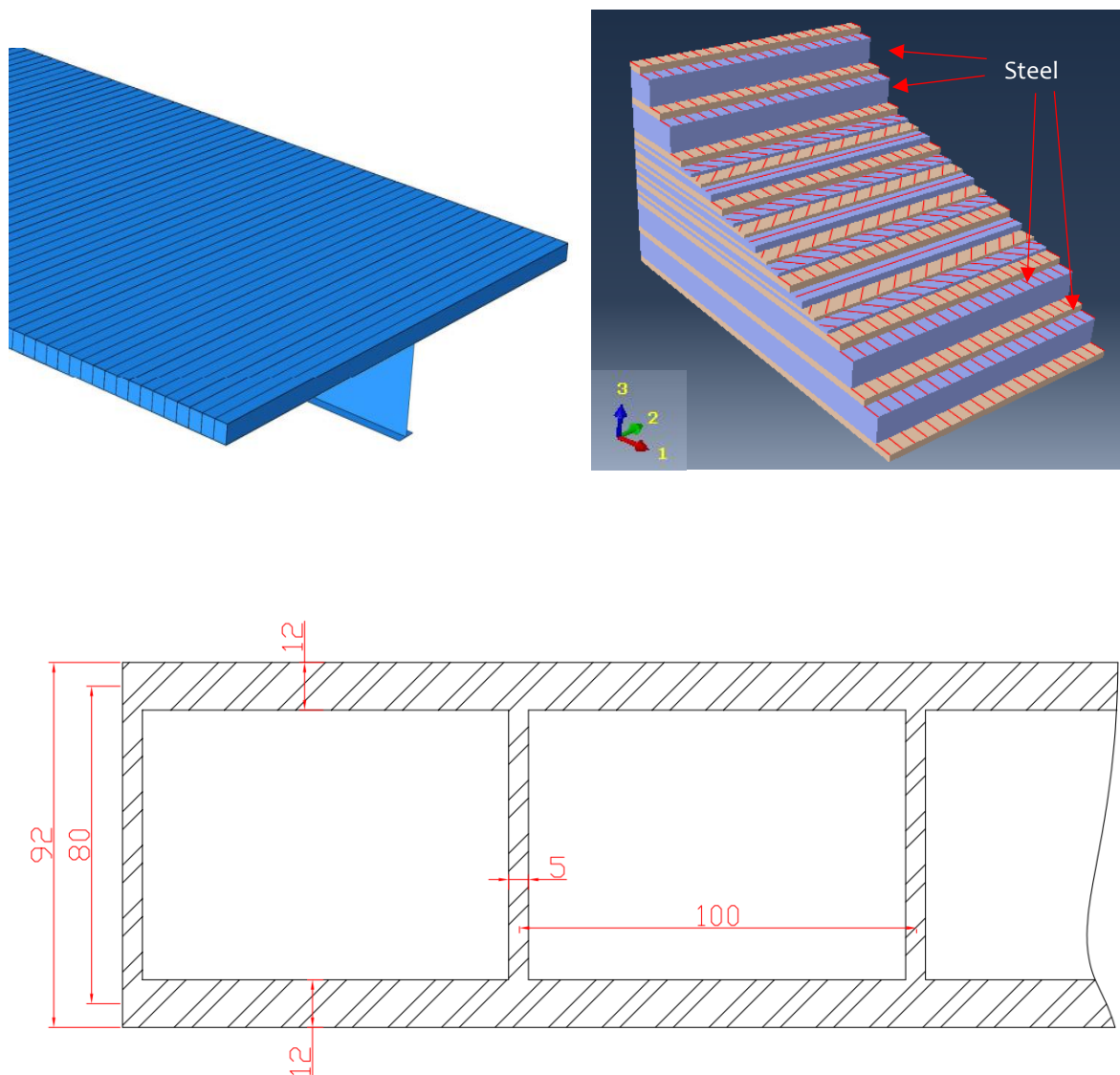


Figure 4.17: FSL Cellular Deck Isotropic View, Skin Laminate Layup & Cross-Section

Table 4.8: FSL Cellular Deck Verifications

	Verification	Utilisation Ratio
ULS	Composite System Plastic Moment	0.96
	Beam Stress Verification	0.99
	Longitudinal Facing Failure (UDL)	0.99
	Longitudinal Facing Failure (PL)	0.29
	Transverse Facing Failure (UDL)	0.57
	Transverse Facing Failure (PL)	0.23
	Transverse Shear Failure (UDL)	0.16
	Transverse Shear Failure (PL)	0.29
	Strain Failure 0°	0.08
	Strain Failure 90°	0.12
	Face Wrinkling	0.09
	Local Buckling of Webs (JRC)	0.005
	Local Buckling of Webs (Kassapoglou)	0.002
	Global Buckling	0.84
Shear Crimping 0°	0.005	
Shear Crimping 90°	0.008	
SLS	Global Deflection	0.39
	Transverse Deflection (Global Load)	0.04
	Transverse Deflection (Local Load)	0.18
	Vibrations	0.95

In the design of this deck, the most critical criteria are the ultimate limit state criteria with the exception of the vibration analysis which is often critical in the design of light-weight deck structures. The vibration checks are based on a basic hand-calculation which is limited to a human comfort level of 3Hz. It is difficult to accurately predict the response of the deck without performing a detailed dynamic analysis, which is beyond the remit of this study. The composite plastic moment and longitudinal facing failure verifications are governing due to the weaker plane of the laminate being oriented in the longitudinal direction of the bridge. This means that the weaker secondary direction strength value is used in combination with the greater safety factors for the verifications in the longitudinal direction of the deck – resulting in critical utilisation values. The stress in the beam is also governing due to the low depth and high stiffness of the FSL deck, which increases the height of the composite neutral axis meaning more of the stress is focused in the bottom flange of the beam.

4.2.3 FSL Solid Slab Deck Design

The second type of system to be investigated is a solid slab deck system, similar to a concrete deck, that will feature a solid panel of FSL supported by a series of steel beams. This type of design is expected to produce a much thinner system, given that it doesn't have the foam cores in the centre. However, by decreasing the depth of the deck and not having foam cores present, the geometric properties of the deck are significantly reduced. Furthermore, without the foams to provide geometric properties at a low weight, the inertial properties must be provided by more hybrid-composite material, leading to a costlier, heavier deck with potentially larger supporting beams.

Therefore, the deck must be thick enough to satisfy the design verifications or have a representatively higher Young's modulus in order to compensate for the lack of geometric properties. However, as thickness increases the laminate's flexural Young's moduli decrease. It is with these considerations that a balance must be found between the thickness and resulting stiffness of the panel. This is an iterative process that will be complete when the panel can satisfy the design verifications for the car parking application. Whether this type of system is beneficial over the system discussed in the previous sections will be determined in [section 4.3 & 4.4](#).

Some potential benefits of this type of system, over the cellular type, are the increased stiffness of the core – allowing greater transmission of forces through the deck, lower construction depth and reduced production costs. It is expected that the positioning of the steel within a solid slab laminate will be much easier and less costly than the positioning of steel plies within the Z-shaped cellular section.

To help push the steel plies to the extremes of the laminate, a denser and therefore thicker, 1200g/m², set of fibres are used in the centre of the thickness, these are denoted with an asterisk in [table 4.9 & 4.12](#), whilst a thinner set of 300g/m² fibres are used adjacent to the steel in order to keep as far from the neutral axis as possible whilst reducing the number of plies.

Due to the high self-weight of this type of construction, a second design featuring a reduced beam spacing will be produced in order to determine if it is economically beneficial to have a closer supporting structure and thinner deck or a broader supporting structure and thicker deck. A further check this will allow is how the effective width of the composite system changes with beam spacing.

4.2.3.1.1 5m FSL Solid Slab Deck

Table 4.9: 5m Solid Slab Laminate Composition

Laminate Layup	[0, steel, 0, steel, 0, steel, 0, steel, 0, steel, 0, 0/90 ₁₈ [*] , ±45] _s
Laminate thickness	50mm
Total thickness of steel	10mm
Ply thickness	0.26mm & 0.98mm
Fibre areal density	300g/m ² & 1200g/m ²
Laminate density	3040kg/m ³
Primary Orientation (o°)	Transverse
Mass of Deck	153kg/m ²

The resulting flexural and axial stiffness values for this laminate are given respectively as:

- $E_{xx} = 114700 \text{ MPa}$
- $E_{yy} = 110600 \text{ MPa}$
- $G_{xy} = 27300 \text{ MPa}$
- $E_{xx} = 60120 \text{ MPa}$
- $E_{yy} = 58680 \text{ MPa}$
- $G_{xy} = 14000 \text{ MPa}$

A summary of the design verifications for this system can be seen in [table 4.10](#).

Table 4.10: 5m Solid Slab Deck Verifications

	Verification	Utilisation Ratio
ULS	Composite System Plastic Moment	0.93
	Beam Stress Verification	1.15*
	Longitudinal Facing Failure (UDL)	0.41
	Longitudinal Facing Failure (PL)	0.07
	Transverse Facing Failure (UDL)	0.12
	Transverse Facing Failure (PL)	0.12
	Transverse Shear Failure (UDL)	0.004
	Transverse Shear Failure (PL)	0.05
	Strain Failure 0°	0.03
	Strain Failure 90°	0.11
	Face Wrinkling	N.A
	Local Buckling of Webs (JRC)	N.A
	Local Buckling of Webs (Kassapoglou)	N.A

	Global Buckling	0.87
	Shear Crimping 0°	N.A
	Shear Crimping 90°	N.A
SLS	Global Deflection	0.40
	Transverse Deflection (Global Load)	0.19
	Transverse Deflection (Local Load)	0.37
	Vibrations	1.06*

The composite plastic moment verification in this design is highly utilised due to the high loading caused by the greater self-weight of the deck and because of the weaker secondary axis of the FSL being oriented in the longitudinal direction of the system. The stress in the beam for the solid slab deck has exceeded the yielding value (355MPa) and so this verification is determined to have failed. This is again due to the height of the composite neutral axis but further affected by the increased mass of the deck (when compared to the cellular decks).

The most critical criteria in this system is the vibration verification, which has also failed, this is again due to the low depth of the deck caused by the specification of a solid slab compared to a cellular section. To improve this, the inertia of the deck should be increased, however, by increasing the thickness of the deck, the flexural stiffness decreases and the mass increases, which negatively affects this verification. For this reason, the verification has remained unsatisfied and would have to be counteracted by secondary measures and a further dynamic investigation beyond the scope of this case study.

The prescription of an increased beam section (to IPE550) would satisfy the failed verifications, as shown in [table 4.11](#). For the purpose of performance comparisons with the cellular deck, the profile used will remain as the IPE500 previously specified, however, for comparison of general details and costs the IPE550 section will be used.

Table 4.11: Critical Verifications for 5m Solid Slab with IPE500 & IPE550 Supporting Beams

	Solid Slab with IPE500	Solid Slab with IPE550
Composite Plastic Moment	0.93	0.75
Beam Stress	1.15	0.98
Vibrations	1.06	0.97

4.2.3.1.2 2.5m FSL Solid Slab Deck

Table 4.12: 2.5m Solid Slab Laminate Composition

Laminate Layup	[0, steel, 0, steel, 0, steel, 0, steel, 0, 0/90 ₂ *, 0 ₃ *, ±45] _s
Laminate thickness	26mm
Total thickness of steel	10mm
Ply thickness	0.26mm & 0.98mm
Fibre areal density	300g/m ² & 1200g/m ²
Laminate density	3686kg/m ³
Primary Orientation (o°)	Transverse
Mass of Deck	96kg/m ²

The resulting flexural and axial stiffness values for this laminate are given respectively as:

- $E_{xx} = 144985 \text{ MPa}$
- $E_{yy} = 139160 \text{ MPa}$
- $G_{xy} = 34835 \text{ MPa}$
- $E_{xx} = 85450 \text{ MPa}$
- $E_{yy} = 77895 \text{ MPa}$
- $G_{xy} = 19870 \text{ MPa}$

A summary of the design verifications for this system can be seen in table 4.13.

Table 4.13: 2.5m Solid Slab Deck Verifications

	Verification	Utilisation Ratio
ULS	Composite System Plastic Moment	0.47
	Beam Stress Verification	0.59
	Longitudinal Facing Failure (UDL)	0.56
	Longitudinal Facing Failure (PL)	0.15
	Transverse Facing Failure (UDL)	0.08
	Transverse Facing Failure (PL)	0.18
	Transverse Shear Failure (UDL)	0.005
	Transverse Shear Failure (PL)	0.08
	Strain Failure 0°	0.04
	Strain Failure 90°	0.05
	Face Wrinkling	N.A
	Local Buckling of Webs (JRC)	N.A
	Local Buckling of Webs (Kassapoglou)	N.A

	Global Buckling	0.73
	Shear Crimping 0°	N.A
	Shear Crimping 90°	N.A
SLS	Global Deflection	0.25
	Transverse Deflection (Global Load)	0.14
	Transverse Deflection (Local Load)	0.53
	Vibrations	0.76

As shown in the table the system is largely underutilised, the prescription of a smaller beam section (to IPE450) would help to further utilise the system, as shown in table 4.14. A further reduction of the beam to an IPE400 section is only prohibited by the vibration verification which would be exceeded by 9%. For the purpose of performance comparisons with the 5m solid slab deck, the profile used will remain as the IPE500 previously specified, however, for comparison of general details and costs the IPE450 section will be used.

Table 4.14: Critical Verifications for 2.5m Solid Slab with IPE500 & IPE450 Supporting Beams

	2.5m Solid Slab with IPE500	2.5m Solid Slab with IPE450
Composite Plastic Moment	0.47	0.73
Beam Stress	0.59	0.76
Longitudinal Facing Failure (UDL)	0.56	0.62
Global Buckling	0.73	0.82
Vibrations	0.76	0.92

4.2.4 GFRP Cellular Deck

The GFRP deck used for comparison with the FSL systems will use stiffness values obtained from the experimental procedure previously conducted and detailed in [section 3](#). This will allow the GFRP case to form as a benchmark for the performance and economic viability of the fibre-steel hybrid composite. For this reason, much of the design is kept the same as from the FSL cellular deck, such as the skin thickness, web spacing and thickness, fibre selection and supporting structure.

Table 4.15: GFRP Laminate Composition

Laminate Layup	$[0_3, 90_3, \pm 45_2, 0_3, 90_3, 0/90, \pm 45_2, 0/90, \pm 45_2]_S$
Laminate thickness	12mm
Ply thickness	0.26mm
Fibre areal density	300g/m ²
Laminate density	1850kg/m ³
Primary Orientation (°)	Transverse
Mass of Deck	55kg/m ²

The resulting local flexural and axial stiffness values for this laminate are given respectively as:

- $E_{xx} = 19300$ MPa
- $E_{yy} = 15825$ MPa
- $G_{xy} = 4000$ MPa
- $E_{xx} = 17510$ MPa
- $E_{yy} = 16500$ MPa
- $G_{xy} = 4560$ MPa

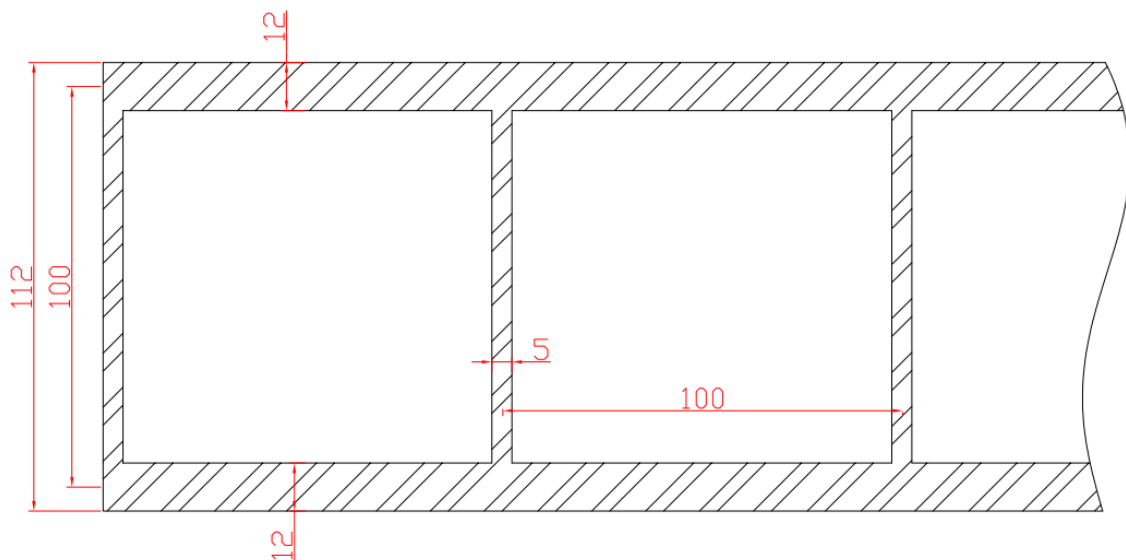


Figure 4.18: GFRP Deck Dimensions

Table 4.16: GFRP Cellular Deck Verifications

	Verification	Utilisation Ratio
ULS	Composite System Plastic Moment	0.78
	Beam Stress Verification	0.98
	Longitudinal Facing Failure (UDL)	0.67
	Longitudinal Facing Failure (PL)	0.46
	Transverse Facing Failure (UDL)	0.34
	Transverse Facing Failure (PL)	0.31
	Transverse Shear Failure (UDL)	0.18
	Transverse Shear Failure (PL)	0.37
	Strain Failure 0°	0.17
	Strain Failure 90°	0.51
	Face Wrinkling	0.19
	Local Buckling of Webs (JRC)	0.09
	Local Buckling of Webs (Kassapoglou)	0.03
	Global Buckling	0.76
Shear Crimping 0°	0.008	
Shear Crimping 90°	0.02	
SLS	Global Deflection	0.71
	Transverse Deflection (Global Load)	0.30
	Transverse Deflection (Local Load)	0.76
	Vibrations	0.99

The primary criteria that govern the design of the GFRP deck are serviceability limit state checks; this is due to the lower stiffness of the facings and can be noticed when comparing the utilisation of the global deflection with the FSL decks that have a much-improved stiffness. The beam stress utilisation is also critical in this case, but unlike the FSL decks not due to the high self-weight of the deck, but this time due to the low stiffness of the deck, causing a lower stress in the deck – meaning more of the stress is taken by the beam.

4.2.5 Design Summary

To summarise the four designs presented in the previous section, the following table will list some of the most important details of the design.

Table 4.17: Summary of Deck Designs

	FSL Cellular Deck	GFRP Cellular Deck	5m Solid Slab FSL Deck	2.5m Solid Slab FSL Deck
Minimum Construction Depth (minimum beam + deck) (mm)	500 + 92 592	500 + 112 612	550 + 50 600	450 + 26 476
Total Construction Depth (IPE500 + deck) (mm)	500 + 92 592	500 + 112 612	500 + 50 550	500 + 26 526
Deck Mass (kg/m ²)	109	55	153	96
Total ULS Loading (kN/m ²)	6.10	5.40	6.70	6.20
Beam Deflection to be Cantilevered (Self-Weight: IPE500 & Deck) (mm)	53	31	71	28
Longitudinal Composite Stiffness from FEA (IPE500) (*10 ⁶ kN.m ²)	2.62	1.78	2.55	2.08

Table 4.18: Critical Verifications for Each Deck Type

	FSL Cellular Deck	GFRP Cellular Deck	5m Solid Slab FSL Deck	2.5m Solid Slab FSL Deck
Critical Verifications	<ul style="list-style-type: none"> • Composite Plastic Moment • Beam Stress • Longi. Facing Failure (UDL) • Vibrations 	<ul style="list-style-type: none"> • Beam Stress • Vibrations 	<ul style="list-style-type: none"> • Composite Plastic Moment • Beam Stress • Vibrations 	<ul style="list-style-type: none"> • Vibrations

4.3 RESULTS & COMPARISON

This section will look to compare and analyse the results of the investigation into the optimised decks, providing an in-depth look at the results before comparing them between designs and evaluating the optimisation level. It should be noted that for the purpose of the performance comparisons the IPE500 supporting girder will be maintained throughout each design, whereas, when comparing the general details such as cost and construction depth the minimum system will be considered. This ensures that differences in performance comparisons are a result of the deck design not the beam section, however, the practical comparisons take into account the realistic system. Furthermore, the SLS loading will be used when comparing stress distributions in the deck, this is to ensure the same load is applied in each case, given that ULS load varies with self-weight and the SLS load does not.

It should also be noted that the solid slab deck doesn't have a top 'skin' or bottom 'skin' as in the cellular decks and so the equivalent 'skin' will be taken as the top and bottom 12mm (the same as the skin thickness in the cellular decks). Comparisons drawn between the 2.5m and 5m solid slab FSL deck will be restricted to general details and composite properties, this is due to the incomparability of the two systems with regards to the different beam spacing.

4.3.1 System Verifications

The system verifications for each deck can be found and compared in [table 4.19](#). It is expected that due to the lower stiffness the serviceability criteria will govern the design of the GFRP deck and that the ultimate limit state criteria will be less utilised. This is the case with the global deflection criterion (GFRP deck almost twice as utilised as FSL decks), although due to the beam stress verification (ULS), the deck cannot be shallow enough to further utilise the transverse deflection criteria. Furthermore, the beam stress verification is highly utilised as a result of the lack of stiffness in the deck - as the beam must now take the majority of the stress from the system.

By including steel in the laminate, the stiffness of the new material is increased greatly, therefore it is expected that the serviceability criteria no longer lead to over design with regards to ultimate limit state. This is evidenced from the verifications by the critical composite plastic moment verifications in the FSL decks. Further evidence can be seen in the cellular FSL deck where the longitudinal facing failure is also critical. This verification is critical because of the selection of the primary orientation of the fibres (transverse across the deck in each case), meaning that the compression induced by the longitudinal bending of the system is resisted by the weaker plane of the laminate. The reason for this verification being critical in the cellular FSL deck but not in the FSL solid slab deck is because of the difference in thickness of the section that the stress is acting upon (12mm for the skins of the cellular deck compared to 50mm for the solid slab). The verification is less critical in the GFRP deck, despite also having a 12mm skin, due to the lower ULS load as a result of the lower self-weight of the deck.

Table 4.19: Verification Comparison with IPE500

	Verification	FSL Cellular Deck IPE500	GFRP Cellular Deck IPE500	Solid Slab FSL Deck IPE500
ULS	Beam Plastic Moment	0.35	0.20	0.47
	Beam Shear	0.20	0.18	0.22
	Composite System Plastic Moment	0.96	0.78	0.93
	Beam Stress Verification	0.99	0.98	1.15*
	Longitudinal Facing Failure (UDL)	0.99	0.67	0.41
	Longitudinal Facing Failure (PL)	0.29	0.46	0.07
	Transverse Facing Failure (UDL)	0.57	0.34	0.12
	Transverse Facing Failure (PL)	0.23	0.31	0.12
	Transverse Shear Failure (UDL)	0.16	0.18	0.004
	Transverse Shear Failure (PL)	0.29	0.37	0.05
	Strain Failure 0°	0.08	0.17	0.03
	Strain Failure 90°	0.12	0.51	0.11
	Face Wrinkling	0.09	0.19	N.A
	Local Buckling of Webs (JRC)	0.005	0.09	N.A
	Local Buckling of Webs (Kassapoglou)	0.002	0.03	N.A
	Global Buckling	0.84	0.76	0.87
	Shear Crimping 0°	0.005	0.008	N.A
Shear Crimping 90°	0.008	0.02	N.A	
SLS	Global Deflection	0.39	0.71	0.40
	Transverse Deflection (Global Load)	0.04	0.30	0.19
	Transverse Deflection (Local Load)	0.18	0.76	0.37
	Vibrations	0.95	0.99	1.06*

Table 4.20: Normalised System Verifications with Minimum Supporting Girder

	Verification	FSL Cellular Deck IPE500	GFRP Cellular Deck IPE500	5m Solid Slab FSL Deck IPE500
ULS	Beam Plastic Moment	0.35	0.20	0.47
	Beam Shear	0.20	0.18	0.18
	Composite System Plastic Moment	0.97	0.79	0.76
	Beam Stress Verification	1.00	0.99	1.00
	Longitudinal Facing Failure (UDL)	1.00	0.68	0.43
	Longitudinal Facing Failure (PL)	0.29	0.46	0.07
	Transverse Facing Failure (UDL)	0.58	0.34	0.13
	Transverse Facing Failure (PL)	0.23	0.31	0.12
	Transverse Shear Failure (UDL)	0.16	0.18	0.00
	Transverse Shear Failure (PL)	0.29	0.37	0.05
	Strain Failure 0°	0.08	0.17	0.05
	Strain Failure 90°	0.12	0.52	0.04
	Face Wrinkling	0.09	0.19	N/A
	Local Buckling of Webs (JRC)	0.01	0.09	N/A
	Local Buckling of Webs (Kassapoglou)	0.00	0.03	N/A
	Global Buckling	0.85	0.77	0.78
	Shear Crimping 0°	0.01	0.008	N/A
Shear Crimping 90°	0.01	0.02	N/A	
SLS	Global Deflection	0.39	0.72	0.31
	Transverse Deflection (Global Load)	0.04	0.30	0.09
	Transverse Deflection (Local Load)	0.18	0.77	0.38
	Vibrations	0.96	1.00	0.99

Table 4.20 shows the normalised verifications for each system using the minimum supporting member, compared to the previous table which compared each system when using the same supporting member. With normalised utilisation ratios it becomes easier to compare the systems on the basis that each of the most governing design checks are now at 100%.

From the normalised values it can be seen that each of the systems struggle with the vibration analysis and the yielding of the beam. The response to the vibrations is a more complex issue and can be addressed with supplementary dynamic measures or further analysis. The beam stress verification causes an interesting problem that should be further investigated. The highest stress in the beam is found at the bottom flange, the use of an asymmetric profile with a thicker bottom flange would help to reduce the stress at this location, however, it would lower the neutral axis of the composite system and cause a greater stress in the deck. This would not be an issue for the solid slab deck as the design checks for the ultimate limit state of the deck are underutilised, but for the cellular FSL deck this would likely push the design checks beyond the limit. A further consideration is that it is a more structurally sound system if the beam yields prior to the failure of the deck, this is due to the ductile failure of the beam which would allow a slower failure of the structure compared to the failure of the deck which is expected to be a relatively brittle failure. This provides evidence of failure allowing the use of the structure to be prohibited until further investigation. If the asymmetric beam profile changed this order of failure, the deck would fail first and may lead to a quick and catastrophic failure of the structure.

4.3.2 Shear Interaction

In order to check how much extra capacity that the shear interaction between the deck and the beam gives to the composite system, the plastic moment verification can be performed with the plastic moment resistance of the beam and the whole composite system.

Table 4.21: Comparison of Moment Verifications with and without Shear Interaction

	FSL Cellular Deck	GFRP Cellular Deck	5m Solid Slab FSL Deck
Without Interaction	1.26	1.11	1.38
With Interaction	0.96	0.78	0.93

From the verifications (table 4.21) it can be seen that through the shear interaction with the deck, each system is allowed a 30-40% increase in bending moment resistance. This assumes a perfect connection through the adhesive connection (simulated by the tie constraint in the FE model). The applicability of this connection type and its performance comparison with a bolted connection is beyond the scope of this project.

4.3.3 Longitudinal Direction

The first result to be extracted from the models is the effective width of the deck. This represents the portion of the deck that effectively contributes to the composite system, acting in unison with the supporting beam, as a compression flange to the system. This is one of the most important results as it determines the effective geometry of the deck, which is used to determine the effective stiffness of the composite system. The effective width is established from the FE model by extracting the distribution of longitudinal stresses across the width of the deck, shown in figure 4.19. With this distribution one can calculate the area under the curve and divide it by the maximum value, to obtain an equivalent length at which the maximum stress can be uniformly distributed over. This is necessary due to the presence of the shear lag effect, which is the phenomenon of shear strains in the deck, induced by the connection with the beam, causing a reduction in bending stresses in the deck as the distance from the beam is increased. This phenomenon can be seen in figure 4.19 with the stress being highest at the centre of the graph (above the beam) and lowest at the extremes of the graph (furthest point from beam).

Table 4.22: Effective Width at ULS/SLS

	5m FSL Cellular Deck	5m GFRP Cellular Deck	5m Solid Slab FSL Deck	5m Concrete Deck	2.5m Solid Slab FSL Deck
$\frac{B_{eff}}{B}$ (ULS)	0.88	0.84	0.87	0.92	0.97
$\frac{B_{eff}}{B}$ (SLS)	0.88	0.88	0.89	0.92	0.97

Table 4.23: Height of Composite Neutral Axis

	FSL Cellular Deck	GFRP Cellular Deck	5m Solid Slab FSL Deck	2.5m Solid Slab FSL Deck
Total Construction Depth (with IPE500) (mm)	592	612	550	526
Height of Composite Neutral Axis as Ratio of Total Depth	0.80	0.59	0.87	0.81
Distance to Bottom Skin of Deck (mm)	24.77	140.93	20.62	73.18
Distance to Top Skin of Deck (mm)	104.77	240.93	70.62	99.18

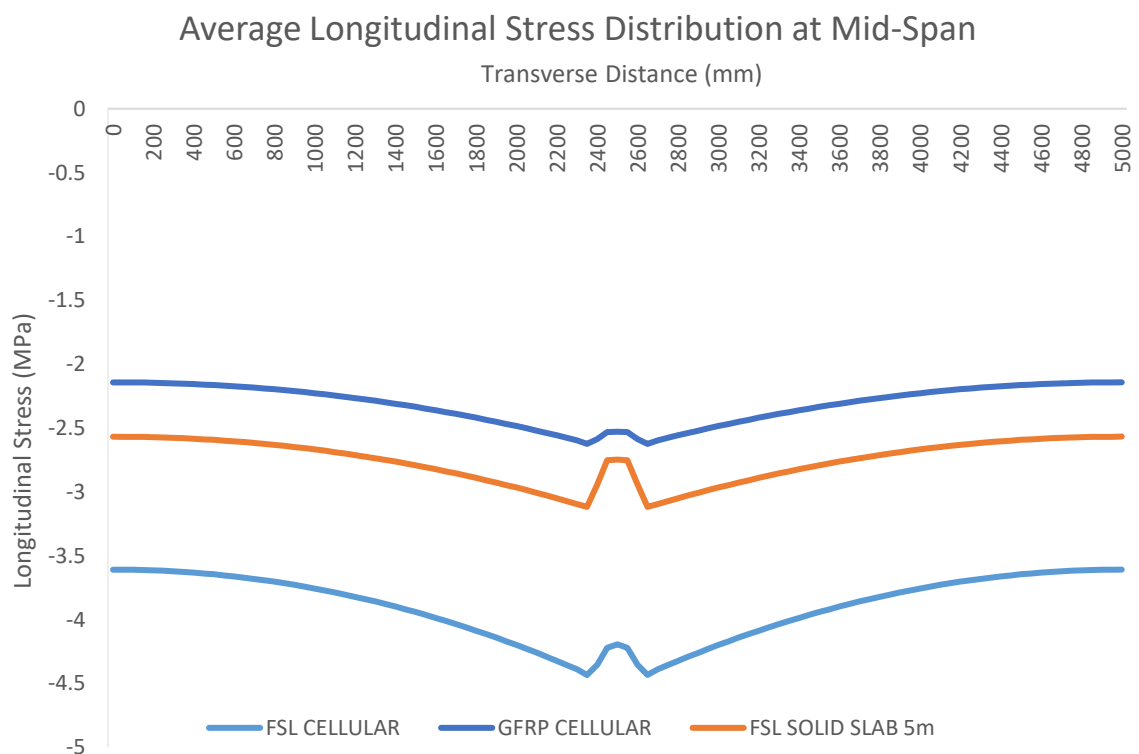


Figure 4.19: Average Longitudinal Stress Distribution Across Width of Various Decks

From the distributions shown in [figure 4.19](#), it can be seen that the stress distribution across the deck is almost uniform, leading to a high effective width. [Table 4.22 & 4.23](#) provide some rationale behind the magnitude of the stress in each of the decks. First of all, the GFRP deck has the lowest composite neutral axis at around 60% of the total depth, due to the increased depth of the deck and the low Young's moduli of the deck material. This attracts a large amount of stress to the top of the system. However, the deck itself doesn't have a high enough Young's modulus to sustain such stress and so the majority of the stress remains in the beam, hence the high beam stress verification (98% utilised), despite the comparatively low self-weight. The two FSL decks have a much higher stiffness than the GFRP deck and therefore have a higher average stress across the deck. Furthermore, due to the increased core stiffness, particularly in the solid slab deck, more of the thickness of the deck can be utilised, allowing a higher stress.

For reference, a 120mm concrete solid slab deck has been included in [table 4.22](#) to show how the effective width of the FSL decks compares. The effective width of the concrete deck is around 5% greater than the maximum achieved in the FSL decks. A possible reason for this is that the concrete is homogeneous throughout the thickness meaning the core can perfectly transfer forces through the deck. At the ULS level it can be seen that the cellular FSL deck actually has a higher effective width than the solid slab deck, albeit by only 16mm, the reason for this small difference can be due to a number of things, such as the difference in self-weight loading. From the SLS effective widths (when the same loading is present on each of the systems), it can be seen that the solid FSL deck now has a greater effective width. It is also interesting to note the effect of the span/breadth ratio on the effective width – the 2.5m FSL solid slab deck has an almost complete (97%) effective width, whereas, each of the 5m decks have a reduced effective width in comparison.

[Figure 4.20 & 4.21](#) show the distribution of longitudinal stress in the bottom skin of the decks. The GFRP deck has the greatest distance from the bottom skin to the neutral axis (~120mm greater than the other two decks), explaining the high stress seen in the bottom skin of the GFRP deck despite its low stiffness. The most notable difference between the decks from [figure 4.20](#) is the difference in the amount of shear lag between the FSL decks and the GFRP deck. The GFRP deck has an almost linear distribution of stresses becoming minorly more compressive towards the centre of the graph, suggesting less shear lag. Conversely, the FSL decks feature a dramatic increase in compressive stress as the centre of the graph is approached. This is because there is a greater amount of shear lag taking place in the bottom skin of the FSL decks. The reason for this can be associated to two factors: the increased stiffness and reduced depth of the FSL decks. Increased amount of shear lag would usually mean a lower effective width, however, due to the difference in magnitude of the stresses, especially in the top skin, the effective width and resulting composite stiffness are higher in the FSL decks.

The discontinuity at the centre of the graph for the FSL solid slab deck is much greater than for the other decks, this is due to the greater amount of transverse redistribution taking place. This is more prevalent in the solid slab than the cellular deck because of the presence of the foams, which do not have a high enough stiffness to redistribute stresses as efficiently as the GFRP and steel plies in the solid slab deck.

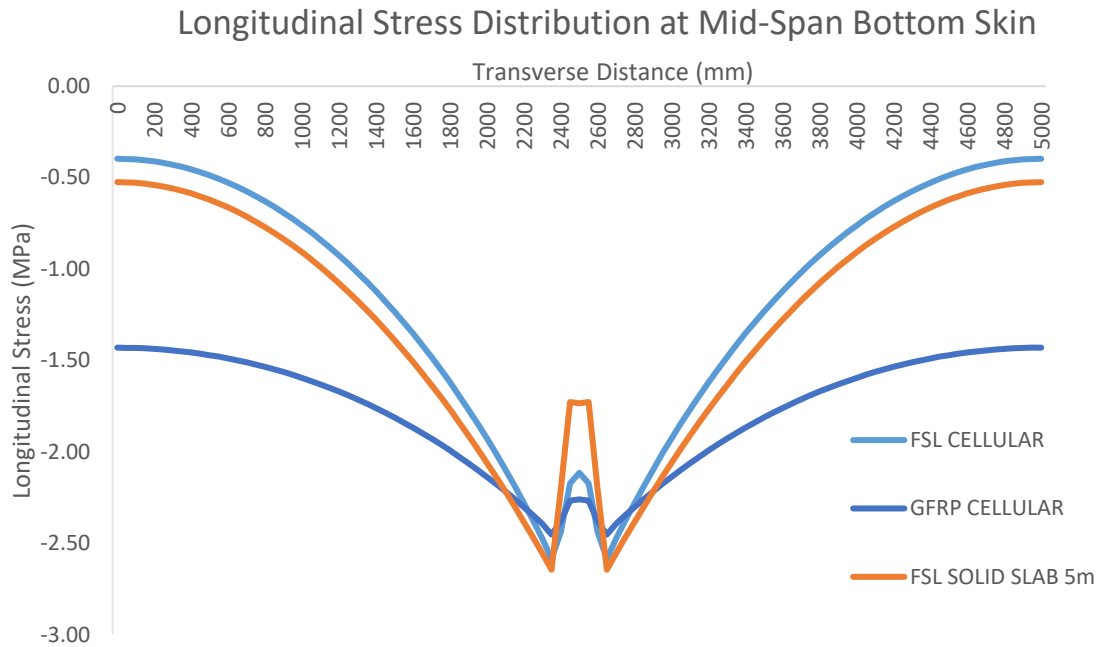


Figure 4.20: Longitudinal Stress Distribution Across Width of Bottom Skin of Deck

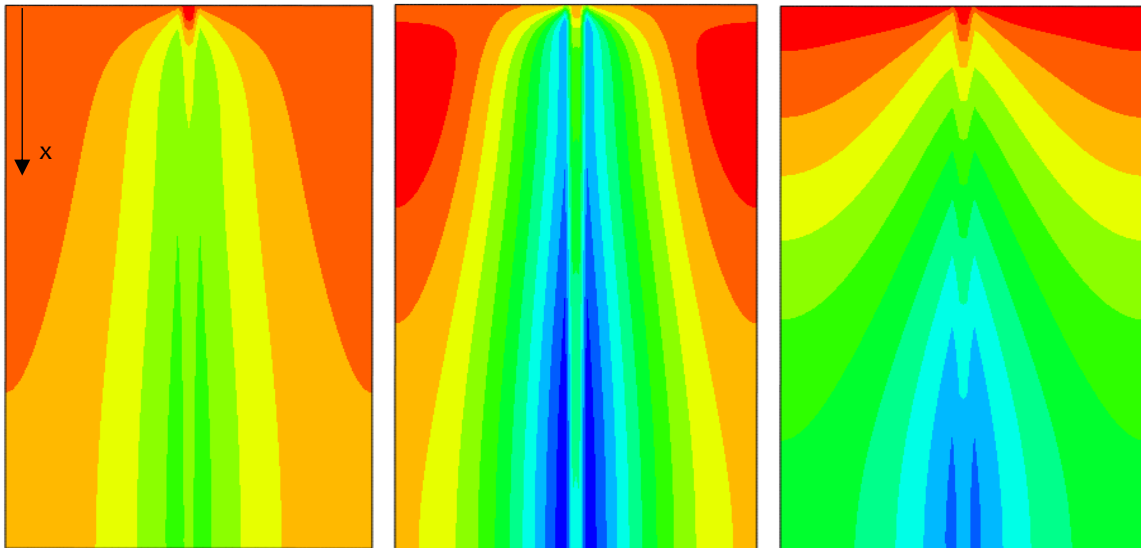


Figure 4.21: FE output showing the longitudinal stress distributed over bottom skin of each deck, from left to right: FSL Cellular, FSL Solid Slab, GFRP Cellular

It is important to note that from the FE screens shown in figure 4.21, the magnitude of the stress is different per image and only the distribution should be compared between decks. This is because of the stress averaging used for the top and bottom skin in the cellular decks – giving an average stress for the laminate, whereas there is no top and bottom skin in the solid slab and so for the FSL solid slab images the most extreme steel ply will be used to illustrate the distribution of stresses. For the magnitude of stresses distributed at the mid-span cross-section the graph in figure 4.20 should be used.

In the top skin of the decks, shown in figures 4.22 & 4.23, the magnitude of the stress is affected by the decks ability to transfer forces through the deck from the bottom to the top skins. The level of this transmission is governed by the stiffness of the core of the deck. From the stress distribution curves, it is clear to see that the GFRP deck has the lowest level of transmission, due to the larger centre-to-centre distance between the facings and the less stiff, GFRP webs – the key signs of this are the higher stress in the bottom skin and lower stress in the top skin. Furthermore, the change in gradient at the deck-beam interface shown in figure 4.24 reinforces this theory. Whereas, in the FSL decks which feature a stiffer core, compared to the GFRP deck, there is more transmission and both skins can be seen to experience a high stress.

The vertical distribution of longitudinal stress and strain at mid-span and resulting position of the composite neutral axes can be found in figure 4.24 and table 4.23. The composite neutral axis of the FSL decks are higher due to the increased stiffness of the deck when compared to the GFRP deck. The difference in stiffness between the deck and the beam can be seen in the stress distribution by the jump in stress at the interface between the beam and deck ($h=500\text{mm}$). In the GFRP deck this jump is much larger than the in the stiffer FSL decks. From the strain distribution the rate of transmission of strains through the deck can be noticed. The vertical strain distribution in the FSL systems is (almost) linear, meaning the strain can pass through to the top of the deck without restriction. Conversely, in the GFRP deck there is a distinct change in gradient of the strain distribution line, suggesting that there is a more restricted load path to the top of the deck. This is caused by the lower stiffness of the core of the deck when compared to the two FSL decks, to be expected as a result of the increased centre-to-centre distance of the facings and less stiff GFRP webs. With regards to the solid slab FSL deck, it may be useful to investigate the use of asymmetric supporting profiles that would lower the neutral axis, increasing the stress in the deck and decreasing the stress in the beam. However, a careful balance must be met given the limited strength values of the deck.

Figure 4.25 depicts the force displacement curves for each of the systems under serviceability and ultimate limit state loading. When looking at the SLS curves, it can be observed that under the same load the FSL decks have a very similar global deflection (4% difference), owing to their similar composite stiffness values. Interestingly though, the solid slab FSL deck uses approximately twice as much material to achieve this stiffness and resulting deflection. The GFRP deck has a 70% greater deflection at mid-span, highlighting its low stiffness. This is reinforced by the ULS curves where the GFRP deck has the lowest ULS load (due to its low self-weight) but the highest displacement. The FSL decks have a different ULS load so it becomes harder to compare but it should be noted that the solid slab system does have a 12% higher deflection but also has an 8% higher loading.

Longitudinal Stress Distribution at Mid-Span Top Skin

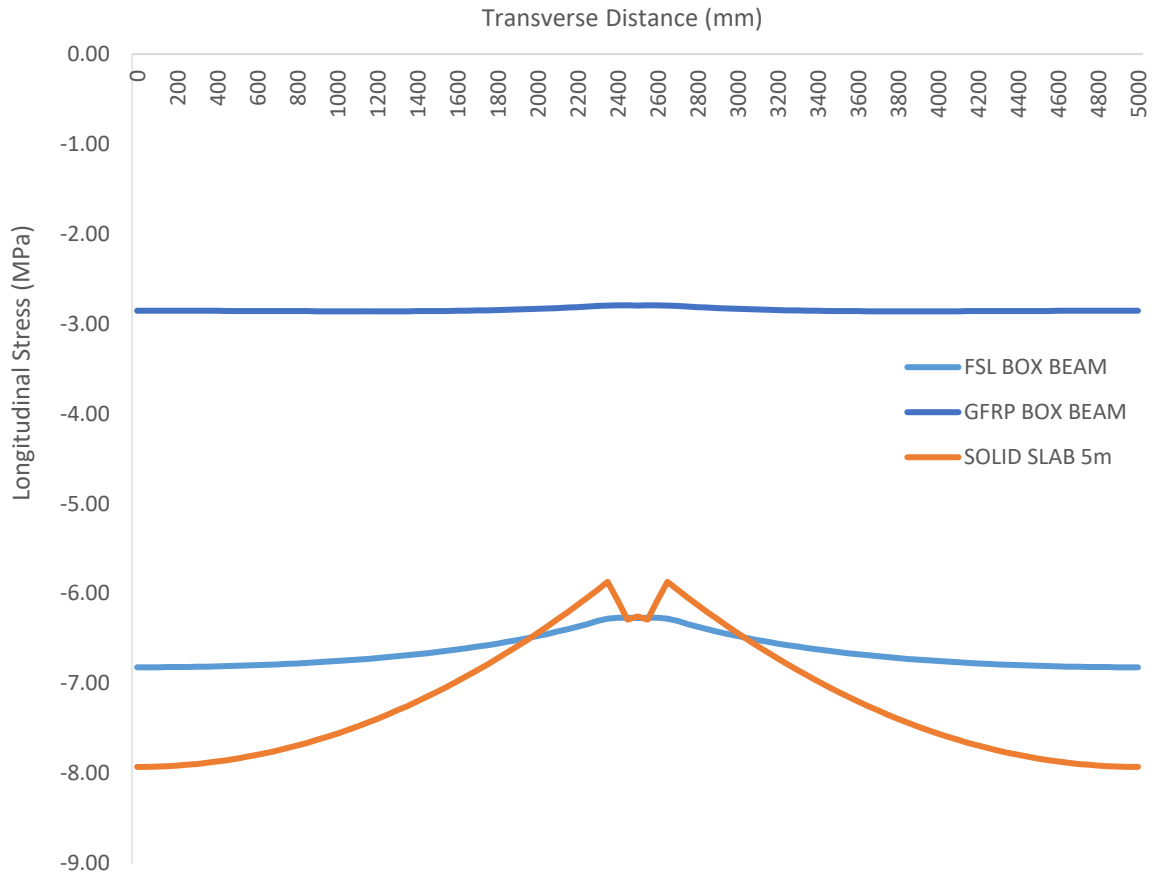


Figure 4.22: Longitudinal Stress Distribution Across Width of Top Skin of Deck

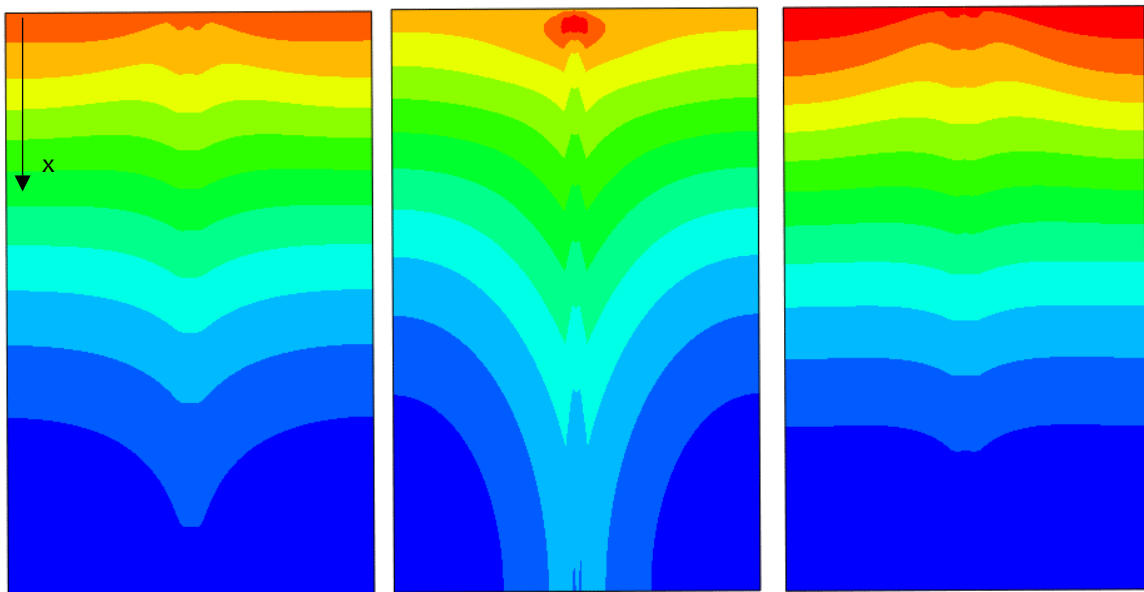
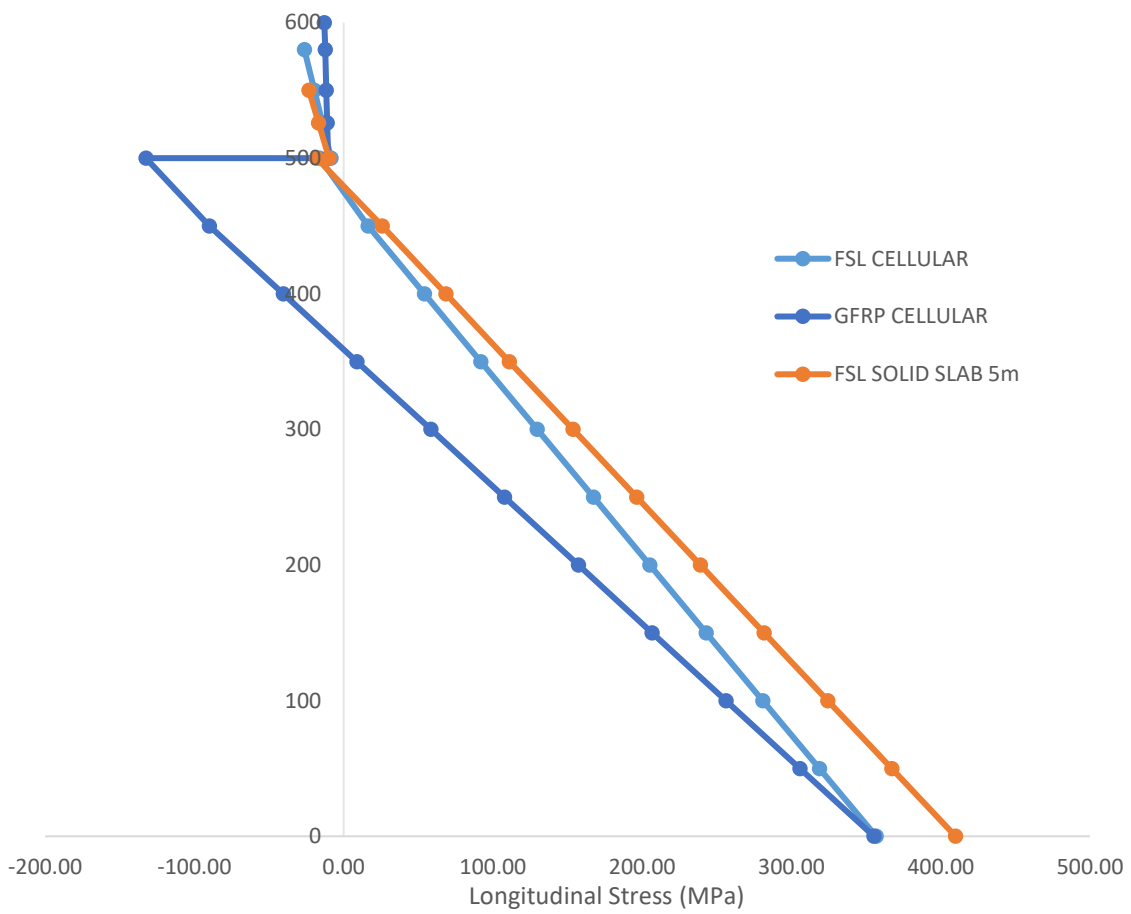


Figure 4.23: FE output showing the longitudinal stress distributed over top skin of each deck, from left to right: FSL Cellular, FSL Solid Slab, GFRP

Vertical Distribution of Longitudinal Stress at Mid-Span Cross-Section



Vertical Distribution of Longitudinal Strain at Mid-Span Cross-Section

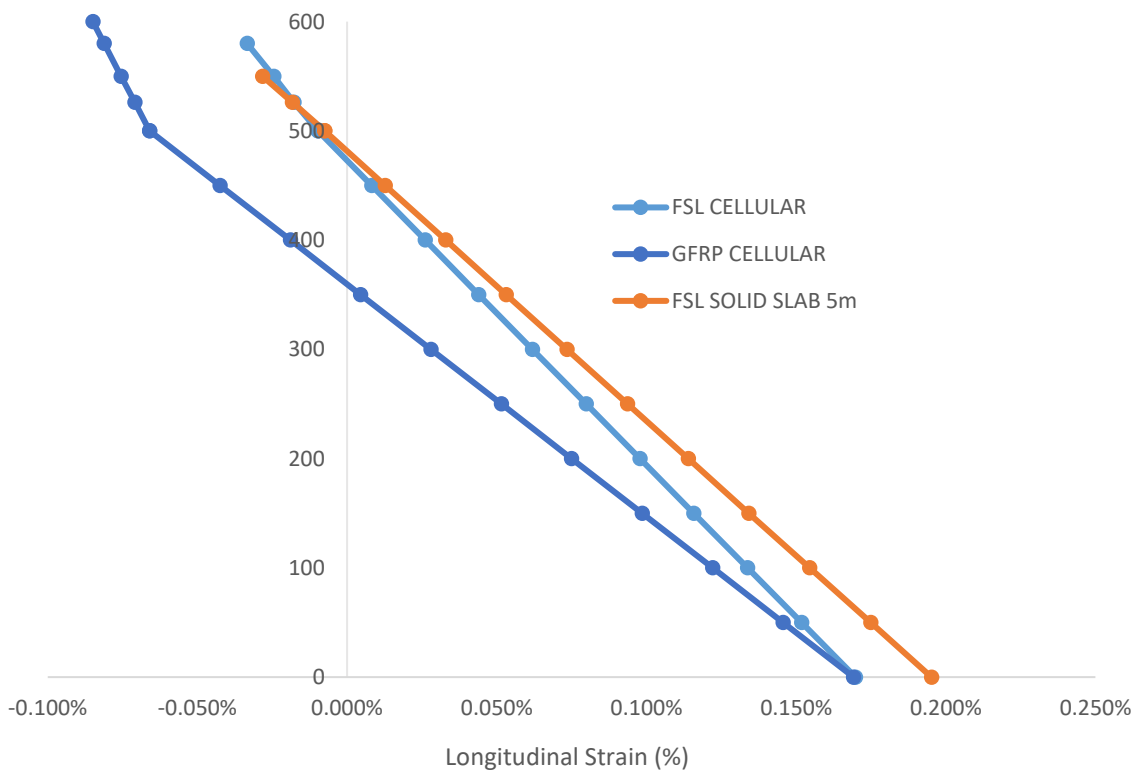


Figure 4.24: Vertical Distribution of Longitudinal Stress/Strain at Mid-Span Cross-Section

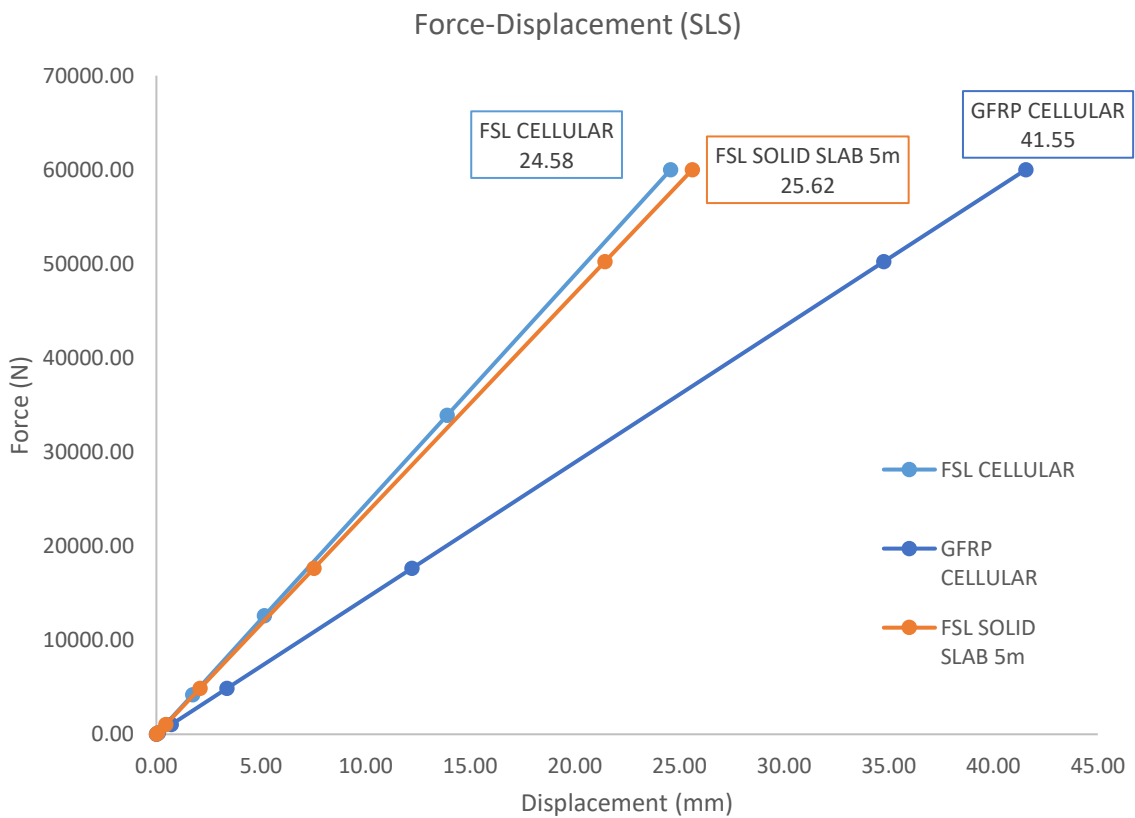
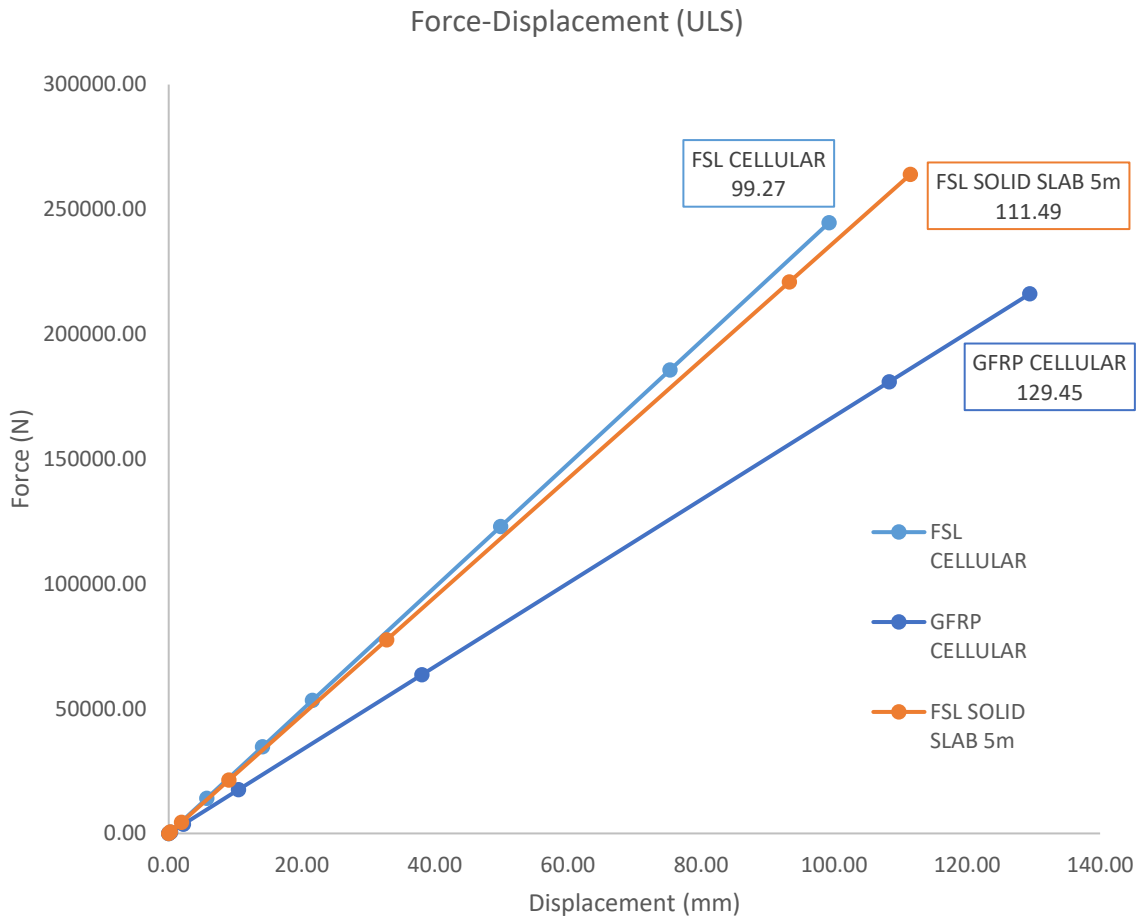


Figure 4.25: Force v Displacement Curves for ULS/SLS

4.3.4 Transverse Direction

The second area of the designs to look at is the bending between the beams in the transverse direction. This is important in FRP decks because the deck material is anisotropic and is often weaker and less stiff in its secondary direction, hence, many FRP decks are designed to have the primary axis of the fibres oriented in the transverse direction of the deck. Each of these designs also utilises this philosophy, as the 5m span between beams makes the transverse stresses induced in the deck greater than those from the longitudinal bending of the composite system.

Table 4.24: FE Output for Maximum Transverse Deflection of Each Deck at Mid-Span

FSL Cellular Deck	GFRP Cellular Deck	5m Solid Slab FSL Deck
1.38	5.97	2.40

Using [table 4.24](#), it is clear to see the less stiff GFRP deck is bending the most in between the beams when at the serviceability limit state. This causes the relatively high stresses that can be seen in the top skin of the deck above the beam, shown in [figure 4.29](#). The two FSL decks are bending less because of their high stiffness but are also sustaining a higher stress because of this. The difference in stress in the top skin of the two FSL decks is caused by the greater bending in the solid slab deck, whilst having a similarly high Young's modulus. The FSL cellular deck struggles to eclipse the tensile line of the graph due to the low amount of bending taking place.

In the bottom skin, the large discontinuity observed in each of the decks is due to the longitudinal redistribution of stresses in the deck and the sharing of stresses with the supporting girder ([figure 4.28](#)). It can be seen that this discontinuity occurs at the middle 200mm of the graph, coincident with the flange breadth of 200mm. In general, the solid slab FSL deck has a higher stress across the bottom skin than each of the other two decks, this is again due to the high stiffness of the deck compared to the GFRP deck and the increased bending compared to the FSL cellular deck.

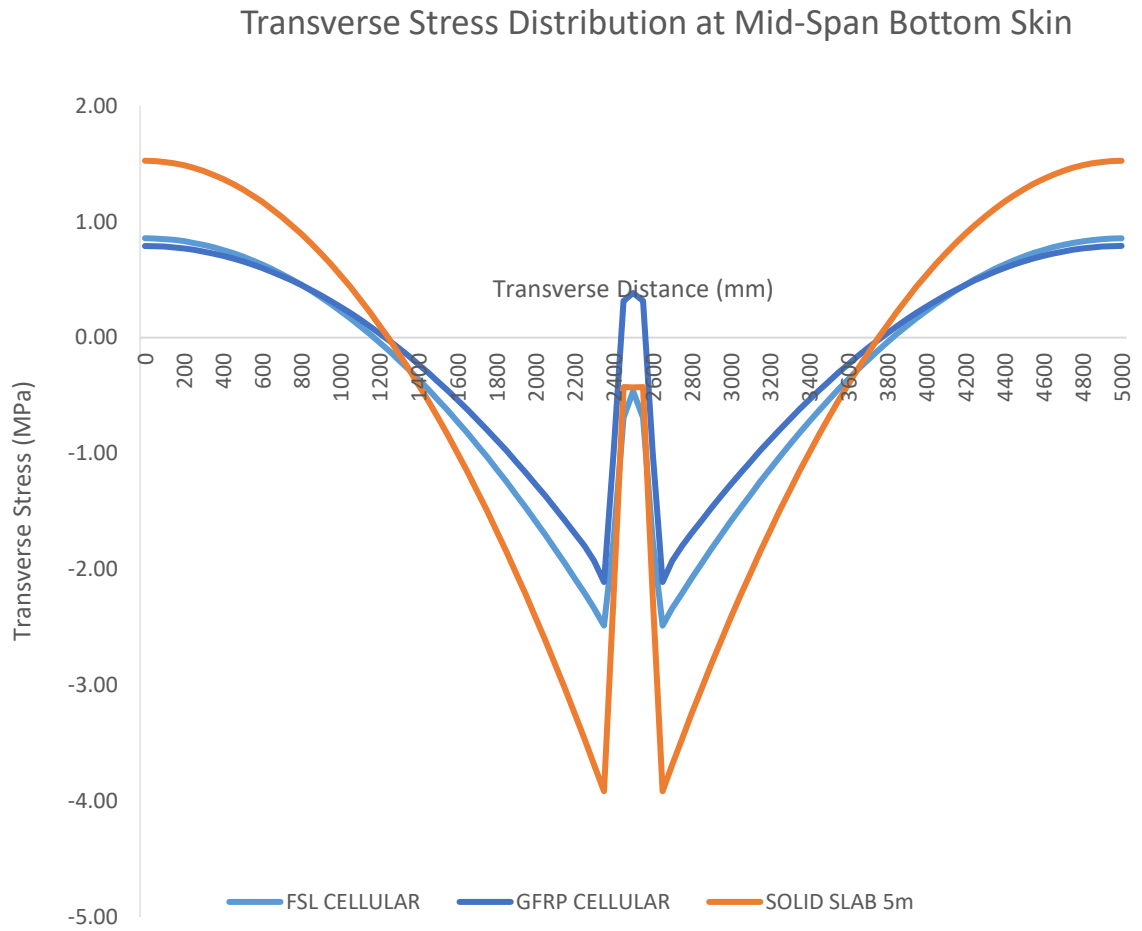


Figure 4.28: Transverse Stress Plotted Across Width of Bottom Skin of Deck Plotted at Mid-Span

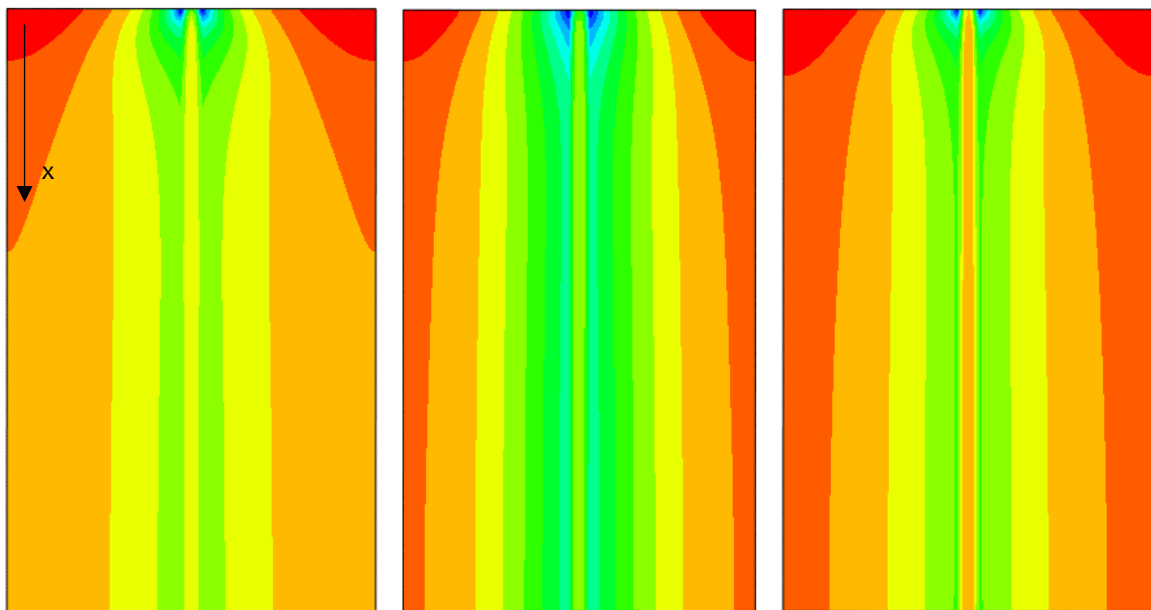


Figure 4.27: Transverse Stress Distribution Over Bottom Skin, from left to right: FSL Cellular, FSL Solid Slab, GFRP Cellular

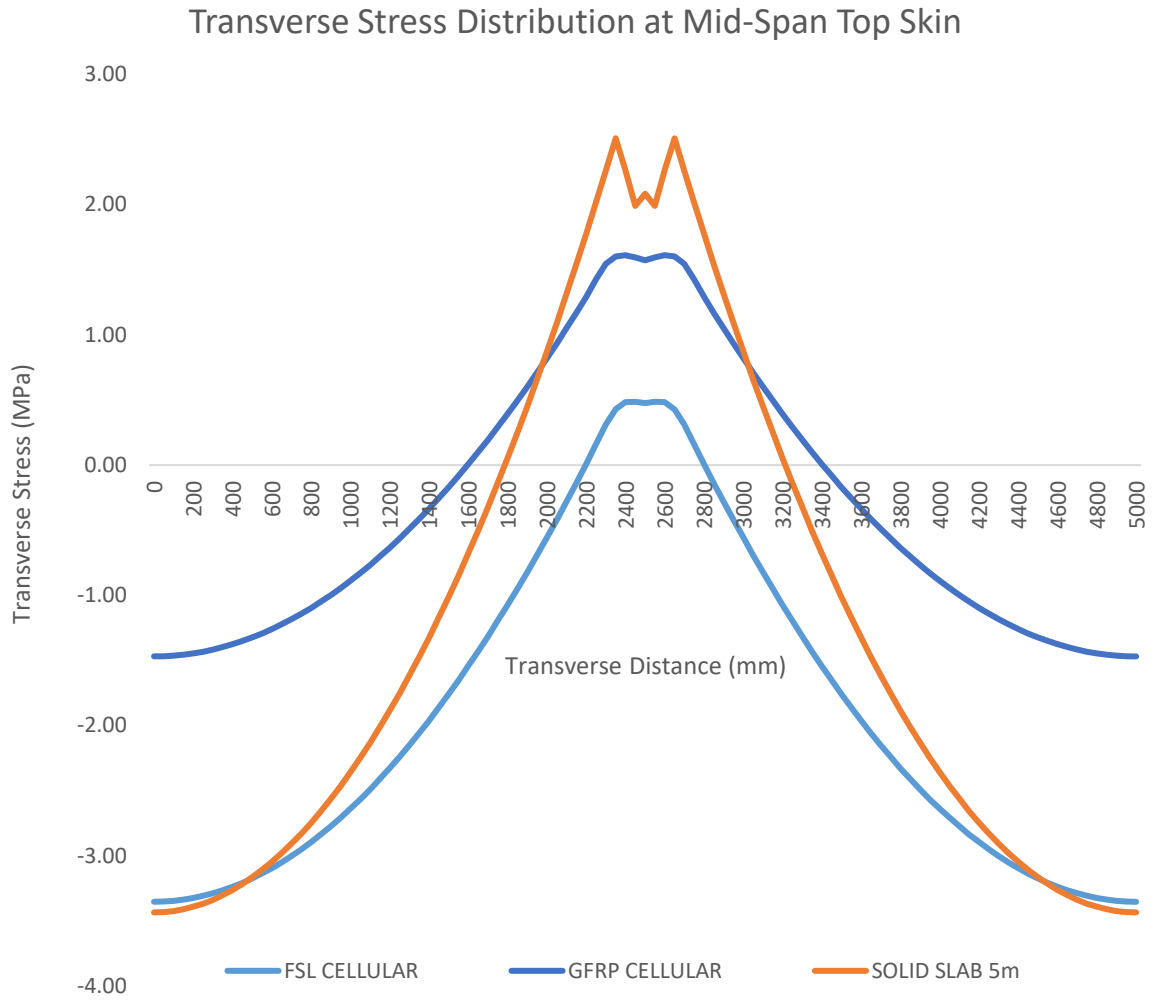


Figure 4.29: Transverse Stress Plotted Across Width of Top Skin of Deck Plotted at Mid-Span

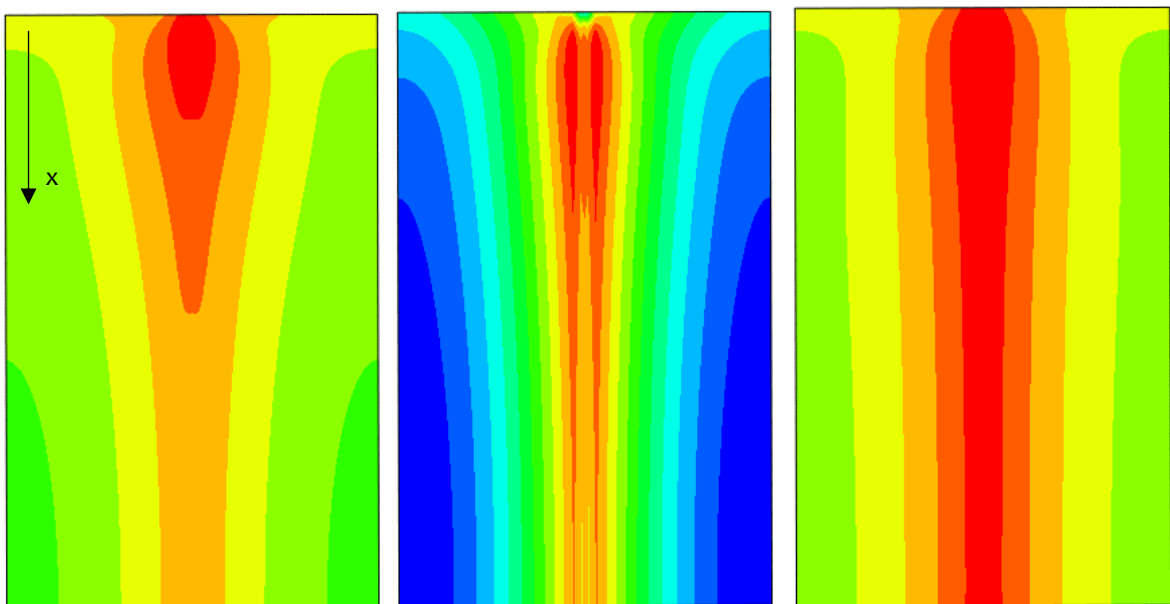


Figure 4.30: Transverse Stress Distribution Over Top Skin, from left to right: FSL Cellular, FSL Solid Slab, GFRP Cellular

4.3.5 Global Buckling Analysis

In order to gain a more accurate impression of the onset of instability in the system, a finite element buckling analysis has been employed. To perform the linear buckling analysis on the systems, the Linear Perturbation/Buckling analysis module in Abaqus CAE 6.14 was used. This allows a modal analysis of the first eigen modes of the system and the equivalent buckling factors (λ_i); the buckling factor that is output from the model is multiplied with the applied load to give the load required to cause that mode of buckling. Hence, a buckling factor less than one means that the applied load is sufficient to cause the onset of instability within the system.

$$\sigma_{buck,i} = \lambda_i * \sigma_{Applied}$$

Where:

$\sigma_{buck,i}$ – Load required to cause buckling mode i

λ_i – Buckling factor for mode i

$\sigma_{Applied}$ – Load applied

Table 4.25: Buckling Factor for First Eigenmode

	FSL Cellular Deck	GFRP Cellular Deck	5m Solid Slab FSL Deck
Buckling Factor Mode 1 (λ_1)	2.46	2.72	2.36

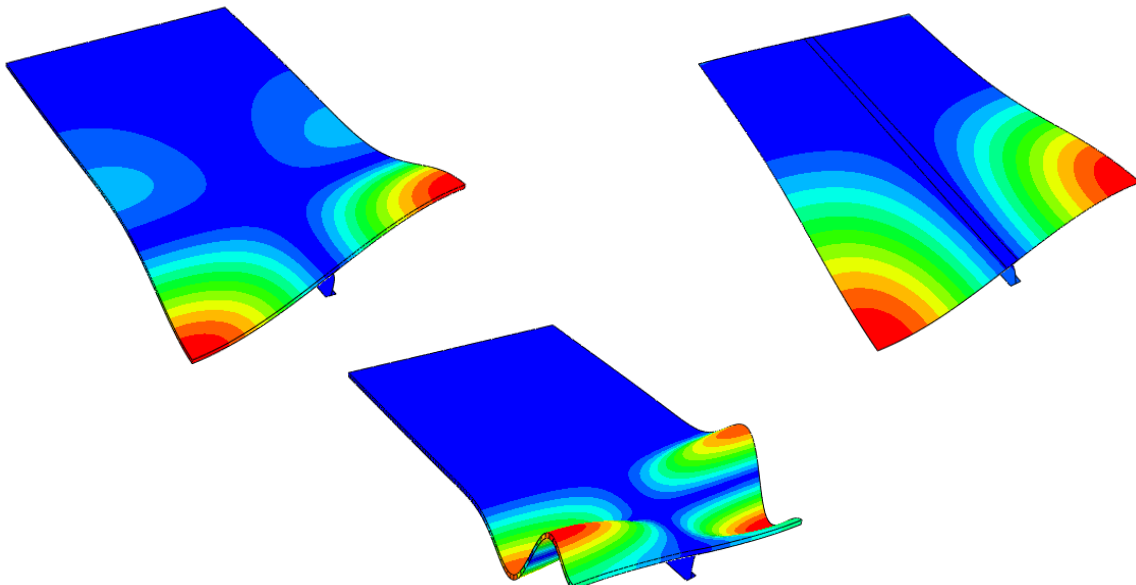


Figure 4.31: Buckling Modes Incorporating Deck Buckling, clockwise from left: FSL Cellular, FSL Solid Slab FSL, GFRP Cellular

The buckling analysis found the buckling factor for the first mode to be approximately 2.5 for each of the decks in this case study, resulting in a buckling utilisation ratio of 0.75-0.85. The lowest buckling factors are found in the FSL decks due to the lower depth of the decks, when compared to the GFRP deck. However, given that the buckling factor depends on the loading, it should also be noted that the factor alone does not signify the resistance to buckling. The resistance values ($\sigma_{buck,i}$), presented in [table 4.26](#), also take into account the difference in loading and the JRC instability safety factors.

Table 4.26: Design Global Buckling Resistance Comparison

	FSL Cellular Deck	GFRP Cellular Deck	5m Solid Slab FSL Deck
Design Global Buckling Resistance (MPa)	34	18	12

The first eigenmode in each of the decks causes the local buckling of the web of the beam at the support location – to be expected, and likely rectified in application with a stiffener at this location. By mode 3 the deck begins to buckle in each of the cases ([figure 4.31](#)).

The resulting values from the eigenvalue buckling analysis assume there are no imperfections or discontinuities resulting from manufacture or erection, this leads to values that can be overstated when compared to reality. For this reason, non-linear buckling analysis is recommended when searching for a more precise value, this is however not required for this study.

4.3.6 Inter-Laminar Shear Strength

Given that the experimental phase of this research will be used to determine the inter-laminar shear strength of the material, the finite element model can be used to examine the shear stresses through the thickness of the laminate when in application. It has been highlighted in previous studies (10) that this is the likely weak link of the material and may inhibit its further use in infrastructure.

Figure 4.32 shows the inter-laminar shear stress in the decks due to the ULS loading, where 1 and 2 are the in-plane directions of the deck (1 is transverse across the deck). As can be seen the magnitude of the stress varies depending on the orientation of the ply, it can also be seen that the distribution is not continuous. This is due to the shell elements used to model the deck, with only one element through the whole thickness of the deck, equilibrium cannot be enforced between plies. However, the general parabolic trend expected from shear stresses can be observed. To gain a more accurate insight into the applied interlaminar stress it is recommended that continuum shell elements are used, this is however more computationally expensive.

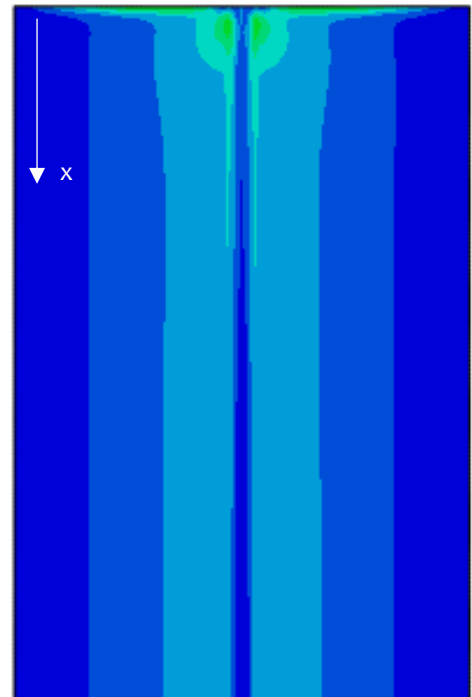
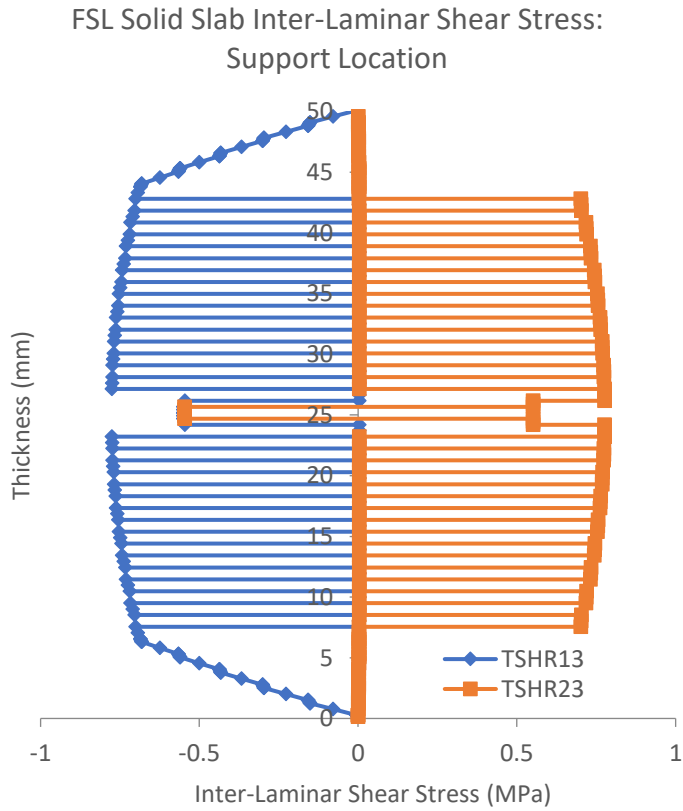
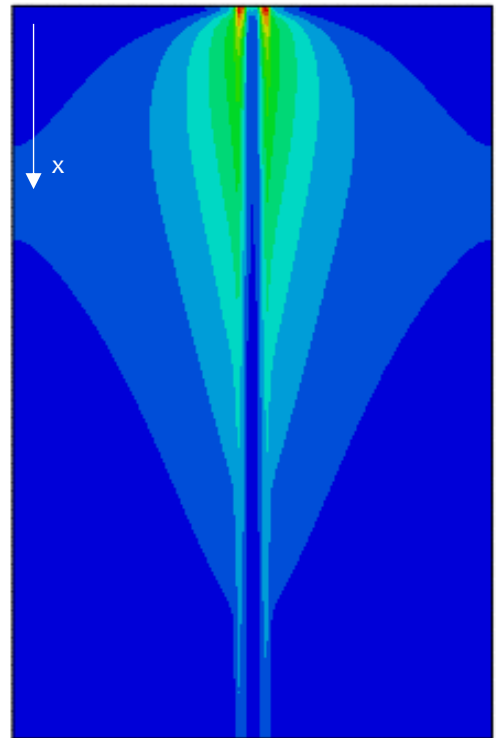
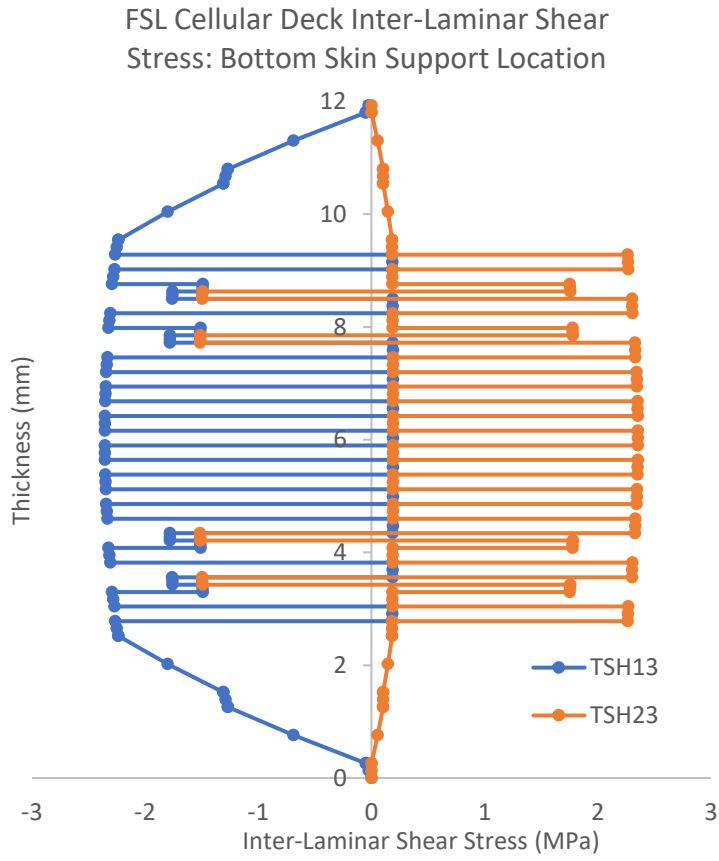


Figure 4.32: Inter-Laminar Shear Stress at Support Location

4.3.7 Cost Comparison

To evaluate the cost of the system, two factors come into consideration: material costs and labour costs. To take into account the different amounts of labour required for the manufacture of each deck a labour cost of €45/hour will be multiplied by an estimated number of hours calculated from industry data. The base labour time for a 16m GFRP bridge is set at 96 hours (2 people * 6 days * 8 hours/day). There will be a reduction of 20% of the time taken for the manufacture of GFRP cellular decks to arrive at the time taken for the manufacture of the FSL cellular deck. It is much easier to manufacture a solid slab type deck and so half of the labour time (for a GFRP cellular deck) will be required. The base rates used for cost calculations can be found in [Appendix D](#).

It should be noted that the labour cost does not include costs for engineering, administration and other related overheads, which could have further influence on the viability of the systems. This metric however provides a basic understanding of how the advantages of the less complex manufacturing can be exploited commercially.

[Figure 4.33](#) shows that due to the extra material used in the solid slab deck and subsequently larger beam section, the material cost is much greater (47%) than with the cellular deck, however the deck is less complex and costly to manufacture. Although, this doesn't reduce the total costs below that of the FSL cellular deck, they remain around 30% higher.

The GFRP deck proves to be the cheapest option based on this metric which is somewhat surprising given the dramatic increase in stiffness in the FSL decks. The reason that this doesn't lead to a cheaper deck is because of the span and support conditions of the deck. If the span of the deck were longer the serviceability criteria of the GFRP deck would be more critical and the deck would have to be thicker to compensate.

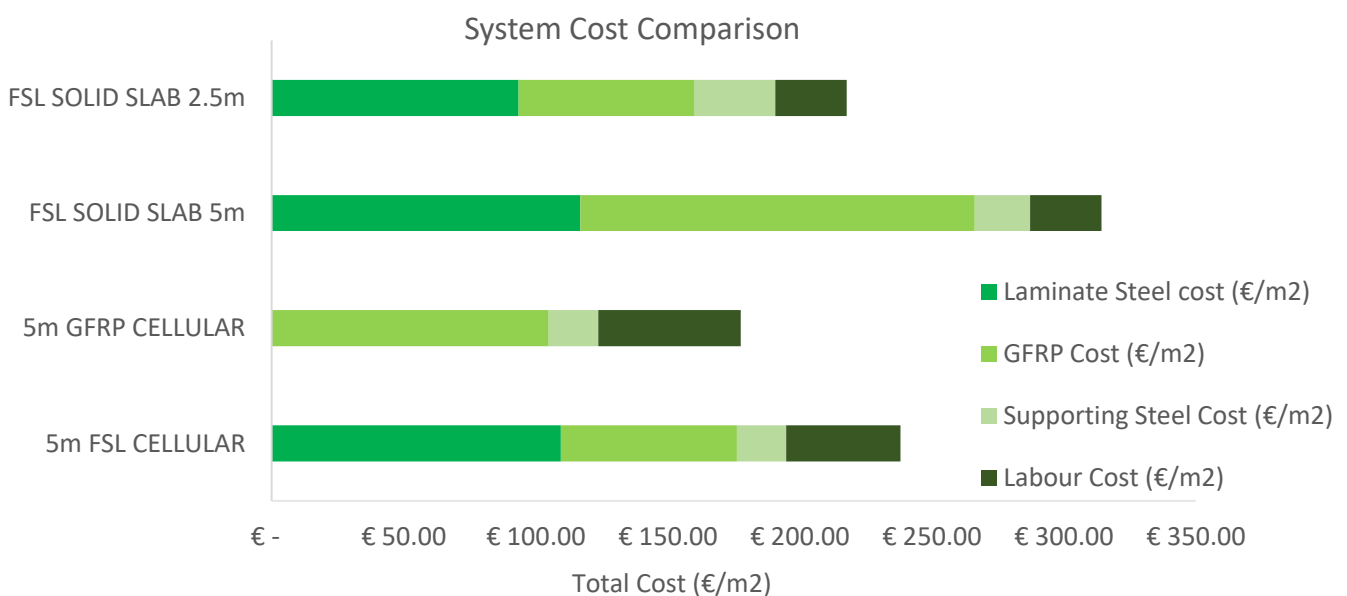


Figure 4.33: System Cost Comparison

Additionally, the combination with the steel beam means that the majority of the stiffness, that satisfies the serviceability criteria, comes from the beam rather than the deck. A rudimentary analysis of a 30m self-supporting deck made from cellular GFRP or FSL is given in [Appendix E](#).

To take into account the increased stiffness of the FSL decks and the difference in supporting girders, a new metric will be introduced, cost per composite stiffness unit. This will be obtained by dividing the total system cost by the longitudinal composite stiffness of the system. This is useful because it allows the inclusion of the different beam sections; for example, the FSL solid slab deck uses a bigger supporting girder and so this will cost more, however it will also provide the system with a greater stiffness.

By comparing the cost per longitudinal composite stiffness unit, in [figure 4.34](#), it can be seen that the three 5m decks all have a quite similar cost per composite stiffness unit despite the GFRP deck being much cheaper. This is because of the GFRP deck's low stiffness in comparison to the two FSL deck's. When using this metric, the FSL cellular deck is the superior of the three 5m decks, thanks to the geometric properties provided by the foam cores, enabling the use of less material whilst still providing a high stiffness.

The case of the 2.5m solid slab deck shows that the solid slab type section is uneconomical even at half the width. This again is due to the amount of material required to satisfy the design criteria.

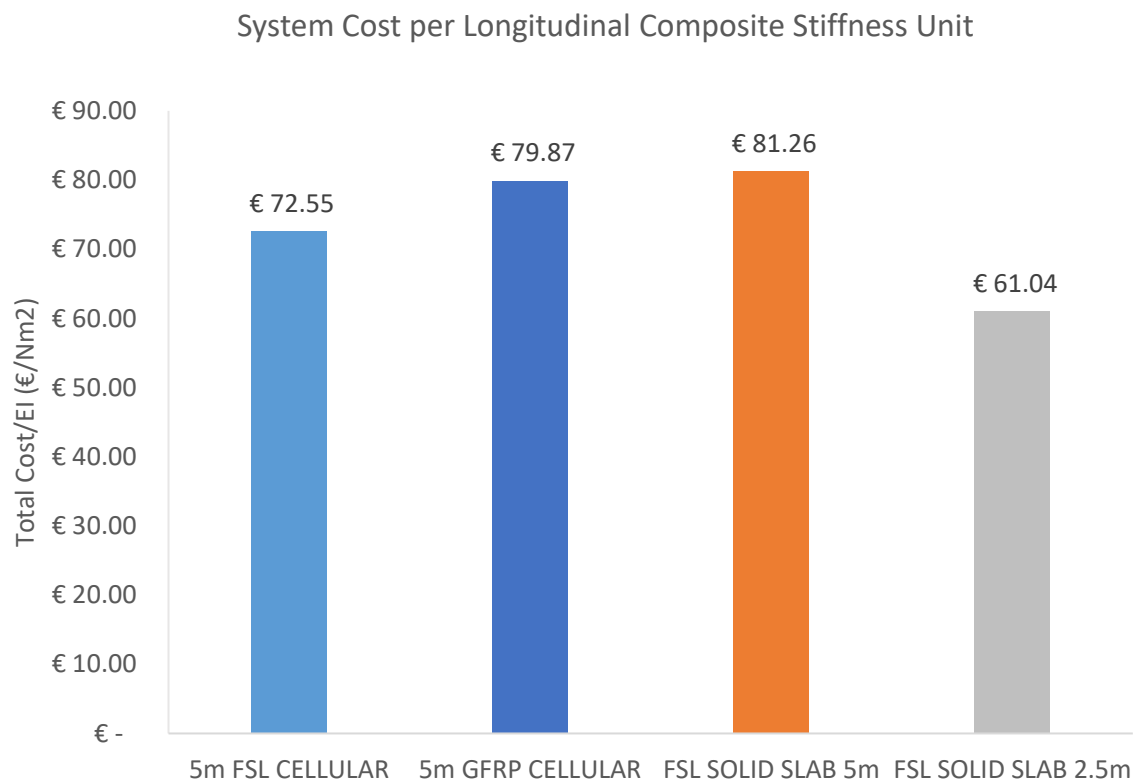


Figure 4.34: Cost per Longitudinal Composite Stiffness Unit Comparison

4.4 SUMMARY & DISCUSSION

Table 4.27: Comparison of System Details

System	Cross-Sectional Area of FSL/FRP material (m ²)	Construction Height (mm)	Deck Mass (kg/m ²)	$\frac{B_{eff}}{B}$ (SLS)	Longitudinal Composite Stiffness (kNm ²)	System Material Cost (€/m ²)	System Total Cost (€/m ²)	Total Cost per Composite Stiffness Unit (€/Nm ²)
FSL Cellular Deck & IPE500	0.438	592	109	0.88	262600	195	238	72.55
GFRP Cellular Deck & IPE500	0.454	612	55	0.88	178000	124	178	79.87
5m Solid Slab FSL Deck & IPE550	0.806	600	153	0.89	309400	288	315	81.26
2.5m Solid Slab FSL Deck & IPE450	0.416	476	96	0.97	142700	191	218	61.04

4.4.1 FSL Cellular Deck

The cross-section shape is the primary component that enables the cellular deck to achieve the same capacities as a solid section deck while using 45% less material. This increases the distance from the skins to the neutral axis of the deck, which provides the deck with an increased second moment of area. The foam cores that infill the cells are designed to be light-weight so as to not increase the mass of the deck by too much, whilst providing local stability to the webs and improving the stiffness of the load path in which forces are transmitted through from the bottom skin to the top. The magnitude of the transmission of forces can be increased by prescribing an even stiffer foam core, in this investigation the foams utilised have a Young's modulus of 6MPa, which for the purpose of force transmission is relatively low. The cellular type section including the foam cores allows less material to be used, resulting in a lighter deck with lower material costs when compared to a solid section deck.

The stiffening of the webs through the addition of steel plies at the extremes of the laminate, further increase the stiffness of the core of the deck and allow a much greater transmission of forces through the thickness. The case presented in [section 4.2.2.2](#) examines this closer and concludes that despite an increase in self-weight and complexity in the manufacturing process the additional stiffness provided to the load path is beneficial, as the two skins can be more effectively utilised.

In the FSL cellular deck the most critical criteria include the longitudinal failure of the facing (caused by the compressive stress in the deck) and the composite plastic moment verification – both ULS criteria that are governed by strength values. Whereas in the GFRP deck the critical criteria are governed by the stiffness of the material: the vibration and the beam stress verifications. Conclusively, the GFRP deck is designed with the stiffness as a limiting factor, whereas this is successfully negated in the FSL deck through the extra stiffness provided by the steel plies.

The onset of the yielding of the beam is likely to happen at around the same load level as the failure of the deck. The deck failure is likely to be a somewhat brittle failure mode and so the most appropriate design is to allow for the ductile yielding of the beam prior to the failure of the deck material.

Through the switch to the hybrid-composite material and stiffening of the core, the FSL cellular deck (compared to the GFRP cellular deck) offers a superior structural solution with regards to performance. A 47.5% greater composite stiffness, higher ULS utilisation and transmission of forces through the deck provide evidence to support this. These advantages allow for a more optimised deck which means less material is used to achieve the same structural performance.

One disadvantage of the cellular type deck is the complexity and time-consuming nature of the manufacturing process. The Z-shaped interlocking profile must be created by hand, requiring a greater number of labour hours, which compromises the low material cost of the deck when compared to the solid section decks.

4.4.2 Solid Slab FSL Deck

One of the key benefits of GFRP deck systems is their low self-weight, however, with the solid section FSL deck this advantage is compromised somewhat. When compared to the GFRP deck the FSL solid slab deck has a much greater mass (100kg/m^2 greater), due to the presence of the steel and the absence of the foam cores, meaning more material is required. Furthermore, due to this higher self-weight an increase in the supporting structure is required; IPE550 beam sections must be used, where in both of the cellular systems IPE500 beam sections are sufficient. However, the benefit of a heavy FSL slab compared to a similarly heavy conventional concrete slab is that it is very difficult to pre-camber a concrete deck. Whereas, in FRP/FSL decks produced through VARTM, pre-camber can be easily incorporated into the manufacturing process by cambering the mould for the injection. As a result of this the high self-weight of the deck becomes less of an issue with regards to SLS criteria but the increase in supporting structure can have knock-on effects throughout the entire structure – particularly in multi-storey constructions.

Compared to the GFRP deck the solid slab FSL deck also provides a superior structural solution when applied in a car parking facility. This is similarly evident from the higher transmission through the deck and 43% higher composite stiffness achieved (when using IPE500). Furthermore, even given the increase in sub-structure elements, the construction depth of the solid slab deck is still lower.

The solid slab decks, due to their high composite neutral axis generate a lot of stress in the bottom flange of the beam, meaning that the beam will yield long before the failure of the deck material. In comparison to the cellular FSL deck this is a much more structurally appropriate order of failure. The solid slab FSL deck would potentially benefit from being supported by an asymmetric beam, this would allow later on set of yielding, thus leading to a more optimised deck, however, a careful balance would need to be found that allows later yielding of the beam without allowing the deck to fail before-hand.

The simplicity of the manufacture of this type of deck makes it much quicker and therefore cheaper to produce than the cellular type decks with Z-shaped ply profiles. However, due to the cost of the extra amount of material required to provide the same performance as the other decks (a result of the solid cross-section), this benefit is redundant as the final cost of the system is greater than the other systems. Furthermore, the increased mass of the deck leads to elevated sub-structure and erection costs, which combined with the higher system cost, call the economic viability of this type of system into question.

The 2.5m FSL solid slab provides a case for the comparison of the effect of changing the breadth of the deck. It can be seen that the effective width and resulting composite stiffness is a function of the width of the deck – a much higher ratio of effective width can be achieved with a higher span/breadth ratio. However, the drawbacks of the type of cross-section remain across deck widths, more material is required to achieve sufficient properties to satisfy the design criteria; leading to a thin but heavy deck with high material costs.

4.4.3 Most Effective System

Ultimately both FSL systems are superior in performance to the GFRP system, resulting in systems with a higher composite stiffness and smaller construction depths. When comparing the two FSL systems, the cellular deck is the more effective system due to the greater performance achieved (higher ULS utilisation, 2.5% greater composite stiffness) whilst using 45% less material. The lower amount of material required is thanks to the cross-section shape that provides advantageous geometric properties to the deck by pushing the skins, that provide the stiffness to the deck, further away from its neutral axis. Furthermore, the lower amount of material used means lower material costs and a 60kg/m² lighter deck, when compared to the solid section deck. This means that a smaller set of supporting beams can be used, which also has cost benefits and lowers the total construction depth.

Finally, the main advantage of the cellular type deck with Z-shaped interlocking plies, is the prevention of crack propagation through the deck. In the solid section deck the interface between the fibres and steel is known to be of poor inter-laminar shear strength due to the difference in material Young's modulus causing stresses in the region. Moreover, this weak region is unrestricted – in that there is no discontinuity or fibre-bridging effect (as in the cellular deck) that can inhibit the propagation of a crack through the full length of breadth of the deck. However, under this level of mechanical loading the experimentally established inter-laminar shear strength was not exceeded in either of the cases.

From an economic point of view, it is hard to see how fibre-steel laminates could make an impact on the infrastructure market when utilised in this capacity, given the higher material cost and likely additional costs required to improve the steel-GFRP interface. The improved structural performance of the material doesn't allow for the structure to be optimised enough to make it cheaper than a GFRP equivalent. Therefore, it is unlikely that stakeholders would view the additional structural performance of the hybrid-composite as being worth the increased financial outlay.

5 THESIS SUMMARY & CONCLUSIONS

This research project begins with a review of current literature (**section 2**) that guides the reader through the progression of materials from fibre-reinforced polymers (FRP), to the inclusion of metal inter-plyes to make a hybrid-composite known as a fibre-metal laminate (FML), to the switch from aerospace-based materials and manufacturing to infrastructure-based methods creating a fibre-steel laminate (FSL). Important details regarding the design, improvement and testing of the steel-FRP interface are also given. Finally, a brief overview of composite deck systems is given in section 2.4.

In **section 3** the materials' properties are established through experimental and analytical means. Inter-laminar shear strength and the axial strength and stiffness of the individual components (GFRP and perforated-steel) are experimentally evaluated, whilst the axial, flexural and thermal behaviours of the fibre-steel laminate are evaluated analytically through classic laminate theory (CLT) and finite element analysis (FEA).

Section 4 uses the properties established in section 3 to design different FSL and GFRP composite deck-beam systems, which are compared on a laminate level for various performance indicators and are compared on a system level with regards to overall cost.

The research questions addressed in this study are as follows:

1. Based on the VARTM manufacturing technique what are the properties of a fibre-steel laminate?
 - Using basic interface improvements, what is the achievable inter-laminar shear strength of a fibre-steel laminate?
 - Will this strength inhibit the use of the material in commercial application?
2. Can fibre-steel laminates be effectively used in a composite system?
 - What is the most effective configuration of an FSL composite system, with regards to material and cost reduction?
 - Is it superior to the GFRP equivalent?

The first question is addressed in **section 2 & 3**, where the best manufacturing and cutting methods are researched before section 3 details the testing and results of the FSL material investigation. The second question is addressed through the use of a case - study of the composite deck system of a car parking facility, which is reported in **section 4**.

Section 5 will give an overview of the project before detailing the key outcomes of the research project.

5.1 FIBRE-STEEL LAMINATE MATERIAL INVESTIGATION

Fibre-steel laminates produced using VARTM should be cut with a band saw ahead of an abrasive waterjet device to avoid delamination and water ingress. However, limitations on specimen dimensions and shape must be accepted. Milling with a CNC machine allows for these limitations to be overcome.

Using the values experimentally established for the individual components, the bi-linear axial stress-strain relationship of the hybrid composite has been estimated following the rule of mixtures. Axial and flexural stiffness values have also been estimated using classic laminate theory (CLT) and validated with finite element analyses (FEA) showing good agreement between values.

The experimentally established inter-laminar shear strength (ILSS) of the FSL (13.4MPa) was approximately half of that found for pure-GFRP (24.5MPa), a ratio which is consistent with literature. This strength was exceeded by the differential thermal expansion of the two component materials, at a service temperature of 50°C, however, only at the edges of the sample. Experimental investigation is required to determine the effect this would have in closer proximity to the centre of the sample.

Using finite element analysis, the through-thickness distribution of the inter-laminar shear stresses was found, proving that the given formula for applied shear stress in the experimental standard (ASTM D2344 & NEN-ISO 14130) still applies to FSL materials with reasonable accuracy although it depends on the distribution of steel in the laminate.

5.2 COMPOSITE DECK CASE-STUDY

The cellular configuration was found to be the most effective way to utilise fibre-steel laminates in a hybrid system. When compared to the solid FSL deck 45% less material is used, leading to a 44% lighter and 24% cheaper system.

The change from GFRP to FSL brings an increase in longitudinal composite stiffness of at least 40%. This allows the serviceability driven design of GFRP to be overcome, and a reduction of at least 20mm in deck construction depth. The added stiffness provided by the supporting girder prevents further optimisation, which inhibits the possibility for FSL to provide a more economical solution than GFRP in a composite system. Thus, the GFRP system is 25% cheaper and 50% lighter than the FSL cellular deck and 44% cheaper and 64% lighter than the solid FSL deck. Conversely, based on the cost per stiffness unit metric, the cellular FSL deck is the superior option - being 9% cheaper than the next 5m system.

Over a 30m span of a self-supporting deck, an FSL deck uses 40% less material and costs 8% less than the GFRP equivalent, based on long term global deflection criteria.

At ultimate limit state the inter-laminar shear strength expected of the material will not be exceeded in either of the cases, nor the in-plane strengths of the material.

5.3 OUTLOOK & FUTURE STUDIES

The goal of this study was two-fold: to find the properties of the material and to find the most effective way to use the material in a composite system. The properties of the material were established or estimated through experimental and analytical means. These properties were used in the case-study of the car parking facility to find the economic viability of an FSL composite system in comparison to a GFRP system.

From the analyses conducted in this project it is evident that FSL can be used, in the right application, to optimise the stiffness of GFRP, enabling new spans or thinner decks. Furthermore, with increasing spans it becomes cheaper to use FSL ahead of GFRP. However, the material is not without its limitations, an increase in self-weight, lower strength and difficulties with interface quality must all be accounted for in design. To further enable the feasibility of this material, interface improvements are essential which may compromise any economic advantages achieved through the use of FSL ahead of GFRP.

Due to the infancy of this hybrid-composite and the surrounding research, it remains too early to provide a definitive case for the use of this material, however, some promising signs have been exhibited and can be exploited upon further research providing the inter-laminar shear strength obstacle can be overcome.

With regards to the use of FSLs in hybrid deck systems, the author recommends the following topics for future studies:

- Experimental investigation to supplement analysis and validate assumptions
 - Connection type
 - Bolted connection
 - Level of shear connectivity (pull-out tests)
 - Adhesive connection
 - Capacity with FSLs
 - Full scale testing of composite deck to determine effective properties and validate analytical approaches
- Asymmetric beam profiles to lower the composite neutral axis of the system
 - Care should be taken to ensure that the beam still yields prior to the failure of the deck to ensure ductile failure of the system

With regards to the further investigation of the material's properties, the author recommends the following research points for the next steps of the development of FSLs:

- Comparison of various steel-GFRP interface improvements and modifications to establish most applicable method for commercial production using VARTM
 - Mechanical and/or chemical improvements
 - Use of other material variations
 - Steel fibres
 - Stainless steel
 - Larger perforations
 - Different resin
- Further experimental investigations:
 - Failure modes and capacities of FSL
 - Axial
 - Flexural
 - Inter-laminar
 - Long term behaviour
 - Creep
 - Fatigue
 - Environmental behaviours
 - Corrosion
 - Temperature
- The use of high strength steel within the laminate instead of mild (S235) steel, enabling higher strength and possibly further optimisation on laminate and structural member levels.
- The suitability of an FSL member/deck under fire conditions with regards to:
 - Toxicity of smoke
 - Applicability of passive fire suppressants
 - Retardants
 - Coatings

REFERENCES

1. **Barbero, Ever.** *Introduction to Composite Materials Design*. Second. Boca Raton : Taylor & Francis, 2011.
2. *Deformation behaviour of steel/SRPP fibre metal laminate characterised by evolution of surface strains.* **Nam, J, et al.** 1, 2016, *Advances in Aircraft and Spacecraft Science*, Vol. 3, pp. 61-75.
3. *Advanced Fiber Reinforced Polymer Composites for Corrosion Mitigation in Water Infrastructure.* **Liang, Ray and Hota, GangaRao.** Washington DC : US NSF Industry/Univeristy Collaborative Research Centre - CICI, 2016. The 4th Biennial TRB-CMTS Conference: From Sail to Satellite: Delivering Solutions for Tomorrow's Marine Transportation Systems Conference, June 21-23, 2016, Washington, DC.
4. **Selcom Multiaxial Technology.** UNIE200 Technical Data Sheet. Fregona, Treviso, Italy : s.n., 2017.
5. **Vlot, Ad.** *Glare, history of the development of a new aircraft material.* Delft : TU Delft, 2001.
6. *The mechanical behaviour of GLARE laminates for aircraft structures.* **Wu, Guocai and Yang, J M.** January, 2005, *JOM*, pp. 72-79.
7. **Granta Design.** *CES Selector Material Database.* [Software] Cambridge : Granta Design, 2017.
8. **Aliiyncys.** Synolite 1967-G-9 Product Data Sheet. 2015.
9. **Cid Alfaro, Marcela.** *Multiscale Analyses of Fibre Metal Laminates.* Delft : TU Delft, 2008.
10. **ASM International.** *ASM Composites Handbook.* s.l. : ASM, 2001. Vol. 21.
11. **Vlot, Ad and Gunnink, Jan Willem.** *Fibre Metal Laminates: An Introduction.* Delft : Springer, 2001.
12. **Alderliesten, Rene.** *Fatigue Crack Propagation and Delamination Growth in Glare.* Delft : TU Delft, 2005.
13. **Marissen, Roelof.** *Fatigue Crack Growth in ARALL.* Delft : TU Delft, 1988.
14. *A Review on the Development and Properties of Continuous Fiber/epoxy/aluminium Hybrod Composites for Aircraft Structures.* **Botelho, Edson, et al.** 3, 2006, *Materials Research*, Vol. 9, pp. 247-256.
15. **Beumler, Thomas.** *A contribution to aircraft certification issues on strength properies in non-dmaged and fatigue damaged GLARE structures.* Delft : DUP Science, 2004.
16. **Rodi, Riccardo.** *The Residual Strength Failure Sequence in Fibre Metal Laminates.* Delft : TU Delft, 2012.

17. *Fatigue and damage tolerance issues of Glare in aircraft structures*. **Alderliesten, R C and Homan, J J.** 28, Delft : Elsevier, 2006, International Journal of Fatigue, pp. 1116-1123.
18. **Barrett-Gonzalez, R, et al.** Extending the fatigue life of steel bridges using fiber-reinforced polymer (FRP) composites. [book auth.] Vistasp Karbhari. *Rehabilitation of Metallic Infrastructure*. Kansas : Woodhead Publishing, 2014.
19. *A review: Fibre metal laminates, background, bonding types and applied test methods*. **Sinmazcelik, Tamer, et al.** 32, 2011, Materials and Design, pp. 3671-3685.
20. **Vassilopoulos, A.** *Fatigue Life Prediction of Composites and Composite Structures*. Oxford : Woodhead Publishing, 2010.
21. **Campbell, F C.** *Structural Composite Materials*. Ohio : ASM International, 2010.
22. *Low-velocity behaviour of fibre metal laminates*. **Tsartsaris, N, et al.** 7, s.l. : Sage, 2011, Journal of Composite Materials, Vol. 45, pp. 803-814.
23. *Creep phenomena in FRP materials*. **Ascione, Luigi, Berardi, Valentino and D'Aponte, Anna.** 43, s.l. : Elsevier, 2012, Mechanics Research Communications, pp. 15-21.
24. **Bagherpour, Salar.** *Fibre Reinforced Polyester Composites*. [book auth.] Hosam El-Din Saleh. Polyester. s.l. : InTech, 2012.
25. **Cusson, Renee and Xi, Yunping.** *The Behaviour of Fibre-Reinforced Polymer Reinforcement in Low Temperature Environmental Climates*. Boulder : Colorado Department of Transportation, 2002.
26. *Development of fibre laminates for advanced aerospace structures*. **Vogelingsang, L B and Vlot, A.** 103, 2000, Journal of Materials Processing Technology, pp. 1-5.
27. *Fibre-metal laminates recent developments and applications*. **Roebroeks, G H.J.J.** 1, Delft : Butterworth-Heinemann, 1994, Fatigue, Vol. 16.
28. **Langdon, G S and Rowe, L A.** *The response of steel-based fibre-metal laminates to localised blast loading*. Cape Town : University of Cape Town, 2004.
29. *Debonding and impact damage in stainless steel fibre metal laminates prior to metal fracture*. **Pärnänen, T, et al.** 119, Espoo : Elsevier, 2015, Composite Structures, pp. 777-786.
30. *Delamination in UD-CFRP steel hybrid laminates - part 1: method implementation and interface variation*. **Gall, M, et al.** Kaiserslautern : Institute of Composite Materials, 2016, Euro Hybrid Materials and Structures, Vol. April.

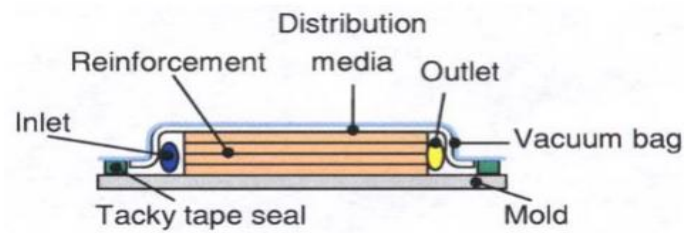
31. *Evaluation of surface modified CFRP-metal hybrid laminates.* **Monden, A, et al.** Stade : Private University of Applied Sciences, Stade, 2014. Euro Hybrid Materials and Structures.
32. *Investigations of bonding approaches and initial bond strength for the intrinsic manufacturing of laminary bonded hybrids made of thermoplastic composite and metal.* **Hopmann, Ch, Bottcher, A and Fischer, K.** 6, Munchen : Carl Hanser Verlag, 2013, Journal of Plastics Technology, Vol. 9.
33. *An innovative approach for joining hybrid CFRP-metal parts by mechanical undercuts.* **Droder, K, et al.** Stade, Germany : Private University of Applied Sciences, 2014. Euro Hybrid Materials and Structures 2014.
34. *Enhancing the tensile strength in hybrid metal-FRP materials through various interlocking structural patterns.* **Brand, Michael, et al.** Kaiserslautern : Institute of Composite Materials, 2016. Vol. April.
35. *Numerical and experimental analyses on the influence of array patterns in hybrid metal-FRP materials interlocked by mechanical undercuts.* **Droder, K, Brand, M and Kuhn, M.** Ischia : Elsevier, 2017. 10th CIRP Conference on Intelligent Computation in Manufacturing Engineering - CIRP ICME '16. pp. 51-55.
36. *Increasing the mechanical properties of metal-plastic-hybrids by improvement of the interface - a microscopic approach.* **Muller, S, et al.** Kaiserslautern : Institute of Composite Materials, 2016. Euro Hybrid Materials and Structures. pp. 185-188.
37. *Cold metal transfer joining aluminium alloys to galvanised mild steel.* **Cao, R, et al.** 10, s.l. : Elsevier, 2013, Journal of Materials Processing Technology, Vol. 213, pp. 1753-1763.
38. *Experimental investigation of a novel hybrid metal-composite joining technology.* **Ucsnik, S, et al.** A, s.l. : Elsevier, 2010, Composites, Vol. 41, pp. 369-374.
39. **Cambridge Vacuum Engineering.** Surfi-Sculpt™: Precision Controlled Surface Shaping. Cambridge Vacuum Engineering. [Online] 2017. http://www.camvaceng.com/assets/uploads/documents/Surfi-Sculpt_UK_05.pdf.
40. **Smith, Faye.** Comeld - An innovation in composite to metal joining. s.l. : TWI Global, 2004.
41. *Improving the adhesion of thin stainless steel sheets for fibre metal laminate applications.* **van Rooijen, R G.J, Sinke, J and van der Zwaag, S.** 16, s.l. : Taylor & Francis, 2012, Journal of Adhesion Science and Technology, Vol. 19, pp. 1387-1396.
42. **Dymáček, Petr.** Fibre-Metal Laminates Steel-C/Epoxy. Brno University of Technology. Brno : s.n., 2001.
43. **Naeem, M.** Laser machining fiber-reinforced composites. s.l. : Industrial Laser Solutions, 2011.

44. *Investigation on interlaminar shear strength properties of disc laser machined consolidated CF-PPS laminates.* **Jaeschke, P, et al.** 3, s.l. : Budapesti Műszaki és Gazdaságtudományi Egyetem. Polimertechnika Tanszék, 2011, Express Polymer Letters, Vol. 5, pp. 238-245.
45. *Process chains for fibre-metal laminates.* **Neugebauer, R, Krausel, V and Graf, A.** s.l. : Trans Tech Publications, 2014, Advanced Material Research, Vol. 1018, pp. 285-292.
46. *A study of delamination on graphite/epoxy composites in abrasive waterjet machining.* **Shanmugam, D K, Nguyen, T and Wang, J.** 39, Sydney : Elsevier, 2008, Composites, Vol. Part A, pp. 923-929.
47. *Prefabricated Demountable Concrete and FRP Decks in Composite Structures.* **Pavlovic, Marko and Veljkovic, Milan.** Copenhagen : s.n., 2017. EUROSTEEL 2017.
48. **European Commission.** *Prospect for New Guidance in the Design of FRP.* s.l. : JRC, 2016.
49. **The Steel Construction Institute (SCI).** *SCI P185 Guidance Notes on Best Practice in Steel Bridge Construction.* s.l. : SCI, 2015.
50. **European Committee for Standardisation.** *EN 1991-1-1: Actions on Structures.* 2002. EN 1991-1-1:2002.
51. —. *Basis of Structural Design.* s.l. : European Commission for Standardisation, 2002. EN1990:2002.
52. **The Netherlands Standardisation Institute.** *Parkeren en stallen van personenauto's op terreinen en in garages.* s.l. : NEN, 2013. NEN 2443.
53. **Gurtler, Herbert W.** *Composite Action of FRP Bridge Decks Adhesively Bonded to Steel Main Girders.* Lausanne : University of Lausanne, 2004.
54. **European Committee for Standardisation.** *EN 1994-1-1: Design of Steel and Concrete Composite Structures.* 2004.
55. *Manufacturing Principles for Fibre Metal Laminates.* **Sinke, J.** London : IOM, 2009. ICCM-17. pp. 1-10.
56. **Peeters, Jan.** *Fibre Reinforced Polymer Composites: Lecture 3 - Design for Robustness.* Delft : Infracore, 2016.
57. *Numerical Simulation of Mechanical Fracture Testings.* **Medeiros, E E, da Silva Dias, A M and Christoforo, A L.** 5, s.l. : Scientific & Academic Publishing, 2012, International Journal of Materials Engineering, Vol. 2, pp. 61-66.
58. *Kerf taper and delamination damage minimization of FRP hybrid composites under abrasive water-jet machining.* **Wong, I MM, et al.** London : Springer-Verlag, 2016, International Journal of Advanced Manufacturing Technology.

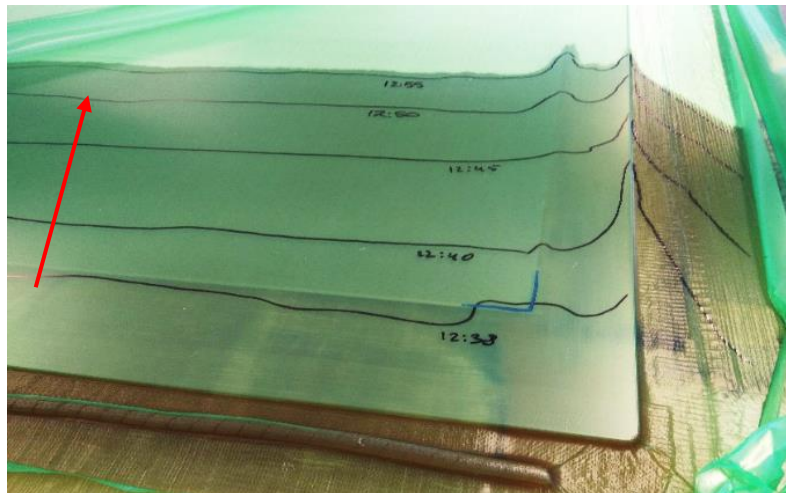
59. **ESDEP**. Lecture 10.1: Composite Construction - General. *ESDEP Course*. [Online] 2017. <http://fgg-web.fgg.uni-lj.si/~pmoze/esdep/master/wg10/l0100.htm>.
60. **REIDsteel**. Composite Bridges. *REIDsteel*. [Online] 2017. <http://www.steel-bridges.com/composite-beam-bridge.html>.
61. **Pavlovic, Marko**. *Sandwich Panels and FRP Decks*. [Lecture Slides] Delft : TU Delft CiTG, 2017.
62. *Effective Flange Width for Composite Steel Beams*. **Salama, T and Nassif, H H.** 1, 2011, *The Journal of Engineering Research*, Vol. 8, pp. 28-43.

APPENDIX A: PRODUCTION & CUTTING OF FSL

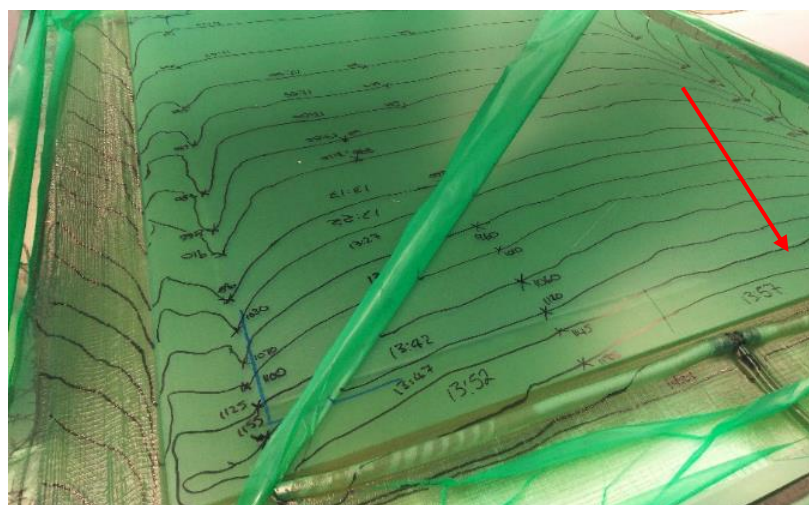
GFRP and FSL samples were produced through the vacuum assisted resin transfer moulding (VARTM) technique, the process of which is depicted below. The VARTM process involves the use of a vacuum to pull resin through the dry material (fibres and steel in the case of FSL) which is set in a mould that will yield the required shape. For the purpose of this investigation the required shape is a rectangular plate, so a flat mould was used.



Resin Flow
Direction



Resin Flow
Direction



(top) VARTM Mould Schematic, (bottom) Various Stages of Injection

Component Materials

Perforated Steel

The steel to be used within the fibre-steel laminate is grade S235 perforated mild steel. The perforations to the steel have been specified to increase vertical resin flow through the thickness of the laminate. A further hypothesised advantage of the perforations within the steel is to allow the formation of small resin structures that will cause an interlocking effect between plies, such structures are formed as the resin flows through the perforations, shown in [figure A.2](#). The effectiveness of these structures will not be tested; however, their presence should be noted as it indicates through-thickness resin flow.

With the intention of only providing the most basic treatments to the steel in order to determine the minimum inter-laminar shear strength, the surface treatment of the steel was restricted to abrasion with hand-held, multi-purpose tools and degreasing with acetone. An investigation into the most effective abrasion medium to be used with the hand-held, rotatory tool was performed.

Following this investigation, the 1m * 1m perforated steel plates were treated in acetone before and after abrasion with grade-40 sandpaper. The effect this had on the surface area of the steel can be seen in [figure A.3](#).



Figure A.o.1: Resin Micro-Structures Forming Through the Perforations in the Steel

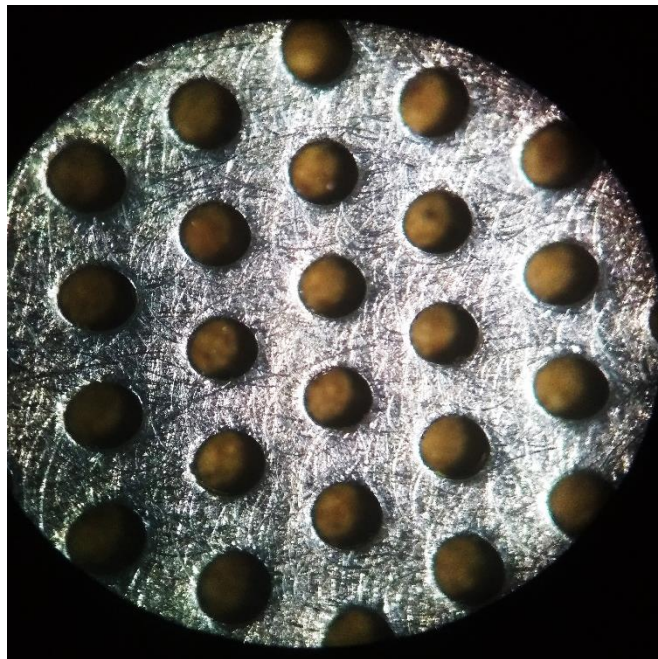


Figure A.o.2: Magnified Image of Treated Steel

Glass Fibre-Reinforced Polymer

The FRP component of the fibre-steel laminate will be comprised of E-Glass fibres with an areal density of 300g/m^2 , this will yield a lower ply thickness and ultimately laminate than with a denser set of fibres. The fibres (and steel plies) are combined with a polyester resin in the vacuum mould. The resin must be mixed with a solidifying reagent and de-gassed prior to injection, to minimise air voids and improper impregnation of the plies. Close-up images of the fibres can be seen in [figure A.4](#). No further treatment of the fibres was undertaken once cut and placed into the injection mould.

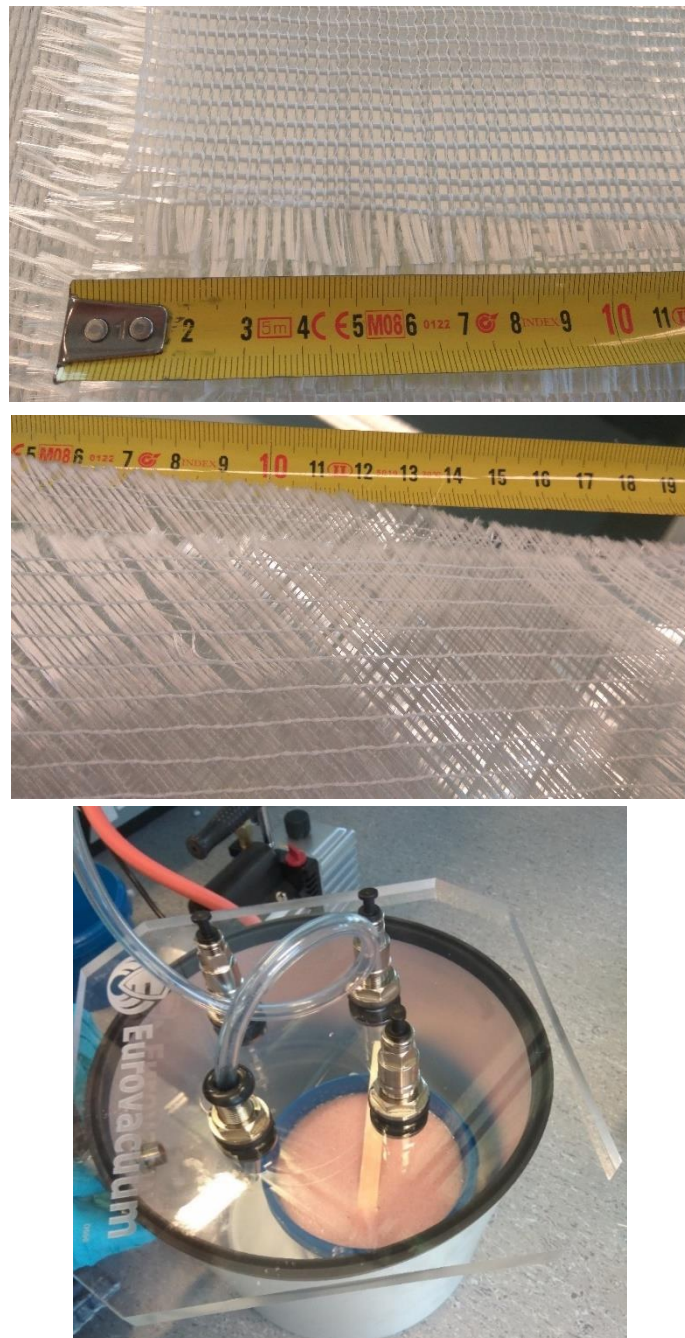


Figure A.o.3: (top) Dry E-Glass Fibres, (bottom) De-gassing of Resin

CUTTING

After the production of the FSL panel, the final thing to do prior to testing was to cut the panel into test specimens. Issues arise with the cutting of the hybrid-composite because of the difference in the two materials. There are mechanical saws that can cut steel and saws that can cut through GFRP, but the combination of the two materials causes difficulties with some conventional techniques. The first place to start was with the technique used most commonly to cut GFRP, an abrasive waterjet cutter.

Initial attempts to cut the material with the abrasive water-jet cutter were not successful. Local delaminations were induced in the material and were seen to propagate to the surrounding area. The initial delamination is due to the difference in material properties between the steel and GFRP plies; the waterjet experiences much greater resistance when cutting through the steel than the FRP, leading to delamination between plies as the water disperses on contact with the steel, [figure A.6](#). A secondary drawback of this is that water is introduced into the material, which could propagate and cause further delamination and corrosion of the steel, evidence of this was noticed a number of weeks after cutting, see [figure A.7](#).

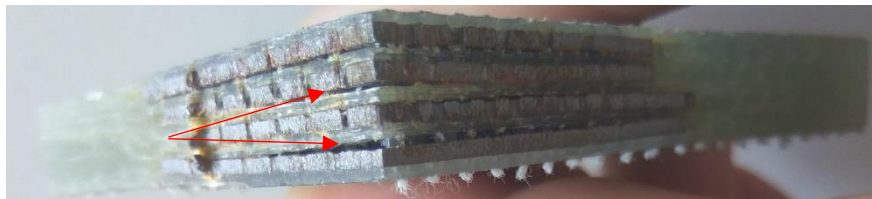


Figure A.0.4: Delamination Caused by Abrasive Water-jet Cutter



Figure A.0.5: Non-localised Corrosion of Steel due to Water Ingress from Cutting Attempt

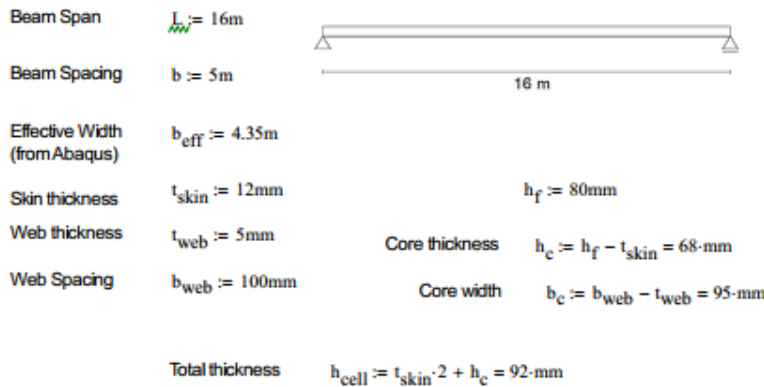


Figure A.0.6: Material Damaged by Inappropriate Saw

Further investigations were performed into the suitability of various rotary, bladed tools and saws, with the most success being found with a band-saw. Pieces of wood were used to slow the introduction of the blade into the material; introducing the blade too quickly or using an excessive rotary speed may lead to serious delaminations as shown in [figure A.8](#). However, due to a change in direction of the experimental phase only the inter-laminar shear test samples were required, which are much smaller – significantly reducing the restrictions on machine selection. The author recommends trial cuts to be made, prior to the cutting of desired samples in any future investigations, due to the uncertainty surrounding the quality of manufacture and suitability of the various cutting techniques given that none of them are designed to cut such a material.

FSL CELLULAR

General Details & Geometry



$$A_{\text{sp}} := (h_{\text{cell}} \cdot b_{\text{eff}}) - h_c \cdot b_{\text{eff}} = 1.044 \times 10^5 \cdot \text{mm}^2 \quad \text{Cross-sectional area per beff (FSL only)}$$

$$A_{\Sigma\text{FSL, longi}} := (h_{\text{cell}} \cdot b) - h_c \cdot b = 0.12 \text{ m}^2$$

$$A_{\Sigma\text{FSL, trans}} := (h_{\text{cell}} \cdot L) - h_c \cdot b_c \left(\frac{L}{b_{\text{web}}} \right) = 0.438 \text{ m}^2$$

$$I_{\text{sp}} := \frac{(h_{\text{cell}}^3) \cdot b_{\text{eff}}}{12} - \frac{b_{\text{eff}} \cdot h_c^3}{12} = 1.683 \times 10^8 \cdot \text{mm}^4 \quad \text{Second moment of area per beff (FSL only)}$$

	Area (mm ²)	z (mm)	I _c (mm ⁴)	d (mm)	I _x (mm ⁴)
Btm Skin	52200	6	626400	40	84146400
Top Skin	52200	86	626400	40	84146400
Webs	3740	46	1441146.7	0	1441147
					1.7E+08

$$I_x = I_c + A \cdot d^2$$

$$M_{\text{Deck}} := b \cdot \left[(2 \cdot t_{\text{skin}} \cdot L) \cdot \rho_{\text{FSL}} + \left(\frac{L}{b_{\text{web}}} + 1 \right) \cdot h_c \cdot t_{\text{web}} \cdot \rho_{\text{FSL, WEB}} + \rho_{\text{foam}} \left(\frac{L}{b_{\text{web}}} \right) \cdot h_c \cdot b_c \right] = 8.754 \times 10^3 \text{ kg}$$

$$\frac{M_{\text{Deck}}}{L \cdot b} = 109.428 \frac{\text{kg}}{\text{m}^2}$$

$$F_{\text{GFRP,1}} := 29.3\text{GPa} \cdot 0.012 \cdot 8\text{mm} = 2.813 \times 10^6 \frac{\text{N}}{\text{m}}$$

$$F_{\text{GFRP,2}} := 6.5\text{GPa} \cdot 0.012 \cdot 8\text{mm} = 6.24 \times 10^5 \frac{\text{N}}{\text{m}}$$

$$F_{\text{GFRP,S}} := 3.8\text{GPa} \cdot 0.016 \cdot 8\text{mm} = 4.864 \times 10^5 \frac{\text{N}}{\text{m}}$$

$$F_{\text{Steel,1}} := 180\text{MPa} \cdot 4\text{mm} = 7.2 \times 10^5 \frac{\text{N}}{\text{m}}$$

$$\sigma_{1\text{tRk}} := \frac{F_{\text{Steel,1}} + F_{\text{GFRP,1}}}{t_{\text{skin}}} = 294.4 \text{ MPa}$$

$$\sigma_{2\text{tRk}} := \frac{F_{\text{Steel,1}} + F_{\text{GFRP,2}}}{t_{\text{skin}}} = 112 \text{ MPa}$$

$$f_{\text{f,t,Rd}} := \eta_{\text{c,s,L}} \cdot \frac{\sigma_{1\text{tRk}}}{\gamma_{\text{M,s}}} = 90.281 \text{ MPa}$$

$$f_{\text{f,t,Rd2}} := \eta_{\text{c,s,T}} \cdot \frac{\sigma_{2\text{tRk}}}{\gamma_{\text{M,s}}} = 28.59 \text{ MPa}$$

$$f_{\text{f,c,Rd}} := \eta_{\text{c,s,L}} \cdot \frac{\sigma_{1\text{tRk}}}{\gamma_{\text{M,s}}} = 90.281 \text{ MPa}$$

$$f_{\text{f,c,Rd2}} := \eta_{\text{c,s,T}} \cdot \frac{\sigma_{2\text{tRk}}}{\gamma_{\text{M,s}}} = 28.59 \text{ MPa}$$

$$\tau_{12\text{R}} := \frac{F_{\text{Steel,1}} + F_{\text{GFRP,S}}}{t_{\text{skin}}} = 100.533 \text{ MPa}$$

Fibre-Steel Laminate

$$\begin{aligned}
 E_{xx} &:= 146.07 \text{ GPa} & E_{yy} &:= 140.80 \text{ GPa} & G_{xy} &:= 35.39 \text{ GPa} & \nu_{12} &:= 0.28 & G_{xy,web} &:= 26.4 \text{ GPa} \\
 E_{Lc.ax} &:= 88.13 \text{ GPa} & E_{Tc.ax} &:= 85.62 \text{ GPa} & \tau_{ILSS} &:= 20 \text{ MPa} & \nu_{LT} &:= \nu_{12} \\
 E_{Lc} &:= E_{xx} & E_{Tc} &:= E_{yy} & G_{LT} &:= G_{xy} & \nu_{TL} &:= \nu_{LT} \frac{E_{Tc}}{E_{Lc}} = 0.27 \\
 \rho_{FSL} &:= 3860 \frac{\text{kg}}{\text{m}^3} & \rho_{FSL,WEB} &:= 4246 \frac{\text{kg}}{\text{m}^3} & \rho_{foam} &:= 35 \frac{\text{kg}}{\text{m}^3} & E_{core} &:= 6 \text{ MPa} & \nu_{core} &:= 0.1 & G_{core} &:= \frac{E_{core}}{2 + 2 \cdot \nu_{core}} = 2.727 \text{ MPa}
 \end{aligned}$$

Stiffness Constants

$$\begin{aligned}
 D_{11} &:= E_{Lc} \cdot \frac{t_{web}^3}{12 \cdot (1 - \nu_{LT} \cdot \nu_{TL})} = 1.646 \times 10^3 \cdot \text{N} \cdot \text{m} & D_{22} &:= E_{Tc} \cdot \frac{t_{web}^3}{12 \cdot (1 - \nu_{LT} \cdot \nu_{TL})} = 1.587 \times 10^3 \cdot \text{N} \cdot \text{m} \\
 D_{12} &:= \nu_{LT} \cdot D_{22} = 444.238 \cdot \text{N} \cdot \text{m} & D_{66} &:= G_{LT} \cdot \frac{t_{web}^3}{12} = 368.646 \cdot \text{N} \cdot \text{m} \\
 D_{11y} &:= D_{22} = 1.587 \times 10^3 \cdot \text{N} \cdot \text{m} & D_{12y} &:= D_{12} \cdot \frac{D_{11}}{D_{22}} = 460.866 \cdot \text{N} \cdot \text{m} \\
 D_{22y} &:= D_{11} = 1.646 \times 10^3 \cdot \text{N} \cdot \text{m} & D_{66y} &:= D_{66} = 368.646 \cdot \text{N} \cdot \text{m}
 \end{aligned}$$

Loading:

$$\begin{aligned}
 SW_{Deck} &:= \left(M_{Deck} \cdot \frac{9.81 \text{ m}}{1 \text{ s}^2} \right) = 85.879 \cdot \text{kN} & q_{finishing} &:= 0.5 \frac{\text{kN}}{\text{m}^2} \\
 SW_{Beam} &:= A_a \cdot \gamma_a \cdot L = 14.417 \cdot \text{kN} & g_{SW} &:= \frac{(SW_{Deck} + SW_{Beam})}{L} = 6.268 \frac{\text{kN}}{\text{m}} \\
 SW_{Finishing} &:= b \cdot q_{finishing} = 2.5 \frac{\text{kN}}{\text{m}} & g_2 &:= SW_{Finishing} = 2.5 \frac{\text{kN}}{\text{m}} \\
 q_{Carpark} &:= 2.5 \frac{\text{kN}}{\text{m}^2} & q &:= b \cdot q_{Carpark} = 12.5 \frac{\text{kN}}{\text{m}}
 \end{aligned}$$

$$Q_k := 10 \text{ kN} \quad a_{Qk} := 100 \text{ mm} \quad \varphi_2 := 0.6$$

$$q_{SLS} := \varphi_2 \cdot \frac{q}{b} = 1.5 \frac{\text{kN}}{\text{m}^2}$$

$$q_{ULS} := 1.35 \cdot \frac{(g_{SW} + g_2)}{b} + 1.5 \cdot q_{Carpark} = 6.117 \frac{\text{kN}}{\text{m}^2}$$

Section Forces:

$$M_{a,Ed} := 1.35 \cdot g_{SW} \cdot \frac{L^2}{8} = 270.798 \cdot \text{kN} \cdot \text{m}$$

$$M_{Ed} := M_{a,Ed} + (1.35 \cdot g_2 + 1.5 \cdot q) \cdot \frac{L^2}{8} = 978.798 \cdot \text{kN} \cdot \text{m}$$

$$V_{Ed} := [1.35 \cdot (g_{SW} + g_2) + 1.5 \cdot q] \cdot \frac{L}{2} = 244.7 \cdot \text{kN}$$

Composite Properties

$$n := \frac{E_{yy}}{E_a} = 0.67 \quad \text{Modular ratio}$$

$$A_i := A_a + n \cdot A_{sp} = 8.155 \times 10^4 \cdot \text{mm}^2 \quad \text{Area of composite section}$$

$$z_G := \frac{h_{\text{cell}}}{2} = 46 \cdot \text{mm} \quad z_a := h_{\text{cell}} + \frac{h_a}{2} = 342 \cdot \text{mm} \quad \text{Neutral axis (from top)}$$

$$z_{el} := \frac{(z_a \cdot A_a + z_G \cdot A_{sp} \cdot n)}{A_i} = 87.93 \cdot \text{mm} \quad \text{Elastic neutral axis of composite section: located in BEAM}$$

$$I_i := I_a + A_a \cdot (z_a - z_{el})^2 + n \cdot [I_{sp} + A_{sp} \cdot (z_G - z_{el})^2] = 1.464 \times 10^5 \cdot \text{cm}^4 \quad \text{Second moment of area - composite section}$$

$$W_{a,el} := \frac{I_i}{(h_{\text{cell}} + h_a - z_{el})} = 2.904 \times 10^3 \cdot \text{cm}^3 \quad W_{G,el} := \frac{I_i}{n \cdot z_{el}} = 2.483 \times 10^4 \cdot \text{cm}^3 \quad \text{Elastic section moduli}$$

Plastic Resistance: Full shear connection

$$F_G := A_{sp} \cdot f_{c,Rd2} = 2.985 \times 10^3 \cdot \text{kN} \quad \text{Force in FSL}$$

$$F_a := A_a \cdot \frac{f_y}{\gamma_{M,a}} = 4.101 \times 10^3 \cdot \text{kN} \quad \text{Force in Steel}$$

$$z_w := \frac{F_G}{\left(\frac{2 \cdot t_w \cdot f_y}{\gamma_{M,a}} \right)} = 0.412 \cdot \text{m}$$

$$z_{pl} := \frac{F_a}{F_G} \cdot h_{\text{cell}} = 126.402 \cdot \text{mm} \quad \text{Plastic neutral axis}$$

$$M_{pl,a,Rd} := W_{pl,a} \cdot \frac{f_y}{\gamma_{M,a}} = 778.977 \cdot \text{kN} \cdot \text{m} \quad \text{Plastic moment resistance of steel beam}$$

$$M_{pl,Rd} := M_{pl,a,Rd} + F_G \cdot \left(\frac{h_a}{2} + \frac{h_{\text{cell}}}{2} - \frac{z_w}{2} \right) = 1.047 \times 10^3 \cdot \text{kN} \cdot \text{m} \quad \text{Plastic moment resistance of composite beam}$$

$$V_{c,Rd} := A_v \cdot \frac{f_y}{\sqrt{3}} = 1.227 \times 10^3 \cdot \text{kN} \quad \text{Shear resistance of steel beam}$$

$$\frac{M_{a,Ed}}{M_{pl,a,Rd}} = 0.348$$

$$\frac{M_{Ed}}{M_{pl,Rd}} = 0.935$$

$$\frac{V_{Ed}}{V_{c,Rd}} = 0.199$$

Gurtler Method

Cross-section 1

$$E_1 := E_{xx} = 146.07 \text{ GPa}$$

$$n_1 := \frac{E_a}{E_{xx}} = 1.438$$

$$A_1 := t_{\text{skin}} \cdot b_{\text{eff}} = 5.22 \times 10^4 \cdot \text{mm}^2$$

$$I_1 := \frac{t_{\text{skin}}^3 \cdot b_{\text{eff}}}{12} = 6.264 \times 10^5 \cdot \text{mm}^4$$

$$e_1 := \left(h_a + h_{\text{cell}} - \frac{t_{\text{skin}}}{2} \right) - \left(\frac{h_a + t_{\text{skin}}}{2} \right) = 330 \cdot \text{mm}$$

$$K := \frac{0.5 \text{ MPa}}{h_{\text{cell}}} = 5.435 \times 10^{-3} \cdot \frac{\text{N}}{\text{mm}^3}$$

$$b_1 := \left[\frac{(E_1 \cdot A_1 + E_2 \cdot A_2) \cdot K \cdot b_{\text{eff}}}{E_1 \cdot A_1 \cdot E_2 \cdot A_2} + \frac{K \cdot b_{\text{eff}} \cdot e_1^2}{(E_1 \cdot I_1 + E_2 \cdot I_2)} \right]^{\frac{1}{2}}$$

$$b_1^2 = 3.084 \times 10^{-8} \cdot \frac{1}{\text{mm}^2}$$

$$\lambda_1 := b_1^2 \cdot L^2 = 7.896$$

Cross-section 2

$$E_2 := E_a = 210 \text{ GPa}$$

$$A_2 := A_a + \left(t_{\text{skin}} \cdot \frac{b_{\text{eff}}}{n_1} \right) = 4.786 \times 10^4 \cdot \text{mm}^2$$

$$I_2 := I_a + \frac{t_{\text{skin}}^3 \cdot \frac{b_{\text{eff}}}{n_1}}{12} = 4.824 \times 10^8 \cdot \text{mm}^4$$

Distance between neutral axis of each cross-section

Input from Gurtler thesis

$$\xi := 0.5 \quad \text{Mid-span location coefficient}$$

Geometry, stiffness and material parameters

$$B := E_1 \cdot I_1 + E_2 \cdot I_2 + \frac{E_1 \cdot A_1 \cdot E_2 \cdot A_2 \cdot e_1^2}{E_1 \cdot A_1 + E_2 \cdot A_2} = 5.736 \times 10^5 \cdot \text{kN} \cdot \text{m}^2$$

Total bending stiffness of composite section

Longitudinal

Deflections

$$w_a := \frac{5 \cdot g_{SW} L^4}{384 \cdot E_a \cdot I_a} = 52.846 \text{ mm}$$

Deflection of beam if solely taking entire self-weight

$$\alpha_c := 1$$

$$\Delta w_a := \frac{5 \cdot \Delta q \cdot L^4}{384 \cdot E_a \cdot I_a} = 0$$

$$w_c := \alpha_c \cdot (w_a + \Delta w_a) = 52.846 \text{ mm}$$

$$k_{sc} := 2 \frac{70 \text{ kN}}{\text{mm}} = 1.4 \times 10^8 \frac{\text{kg}}{\text{s}^2}$$

Shear stiffness of one row of connectors

$$\eta := 1 \quad s_{sc,\eta} := \frac{L \cdot P_{Rd} \cdot 0}{\eta \cdot N_{cf}} = 0$$

Assuming infinitely stiff shear connection (adhesive)

$$w_{\max} := \frac{L}{250} = 64 \text{ mm}$$

Limiting deflection

$$I_{i,\text{eff},100} := I_a + \frac{n \cdot A_{sp} \left(\frac{h_a}{2} + \frac{h_{\text{cell}}}{2} \right)^2}{1 + \frac{n \cdot A_{sp}}{A_a} + \frac{\pi^2}{L^2} \cdot \frac{E_a \cdot s_{sc,\eta}}{k_{sc}} \cdot n \cdot A_{sp}} = 1.351 \times 10^9 \cdot \text{mm}^4$$

Second moment of area - composite section taking into account infinite stiffness of shear connection

$$w_{\text{FEALT}} := 25.20 \text{ mm}$$

$$w_{\text{FEA,ULS}} := 99.39 \text{ mm}$$

$$UC_{\text{FEA}} := \frac{w_{\text{FEALT}}}{w_{\max}} = 0.394$$

$$EI_{\text{FEA}} := \frac{5}{384} \cdot \frac{(q_{\text{ULS}} \cdot b) \cdot L^4}{w_{\text{FEA,ULS}}} = 2.626 \times 10^5 \cdot \text{kN} \cdot \text{m}^2$$

$$E_a \cdot I_{i,\text{eff},100} = 2.837 \times 10^5 \text{ m}^4 \cdot \frac{\text{kN}}{\text{m}^2}$$

$$w_{\text{comp,SW}} := \frac{5 \cdot g_{SW} L^4}{384 \cdot EI_{\text{FEA}}} = 20.369 \text{ mm}$$

Vibrations

$$w_{\text{sw,d},100} := \frac{5}{384} \cdot \frac{(g_{SW} + g_2 + 0.1 \cdot q) \cdot L^4}{EI_{\text{FEA}}} = 32.554 \text{ mm}$$

Deflection due to dead-load and 10% of imposed load.

$$f_{100} := \frac{18}{\left(\frac{w_{\text{sw,d},100}}{\text{mm}} \right)^2} \cdot \text{Hz} = 3.155 \text{ Hz}$$

$$UC_{3\text{Hz},100} := \frac{3\text{Hz}}{f_{100}} = 0.951$$

Transverse

	Area (mm ²)	z (mm)	I _c (mm ⁴)	d (mm)	I _x (mm ⁴)
Btm Skin	12000	6	144000	40	19344000
Top Skin	12000	86	144000	40	19344000
Webs	3740	46	1441147	0	1441147
					40129147

$$\delta_{\max,trans} := \frac{b}{250} = 20 \cdot \text{mm}$$

$$I_x = I_c + A \cdot d^2$$

$$I_{sp,1m} := 40129147 \text{mm}^4$$

$$n_{w,1m} := \frac{1m}{b_{web}} + 1 = 11$$

$$G_{xy,web} = 2.64 \times 10^4 \cdot \text{MPa}$$

$$G_c := \frac{n_{w,1m} \cdot t_{web}}{1m} \cdot G_{xy,web} \cdot \frac{5}{6} = 1.21 \cdot \text{GPa}$$

$$I_{sp,1m} = 4.013 \times 10^7 \cdot \text{mm}^4$$

$$f_1 := \frac{1}{384} \cdot (q_{SLS}) \cdot 1m \cdot b^4$$

$$f_2 := (q_{SLS}) \cdot \frac{(1m)^2}{8}$$

$$w_1 := \frac{f_1}{E_{xx} \cdot I_{sp,1m}} = 0.417 \cdot \text{mm}$$

$$w_2 := \frac{f_2}{(G_c \cdot h_{cell})} = 1.684 \times 10^{-3} \cdot \text{mm} \quad \Delta_{HC} := w_1 + w_2 = 0.418 \cdot \text{mm}$$

$$\frac{w_1}{\eta_{c,t,L}} = 0.798 \cdot \text{mm}$$

$$\frac{w_2}{\eta_{c,t,T}} = 3.899 \times 10^{-3} \cdot \text{mm}$$

$$\delta_{SLS} := \frac{w_1}{\eta_{c,t,L}} + \frac{w_2}{\eta_{c,t,T}} = 0.802 \cdot \text{mm}$$

$$w_{FEA,trans} := 1.38 \text{mm}$$

$$UR := \frac{\delta_{SLS}}{\delta_{\max,trans}} = 0.04$$

$$\frac{w_{FEA,trans}}{\delta_{\max,trans}} = 0.069$$

Concentrated Force

$$n_{w,Q,1} := 2$$

$$G_{c,Q} := \frac{n_{w,Q,1} \cdot t_{web}}{1m} \cdot G_{xy,web} \cdot \frac{5}{6} = 220 \cdot \text{MPa}$$

$$k_{tim} := \frac{80}{192 + 33 \cdot \frac{v_{TL} \cdot G_{LT}}{E_{Lc,ax}}} = 0.409$$

$$f_{1,Q} := \frac{Q_k \cdot b^3}{192}$$

$$f_{2,Q} := Q_k \cdot \frac{b}{4 \cdot 1m}$$

$$w_{1,Q} := \frac{f_{1,Q}}{E_{xx} \cdot I_{sp,1m}} = 1.111 \cdot \text{mm}$$

$$w_{2,Q} := \frac{f_{2,Q}}{k_{tim} \cdot (G_{c,Q} \cdot h_{cell})} = 1.51 \cdot \text{mm}$$

$$\Delta_Q := w_{1,Q} + w_{2,Q} = 2.621 \cdot \text{mm}$$

$$\delta_{SLS,Q} := \frac{w_{1,Q}}{\eta_{c,st}} + \frac{w_{2,Q}}{\eta_{c,st}} = 3.595 \cdot \text{mm}$$

$$\frac{\delta_{SLS,Q}}{\delta_{\max,trans}} = 0.18$$

Facing Failure

Longitudinal

$$\sigma_{f.Sd.FEA} := 28.30 \text{ MPa}$$

$$\frac{\sigma_{f.Sd.FEA}}{f_{f.L.Rd2}} = 0.934$$

$$\sigma_{f.Sd.Qk.local.FEA} := 8.25 \text{ MPa}$$

$$\frac{\sigma_{f.Sd.Qk.local.FEA}}{f_{f.L.Rd2}} = 0.272$$

$$\epsilon_{L.Rd} := \eta_{c.s.L} \cdot \frac{1.2}{\gamma_{M2}} = 0.497$$

$$\epsilon_{L.Sd} := 0.033$$

$$\frac{\epsilon_{L.Sd}}{\epsilon_{T.Rd}} = 0.08$$

$$q_{ULS} = 6.117 \frac{\text{kN}}{\text{m}^2}$$

Transverse

$$\sigma_{f.Sd.db.FEA} := 51.09 \text{ MPa}$$

$$\frac{\sigma_{f.Sd.db.FEA}}{f_{f.L.Rd}} = 0.553$$

$$\sigma_{f.Sd.Qk.local.FEA.db} := 20.76 \text{ MPa}$$

$$\frac{\sigma_{f.Sd.Qk.local.FEA.db}}{f_{f.L.Rd}} = 0.225$$

$$\epsilon_{T.Rd} := \eta_{c.s.T} \cdot \frac{1.2}{\gamma_{M2}} = 0.414$$

$$\epsilon_{T.Sd} := 0.061$$

$$\frac{\epsilon_{T.Sd}}{\epsilon_{L.Rd}} = 0.123$$

Transverse Shear Failure

$$V_{Edt} := q_{ULS} \cdot \frac{b}{2} \cdot 1\text{m} = 15.294 \text{ kN}$$

$$\tau_{w.Ed} := \frac{V_{Edt}}{n_{w.1m} \cdot t_{web} \cdot h_c} = 4.089 \text{ MPa}$$

$$f_{V.d} := \eta_{c.s.T} \cdot \frac{\tau_{12R}}{\gamma_{M.s}} = 25.663 \text{ MPa}$$

$$\frac{\tau_{w.Ed}}{f_{V.d}} = 0.159$$

Concentrated Force

$$V_{Ed.Q} := \frac{Q_k}{2} = 5 \text{ kN}$$

$$\tau_{w.Ed.Q} := \frac{V_{Ed.Q}}{n_{w.Q.1} \cdot h_c \cdot t_{web}} = 7.353 \text{ MPa}$$

$$\frac{\tau_{w.Ed.Q}}{f_{V.d}} = 0.287$$

Beam Failure

$$\sigma_{beam} := 350.4 \text{ MPa}$$

$$\frac{\sigma_{beam}}{f_y} = 0.987$$

Instability

Local Buckling of Webs

JRC Method

$$\sigma_{y,nom} := \frac{Q_k}{n_{w,Q,1} \cdot a_{Qk} \cdot t_{web}} = 10 \cdot \text{MPa}$$

$$\sigma_{y,max,FEA} := 9.6 \text{MPa}$$

$$b_{eff,webs} := a_{Qk} \cdot \frac{\sigma_{y,nom}}{\sigma_{y,max,FEA}} = 104.167 \cdot \text{mm}$$

$$N_{y,cr} := \frac{\pi^2}{b_{eff,webs}^2} \cdot \left[4.53 \cdot \left[(D_{11y} \cdot D_{22y})^{\frac{1}{2}} \right]^2 + 2.44 \cdot (D_{12y} + 2 \cdot D_{66y}) \right] = 9.318 \times 10^3 \cdot \frac{\text{kN}}{\text{m}}$$

$$\sigma_{cr,JRC} := \frac{N_{y,cr}}{t_{web}} = 1.864 \times 10^3 \cdot \text{MPa}$$

$$\frac{\sigma_{y,max,FEA}}{\sigma_{cr,JRC}} = 5.151 \times 10^{-3}$$

Kassapoglou Method

$$\lambda := \frac{h_c}{b_{eff,webs}} \cdot \left(\frac{D_{22y}}{D_{11y}} \right)^{0.25} = 0.659 \quad m_b := 1$$

$$K_1 := \frac{m_b^4 + 8 \cdot m_b^2 + 1}{\lambda^2 \cdot (m_b^2 + 1)} + 2 \cdot \frac{(D_{12y} + 2 \cdot D_{66y})}{\sqrt{D_{11y} \cdot D_{22y}}} + \frac{\lambda^2}{m_b^2 + 1} = 13.219$$

$$N_o := \left(\frac{\pi^2}{b_{eff,webs}^2} \cdot \sqrt{D_{11y} \cdot D_{22y}} \cdot K_1 \right) = 1.943 \times 10^4 \cdot \frac{\text{N}}{\text{mm}}$$

$$\sigma_{cr,Kass} := \frac{N_o}{t_{web}} = 3.886 \cdot \text{GPa}$$

$$\frac{\sigma_{y,max,FEA}}{\sigma_{cr,Kass}} = 2.47 \times 10^{-3}$$

Face Wrinkling

$$\lambda_{fw} := 21.8$$

$$\sigma_{c,skin,FEA} := \sigma_{fSd,FEA} = 28.3 \cdot \text{MPa}$$

$$\sigma_{wr,FEA,Rd} := \frac{\eta_{c,b}}{\gamma_{M2,b}} \cdot \sigma_{fSd,FEA} \cdot \lambda_{fw} = 299.833 \cdot \text{MPa}$$

$$\frac{\sigma_{c,skin,FEA}}{\sigma_{wr,FEA,Rd}} = 0.094$$

Shear Crimping

$$P_{cs,Rd,2} := \frac{\eta_{c,s,L}}{\gamma_{M2}} \cdot \frac{G_{xy} \cdot t_{web}}{k_3} = 7.326 \times 10^4 \cdot \frac{\text{kN}}{\text{m}} \quad k_3 := 1$$

$$\sigma_{c,skin,FEA,1} := \sigma_{c,skin,FEA} = 28.3 \cdot \text{MPa}$$

$$\sigma_{s,crimp,Rd} := \frac{P_{cs,Rd,2}}{t_{skin}} = 6.105 \times 10^3 \cdot \text{MPa}$$

$$\frac{\sigma_{c,skin,FEA,1}}{\sigma_{s,crimp,Rd}} = 4.636 \times 10^{-3}$$

Global Buckling

$$\lambda_{global} := 2.46$$

$$\sigma_{global,FEA,Rd} := \frac{\eta_{c,b}}{\gamma_{M2,b}} \cdot \sigma_{fSd,FEA} \cdot \lambda_{global} = 33.834 \cdot \text{MPa}$$

$$\frac{\sigma_{c,skin,FEA}}{\sigma_{global,FEA,Rd}} = 0.836$$

$$\sigma_{c,skin,FEA,2} := \sigma_{fSd,db,FEA} = 51.09 \cdot \text{MPa}$$

$$\frac{\sigma_{c,skin,FEA,2}}{\sigma_{s,crimp,Rd}} = 8.369 \times 10^{-3}$$

Global

$$\frac{M_{a.Ed}}{M_{pl.a.Rd}} = 0.348 \quad \frac{M_{Ed}}{M_{pl.a.Rd}} = 1.257 \quad \frac{M_{Ed}}{M_{pl.Rd}} = 0.935 \quad \frac{V_{Ed}}{V_{c.Rd}} = 0.199 \quad \frac{M_{a.Ed} + \Delta M_{a.Ed}}{M_{pl.a.Rd}} = 0.348 \quad \frac{\sigma_{beam}}{f_y} = 0.987$$

Global Deflection/Vibration

Transverse

$$\frac{w_{FEA.LT}}{w_{max}} = 0.394 \quad \frac{\delta_{SLS}}{\delta_{max.trans}} = 0.04 \quad \frac{w_{FEA.trans}}{\delta_{max.trans}} = 0.069 \quad \frac{\delta_{SLS.Q}}{\delta_{max.trans}} = 0.18$$
$$\frac{3Hz}{f_{100}} = 0.951$$

Facing Failure (longitudinal)

$$\frac{\sigma_{f.Sd.FEA}}{f_{f.t.Rd2}} = 0.99 \quad \frac{\sigma_{f.Sd.Qk.local.FEA}}{f_{f.t.Rd2}} = 0.289 \quad \frac{\epsilon_{L.Sd}}{\epsilon_{T.Rd}} = 0.08$$

Facing Failure (transverse)

$$\frac{\sigma_{f.Sd.db.FEA}}{f_{f.t.Rd}} = 0.566 \quad \frac{\sigma_{f.Sd.Qk.local.FEA.db}}{f_{f.t.Rd}} = 0.23 \quad \frac{\epsilon_{T.Sd}}{\epsilon_{L.Rd}} = 0.123$$

Transverse Shear Failure

$$\frac{\tau_{w.Ed}}{f_{v.d}} = 0.159 \quad \frac{\tau_{w.Ed.Q}}{f_{v.d}} = 0.287$$

Face Wrinkling

Local Buckling of Webs

Global Buckling

$$\frac{\sigma_{c.skin.FEA}}{\sigma_{wr.FEA.Rd}} = 0.094 \quad \frac{\sigma_{y.nom}}{\sigma_{cr.JRC}} = 5.366 \times 10^{-3} \quad \frac{\sigma_{y.max.FEA}}{\sigma_{cr.Kass}} = 2.47 \times 10^{-3} \quad \frac{\sigma_{c.skin.FEA}}{\sigma_{global.FEA.Rd}} = 0.836$$

Shear Crimping

$$\frac{\sigma_{c.skin.FEA.1}}{\sigma_{s.crimp.Rd}} = 4.636 \times 10^{-3} \quad \frac{\sigma_{c.skin.FEA.2}}{\sigma_{s.crimp.Rd}} = 8.369 \times 10^{-3}$$

APPENDIX C: HYBRID SYSTEM FINITE ELEMENT MODEL

The finite element model used for this case study was created using Abaqus CAE 6.14. The elements used were of a quadrilateral shape, utilising shell elements (S4R) for the beam and deck structures and solid elements (C3D8R) for the foam cores where applicable. Abaqus/Standard was used to obtain all of the data in this study, with Static/General used for the majority of the analyses whilst Linear Perturbation/Buckling was used for the buckling analysis disclosed in [section 4.3.5](#).

Model Geometry

In order to simplify the problem and reduce the calculation time, symmetry has been utilised in the lengthwise direction of the beam and across the width of the deck. These simplifications will be implemented through the use of boundary conditions at the planes shown in [figure C1](#).

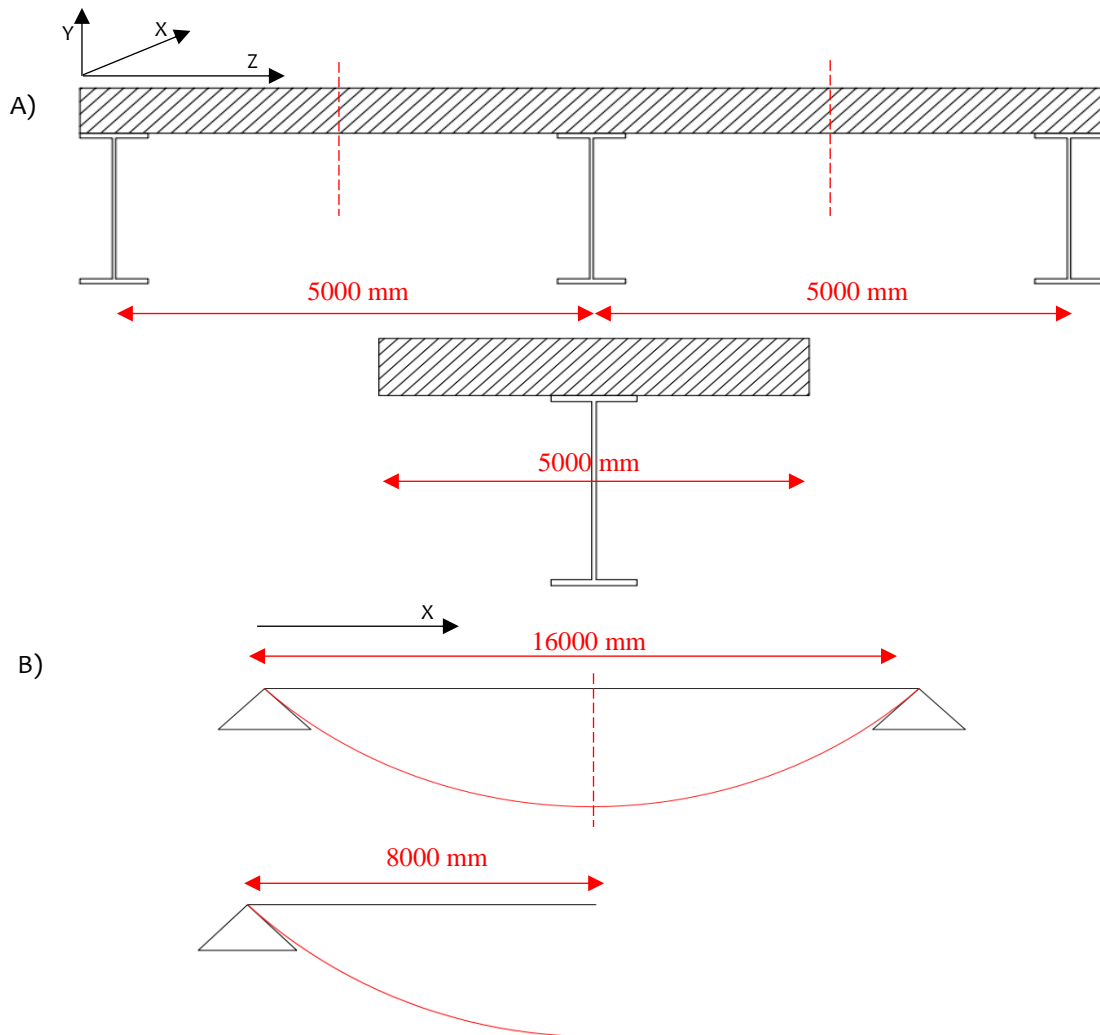
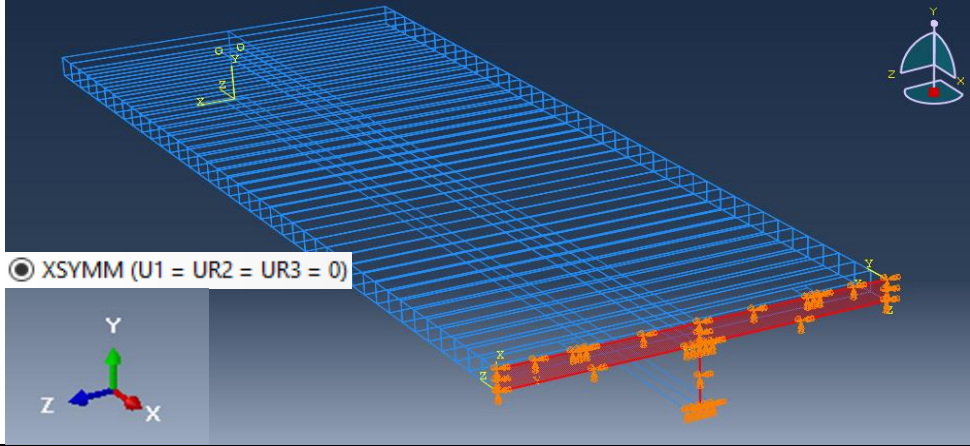
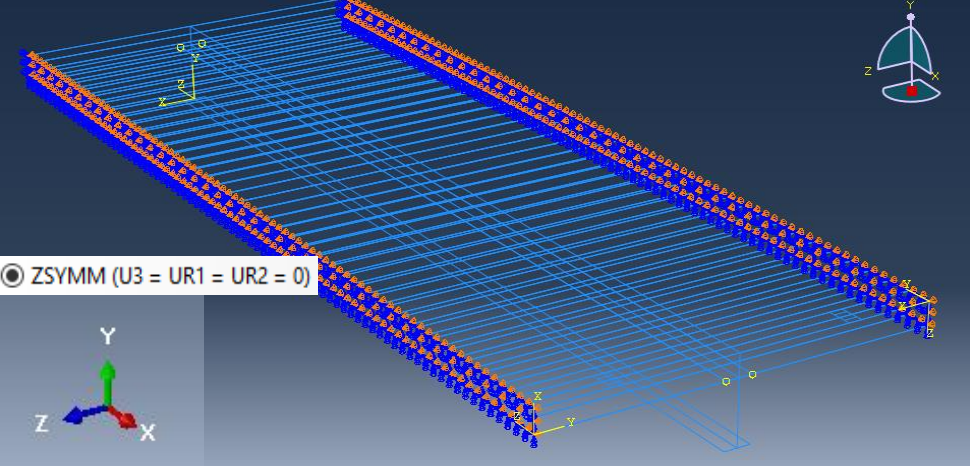


Figure C1: A) Deck span symmetry, B) Beam span symmetry

Boundary Conditions & Constraints

To enable the symmetry discussed in the previous section, boundary conditions are applied that simulate the mid-span location in each direction respectively. These are shown in the following table.

Table C.1: Symmetry boundary conditions

<p>Beam mid-span symmetry</p>	
<p>Deck span symmetry</p>	

The steel beams are treated as simply supported, so within the model, the displacements at the support end of the beam are restrained in the Y and Z directions. The deck at the end of the support is not restrained, other than its tie to the beam.

For the cellular decks, the foams that infill the gaps in between the skins are tied to their respective counter-faces and the underside of the deck is similarly tied to the top face of the upper flange of the beam. The beam-deck tie simulates an adhesive connection which will be assumed for the purpose of this study.

Evaluation of FE Model

The model has been designed so as to represent a central beam in a continuous system, this is enabled by the symmetry boundary conditions discussed above. Given this information, combined with knowledge acquired from the application of concrete-steel composite systems, the expected behaviour of the system is known. To evaluate the model, simple hand-calculations can be compared to the outcomes of the finite-element analysis to see how closely the model follows these behaviours.

Longitudinal Direction

As a rudimentary check of the model, the longitudinal bending moment at the mid-span can be compared between a simple hand calculation and the finite element models:

$$M_{Max} = \frac{q * L^2 * b}{8} = \frac{3.0kN/m^2 * 16m^2 * 5m}{8} = 480 kN.m$$

As can be seen from [figure C2](#), the bending moment in both solid slab and cellular models comply with the expected result from the hand-calculation.

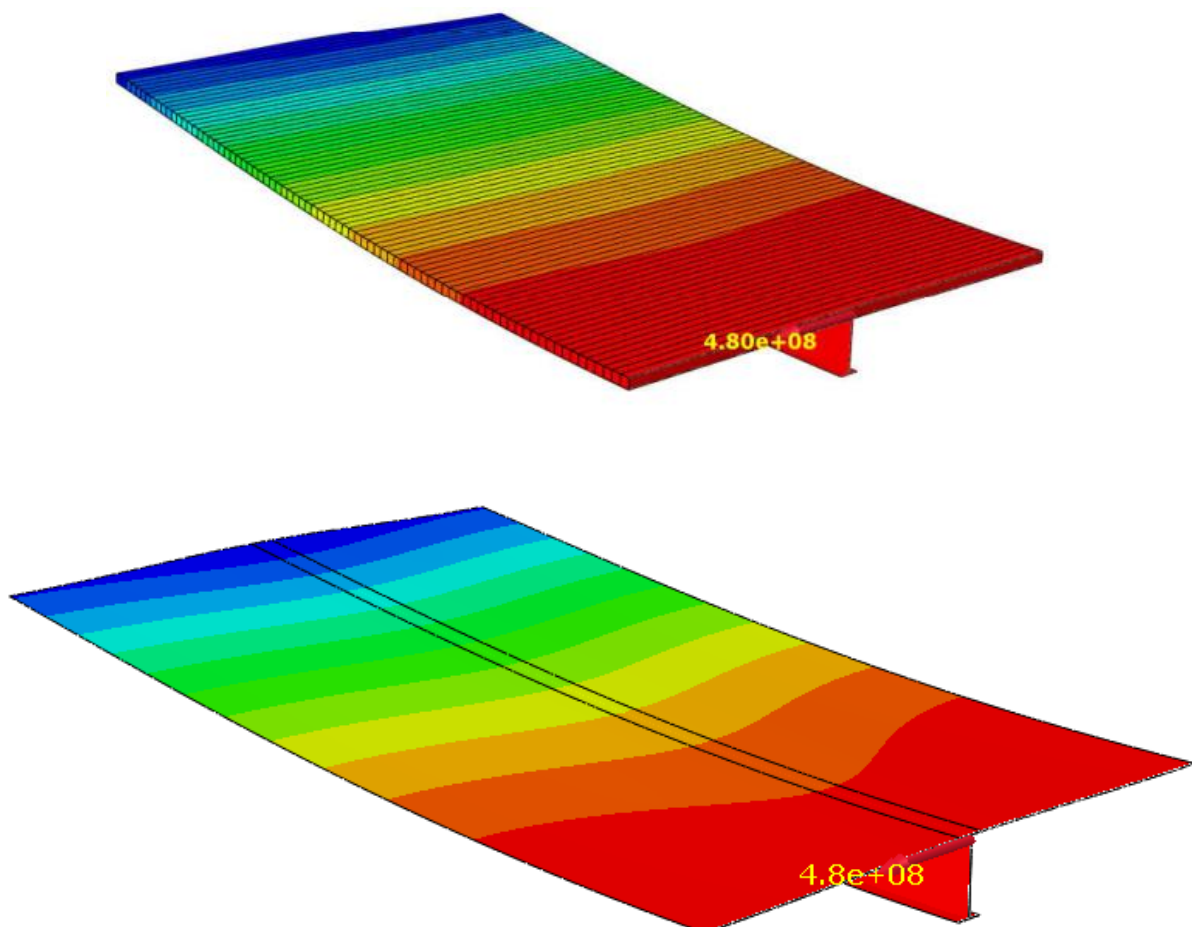


Figure C2: Longitudinal Bending Moment at Mid-Span in FE Model Expressed in N.mm

In the FE models, the beam and deck are tied emulating an adhesive connection, which provides full shear interaction, this means the shell elements in the model share the stresses between the deck and top flange of the beam at an approximate ratio of their stiffness. This is highlighted in figure C3 where the bottom skin is isolated and the longitudinal stresses are plotted across the width of the deck. The general shear lag trend can be observed (becoming more compressive as the beam is approached), however, the elements that share the beam connection show a decrease in stress. This is partly due to the differing degree of stiffness in the two materials, resulting in a stress that is shared, unlike the parts of the deck not in contact with the beam. A further reason for this behaviour is the redistribution of the stresses into the transverse direction. The amount of stress reduction in this area therefore depends on the difference in longitudinal Young's modulus between the deck and the beam, on the transverse Young's modulus of the deck and on the connection type.

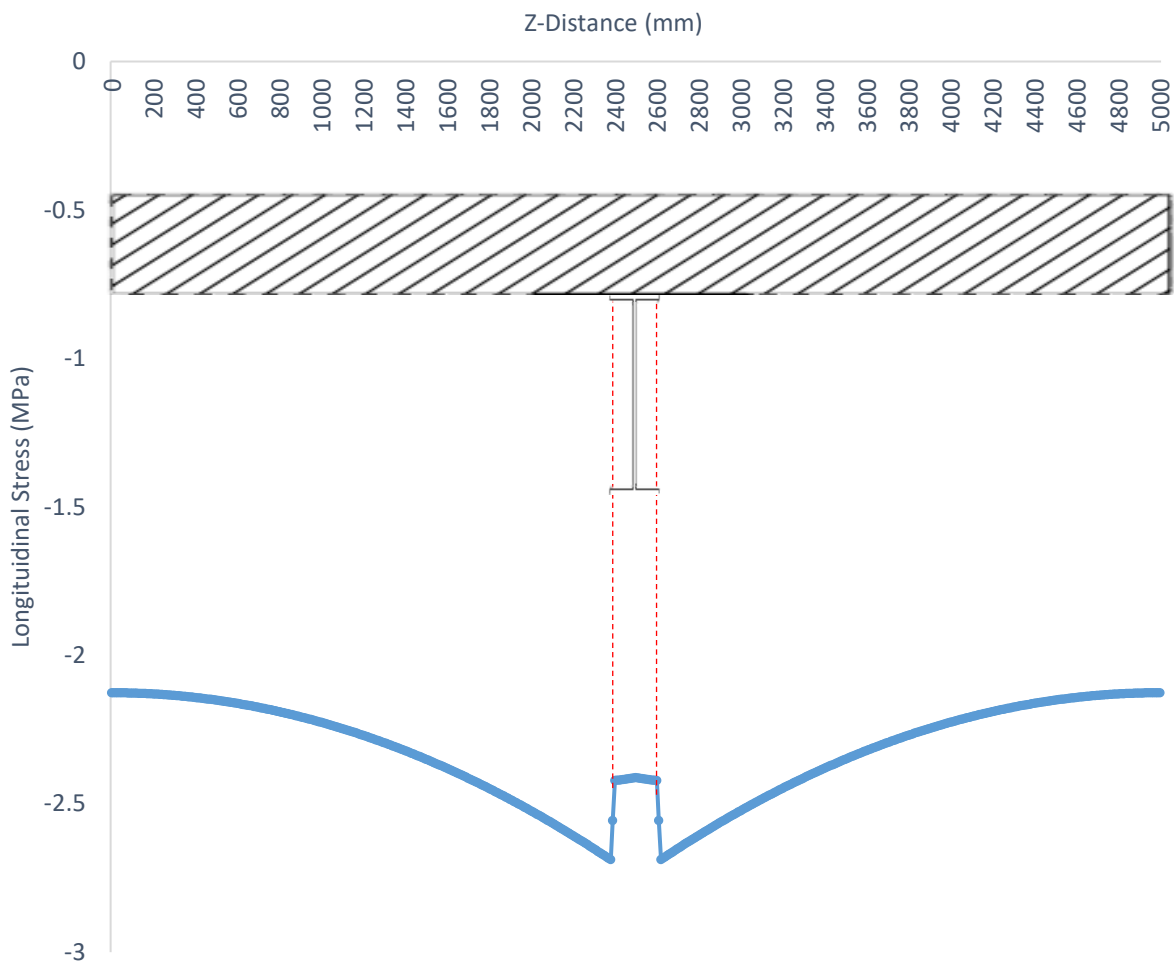


Figure C3: Reduction in Longitudinal Stress in Deck due to Interaction with Beam

Transverse Direction

In the transverse direction, the deck can be treated as a continuous beam. From this we can expect the following indicative values:

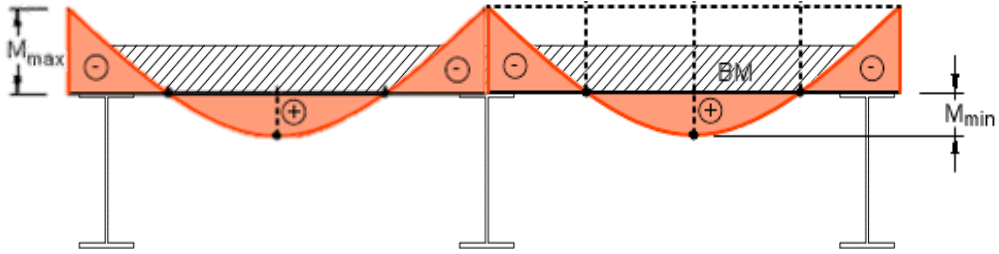
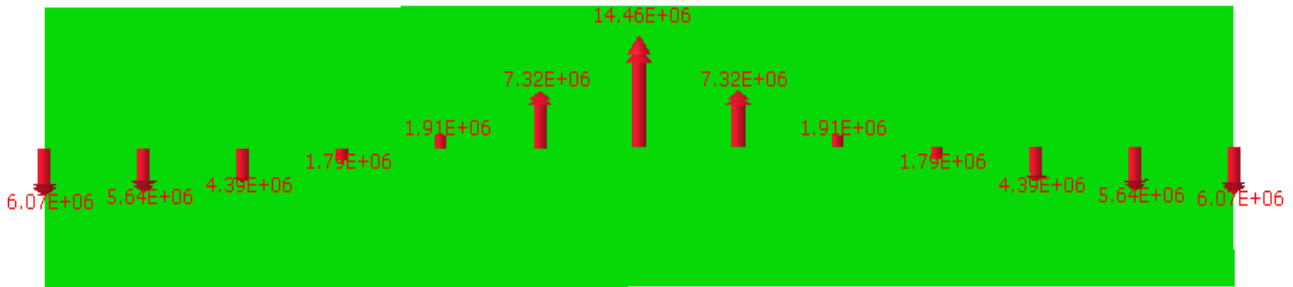


Figure C4: Theoretic Bending Moment Curve for Central Section of Continuous Beam

$$M_{min} = \frac{qb^2}{28} = \frac{2.68 \text{ kNm}}{m}$$

$$M_{max} = \frac{qb^2}{14} = \frac{5.35 \text{ kNm}}{m}$$



$$M_{min,support,FEA} = \frac{6.07 \text{ kNm}}{m}$$

$$M_{max,support,FEA} = \frac{14.46 \text{ kNm}}{m}$$

Figure C5: Transverse Bending Moment at Support Location from FE Model (N.mm/m)

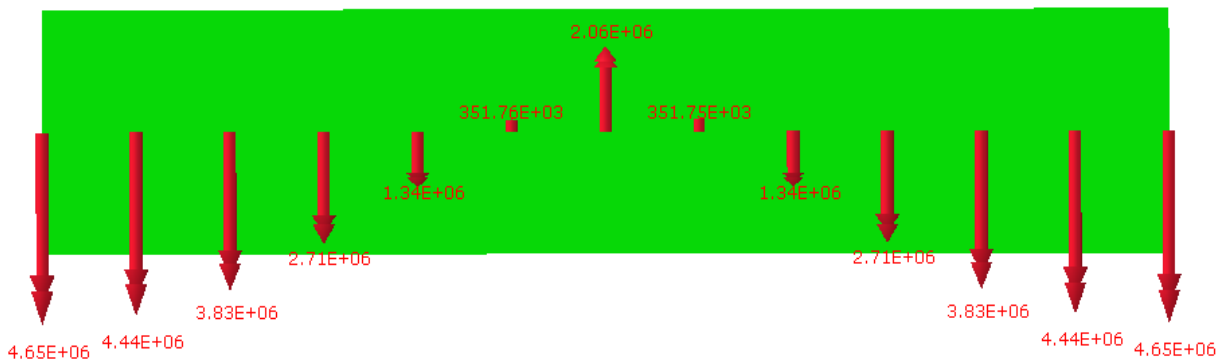


Figure C6: Transverse Bending Moment at mid-span Location from FE Model (N.mm/m)

$$M_{min,mid-span,FEA} = \frac{4.65 \text{ kNm}}{m}$$

$$M_{max,mid-span,FEA} = \frac{2.06 \text{ kNm}}{m}$$

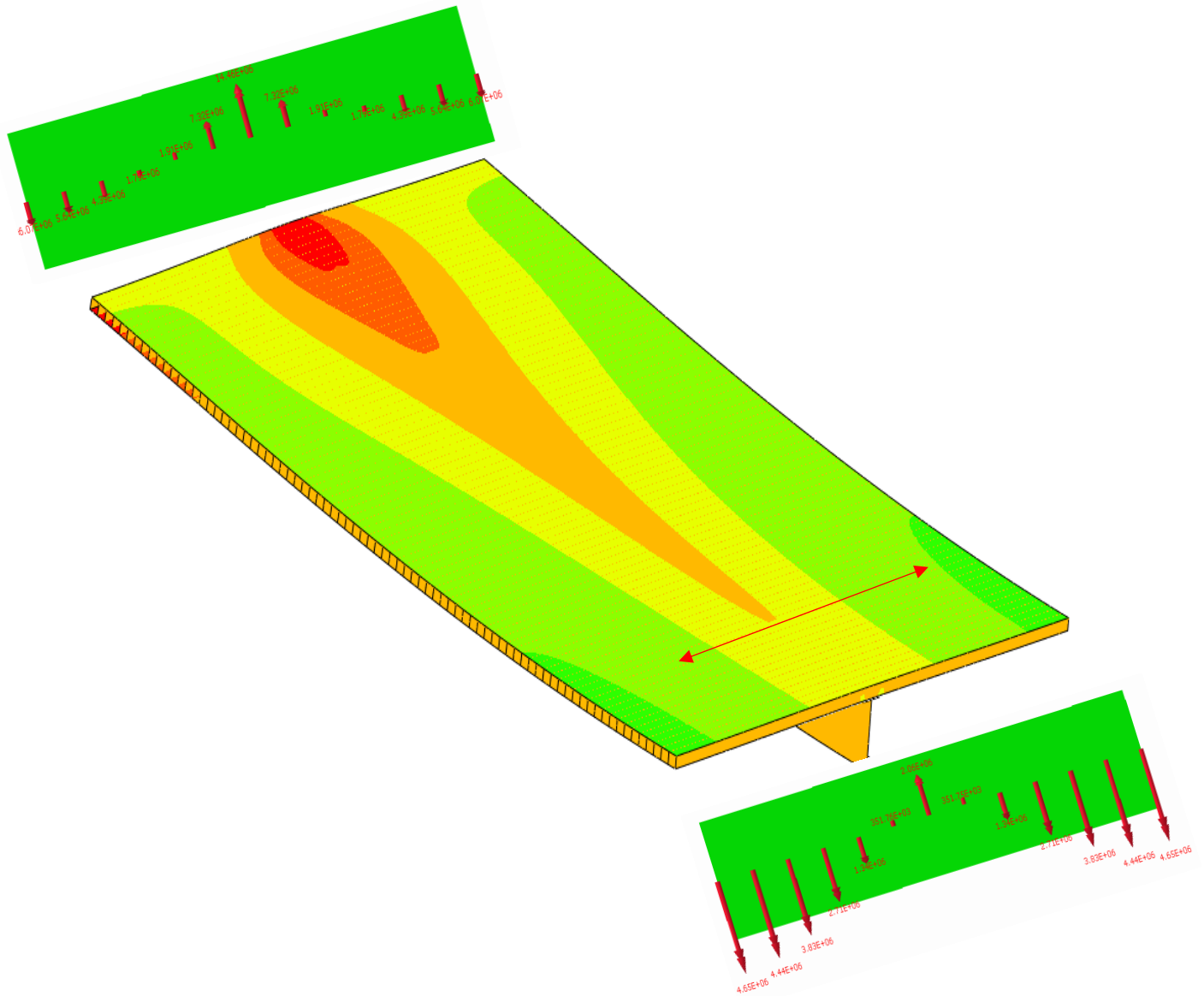


Figure C7: Transverse Stress Distribution Across Deck with Mid-Span and Support Location Transverse Moments Superimposed

In figure C5 & C6, the extremes of the FE image are the equivalent of the mid-span locations in the bending moment diagram from beam theory (figure C4). From the FE model, it can be seen that the values do not match with the beam theory values and that they vary with the position along the deck. Above the beams one would expect a hogging moment with an absolute value which is greater than the moment at mid-span – which is the case at the support location but is not the case at the mid-span location. This is due to the bending in the longitudinal direction and the effect this has on the transverse stress distribution moving along the span of the beam, shown in figure C7. Another reason for the difference in values is that the beam theory expects the formation of a hinge at the beam location, which isn't fully developed with the adhesive connection. Furthermore, the stresses have an interaction between the longitudinal and transverse directions through the Poisson's effect, which is not taken into account in the standardised beam formulae.

Shear Interaction

It is important to check that the deck and beam are connected correctly in the model and that this connection will simulate the desired shear interaction properties expected from an adhesive connection.

A simple way to determine if the system has composite interaction or not is to look at the vertical distribution of the longitudinal stresses and strains, at the mid-span cross section, shown in [figure C8](#). A further check can be to analyse the slip at the ends of the deck-beam interface. The indicative decks used in this example are 200mm deep GFRP cellular decks. In the system that has no interaction (orange line), the deck and beam bend individually (note compression at the top, tension at the bottom of each member). A system without interaction should also have two neutral axes, one in the deck and one in the beam. In the system with full interaction between the beam and deck (blue line), it can be seen that the whole system acts as one (with one slightly higher neutral axis – due to the increased stiffness), and that the deck acts solely in compression with the majority of the beam acting in tension.

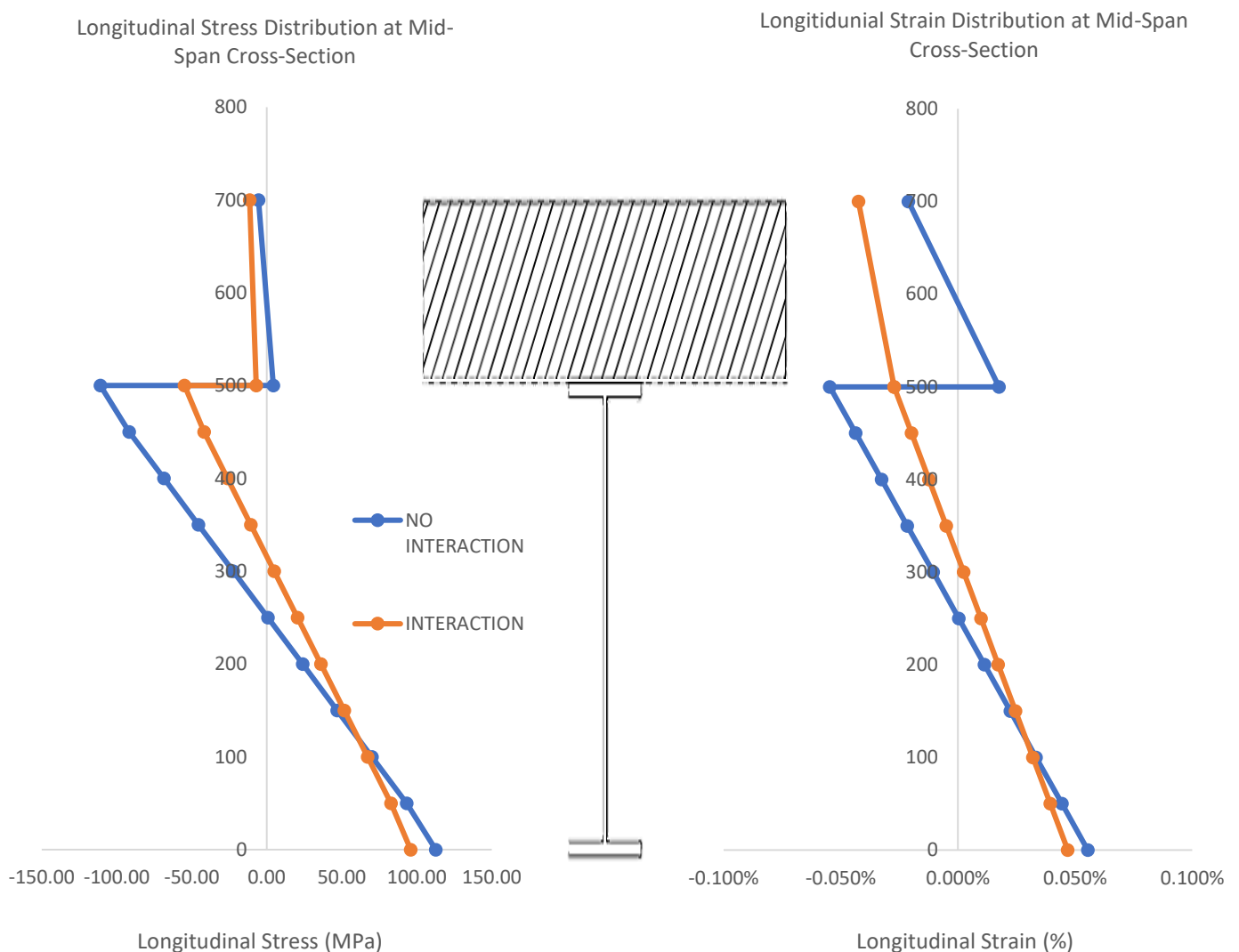


Figure C8: Stress and strain distribution at mid-span of beam plotted across vertical cross-section

When viewing the stresses and strains that occur longitudinally in the deck ([figure C9](#)), a similar difference can be seen. The bottom skin of the deck without interaction, is in tension due to the bending of the deck, however, the bottom skin of the deck with interaction is in compression due to it being above the neutral axis of the composite system. It is also noticeable that the compressive stress in the top skin of the composite deck is (two times) higher than the non-composite deck. This is because the top skin of the composite deck is ~390mm from the shared neutral axis rather than the non-composite deck where the top skin is only ~100mm from the deck's individual neutral axis.

The extra-capacity that this interaction allows can be seen from the comparison of force displacement curves generated by the FE models. Under the same loading applied, this composite deck system has a 32% lower deflection at mid-span than the deck with no interaction. The benefits of the interaction will be further explored in [section 4.4.2](#).

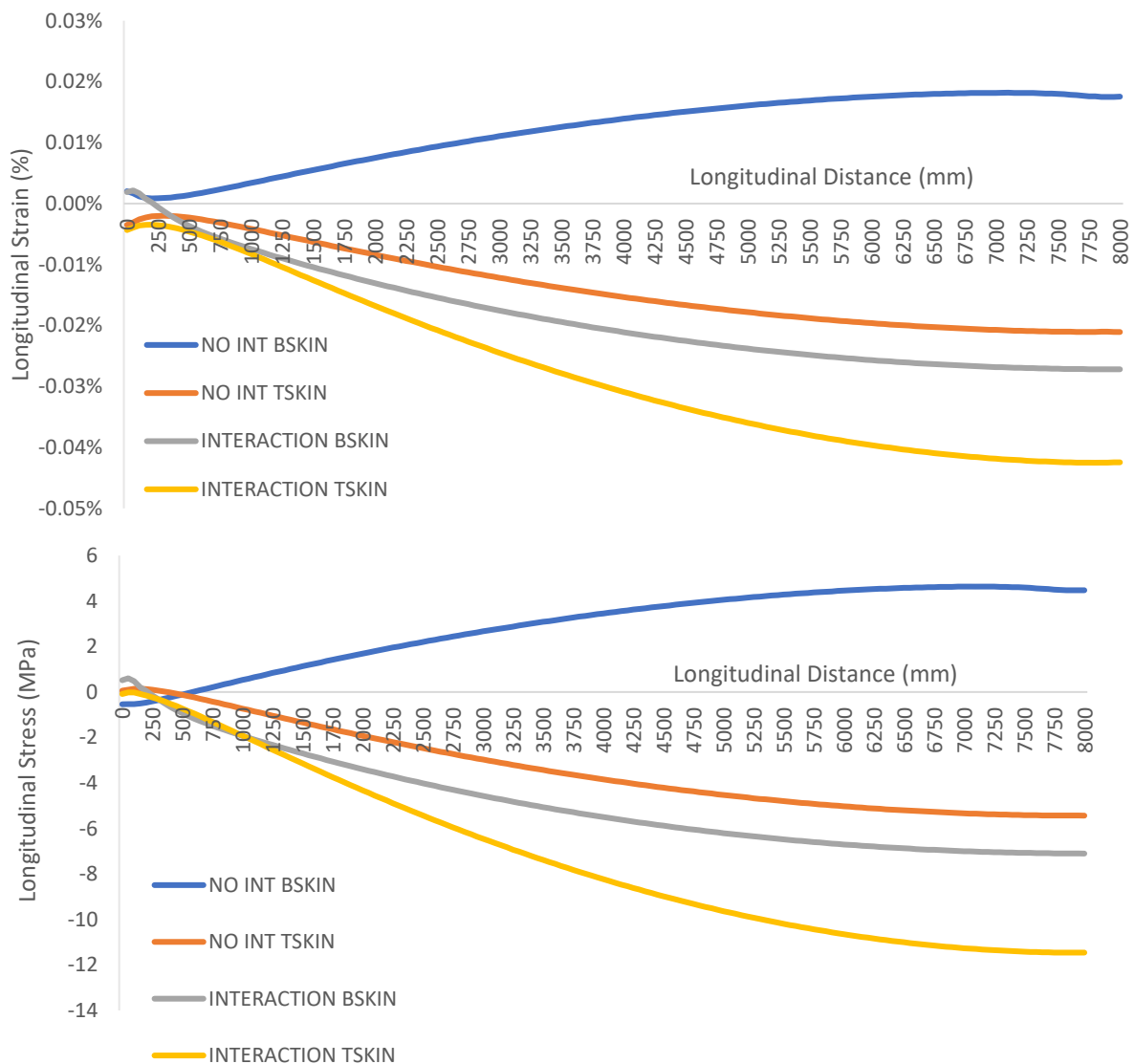


Figure C9: Longitudinal strain and stress distributions along length of deck (to mid-span)

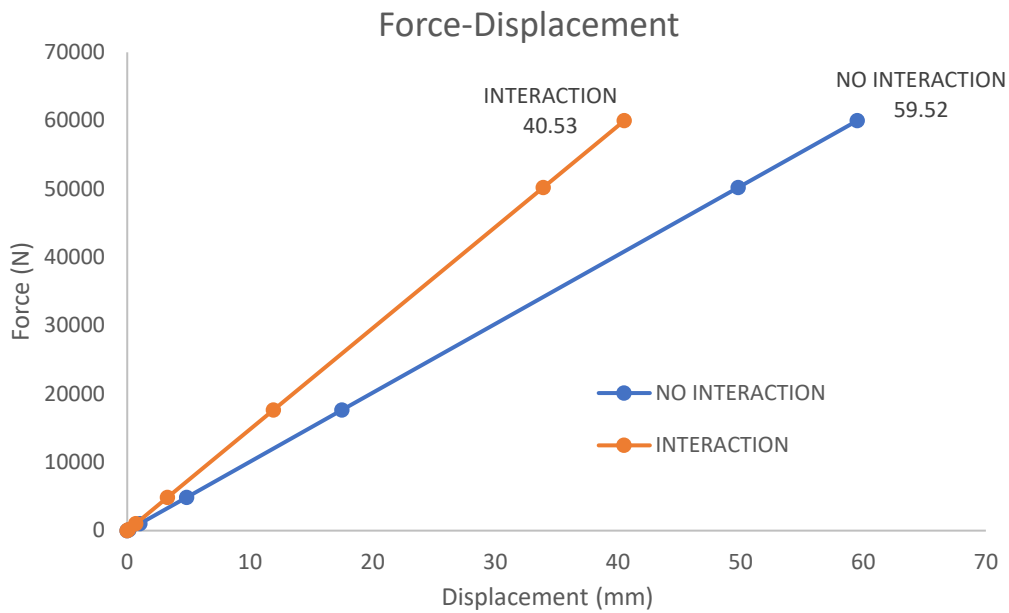


Figure C10: Force - displacement comparison between deck with and without shear interaction

Comparison with Hand-Calculations

In composite systems it can be difficult to estimate the stiffness of the system, due to the complex nature of the shear lag effect and the quantity of the deck that acts as part of the effective system. For this reason, two sets of analytical calculations will be compared to the outcome of the finite element model to gauge the suitability of the analytical methods for this application and material.

The first method presented is based on EN1994 which draws from knowledge of concrete-steel composite deck systems, which are generally solid slab type applications, but may also feature a slab with voids. The second method, Gurtler (53), stems from research of pultruded FRP-steel composite systems connected through an adhesive connection. This requires the composite cross-section to be split into two separate cross-sections, one comprising of the top skin of the deck and the other comprising the equivalent width of the bottom skin and the steel beam, see figure C11. This is based on the principle that if an adhesive connection is used to generate a full shear connection, then the flexible shear joint is actually between the deck skins rather than between the deck and the beam.

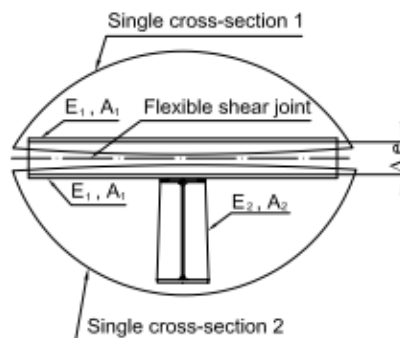


Figure C11: Single cross-section Definition (53)

To determine which hand-calculation model most accurately predicts the composite stiffness of the system, the global deflection from the FE model will be used in a rearranged formula for the deflection of a simply supported beam to give the composite stiffness according to the model. This does, however, neglect the influence of shear deflection. It should also be noted that, for the cellular decks, due to the Vierendeel effect occurring in the webs of the deck, the composite stiffness achieved at the centre of the deck is the maximum and will decrease as proximity to the supports increases. For example, the FE analysis gives a longitudinal composite stiffness for the FSL cellular deck of approximately 214850 kNm² at a distance of 2m from the support location.

Table C2: Composite section stiffness comparison

	EN1994 Method (kN.m ²)	Gurtler Method (kN.m ²)	FE Analysis (kN.m ²)
FSL Cellular Deck & IPE500	283700	573600	262600
GFRP Cellular Deck & IPE500	190100	193900	178000
5m Solid Slab FSL Deck & IPE500	268200	260200	255900
2.5m Solid Slab FSL Deck & IPE500	232500	222600	208800

As per [table C2](#), it is clear to see that, excluding the FSL cellular deck, both methods yield values in reasonable agreement with the output from the FE model, however, it can be said that both methods are unconservative. The Gurtler method struggles with the FSL cellular deck, giving a value of almost double that of the FE analysis, this is likely because of the smaller difference in stiffness values between the deck and the beam ($E_{\text{steel}}/E_{\text{FSL-CELL}}=1.44$), when compared to the GFRP decks which have a much greater difference in stiffness values between the two ($E_{\text{steel}}/E_{\text{GFRP}}=10.88$).

In the transverse direction, the deflection is analytically calculated through the following:

$$\delta_{trans} = \frac{q * b^4}{384 * EI * \eta} + \frac{q * b^2}{8 * G_{23} * h_{cell} * \eta}$$

This value can be compared to the value from the FE model to gauge the accuracy of the hand calculations.

Table C3: Comparison of Transverse Deflections

	Hand Calculation (mm)	FE Model: Maximum Transverse Deflection (mm)	Difference
FSL Cellular Deck	0.80	1.38	-42%
GFRP Cellular Deck	4.16	5.97	-30%
5m Solid Slab FSL Deck	3.83	2.40	60%
2.5m Solid Slab FSL Deck	1.37	0.65	110%

It should be noted that the maximum transverse deflection of the deck in each of these cases, is found at the support section of the beam rather than at the mid-span of the beam. This is consistent with the higher transverse stresses being found here as shown in [figure C7](#). For the purpose of the verifications the maximum value for each deck will be used.

Outcomes

The composite systems studied in this research, involve many complexities regarding; geometry, composite interaction, connection type, redistribution of stresses and material anisotropy. This means that finite element analysis is essential and that analytical hand calculations provide only estimates.

From the analysis of the systems with and without the tie constraint between the deck and the beam it can be seen that the tie constraint does in fact provide the shear interaction desired. Due to this interaction and some redistribution into the transverse direction, there is a reduction in stress at the flange-deck interface.

The longitudinal composite stiffness of decks in solid slab form or in cellular form, using either GFRP or FSL can be reasonably predicted by the method given in EN1994 (54). The Gurtler (53) method predicts the composite stiffness of cellular decks less accurately and is more suited to FRP based composite decks where the modular ratio is much higher than in FSL decks. If the Gurtler method is adapted to fit solid slab decks, the composite stiffness can be reasonably estimated although an overestimation is often found (see [table C3](#)).

The transverse deflection of the decks varies significantly along the length of the system, due to the interaction of the bending in the longitudinal direction. For this reason, it becomes difficult to accurately predict the transverse deflection using analytical methods.

APPENDIX D: BASE MATERIAL COSTS

Steel S235	1.5	€/kg
GFRP	2	€/kg
IPE S355	1	€/kg
Labour	45	€/hr

APPENDIX E: SELF-SUPPORTING DECK ANALYSIS

For the purpose of examining the commercial viability of FSLs it is useful to look at a self-supporting deck that does not benefit from the extra stiffness afforded by a supporting girder. This will ensure that the stiffness the deck requires to satisfy design criteria is provided by the deck material itself.

To demonstrate this, a rudimentary case will be used, in which a 5m*30m simply supported cellular deck will be loaded with the SLS load case presented in [section 4.1.4.3.2](#) and compared on the basis of long term global deflection (creep coefficients applied).

FSL DECK

The design philosophy for the FSL deck is to try to maintain, where possible, the laminate used in the case-study, see [section 4.2.2.4](#). However, given the increased span, the thickness of each steel ply in the laminate of the skins was increased to 1.5mm, the laminate of the webs was maintained. The required centre-to-centre distance of the skins was found iteratively to be approximately 665mm.

GFRP DECK

Similarly, the layup of the GFRP cellular deck was maintained, but doubled in thickness in order to deal with the increased span. The thickness of the webs was also increased to 7mm. The required centre-to-centre distance of the GFRP skins was found iteratively to be approximately 990mm.

COST ANALYSIS

Based on the same methodology set out in [section 4.4.7](#), the costs of each deck can be evaluated as shown in the figure on the following page. It can be seen that with this application the FSL deck is able to provide the same performance (based only on long term global deflection), whilst using around 40% less material, resulting in a deck that is €65/m² cheaper (material costs).

It should be noted that this is a rudimentary analysis based only on the long term global deflection criteria, with the goal of indicating that in certain serviceability driven applications the use of FSL over GFRP can be financially beneficial.

	FSL Cellular Deck	GFRP Cellular Deck
Skin Thickness (mm)	16	24
Web Thickness (mm)	5	7
Total Deck Thickness (mm)	680	1015
Cross-sectional Area (m ²)	2.043	3.469
Material Cost (€/m ²)	737	802

System Cost Comparison

